Modification of Oxide Inclusions due to Steel-Slag Interactions with Special Focus on the Electroslag Remelting Process

A thesis submitted in partial fulfilment of the requirements for
the degree of a Doctor of Metallurgical and Mining Sciences
at the Montanuniversität Leoben

Presented by:
Dipl.-Ing. Susanne K. Michelic
Chair of Metallurgy

Advisors:
ao.Univ.-Prof. Dipl.-Ing. Dr.mont. Christian Bernhard
o.Univ.-Prof. Dipl.-Ing. Dr.mont. Hubert Biedermann

Leoben, June 2011

Preface

Originally I couldn't imagine that "rather unimposing small particles" distributed in steel will fascinate me in a way that sometimes I really lost time when studying them. In fact, this was the beginning of an intense research work as well as of an absolutely valuable and varied time at the *Chair of Metallurgy* five years ago. And surprisingly, exactly these "small particles" haven't released me until today.

First and foremost I would like to say a big thank you to my thesis advisor Christian Bernhard for the balance between the invaluable freedom you gave me to pursue my own ideas and your continuous support not only in scientific questions during the last years. My sincere thanks for your patience until I really discovered my passion for science and your strong backing especially in the final phase of this thesis! I will never miss the manifold discussions we've had.

I also want to express my honest gratitude to Professor Hubert Biedermann for the kind consent of being my second thesis advisor and for the useful suggestions within the preparation of this thesis. Besides the "small particles", I could therefore always pursue my interests in economic questions.

Many thanks are also due to my company partner *Böhler Edelstahl GmbH & Co KG* for the good cooperation over the last years as well as for the financing of the research project accompanying this thesis. Specifically to Wolfgang Schützenhöfer and Robert Tanzer for their support, their practical inputs and the diversified discussions.

My sincere thanks are also due to the *Chair of Metallurgy* and its professors, Wilfried Krieger and Johannes Schenk, and to all colleagues I spent time with. I am especially indebted to Gerhard Wieser for helping me to understand the manifold field of statistics and for his assistance in kinetic calculations, for his unique humour and the fact that he can talk about thousands things within one minute; to Bernd Lederhaas for the numerous hours we've spent in front of the microscope and to Siegfried Schider for introducing me into the fascination of Laser Scanning Confocal Microscopy as well as for being a really good listener; to Gregor Arth for the many refreshing discussions we've had and for the fact that the coffee dispenser was always on the way. Finally, to all students who contributed to the present thesis through their ambition during work.

Special thanks are due to my former colleague Mario Hartl, not only for the endless hours we spent with the evaluation of inclusion data and his enriching ideas in practical questions, but foremost for the one or other glass of wine we drunk together and for becoming a real friend over the years. To my friends Petra, Christoph and Patrick for always reminding me that there is a life outside my office and for spending so many outstanding moments together.

I can only express my deepest thanks to my family, especially to my parents, for your continuous support and belief in me and for being at my side in all aspects of life. To Sebastian, just simply my sincere thanks for taking and loving me as I am which might not always be an easy challenge! Moreover, I'm unbelievably grateful for the love of Gloria and Jonathan who always give me a smile. Finally, in lovely memory to you Marina who will never let me forget that *Every day is a gift, that's why it's called the present!*

I declare in lieu of oath that I wrote this thesis and performed the associated research myself, using only literature cited in this volume.

. . . .
Susanne K. Michelic
Leoben, June 2011

Abstract

English Abstract

The properties of stainless steels can be significantly influenced by the cleanness level. Through Electroslag Remelting (ESR) a considerable improvement of steel cleanness is achieved. This refining effect results from the contact between the liquid metal and the reactive slag bath at several reaction sites. Regarding cleanness improvement, the understanding of reactions at the steel/slag interfaces is indispensable.

Within the present work, the modification of oxides in the steel X38CrMoV5-1 through remelting is studied from the viewpoints of experiments, thermodynamics and kinetics, especially focussing on the spinel inclusion type $MgOAl_2O_3$. Next to a detailed investigation of samples from the ESR process, laboratory experiments in a Tammann Furnace are performed. Subsequent SEM/EDS analyses provide a detailed insight into the size, the composition as well as the morphology of inclusions. Thermodynamic considerations are addressed by the software *FactSage*. Additionally, a Laser Scanning Confocal Microscope enables the in-situ observation of the dissolution behaviour of oxides in fluoride-slags. Since the reliable characterisation of non-metallic inclusions is of major importance for this study, the representativeness of automated SEM/EDS analysis is affirmed for the defined conditions by coupling a geometric-statistical model with experimental considerations. Furthermore, the limitations of this method are critically reviewed.

This thesis especially concentrates on the changes in inclusion morphology which give a strong indication regarding the modification mechanisms during remelting. Next to the determination of the most decisive reaction site, the influence of the electrode quality on the final inclusion landscape in the remelted ingot is assessed. Moreover, the significance of slag composition and dwell time of inclusions in the liquid pool is discussed. The findings provide important knowledge about the essential influencing factors on the overall removal rate of inclusions through Electroslag Remelting and therefore for further process optimisation.

Deutsche Kurzfassung

Die Eigenschaften von Edelstählen stehen in engem Zusammenhang mit ihrem Reinheitsgrad. Das Elektroschlacke Umschmelzen (ESU) bewirkt eine deutliche Abnahme des mittleren Einschlussgehalts, welche durch den Kontakt des flüssigen Metalls mit einem reaktiven Schlackenbad an verschiedenen Reaktionsorten bestimmt wird. Um den Reinheitsgrad zu verbessern, ist das Verständnis der Reaktionen an den Stahl/Schlacke Grenzflächen entscheidend. Im Rahmen der vorliegenden Arbeit wird die Veränderung von Oxiden im Stahl X38CrMoV5-1 durch das Umschmelzen mittels experimenteller, thermodynamischer und kinetischer Betrachtungen untersucht, wobei im Speziellen auf den Spinelltyp $MgOAl_2O_3$ eingegangen wird. Dazu werden Proben aus dem ESU Prozess analysiert als auch Laborversuche in einem Tammann Ofen durchgeführt. Nachfolgende REM/EDX Messungen erlauben einen umfassenden Einblick hinsichtlich Größe, Zusammensetzung und Morphologie der Einschlüsse. Für die thermodynamischen Berechnungen wurde die Software *FactSage* verwendet. Zudem konnte mithilfe eines Laserkonfokalmikroskops das Auflöseverhalten von Oxiden in Flussspat-hältigen Schlacken in-situ beobachtet werden.

Ein entwickeltes geometrisch-statistisches Modell bewertet in Kombination mit experimentellen Analysen die Repräsentativität von automatisierten REM/EDX Messungen unter den definierten Bedingungen. Zudem werden die Grenzen dieser Methode kritisch beleuchtet.

Die morphologische Veränderung der Einschlüsse bildet einen wesentlichen Bestandteil der Arbeit und auch die Grundlage für die Beschreibung der Modifikationsmechanismen während des Umschmelzens. Neben der Bestimmung des maßgeblichen Reaktionsortes, wird der Einfluss der Elektrodenqualität auf die schlussendliche Einlusslandschaft im umgeschmolzenen Block bewertet. Zudem werden die Bedeutung der Schlackenzusammensetzung und der Verweilzeit von Einschlüssen im Pool diskutiert. Die Ergebnisse erlauben Rückschlüsse auf die essentiellen Einflussfaktoren hinsichtlich der Abscheidungsrate nichtmetallischer Einschlüsse im ESU-Prozess und bilden damit die Basis für eine weitere Prozessoptimierung.

Contents

1 Introduction

Clean Steel—a keyword that has occupied steel producers and their customers for a long time already. Depending on the application of steel, the meaning of this word may be interpreted very differently, as already described by Kiessling [1] as follows: *The clean steel of yesterday is not a clean steel today and a steel which is considered to be a clean steel for one specific use is not a clean steel for another use.*

Basically, the *cleanness* is defined by the number, the size, the chemical composition as well as the morphology and distribution of non-metallic inclusions in the steel matrix. The operation conditions for steels have continuously expanded over time. Especially as far as tool steels are concerned, diverse fields of application require not only exactly defined physical and mechanical properties but also demand precise surface conditions and a sufficient resistance against corrosive media. Out of the range of tool steels, hot-work tool steels are generally applied for non-cutting deformation of steels and other alloys, undergoing a constant surface temperature of at least 200 °C in use. The contact times between tool and workpiece can vary between fractions of a second in die-forging and several minutes during extruding. Therefore also an adequate thermal shock resistance is required. Since certain tools can offer very complex geometries and consequently are cost-intensive, a sufficient tool life is very important also from an economic viewpoint.

As described by Klarenfjord *et al.* [2], tool life is influenced by several aspects. Next to tool design, the basic steel composition and heat treatment of the tool, also the surface condition as well as the quality of the tool steel are important. The latter is mainly dependent on microstructure and cleanness. Both factors can be considerably affected by remelting processes, which have become state of the art in stainless steelmaking of high quality steels. These processes are characterised by the melting and solidification of an already solidified cast product, a so-called electrode. Among the remelting processes is Electroslag Remelting (ESR), where the determining refining effect is achieved through the contact of the liquid metal with a reactive slag bath. Besides a remarkable improvement of the ingot structure due to the long solidification times, a significant decrease of the overall content of non-metallic inclusions is accomplished through Electroslag Remelting. Due to the contact between steel and slag during remelting, also a modification of inclusion composition and morphology has to be considered. In the ESR process three metal/slag reaction sites are primarily responsible for the dissolution, separation and modification of non-metallic inclusions.

In order to optimise steel cleanness, the understanding of reactions and interactions between steel and slag is essential. For this purpose also a reliable characterisation of inclusions is indispensable. Various methods for inclusion analysis exist, each of them providing a different degree of information potential on the one hand as well as a varying detectable size spectrum of inclusions on the other hand. Since the inclusion landscape in steels may be unbelievably manifold, ranging between 1 and > 100 µm in diameter and a wide variety of compositions, the need for an appropriate analysing method is extremely high. Out of the pool of methods, nowadays the automated SEM/EDS analysis is the primarily applied method for research purposes, although having some significant limitations mainly as far as the comparatively small analysed sample area and the determination of large inclusions is concerned.

Both—steelmaking processes as well as characterisation methods—have been continuously improved in recent years. Nevertheless there are still questions that have not been examined precisely so far.

Given this background the aim of the present thesis is to study the modification behaviour of non-metallic inclusions due to steel-slag interactions, especially focussing on the Electroslag Remelting process. For this purpose, the inclusion landscape and its modification in the tool steel X38CrMoV5-1 is analysed from an experimental as well as a thermodynamic viewpoint. Inclusion analysis is done primarily using automated SEM/EDS analyses in combination with electrolytic extraction. The thermodynamic calculations are addressed by the commercial software *FactSage*. A Laser Scanning Electron Microscope is used for the in-situ observation of the dissolution behaviour of oxides in fluoride-slags which are applied in the ESR process.

As stated beforehand, automated SEM/EDS analyses are limited to a relatively small measured sample area. Consequently, it was necessary to assess the representativeness of this method for the desired investigations. This is done within the present work by the establishment of a geometric-statistical model in combination with experimental analyses.

Based on the evaluation of the representative sample area, different steps of the Electroslag Remelting process are analysed in detail. Here, the focus mainly lies on oxide inclusions, especially considering $MgOAl_2O_3$, an inclusion type that primarily evolved in the last 25 years and consequently got in the focus of interest of several researchers due to its negative influence on material properties. Next to a detailed investigation of samples out of the ESR process to determine the changes in inclusion landscape as well as the decisive reaction site, laboratory experiments in a Tammann Furnace are performed in order to study the essential influencing factors on inclusion modification. The influence of slag composition and dwell time of inclusions in the liquid metal is examined in detail. Particular attention is paid to the changes in inclusion morphology, providing important indication on their behaviour during remelting.

In the course of this work, first of all the fundamentals of interactions between steel and slag and their effect on inclusion modification according to the knowledge in literature are described. Therefore, in Chapter 2 the different aspects of inclusions formation, separation and dissolution are summarised, especially focussing on $MgOAl_2O_3$ since this is the predominant inclusion type investigated in the experimental part of this thesis. Moreover, essential issues concerning Electroslag Remelting are presented, mainly concentrating on the typically used slag system, the three metal/slag reaction sites and inclusion removal and modification. Subsequently, the state of the art of inclusion characterisation and the related challenges are outlined in Chapter 3. Furthermore, in this chapter the established geometric-statistical model is described and first conclusions regarding the representativeness of the analysed sample area are drawn.

Next to the fundamentals explained in Chapter 2 and the assessment of characterisation methods in Chapter 3, the analysed material as well as the used experimental set-up for laboratory tests and the approaches for thermodynamic and kinetic calculations are described in Chap. 4. This chapter also comprises an evaluation of the representativeness of different sampling positions in the analysed electrodes and ingots, which offers the basis for a reliable observation of changes in the inclusion landscape.

The results of experimental analyses—of industrial samples and laboratory tests—as well as of performed calculations are explained and discussed in Chapter 5. Next to an evaluation of the decisive reaction site in Electroslag Remelting and the determination of essential influencing parameters on the final inclusion landscape, a comparison between laboratory tests and industrial samples is carried out. Finally, the changes in inclusion morphology are used to define the decisive influences on inclusion modification through remelting. A summary of prospects and limitations of automated SEM/EDS analysis as well as an overview on the essential modification mechanisms during remelting and recommendations for future work conclude the thesis.

2 Interactions between Steel and Slag and their Influence on the Inclusion Landscape

Basically, non-metallic inclusions can be classified according to their size, composition or origin. Regarding the latter, two types of inclusions are distinguished: While endogenous inclusions directly emerge from the melt and are mainly the product of chemical reactions or the cooling process, exogenous inclusions often are caused by slag entrapment, breakdown of of refractory material or reoxidation by air. Furthermore, the following distinction by size of inclusions has become state of the art [3]:

- Macro-inclusions (> 100 µm);
- Meso-inclusions (> 30 and < 100 µm);
- Micro-inclusions (> 1 and < 30 µm);
- Submicro-inclusions (< 1 µm).

Depending on the non-metal associated with the metal phase, oxides, sulfides and nitrides have to be distinguished. Next to common single phase types, also mixtures (*e. g.*, oxisulfides) as well as multiphase inclusions, consisting of two or more different phases (*e. g.*, an oxide surrounded by a nitride), exist.

Steel properties are often directly influenced by the presence of non-metallic inclusions. Thus, for example fatigue toughness and strength, impact properties as well as hot workability, corrosion resistance and polishability of steels can be negatively affected by the cleanness level. In order to appraise the effect of inclusions on steel properties, geometry factors of the inclusions as well as properties dependent on inclusion composition such as deformability, thermal expansion coefficient and the modulus of elasticity have to be taken into account. Although the inclusion size is often the major criterion for crack initiation and is primarily decisive for material failure [4, 5], the inclusion's composition is also of special importance for different applications.

Gladman [6] for example reviewed the effect of the thermal expansion coefficient of an inclusion on fatigue properties in the bearing steel 100Cr6: In this case, inclusions with a lower thermal expansion coefficient than the steel matrix are supposed to be more harmful due to their stress-enhancing potential. Under this assumption, Al_2O_3 would be detrimental, whereas MnS would have no significant effect on fatigue properties according to Gladman [6]. Moreover, the inclusion composition may also control the modification behaviour and respectively the growth or dissolution of particles under certain conditions.

In order to be able to influence the inclusion landscape specifically, the understanding of reactions and interactions between steel and slag is essential. In terms of a continuous improvement of steel cleanness and a therewith involved decrease of the overall inclusion content, next to inclusion modification also the removal of inclusion is a primary aim. This removal—as shown in Fig. 2.1—can take place in different aggregates during steelmaking by transportation of the inclusions (1) to the steel/slag interface (2), separation at the steel/slag interface (3) and subsequent dissolution in the slag (4). While the transportation and separation step can be influenced by the fluid flow of liquid steel, the dissolution step is mainly determined by the physico-chemical properties of the inclusion and the slag.

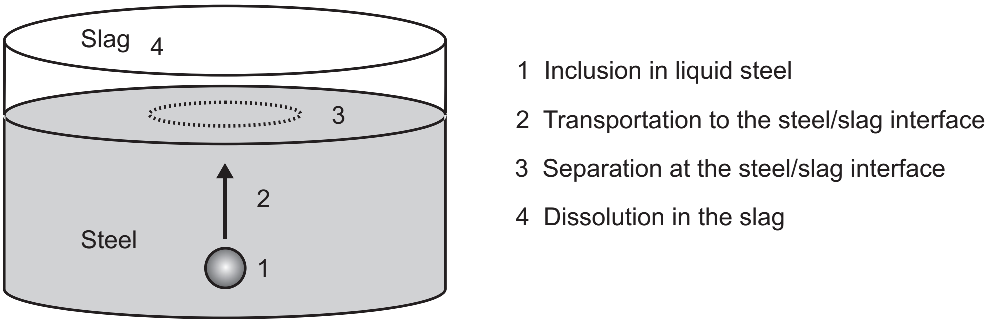

Figure 2.1: Inclusion generation and removal in an industrial vessel according to [7].

The present chapter outlines the fundamentals and the state of the art of inclusion modification and removal, wherein the explanations focus on oxides, since the present thesis concentrates on the modification of inclusions in the liquid steel melt and the formation of sulfides is considerably influenced by solidification processes. The explanations especially concentrate on the formation and modification of spinel inclusions like $MgOAl_2O_3$, since this inclusion type will also be treated in detail in the practical part of this thesis.

Next to an overview on the formation of $MgOAl_2O_3$ and the involved decisive influencing factors, the different removal steps of inclusions are treated in detail. Since Electroslag Remelting is of special importance for the present work, next to the fundamentals of the process, the slag functions and properties are described. Special attention is paid to the metal/slag reactions and the different mechanisms of inclusion removal during remelting.

2.1 Formation and Modification of $MgOAl_2O_3$ Inclusions

The contribution of Yamada *et al.* [8] in 1987 is designated to be the beginning of research on the formation of spinel inclusions in stainless steels. They studied the effectiveness of ceramic filters in the tundish in order to decrease the overall content of non-metallic inclusions of the austenitic stainless steels X5CrNi18-10 and X6CrNiTi18-10. The inclusion type primarily captured at the filters was $MgOAl_2O_3$ and therefore this spinel has become the focus of interest of several research groups in the last 25 years.

Figure 2.2 shows the two phase-system MgO-Al_2O_3, also illustrating that this inclusion type has a melting point > 2000 °C. This is one of the reasons why $MgOAl_2O_3$ can be very harmful to steel properties and is therefore intended to be avoided in the final product. Consequently, due to the continuously increasing requirements on properties of steels for special applications, this inclusion type was intensively studied of many researchers who treated this topic from a thermodynamic and experimental viewpoint.

Spinel inclusions like $MgOAl_2O_3$ are the product of reactions between steel, slag and refractory material during steelmaking. Principally, they can be formed on the basis of Al_2O_3 and/or MgO, although the latter is more unlikely, because Al is more commonly used for metallurgical treatments in steelmaking processes than Mg. While the Al-content in steel primarily results from the deoxidation process, different sources for Mg exist: Next to the reduction of MgO from the slag, also interactions with refractory material have to be taken into account. Regarding the origin of Mg in molten steel in more detail, basically the following four possibilities are described in literature [10, 11]:

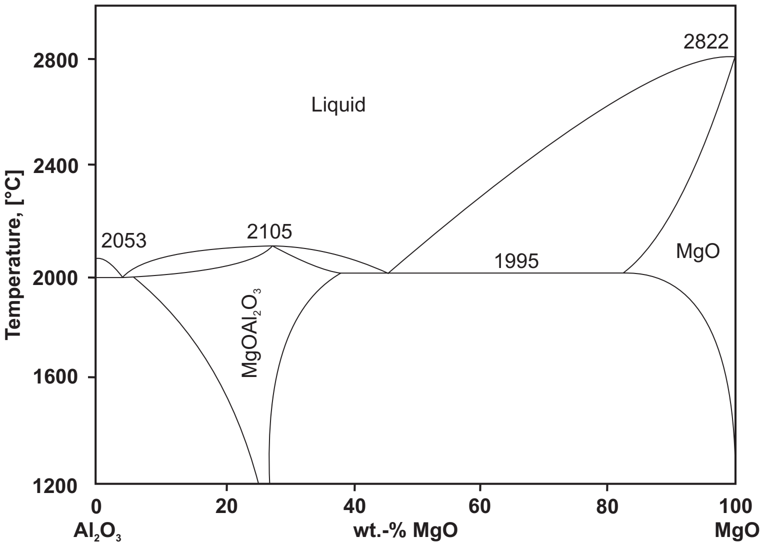

Figure 2.2: The binary phase diagram MgO-Al_2O_3 [9].

1. MgO in the slag is reduced by Al in molten steel.
2. MgO in the slag is reduced by carbon during vacuum treatment.
3. MgO in the refractory material is reduced by Al in molten steel.
4. MgO in the refractory material is reduced by carbon during vacuum treatment.

For the described possibilities the following two reactions are at first substantial:

$$3(MgO) + 2[Al] = (Al_2O_3) + 3[Mg] \tag{2.1}$$

$$(MgO) + [C] = [Mg] + \{CO\} \tag{2.2}$$

In a next step, the Mg dissolved in molten steel is oxidised into MgO, which consequently combines with Al_2O_3 and forms $MgOAl_2O_3$ according to Eqs. (2.3) and (2.4).

$$[Mg] + [O] = (MgO) \tag{2.3}$$

$$(MgO) + (Al_2O_3) = (MgOAl_2O_3) \tag{2.4}$$

The composition of these spinel inclusions is influenced by the used slag composition and the applied refractory material. Thus, by controlling these parameters, also the inclusion composition can be influenced. Although some works [12, 13] report that $MgOAl_2O_3$ are comparatively harmless to fatigue and other properties of steels if they are small, globular and distributed uniformly, the behaviour of these spinel inclusions in different steel grades has been discussed extensively in recent years due to their relatively high melting point and hardness [14] as well as their negative effect on the surface quality and formability of stainless steels [15–18].

2.1.1 The MgO-MgOAl$_2$O$_3$-Al$_2$O$_3$ Phase Stability Diagram

With regard to fundamental studies on the deoxidation equilibria of Ca, Al and Mg in liquid iron [19, 20], Itoh *et al.* [21] investigated the stability range of $MgOAl_2O_3$ inclusions. For this purpose the oxide activities of a_{MgO}, $a_{Al_2O_3}$ and $a_{MgOAl_2O_3}$ are essential. Assuming an ideal solid solution in the system $MgOAl_2O_3$, these activities are used for the examination of the phase boundaries MgO-$MgOAl_2O_3$ respectively $MgOAl_2O_3$-Al_2O_3. The calculations are based on Eqs. (2.5) and (2.7) using the free energy terms given in Eqs. (2.6) and (2.8). Through derivation of the mentioned free energy changes from those of the deoxidation of magnesium and aluminium and of the formation of $MgOAl_2O_3$ from $MgO(s)$ and $Al_2O_3(s)$ (see Eqs. (2.9) and (2.10)), the phase boundaries can be determined. Thus,

$$\langle MgO \rangle + 2[Al] + 3[O] = \langle MgOAl_2O_3 \rangle \tag{2.5}$$

$$\text{with } \Delta G^\circ(T) = -887\,960 + 210.88\,T, \tag{2.6}$$

$$\langle Al_2O_3 \rangle + [Mg] + [O] = \langle MgOAl_2O_3 \rangle \tag{2.7}$$

$$\text{with } \Delta G^\circ(T) = -110\,720 - 93.51\,T, \tag{2.8}$$

$$\langle MgO \rangle + \langle Al_2O_3 \rangle = \langle MgOAl_2O_3 \rangle \tag{2.9}$$

$$\text{with } \Delta G^\circ(T) = -20.740 - 11.57\,T, \tag{2.10}$$

where ΔG° is given in J/mol. Additional thermodynamic values, required for the calculation, are summarised in [21]. The authors also confirmed their calculations with experimental analyses. Iron samples were melted in a high frequency induction furnace. The iron was charged in a dolomite crucible. The crucible material was chosen consciously in order to enhance the Mg-content in the liquid iron. The experiments were principally done under Ar-atmosphere, the melt surface was impinged with H_2, adjusting the dissolved oxygen content to less than 20 *ppm*. After a duration time of several hours at 1600 °C, the deoxidiser—Al in the present case—was dropped into the liquid melt. After reaching deoxidation equilibrium the sample was quenched under He inside the furnace. The contents of dissolved Mg and Al were analysed with ICP-MS, the stable oxide phases were evaluated with XRD. Comparing the results of the experiments with the calculated phase stability diagram of MgO-$MgOAl_2O_3$-Al_2O_3 as a function of Mg and Al-contents in the liquid iron (shown in Fig. 2.3) a good agreement could be observed.

Several subsequent works have been published giving ranges for the phase stability of MgO-$MgOAl_2O_3$-Al_2O_3 [22–28], principally showing similar calculation results as those in Fig. 2.3, although slight differences were observed mainly concerning the boundary between MgO and $MgOAl_2O_3$. The calculation results of Jiang *et al.* [27] for example showed a noticeable smaller stable spinel inclusion region compared to the diagram published by [21]. The authors explained this difference by the fact that Itoh *et al.* [21] assumed the direct formation of MgO inclusions in molten steel if the Al-content is < 0.0010 %, against what in the work of Jiang *et al.* [27] all MgO inclusions are assumed to evolve from $MgOAl_2O_3$ since there is no Mg in molten steel at the beginning of the experiments. Todoroki and Mizuno [28] established a comparable shape of the stable phase region for $MgOAl_2O_3$ as Jiang *et al.* [27], but the threshold value for Al_2O_3-$MgOAl_2O_3$ and $MgOAl_2O_3$-Al_2O_3 transformation were lower than in [27]. The main difference between the calculations was the investigated steel grade. In the work of Jiang *et al.* [27] a 42CrMo4 was analysed, while Todoroki and Mizuno [28] studied the stainless steel X10CrNi18-8. The authors concluded that the steel composition and therewith connected interaction coefficients have a significant influence on the stability range of $MgOAl_2O_3$.

A comparison of several mentioned stability diagrams recently performed by Yang *et al.* [10] showed that displaying their experimental data for dissolved Mg and Al (determined for a 30CrMo steel) in the

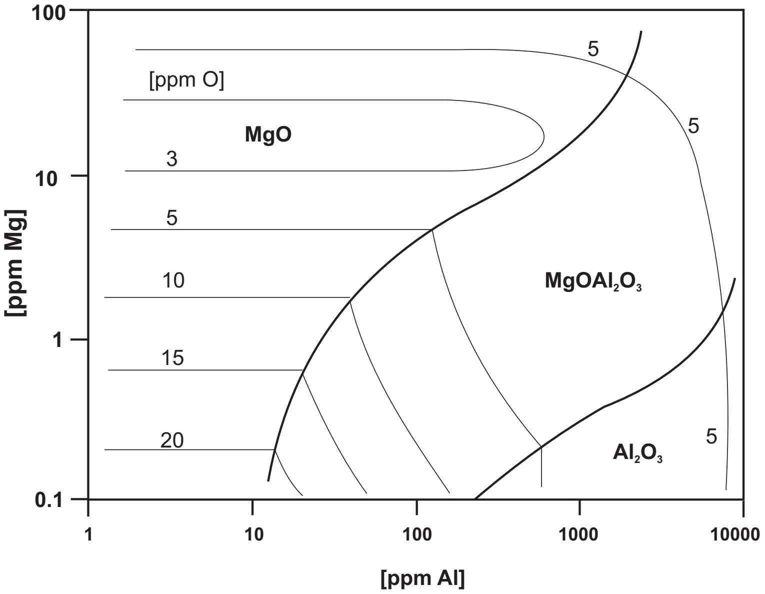

Figure 2.3: Calculated stability diagram of MgO, $MgOAl_2O_3$ and Al_2O_3 inclusions, and iso-oxygen contour lines at 1873 K according to [21].

different published diagrams would in some cases result in $MgOAl_2O_3$ as the main inclusion type, while others would predict pure MgO inclusions, notwithstanding the fact that in the experimentally analysed steel samples pure MgO inclusions were hardly observed. Yang *et al.* [10] tried to reconstruct the found discrepancies in the calculation results of different authors [22–26] by re-calculating the phase stability diagram with the original thermodynamic data stated in literature. Although the discrepancies were not yet clarified in detail, a remarkable influence of steel composition and related interactions in molten steel on the stability range of $MgOAl_2O_3$ was determined.

In order to understand the effect of different elements as well as process conditions on the formation and modification of $MgOAl_2O_3$ more precisely, several influencing aspects will be discussed in the next subsection.

2.1.2 Influencing Factors and Decisive Reactions

2.1.2.1 Formation of $MgOAl_2O_3$ on the Basis of Al_2O_3

In principle, as already stated beforehand the formation of $MgOAl_2O_3$ inclusions is primarily influenced by the presence of other elements in molten steel. These elements may be reduced from the slag or refractory material and consequently assist or inhibit the stability of $MgOAl_2O_3$.

Influence of Calcium Ohta and Suito [29] performed similar calculations and experiments as done by Itoh *et al.* [21] in order to study the Ca-O and Mg-O equilibria in liquid iron in combination with CaO-SiO_2-Al_2O_3-MgO slags at 1600 °C. In contrast to Itoh *et al.* [21], the authors also considered the influence of Ca in the melt on the stability range of $MgOAl_2O_3$. In the calculations this was done by accounting the first and second-order interaction coefficients between Ca and O. In the experiments a CaO crucible was used. Samples of electrolytic iron were melted in a vertical resistance furnace under Ar-atmosphere and the addition of approximately 4 % slag. The melts were stirred by an Al_2O_3 or MgO rod for 1 min at 30 min intervals. After another hour without stirring the sample was rapidly quenched under He followed by water quenching. The experimental results for slag compositions which were double-saturated with MgO and $MgOAl_2O_3$ (31.6 %CaO, 53.4 %Al_2O_3, 14.9 %MgO and < 1 %SiO_2) showed a good agreement with the calculated stability diagram shown in Fig. 2.4. The authors concluded that the $MgOAl_2O_3$ mainly is the equilibrium phase in the range of a *Mg*-content between 0.1 and 1 *ppm*, assuming an *Al*-content < 200 *ppm*. The stability diagram calculated by Itoh *et al.* [21] shows significant differences compared to the one by Ohta and Suito [29]. The latter explained that *Ca* has a considerable influence on the stability range of $MgOAl_2O_3$, determining that the content of *Mg* in the melt saturated with MgO and $MgOAl_2O_3$ respectively with Al_2O_3 and $MgOAl_2O_3$ increases with the addition of *Ca* for a given *Al*-level.

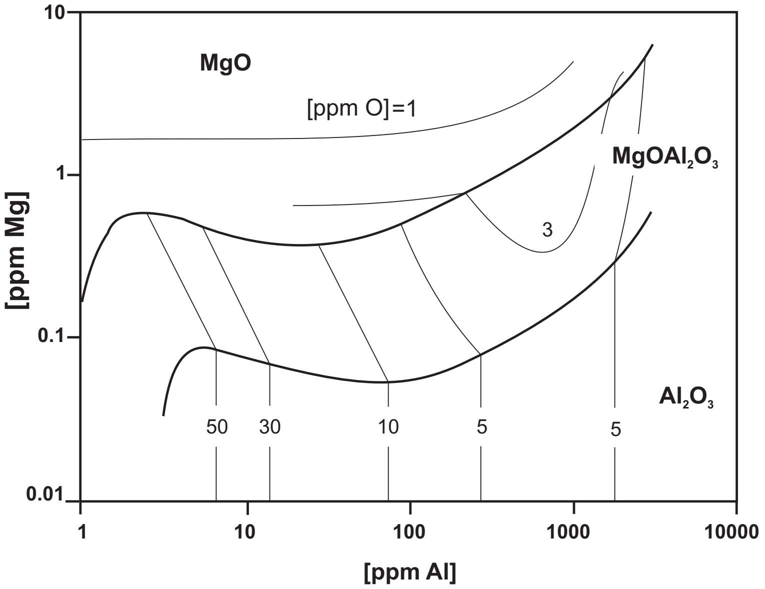

Figure 2.4: Phase stability region of the system *Fe-Al-Mg-O* in a plot of *Mg* vs. *Al*-content according to [29].

Influence of Titanium In other studies, further elements were found to remarkably affect the stability range of $MgOAl_2O_3$. Park *et al.* [30] for example studied the influence of Ti by observing the modification of oxides in a Ti-stabilized Fe-11Cr ferritic stainless steel through the contact with CaO-SiO_2-Al_2O_3-MgO-CaF_2(-TiO_2) slags (> 30 %CaO, 20 %SiO_2, 10 to 20 %Al_2O_3 and MgO and TiO_2 ranging between 4 and 15 %). The steel samples were remelted in a high frequency induction furnace under *Ar*-atmosphere. After a holding time of 40 min, the sample was quenched under *He*. It was found that the spinel potential remains very low and nearly constant when the activity of Al_2O_3 is less than that of TiO_2 in the slag saturated by MgO. Calculations with *FactSage* as well as the laboratory experiments indicated a linearly increase of the spinel potential with increasing the $\log(a_{Al_2O_3}/a_{TiO_2})$ at $(X_{Al_2O_3}/X_{TiO_2}) > 1$.

Influence of Silicon The influence of Si on the stability range of $MgOAl_2O_3$ was evaluated by Jiang *et al.* [27]. The authors performed experiments on a laboratory scale investigating the behaviour of non-metallic inclusions in the steel grade 42CrMo4 through the contact with CaO-SiO_2-Al_2O_3-MgO slags, in which the CaO-content was slightly lower and the Al_2O_3-content remarkably higher than in the investigations performed by Park *et al.* [30]. The used experimental set-up as well as the test conditions were comparable to the experiments by Ohta and Suito [29]. Through the variation of SiO_2-content in the slag between 5 and 20 % the influence on the formation of $MgOAl_2O_3$ inclusions was studied. The results showed that an increased SiO_2-content in the slag stabilizes the spinel phase due to its reaction with soluble Al and Mg, which prohibits the transformation of $MgOAl_2O_3$ into pure MgO.

Similar findings have also been reported by Todoroki and Mizuno [28] who examined the stability of $MgOAl_2O_3$ in the steel X10CrNi18-8 deoxidised with Al and refined by CaO-SiO_2-Al_2O_3-MgO-CaF_2 slags (> 50 %CaO, 20 %CaF_2, SiO_2, MgO and Al_2O_3 approximately 10 % each). For this study also a vertical resistance furnace under Ar-atmosphere and an MgO crucible was used. It was confirmed that SiO_2 in the slag prevents the reduction of MgO and CaO by Al and consequently the supply of soluble Mg or Ca in the molten steel.

Not only the slag may provide a possible source for Si. Todoroki *et al.* [16] also investigated the influence of different $FeSi$-alloys used for the deoxidation of X10CrNi18-8 using the same laboratory set-up as described beforehand. At 1600 °C the melt was deoxidised with $FeSi$, also containing small impurities of Ca and Al, ranging between 0.02 – 3 %Al and < 0.01 – 1.7 %Ca. The used slag was composed of 48 %CaO, 14 %CaF_2, 29 %SiO_2, 3 %Al_2O_3 and 7 %MgO. The impurities of the deoxidant could have a significant influence on the composition of the deoxidation product and therefore on the final inclusion composition. Fig. 2.5 illustrates the considered reactions involving steel, slag, inclusion and refractory material in this study:

1. Adding $FeSi$ with impurities of Ca and Al in the molten steel leads to the formation of CaO-Al_2O_3-SiO_2 inclusions.
2. A small amount of soluble Al and Ca can react with the slag or the refractory material and consequently transfers Mg from the slag to the metal phase. Due to the higher diffusion rate of Mg in the slag, the reaction with slag should be of higher importance.
3. The soluble Mg is used to form CaO-Al_2O_3-MgO-SiO_2.

Assuming that the $FeSi$-alloy does not contain Ca, $MgOAl_2O_3$ is more stable than silicate inclusions. Hence, Al in $FeSi$-alloys seems to enable the formation of $MgOAl_2O_3$, against what Ca would alternatively assist forming silicate inclusions having a remarkably lower melting point than $MgOAl_2O_3$. If the $FeSi$ includes neither Ca nor Al, $MnOSiO_2$ inclusions are formed immediately after deoxidation. Since they are not able to reduce MgO in the slag, this inclusion type is not modified any more [16].

The deoxidation with $FeSi$ can not only influences the formation of $MgOAl_2O_3$ in general, but also affects the morphology of these inclusions. Nishi and Shinme [31] investigated the morphology changes of inclusions in Fe-42 %Ni alloys in laboratory experiments using Si and Mn as deoxidants. Steel samples were remelted with a CaO-SiO_2-19 %Al_2O_3-12 %MgO slag in an induction furnace. The morphology of inclusions was subsequently analysed using SEM/EDS. Their experiments showed — as illustrated in Fig. 2.6 — an with time increasing content of Al_2O_3 and MgO in the $MnOSiO_2$ inclusions formed after deoxidation. In their point of view this is caused by the reduction of Al_2O_3 and MgO from the slag by Si at the slag/metal interface.

Influence of Slag Basicity Next to the mentioned effects of single slag components as well as deoxidation practice, also the slag basicity is stated to have a considerable influence on the behaviour of $MgOAl_2O_3$ inclusions. Nishi and Shinme [32] performed tests with the stainless steel X10CrNi18-8 in contact with a CaO-SiO_2-5 %Al_2O_3-5 %MgO slag. A mass of 15 kg of the mentioned steel was melted in an induction furnace and deoxidised with Al at 1600 °C. At different intervals samples were taken out of the liquid melt and subsequently analysed with SEM/EDS. Figure 2.7 demonstrates the effect of slag basicity on the MgO-content in the inclusions, which is successively increased with time and rising CaO/SiO_2

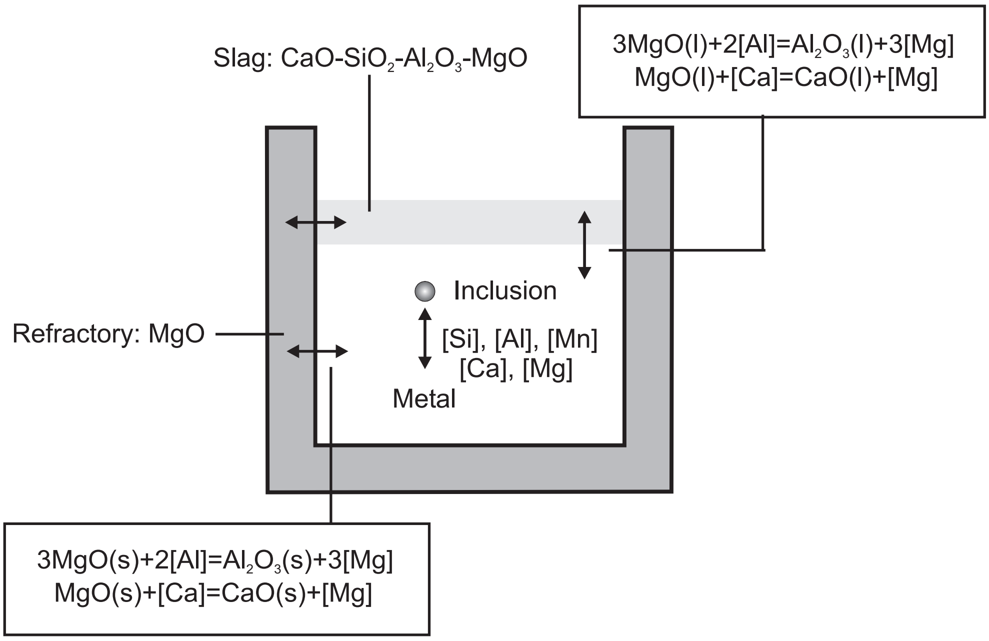

Figure 2.5: Schematic illustration of slag-inclusion-refractory reactions [16].

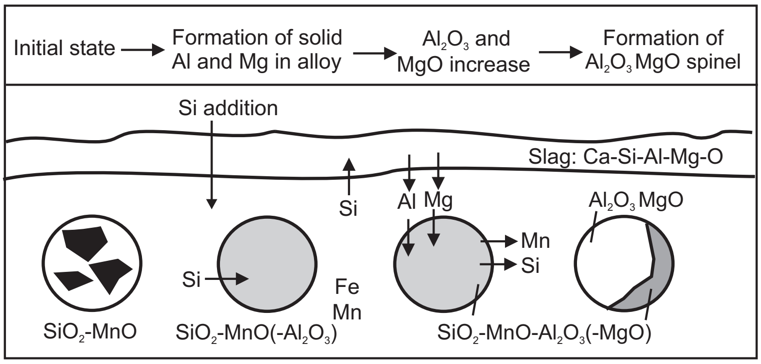

Figure 2.6: Schematic illustration of inclusion morphology change in molten steel due to Si-deoxidation [31].

ratio in the slag. As already stated by several research groups [10, 27, 30], one possibility for the origin of *Mg* in molten steel is supposed to be the reduction of *MgO* from the slag. As shown in Fig. 2.8, the *MgO*-content in inclusions increases with increasing *MgO*-content in the slag, although the basicity influence is considered to be more decisive according to Nishi and Shinme [32]. These findings has also been confirmed by Tang and Li [11].

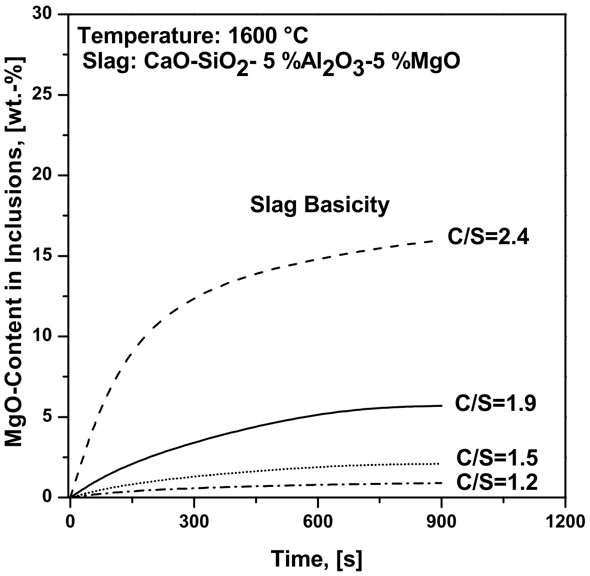

Figure 2.7: Effect of CaO/SiO_2 ratio of the slag on the MgO-content in the inclusions [32].

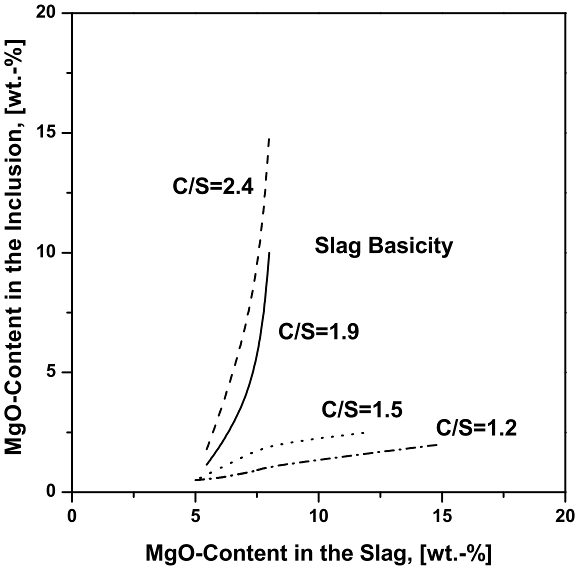

Figure 2.8: Relationship between the MgO-content in the slag and the MgO-content in inclusions [32].

Influence of Refractory Material Cha *et al.* [33] also examined the influencing factors on the formation of $MgOAl_2O_3$ especially focussing on the change of slag composition by the reaction with Al from the melt. Laboratory experiments were carried out in a high frequency induction furnace under Ar-atmosphere equilibrating 150 g of a X6Cr17 featuring varying original levels of Al (addition of pure Al at 1600 °C ranging between 0.03 and 0.75 g) with 1 g of a 44 %CaO-49 %SiO_2-7 %MgO slag. For the tests an MgO crucible was used. After each experiment the sample was quenched by He. Subsequently the sample cross section was analysed with an optical microscope for non-metallic inclusions. Since hardly any inclusions were observed in the centre part of the sample, this positions was used for the evaluation of Al-content by ICP-MS. Their results showed a change of slag composition with increasing Al-content in the melt, from a rather low Al_2O_3-content in the slag (approximately 2 %) to approximately 40 % where $MgOAl_2O_3$ precipitated from the slag.

Based on these performed laboratory tests, Cha *et al.* [33] formulated a model which predicts the composition change of AOD slag particles entrapped in the melt along the process route, especially concentrating on the effect of different refractory materials in the downstream ladle. If the ladle is lined with Al_2O_3, the top slag after AOD tapping would already be saturated with Al_2O_3 and consequently the steel would pick-up a significant amount of *Al* from the slag. Presuming an oxygen level of about 65 *ppm* at 1650 °C at AOD tapping, the equilibrium *Al*-content at Al_2O_3 saturation would be about 53 *ppm*. Since the temperature drops from AOD to tundish, the *Al* would react with the available *O* in the melt and form Al_2O_3. If all formed Al_2O_3 were mixed with entrapped slag particles, the Al_2O_3-content in the slag would increase considerably. In this study it was assumed that 80 g slag were entrapped per ton steel. Regarding this assumption, the Al_2O_3-content in the slag would increase from 5 % up to 45 % where $MgOAl_2O_3$ is formed according to the pseudo-ternary system CaO-Al_2O_3-SiO_2-(10 %MgO) given in [9].

In contrast to this, if the ladle is lined on the basis of *MgO*, the activity of Al_2O_3 in the top slag would be much lower than in the latter case (for an Al_2O_3 activity of 0.01 at 1650 °C, the equilibrium *Al*-content is about 5.5 *ppm* at 65 *ppm O*). Consequently, the amount of formed Al_2O_3 would lie significantly below the level where the formation of $MgOAl_2O_3$ has to be considered.

Thus, the authors concluded that the *Al*-level in the melt is decisive for the spinel formation. Through the *Al* pick-up from the refractory, the Al_2O_3-content in the slag increases significantly, whereas the use of a *MgO* refractory assists keeping the *Al*-level in the liquid considerably lower, hence resulting in a noticeably decreased amount of $MgOAl_2O_3$ inclusions in the final product.

Up to now, all mentioned publications and results were based on laboratory experiments and thermodynamic calculations. Similar conclusions as stated beforehand were also drawn on the basis of investigations on industrial scale. Kim *et al.* [34] and Ehara *et al.* [35] examined the modification of oxides in stainless steels in contact with slags in samples directly taken from industrial processes. Ehara *et al.* [35] analysed the behaviour of spinels during the production of X6CrNi18-8. Samples out of different process steps, including AOD (basic slag composition of 45 %CaO-29 %SiO_2-8 %MgO-10 %CaF_2 with slight amounts of Al_2O_3 and Cr_2O_3), LF and tundish were taken and compared. Their findings showed that the Al_2O_3-content of inclusions increased with the Al_2O_3-content in the slag as well as with increasing slag basicity. Kim *et al.* [34] investigated the same steel grade also by taking samples from different process steps. The authors concluded that the *Al*-content in the melt and the *MgO*-content in the slag significantly affect the formation of $MgOAl_2O_3$.

Influence of CO Partial Pressure So far, in all stated publications the reduction of *MgO* from the slag or refractory material was achieved through the presence of another deoxidising element present in the liquid metal, mostly *Al* or *Si*. Another aspect which influences the *Mg*-content in liquid steel is the *CO* partial pressure. *MgO* (coming from the slag or the refractory material) can be reduced by carbon during vacuum treatment according to

$$[C] + (MgO) = [Mg] + \{CO\} \qquad (2.11)$$

The dissolved *Mg* subsequently combines with the dissolved *O* and forms *MgO*. Finally, *MgO* reacts with Al_2O_3 to form $MgOAl_2O_3$. This relationship was studied in detail by Tang and Li [11] using a thermodynamic approach in combination with SEM/EDS analyses. For their evaluations a casing steel consisting of 0.39 %C, 0.22 %Si, 1.52 %Mn, 0.12 %V, 0.02 %Al as well as slight additions of Mo and Cr and a CaO-SiO_2-5 %MgO-10 %Al_2O_3-0.5 %FeO-slag were used.

For Eq. 2.11 the equilibrium constant of the reaction is given by

$$K = \frac{(p_{CO}\, a_{Mg})}{(a_{MgO}\, a_C)} = \frac{p_{CO} f_{Mg}\, [Mg]}{Y_{MgO} f_C\, [C]}, \tag{2.12}$$

where p_{CO} is the partial pressure of CO, Y_{MgO} represents the mass action concentration of MgO and f_i and a_i are the activity coefficient and the activity of the component i. Inserting the thermodynamic data used in this study, the following relationship is obtained:

$$\log p_{CO}[Mg] = \log Y_{MgO} - 5.70284. \tag{2.13}$$

For the case when MgO is reduced from the refractory material by C, $Y_{Mg} = 1$ and consequently

$$[Mg] = \frac{10^{-5.70284}}{p_{CO}}. \tag{2.14}$$

In the other case, if MgO is reduced from the slag, the relationship is

$$[Mg] = \frac{10^{-5.70284} Y_{MgO}}{p_{CO}}. \tag{2.15}$$

The authors demonstrated that the Mg-content in liquid steel increases rapidly with decreasing p_{CO}. Additionally taking the slag basicity into account, it was shown that at first the Mg-content increases with increasing basicity at the same p_{CO}. The largest Mg-content was observed at a basicity of 4. At the same basicity, the Mg-content decreases with increasing p_{CO}.

2.1.2.2 Formation of $MgOAl_2O_3$ on the Basis of MgO

So far, in all described publications the initially formed inclusions were Al_2O_3 regardless of the slag composition. On the contrary Park and Kim [36] concentrated on the formation of $MgOAl_2O_3$ due to a modification of MgO inclusions in steel melts equilibrated with CaO-Al_2O_3-MgO slags. The Al-content in the investigated ferritic stainless steel grade (pure iron with 16 %Cr) was less than 0.02 %. The experiments were carried out in a MgO crucible positioned in a super Kanthal electric furnace under Ar-atmosphere. ICP-MS was used for the analysis of soluble Al and Mg, the composition and morphology of inclusions was analysed with SEM/EDS.

In the SEM/EDS results of the inclusions an inconsistent distribution of MgO and Al_2O_3 from the surface to the centre of the inclusions was observed. According to [17, 36] these findings may be explained by the following formation steps:

1. Formation of MgO particles in the melt equilibrated with the highly basic slag;
2. Reaction with Al at the MgO/metal interface;
3. Transformation of MgO to $MgOAl_2O_3$.

For a more detailed discussion of the formation mechanisms the authors refer to a model originally developed for the modification mechanism of alumina by calcium treatment [37]. In this model it was

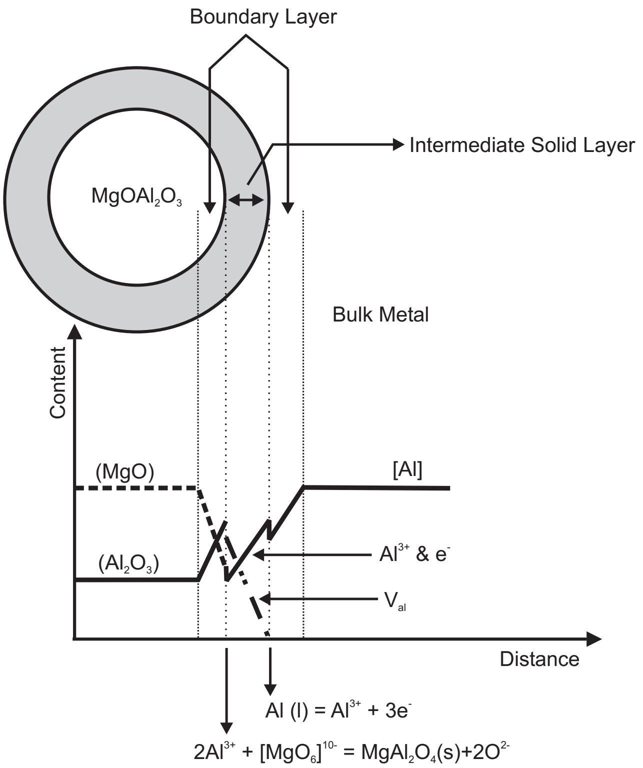

Figure 2.9: Schematic diagram of the modification mechanism of MgO by Al in molten steel [36].

proposed that the solid alumina particles in molten steel could be modified to liquid calcium aluminates by ionic exchange at the interfaces. Presuming a similar structure for the MgO inclusion as for the alumina—in this case $[MgO_6]^{10-}$-octahedral—the modification of MgO to $MgOAl_2O_3$ can be described analogically using the intermediate layer concept like schematically illustrated in Fig. 2.9 and consisting of the following reaction steps:

- Diffusion of aluminium atoms from the bulk to the metal/MgO interface;
- Oxidation of the aluminium atoms to the Al^{3+} ions at the metal/intermediate layer interface;
- Diffusion of Al^{3+} ions and charge balancing electrons through the intermediate layer with diffusion of equimolar vacancies to opposite direction;
- $MgOAl_2O_3$ formation by the reaction between Al^{3+} ions and $[MgO_6]^{10-}$ units at the intermediate layer/inclusion core interface (according to Eq. (2.16)).

$$2[Al]^{3+} + [MgO_6]^{10-} = \langle MgAl_2O_4 \rangle + 2O^{2-} \tag{2.16}$$

All in all, it can be concluded that there are several influencing factors contributing to the formation of $MgOAl_2O_3$, mainly dominated by reactions between steel and slag. In the following, the reactions between steel and slag as well as steel and inclusion will be treated out of a kinetic viewpoint in order to get an impression of the rate determining step of the formation of spinels.

2.1.2.3 Evaluation of the Rate Determining Step

In order to evaluate the formation mechanism of $MgOAl_2O_3$ from a kinetic viewpoint, both slag/metal and metal/inclusion reactions were examined by Okuyama *et al.* [38]. For this purpose laboratory experiments with an *Al*-killed 16 %*Cr* ferritic stainless steels were carried out in a 20 kg high frequency vacuum induction furnace and a *MgO* crucible and CaO-SiO_2-Al_2O_3 slags with 10 %*MgO*. After the addition of *Al* with a wire, samples of the liquid melt were taken successively. The samples were cooled rapidly and the metallographic specimens were investigated with SEM/EDS.

As already stated by several research groups beforehand [10, 27, 30, 34, 35], the experimental results of Okuyama *et al.* [38] also indicated that the *MgO* in inclusions after *Al*-deoxidation is due to the reduction of *MgO* from the slag by *Al*. Although an *MgO* crucible was used in the experiments, the authors did not find $MgOAl_2O_3$ inclusions in experiments without slag addition. Thus, in contrast to Cha *et al.* [33] who assigned a significant influence of refractory material on the formation of $MgOAl_2O_3$, Okuyama *et al.* [38] concluded that the *MgO* concentration of the inclusions is not considerably affected by the refractory material.

On the basis of the described experimental findings, Okuyama *et al.* [38] also adopted a reaction model which was originally applied for dephosphorisation and desulfurisation of iron as well as to reoxidation reactions in molten steel by slag, in order to analyse the reduction reaction of *MgO* from the slag more precisely. The calculations indicated that the increase of dissolved *Mg* in molten steel is the rate-determining step for mass transfer on the metal side. Moreover, the influence of slag composition on the rate of increase in the *Mg*-concentration of inclusions was explained by the changes in the *Mg*-concentration at the slag/metal interface due to the slag composition dependency of *MgO*-activity and oxygen activity at the interface. The results agreed well with the experimental findings.

In a second step, Okuyama *et al.* [38] also analysed the kinetics of the metal/inclusion reaction. Therefore, two different hypotheses were examined and compared applying the unreacted core model:

1. The diffusion of *Mg* in the inclusion surface layer is rate-determining (schematically shown in Fig. 2.10);
2. The diffusion of *Mg* in molten steel is rate-determining (schematically shown in Fig. 2.11).

In their considerations the following assumptions were made:

- *Mg* in molten steel reacts with the Al_2O_3 inclusion, forming a reaction product layer composed of $MgOAl_2O_3$.
- The shape of the inclusions is spherical.
- The outer diameter r_0 of the inclusions does not change with time.
- The *MgO* concentration when the inclusion initially begins to form spinel is 10 %, and the *MgO* concentration finally changes to 28 % spinel.

For the first case—assuming the diffusion of *Mg* in the inclusion surface layer as rate-determining—it was found that diffusion within inclusions progresses extremely rapid. Considering the inclusion size observed experimentally (approximately 3 μm in diameter), the *MgO* concentration reaches saturation in about 2 s. For the second case—assuming the diffusion of *Mg* in molten steel as rate-determining—a significantly lower reaction rate was observed. Consequently, the authors assume that the second hypothesis as shown in Fig. 2.11 is the rate-determining step.

Finally, a comparison between the reaction rates of metal/inclusion and metal/slag reactions was performed. According to [38] under the assumed conditions *Mg* reaches equilibrium in molten steel due to metal/slag reactions after approximately 30 min. Consequently, the slag/metal reaction is considered to be the slowest among the three compared situations in the whole system.

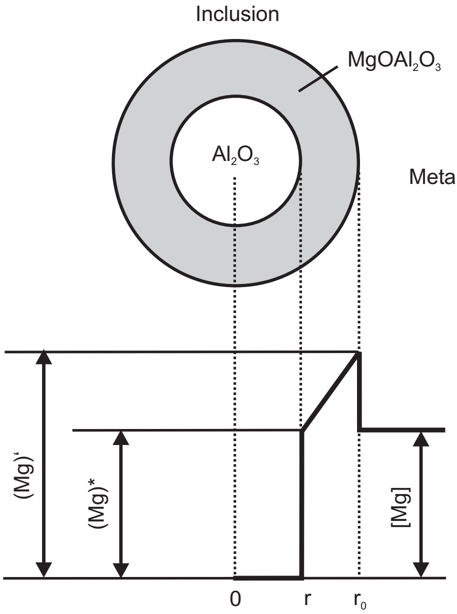

Figure 2.10: *Mg*-content distribution in molten steel and an inclusion based on a model in which the rate determining step is *Mg* diffusion in the inclusion [38].

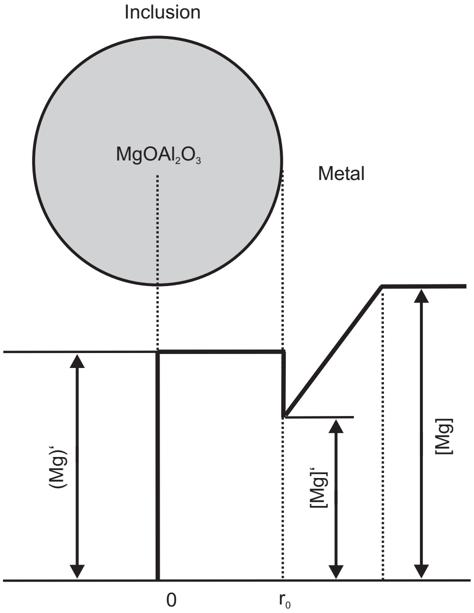

Figure 2.11: *Mg*-content distribution in molten steel and an inclusion based on a model in which the rate determining step is *Mg* diffusion in boundary layer of molten steel [38].

Nightingale and Monaghan [39] studied the formation and growth of $MgOAl_2O_3$ spinel crystals on a single crystal MgO substrate submerged in a 40 %CaO-20 %Al_2O_3-40 %SiO_2 slag in-situ using a Laser Scanning Confocal Microscope (LSCM). Through the transparency of the substrate a very good visibility of the crystals and therefore the measurement of their size was possible. In a first step, the used slag was repeatedly premelted in a Pt-crucible, in order to get a homogeneous slag. Secondly, a thin slice of a MgO (approximately 2 × 3 mm^2) was placed on the top of the cold slag in the Pt-crucible. The samples were heated under air and then held at different temperature steps between 1400 °C and 1460 °C. In a next step crystal sizes were measured and subsequently used to estimate the growth rates. The observations confirmed that $MgOAl_2O_3$ forms and grows on the MgO/slag interface, but may easily break off and therefore be carried away into the slag due to the large difference in lattice parameters between MgO and $MgOAl_2O_3$. According to the authors [39] a growth rate increasing with temperature and following the parabolic law was observed.

Although a comparison between the calculated rates by Okuyama *et al.* [38] with the in-situ observations of Nightingale and Monaghan [39] is rather difficult, because the investigated particle sizes were very different, comparable trends were found. Summing up, it could be concluded that both mathematical approaches as well as experimental analyses determine the slag/metal reaction to be the most significant with regard to kinetic aspects.

2.1.3 Formation of Complex $CaOAl_2O_3MgO$ Inclusions

On the basis of $MgOAl_2O_3$ more complex inclusions consisting of CaO-Al_2O_3-MgO can form due to different reaction mechanisms. This modification can considerably influence inclusion properties and therefore recently got in the focus of interest of several researchers [40, 41].

In order to study these mechanisms laboratory experiments in combination with metallographic analyses have proved to be very useful tools. So, for example Jiang *et al.* [40] performed laboratory tests in a vertical resistance furnace, studying the modification of oxides within the system CaO-Al_2O_3-MgO in a high strength steel (0.58 %C, 1.70 %Si, 0.80 %Mn and 0.18 %Cr) through remelting with high basicity slags containing CaO, Al_2O_3, 6 %SiO_2, 10 %MgO and little fractions of MnO and FeO.

The steel samples were charged into a MgO crucible, covered with slag and heated up under Ar-atmosphere at 1600 °C, where the melt was held for a predetermined time without stirring. Two different slag compositions with different Al_2O_3-contents were applied (Slag A with approximately 30 % and slag B with 40 %). Despite the different slag compositions similar inclusion compositions were found in the remelted samples. For both cases, in SEM-mappings complex oxides consisting of CaO, Al_2O_3 and MgO were found, showing two different inclusion cores, namely Al_2O_3 and MgO. Consequently, the formation of these complex $CaOMgOAl_2O_3$ inclusions can be described by two different mechanisms:

1. $Al_2O_3 \rightarrow MgOAl_2O_3 \rightarrow CaOMgOAl_2O_3$
2. $MgO \rightarrow MgOAl_2O_3 \rightarrow CaOMgOAl_2O_3$

Based on the results of SEM-analyses Jiang *et al.* [40] formulated a model for the evolution process of these complex inclusions which can be summarised as follows:

The deoxidation with Al leads to a quick formation of Al_2O_3; MgO and CaO are reduced from the slag (see Eqs. (2.17) and (2.18)). Equation (2.19) describes the first possible case for the formation of $MgOAl_2O_3$, where the present Al_2O_3 reacts with the Mg dissolved in the liquid melt.

In consequence of a possible concentration gradient of Mg in the liquid steel (no stirring has been used in the experiments), also MgO inclusions can form according to Eq. (2.20), which yields in the initial state for the second case: Assuming that MgO inclusions are not stable under strong Al-deoxidation, they will transform to $MgOAl_2O_3$ with Al in the melt or Al_2O_3 (see Eqs. (2.21) and (2.22)).

$$2[Al] + 3(MgO) = 3[Mg] + (Al_2O_3) \tag{2.17}$$

$$2[Al] + 3(CaO) = 3[Ca] + (Al_2O_3) \tag{2.18}$$

$$[Mg] + \frac{n}{3}\langle Al_2O_3\rangle = \langle MgO\,\frac{n-1}{3}Al_2O_3\rangle + \frac{2}{3}[Al] \tag{2.19}$$

$$[Mg] + [O] = \langle MgO\rangle \tag{2.20}$$

$$4\langle MgO\rangle + 2[Al] = \langle MgOAl_2O_3\rangle + 3[Mg] \tag{2.21}$$

$$y\langle MgO\rangle + z\langle Al_2O_3\rangle = \langle yMgO\,zAl_2O_3\rangle \tag{2.22}$$

As visualised in Fig. 2.12, the formed $MgOAl_2O_3$ inclusions are secondary surrounded by a layer composed of $CaOAl_2O_3MgO$ resulting of the dissolved Ca in the liquid steel as described in Eq. (2.23). Opposing concentration gradients of CaO and MgO in the formed layer determine the reactions inside the layer (see Eq. (2.24)) and reactions at the interface between the $MgOAl_2O_3$ core and the layer of the inclusion (see Eq. (2.25)).

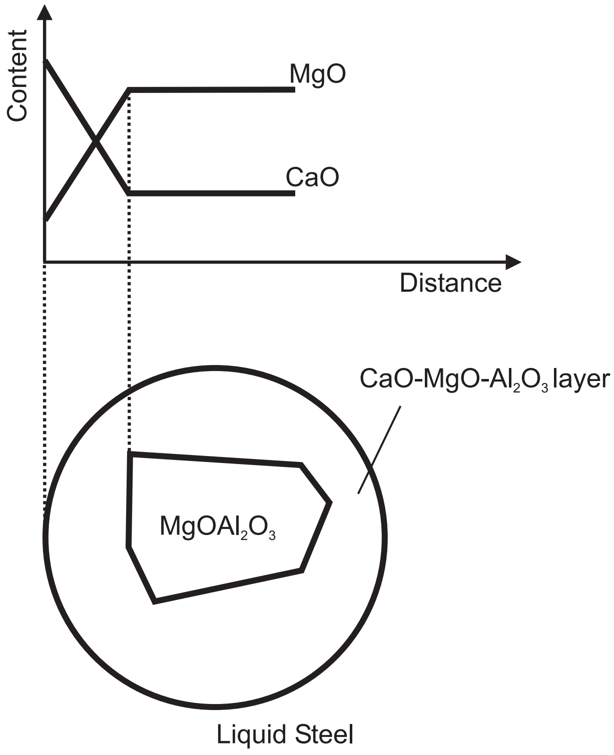

Figure 2.12: Schematic model on the evolution of complex oxides [40].

According to [40] this reaction is also responsible for the final morphology of the inclusions: Given that the diffusion of $[Ca]$ is faster in molten steel than that of CaO or MgO in the inclusion, an increased $[Ca]$ concentration at the inclusion/liquid interface can be assumed. The surface of the formed

$CaOAl_2O_3MgO$ changes towards higher contents of CaO, resulting in a transformation of the rather edged shape inclusion to a spherical shape (considerably lower melting point of $xCaOyAl_2O_3$).

$$x[Ca] + \langle yMgO\, zAl_2O_3 \rangle = \langle xCaO\, (y-x)MgO\, zAl_2O_3 \rangle + x[Mg] \tag{2.23}$$

$$CaO + \langle xCaO\, yMgO\, zAl_2O_3 \rangle = \langle (x+1)CaO\, (y-1)MgO\, zAl_2O_3 \rangle + MgO \tag{2.24}$$

$$CaO + \langle yMgO\, zAl_2O_3 \rangle = \langle CaO\, (y-1)MgO\, zAl_2O_3 \rangle + MgO \tag{2.25}$$

With increasing reaction time MgO diffuses to the outer surface of the inclusion and is reduced by $[Ca]$ according to Eq. (2.26), which leads to a continuous decrease of the MgO-content in the inclusion.

$$[Ca] + \langle xCaO +\ MgO\, zAl_2O_3 \rangle = \langle (x+1)CaO\, zAl_2O_3 \rangle + [Mg] \tag{2.26}$$

Jiang *et al.* [40] concluded that the steel/slag reaction time has a significant impact on the resulting inclusion composition and morphology. In the performed study, longer reaction times result in oxides surrounded by a $CaOAl_2O_3$-layer which would offer advantages for steel properties. Moreover, varying slag composition showed an noticeable influence on the final inclusion landscape: Decreasing the Al_2O_3 content in the slag leads to a higher number of MgO-based inclusions.

The transformation of $MgOAl_2O_3$ to more complex oxides containing CaO was also studied by Tang and Li [11]. The thermodynamic software *FactSage* was applied to analyse the influence of calcium treatment in ladle refining on the behaviour of spinel inclusions. In the referred case, adding only $1\ ppm\ Ca$ to the molten steel leads to the formation of complex $CaOMgOAl_2O_3$ inclusions and the content of MgO and Al_2O_3 in the liquid inclusions decreases rapidly, against what an increase of CaO content is observed. Similar results were obtained by Kang *et al.* [42], who also reported that the level of required dissolved Ca in the melt appears to be very low for the transformation of MgO and Al_2O_3.

A very detailed study on the formation and modification behaviour of complex oxide inclusions over a whole process route was done by Park [18]: Fundamental thermodynamic calculations were combined with laboratory experiments in a high frequency induction furnace and plant data in order to examine inclusion formation and modification in high-alloyed stainless steel melts ($Fe-20\%Cr-13\%Ni\text{-}3\%Si$). Based on the compositions of inclusions in samples taken during plant operation, the formation mechanism of inclusions containing spinel crystals has been developed. It was reported that the composition of the inclusions is a function of the activity of deoxidising elements in the steel melt.

Moreover, the molar content of Al in the inclusions is linearly proportional to the increase of the Al-content. Regarding the modification of inclusions over the whole stainless steel manufacturing route, it was found that the contents of MgO and Al_2O_3 in the calcium silicate type inclusions rose continuously as the steel melt transfers from the AOD converter to the tundish. According to [18] this may be explained by the reduction of MgO and Al_2O_3 in the slag or refractories by silicon in the steel melt. In tundish samples an increasing content of MgO and Al_2O_3 in the inclusions was observed; thus, the spinel phase could crystallize in the $CaSi$-matrix at this stage. During casting and cooling the formed spinel crystals grew. The author also indicates a critical Al-content of $20\ ppm$ for the formation of $MgOAl_2O_3$.

Morphological analyses of the complex inclusions were a major instrument for tracking their modification over the processes [18, 43]. The solidification structure of oxides within the system $CaO\text{-}SiO_2\text{-}MgO\text{-}Al_2O_3$ with additions of CaF_2 and the crystallisation of $MgOAl_2O_3$ has been studied using XRD, SEM/EDS and image analysis [44]: While the liquidus temperature of the oxides containing 5 %CaF_2 increases with increasing alumina content, the solidus temperature is not affected by the alumina content. The size of spinel crystals rises with increasing alumina and decreasing CaF_2-content. An increase of the CaF_2-content would make sure that oxides could spend more time at relatively low temperatures, where nucleation is faster than growth.

2.1.4 Summary

The preceding explanations demonstrated the basic formation mechanisms for $MgOAl_2O_3$ as well as the factors influencing their stability and modification. It was shown that although theoretically this spinel can form based on Al_2O_3 and MgO, the latter is less significant, mainly because Al_2O_3 as a deoxidation product in liquid steel originates the formation of $MgOAl_2O_3$. This was also affirmed by the large number of publications dealing with the formation on the basis of Al_2O_3 [10, 11, 16, 27, 28, 30, 32–35], against what only a minority treated this topic based on primarily formed MgO [36, 37].

The Mg in liquid steel is mostly the reaction product of the reduction of MgO from the slag or refractory material. For this reduction reaction two different mechanisms may be responsible: First, other elements present in liquid steel, mostly Si and Al, can cause the reduction of MgO. Secondly, the CO-partial pressure significantly influences the Mg-content. Due to the reaction with C, the Mg-content in liquid steel increases rapidly with decreasing p_{CO}.

Several researchers [19, 22–28] examined the stability range of $MgOAl_2O_3$ from a theoretic and experimental viewpoint. Although a general concordance was achieved, it was shown that the steel composition and the therewith related interactions have a considerable influence on the stability range. Particularly Ca was demonstrated to noticeably affect the Mg-content in liquid steel [29]. Next to Ca also Si was determined to control the stability of $MgOAl_2O_3$. Due to its reaction with soluble Al and Mg, the transformation of $MgOAl_2O_3$ into pure MgO is prohibited [27, 28]. Thus, on the one hand increased SiO_2-contents in the slag would stabilize the spinel phase. On the other hand, an increased content of MgO was found in inclusions with increasing slag basicity CaO/SiO_2 as well as with increasing MgO-content in the slag [11, 32].

Moreover, the Al-content in molten steel was described to be decisive for the formation of $MgOAl_2O_3$. It was demonstrated that an increased content of Al_2O_3 in the slag as well as the use of Al_2O_3-rich refractories increases the amount of $MgOAl_2O_3$ [33].

Since $MgOAl_2O_3$ inclusions are mostly undesired in steels due to their negative influence on steel properties their formation should be avoided for most applications. Although some controversial conclusions concerning the formation and modification of $MgOAl_2O_3$ were found in literature, the following three main consistent propositions can be concluded in order to prevent the formation of $MgOAl_2O_3$:

- Decrease of basicity in the slag;
- Decrease of MgO and Al_2O_3 content in the slag;
- Decrease of Al-content in the melt.

Furthermore, from a kinetic viewpoint, two different hypotheses for the metal/inclusion reaction were compared, analysing whether the diffusion of Mg in the inclusion surface layer or the diffusion of Mg in molten steel is the rate-determining step. Since the calculated reaction rates were significantly lower for the second hypothesis, the diffusion of Mg in molten steel was concluded to be rate-determining. Comparing the reaction rates of slag/metal and metal/inclusion reaction for the stated inclusion type, the slag/metal reaction was found to be slowest in the whole system.

As far as the formation of complex $CaOAl_2O_3MgO$ inclusions is concerned, the most significant influence according to literature is the reaction time between steel and slag [40, 41]. Longer reaction times were observed to result in oxides surrounded by a $CaOAl_2O_3$-layer. Furthermore, it was stated that already very small additions of Ca change the inclusion composition towards that of complex $CaOAl_2O_3MgO$ oxides[11, 42].

Next to a change of chemical composition, also a considerable influence on inclusion morphology through the presence of Ca was determined [18, 43]. While some authors [40, 41] argue that Ca-treatment would have a positive effect on steel properties due to the modification of $MgOAl_2O_3$ into complex oxides, others like Yang *et al.* [10] contradict this hypothesis. In the latter's point of view, the surrounding $CaOAl_2O_3$-layer would only provide little benefit for example on shape control of $MgOAl_2O_3$ in rolling processes, because the inclusion core remains unchanged and does not participate at any reactions. Thus, it is concluded that more attention should be paid to the avoidance and the removal of $MgOAl_2O_3$ than at their modification through Ca-treatment.

2.2 Separation of Inclusions at the Steel/Slag Interface

2.2.1 Approach of the Inclusion towards the Steel/Slag Interface

In principle, the movement of a non-metallic inclusion in a liquid metal can be described by a simple force balance between the natural buoyancy force of the particle and the fluid drag on the rising inclusion. Assuming a spherical solid particle the buoyancy force is given by Eq. (2.27) and the fluid drag—acting in the opposite direction—is expressed by Eq. (2.28), where r is the inclusion's radius, U_M represents the static velocity of the melt and U the velocity of the inclusion. The latter relationship is also illustrated in Fig. 2.13 [45].

$$F_b = \frac{4}{3}\pi r^3 (\varrho_M - \varrho_I) g \tag{2.27}$$

$$F_d = 6\pi r U_M U \tag{2.28}$$

Thus, the velocity U results in:

$$U = \frac{2}{9} r^2 (\varrho_M - \varrho_I) \frac{g}{U_M} \tag{2.29}$$

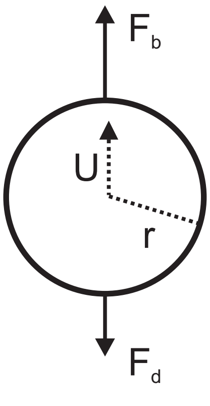

Figure 2.13: Forces acting on a particle inside bulk liquid metal [45].

The relationship stated in Eq. (2.29) depends on the tranquillity of the bath, which is hardly observed for liquid steel. Flow phenomena, for example caused through thermal convection, can influence the movement of the particles and consequently prevent them from reaching the steel/slag interface. Since the tundish in continuous casting is one of the most important sites for inclusion removal in steelmaking, numerous numerical and experimental studies have been performed examining the behaviour of inclusions under different flow conditions [46–51].

According to the mathematical model developed by Miki and Thomas [47] which predicts the removal of Al_2O_3 from molten steel in a tundish, the inclusion removal rate is significantly influenced by the size of the particles: In general large inclusions float to the top surface much faster than smaller ones. In the authors' point of view, in order to fully understand the conditions of an optimum inclusion transport to the top-covering slag phase flow pattern, thermal buoyancy, turbulent motion, collision, flotation as well as reoxidation have to be considered. For their considerations the authors used the computational fluid dynamics code FLUENT, applying the standard $K-\varepsilon$ turbulence model for high Reynolds number flows. The authors calibrated their model through comparison with measured inclusion size distributions of samples taken from the tundish at different time steps. The inclusions were extracted from the steel matrix with the use of an acid and subsequently analysed by a laser diffraction scattering method. A good concordance between calculations and measurements was ascertained. Several works often using water models for the verification of numerical simulations [49, 50] approve the results given in [47].

An effective method in order to advance inclusion removal is gas bubbling: Once the inclusion got in contact with the surface of a gas bubble at a certain contact angle θ according to Young's Equation (Eq. (2.30))[*], the particle would remain at the surface of the bubble and rise with it. For the attachment a certain work of adhesion W_A—as defined by Eq. (2.31)[†]—is necessary. A large, positive flotation coefficient Δ as defined in Eq. (2.32), promotes good flotation. Consequently, a large σ_{MG} and a large contact angle are advantageous [45].

$$\sigma_{IM} + \sigma_{MG} \cos\theta - \sigma_{IG} = 0 \tag{2.30}$$

$$W_A = \sigma_{MG} + \sigma_{IG} - \sigma_{IM} \tag{2.31}$$

$$\Delta = \sigma_{IM} + \sigma_{MG} - \sigma_{IG} \cdot (1 - \cos\theta) \tag{2.32}$$

Several models exist dealing with the separation of a particle at the steel/slag interface [52–54], especially focusing on the movement of the inclusion through the interface. Details to them will be explained in the following subsection. In all these publications, the considerations for the inclusion approach towards the interface neglect that near a boundary the particle motion is affected by an increase in the hydrodynamic drag force that acts upon it.

A detailed study only concentrating on the approach of an inclusion to the interface was performed by Shannon *et al.* [55]. Their investigations include an extra drag force from the interface and the deformation of the interface. The different steps are displayed in Fig. 2.14. The authors showed that this aspect causes an extra delay. Particles with a diameter of 5 µm for example can be delayed up to 2 s by the resultant drag; for particles with a diameter of 100 µm only a delay of 1/10 s is observed. Moreover, it was shown that a decrease of the interfacial tension between the two phases (for instance resulting from the presence of sulfur at the interface) can increase the delay up to 2 %.

---

[*] σ represents the interfacial tension between two phases, where I=inclusion, M=metal and G=gas phase.

[†] assuming a plate-like inclusion

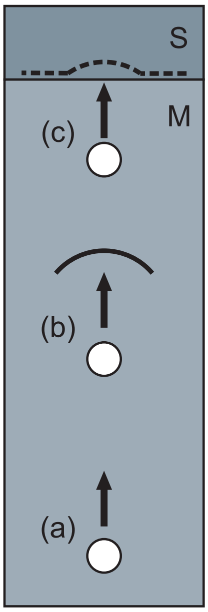

Figure 2.14: Steps in particle separation: a.) The particle is at its constant terminal velocity. b.) The particle is affected by a confined drag field. c.) The particle is close enough to deform the interface in addition to suffering a confined drag field [55].

2.2.2 Mathematical Modelling of the Separation Process

The two main aspects with regard to the separation of non-metallic inclusions from the steel to the slag are the interfacial energies and the bulk properties. First approaches dealing with this topic were made by Kozakevitch and Lucas [56] who developed a model assuming a thin inclusion converging to the steel/slag interface. Because of the high surface-to-volume ratio, only the interfaces were considered in these cases. For the transfer of the inclusion from the steel to the slag, the following condition has to be fulfilled [56–58]:

$$\Delta G = \sigma_{SI} - \sigma_{MS} - \sigma_{IM} < 0 \tag{2.33}$$

The applicability of the proposed model is limited due to the following simplifications [59]:

- Assumption of a thin inclusion shape:

  Interfacial areas change continuously during separation according to Eq. (2.34). Thus, shape and position of the particle will significantly influence the separation process. Caused by an energy change over the distance, a capillary force as given in Eq. (2.35) will act on the inclusion.

$$G = A_{SI}\sigma_{SI} - A_{MS}\sigma_{MS} - A_{IM}\sigma_{IM} \tag{2.34}$$

$$F_{\sigma,Z} = \frac{dG}{dZ} \tag{2.35}$$

- Assumption of steel and slag as continuous liquids:

  This evidence is not valid any more, when the inclusion approximates to the surface due to the need to remove liquid metal between the inclusion and the slag.

In the model by Kozakevitch and Lucas [56], only two possible states exist: Either the inclusion is separated from the metal into the slag phase or it is not separated. Influences, which can delay the separation process, like flow detachment or the drainage of a liquid steel film between the inclusion and the interface are not considered.

Nakajima and Okamura [52] extended this approach for a non-continuous liquid, including the formation of a steel film and also considering the influence of slag viscosity and wettability. The theoretical model is based on the equation of motion: buoyant F_b, added mass F_m, rebound $F_{\sigma,z}$ and drag force F_d acting on an particle trying to cross the steel/slag interface. An overview on the described acting forces is illustrated in Fig. 2.15. This model considers a spherical, solid inclusion with constant volume, which is chemically inert. The interface between steel and slag is flat and the slag phase is assumed to be liquid. Moreover, the interfacial tension is supposed to be uniform along the interface. Similar examinations affirming the considerations of Nakajima and Okamura [52] were done by Bouris and Bergeles [53].

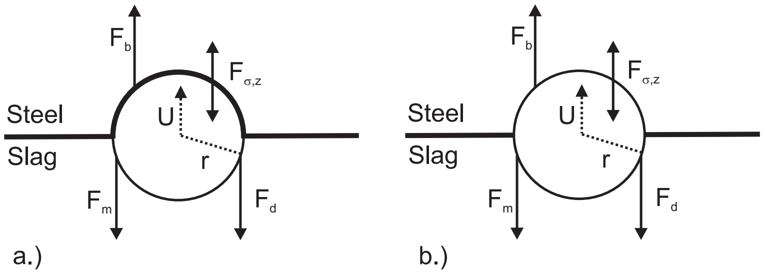

Figure 2.15: Forces acting on a particle once it has reached the steel/slag interface, a.) with a steel film and b.) in contact with both the steel and slag phases [45].

As schematically shown in Fig. 2.16, in the model developed by Nakajima and Okamura [52] the Reynolds number R_e, is decisive for the situation of the inclusion at the interface:

$$R_e = \frac{2\varrho_M U_o r}{n_M} \tag{2.36}$$

Here, U_o defines the terminal or initial velocity of the inclusion as given in Eqs. (2.37) (for a liquid inclusion) and (2.38) (for a solid inclusion), where $\beta = \frac{n_I}{n_M}$.

$$U_o = \frac{2}{3} r^2 (\varrho_M - \varrho_I) \frac{g}{n_M} \frac{1+\beta}{2+3\beta} \tag{2.37}$$

$$U_o = \frac{2}{9} r^2 (\varrho_M - \varrho_I) \frac{g}{n_M} \tag{2.38}$$

In the case where $R_e \geq 1$, the inclusion is always surrounded by steel and hence the steel is not pushed away rapidly. Consequently, a thin steel film exists when the inclusion reaches the steel/slag interface. If $R_e \leq 1$, no steel film is formed and the particle will be in direct contact with the slag at the interface. Nakajima and Okamura [52] concluded that the formation of a steel film is most likely at an particle diameter of about 150 µm. Since the average diameter of inclusions in modern steelmaking processes is commonly much smaller than 150 µm, the non-film case seems to be more relevant. In dependence of the interfacial properties of the system, the size and the initial velocity of the inclusion, three different conditions can be maintained for an inclusion at the steel/slag interface according to the described mathematical model [52]:

1. Instantaneous pass of the inclusion in the slag;

2. Remain of the inclusion at the interface acting as a possible source of clusters that may re-enter the steel bath;

3. Oscillation of the inclusion at the interface.

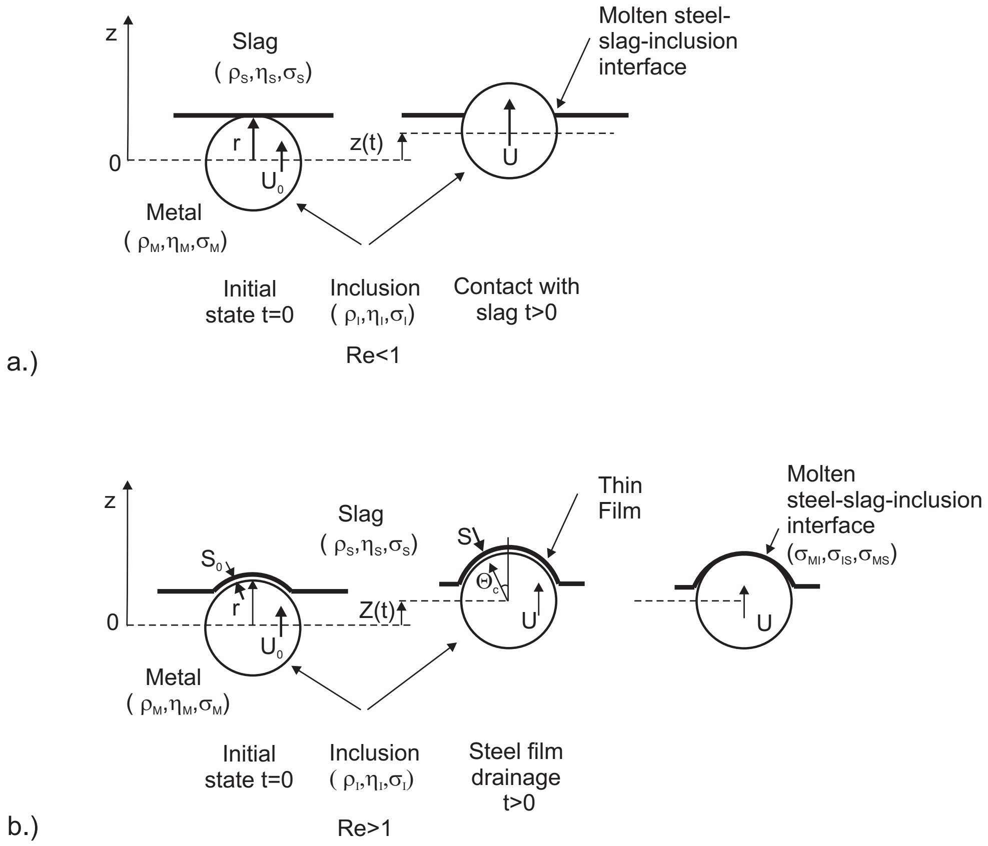

Figure 2.16: Schematic diagram describing the inclusion transfer to the slag phase, a.) without the formation of a film between the inclusion and slag and b.) with the formation of a steel film between the inclusion and the slag [52].

With the help of the model by Nakajima and Okamura [52], the critical parameters for inclusion separation have been evaluated especially focusing on tundish conditions. A hypothetical low carbon, Al-killed steel was chosen for the investigations combined with three different slags representing typical compositions of ladle (36 %Al_2O_3, 59 %CaO and 5 %SiO_2), mould (10 %Al_2O_3, 20 %CaO, 10 %MgO and 40 %SiO_2, 20 %Na_2O as well as slight additions of Li_2O and B_2O_3) and tundish (21 %Al_2O_3, 36 %CaO, 42 %SiO_2 and 0.4 %MgO) slags. While mould and ladle slag offer a viscosity of about 0.05 Nsm^{-2}, the viscosity of the tundish slag is one magnitude higher [60].

Strandh *et al.* [61] applied the model by Nakajima and Okamura [52] to study different influence parameters concerning inclusion separation. The authors concluded that the influence of the parameters is strongly dependent on inclusion size: While the interfacial tensions and the slag viscosity are decisive for smaller inclusions (*e. g.*, a particle diameter of 20 μm), the separation of a 100 μm particle is also influenced by the inclusion and slag density. Furthermore regarding the influence of slag viscosity more closely, for the compared slags a faster separation of inclusions was found for mould and ladle slags, than for the more viscose tundish slag.

Out of their simulations and the application of the model to industrial conditions, the authors in [61] assessed the following conditions to be most favourable for separation:

- The slag viscosity should be as low as possible, without creating conditions for slag entrainment;
- The overall wettability should be positive.

Based on the work of Nakajima and Okamura [52] and the developments of Strandh *et al.* [61], the model was also used for the estimation of the separation behaviour of liquid inclusions at the steel/slag interface [54]. $Al_2O_3(s)$ and $CaOAl_2O_3(l)$ (each with a diameter of 100 μm) inclusions were used in the model. A comparison between both models showed that the pass and oscillation area are larger for the solid inclusion. As a reason, the difference in inclusion density is mentioned, resulting in a higher added mass force. According to [60] another reason for the shift of the oscillating area might be that the slag viscosity affects the solid inclusion more than the liquid. In the case of liquid inclusions the inclusion viscosity also has a significant influence.

Moreover, the basic approach of Nakajima and Okamura [52] was upgraded for different inclusion shapes (octahedral and plate-like) by Shannon and Sridhar [59]. Their analyses showed that particularly the octahedron takes quite long for separation. In order to enhance the separation process, an considerable capillary force may be necessary. In comparison to the two other investigated shapes, the plate separates quite quickly due to its orientation causing a lack of damping forces.

For the performed calculations [54, 60, 61] input parameters for the physical properties are necessary. The authors indicate that it is very difficult to find reliable experimental data in literature and show that there is a need for more experiments in order to determine the physical properties governing inclusion separation, especially concerning the slag viscosity and the interfacial tensions.

2.2.3 Experimental Consideration of the Separation Process

Besides mathematical approaches, several researchers also experimentally dealt with the behaviour of inclusions at the steel/slag interface. One example is the work of Wikstroem [62], who investigated the application of the mathematical model by [54, 61] to industrial ladle and tundish conditions. The author performed experiments using a Laser Scanning Confocal Microscope (LSCM) on a high carbon, calcium-treated steel containing $CaOAl_2O_3$ inclusions and a 36 %CaO-21 %Al_2O_3-43 %SiO_2 slag. Within their work, they studied the agglomeration of liquid inclusions in the slag as well as at the steel/slag interface. For the experiments an Al_2O_3 crucible and Ar-atmosphere were used; the samples were heated up with a rate of 100 °C per min until 50 °C below the observation temperature, from where the temperature was controlled manually. For the experiments a slag thickness of 2 mm was applied. Next to the transparency of the slag, also the thickness was reported to be very important, since the Al_2O_3 crucible would wet the slag if its thinner than 2 mm. Consequently, the liquid slag layer would be either at the crucible walls or under the steel sample.

In the described work, agglomeration between the liquid inclusions was observed at the interface with increasing temperature. The increased temperature also promoted the slag flow; accordingly, the inclusions were pushed towards each other. It was also illustrated that the bigger inclusions are, the easier it is for them to agglomerate. The comparison of the experimental and calculated results showed a rather good agreement [62, 63].

Apart from this work, Lee *et al.* [7] used a LSCM for the investigation of the separation behaviour of Al_2O_3 at the steel/slag interface. In these experiments samples of a low-carbon steel containing Si, *Mn* and *Al* were placed in an Al_2O_3 crucible and covered with a 50 %CaO-50 %Al_2O_3. Their results showed that solid Al_2O_3 inclusions separate across the slag/metal interface under the assumed conditions, but agglomerate once they have separated at the slag side of the interface. Concerning liquid inclusions out of the system MnO-SiO_2-Al_2O_3 it was observed that they do not separate as quickly at the slag/metal interface.

Next to experiments using a LSCM, Beskow *et al.* [64] developed a new sampling technique in order to obtain samples of the actual slag/steel interface in industrial ladles. The sampler, as illustrated in Fig. 2.17, consists of a stainless steel sampling tube, an outer mounting tube and a bottom part that is able to enclose the sample. Before sampling the sampling tube is placed inside the mounting tube and held in position by a retaining pin. During sampling, the retaining pin is released and the sampling tube falls into the melt. In the described study, samples were taken out of a 65 *t* ladle, after deoxidation but before vacuum degassing. Before sampling it is necessary to estimate the thickness of the slag layer in the ladle to assure that the immersion depth of the sampler is deep enough. Subsequent microscope analyses of the samples showed tiny metal droplets in the bulk of the slag, while no slag droplet was detected in the bulk of the metal close to the interface. Based on their first results, the authors concluded that a lot of subsequent systematic samples are needed in order to get a clear understanding of the reactions taking part.

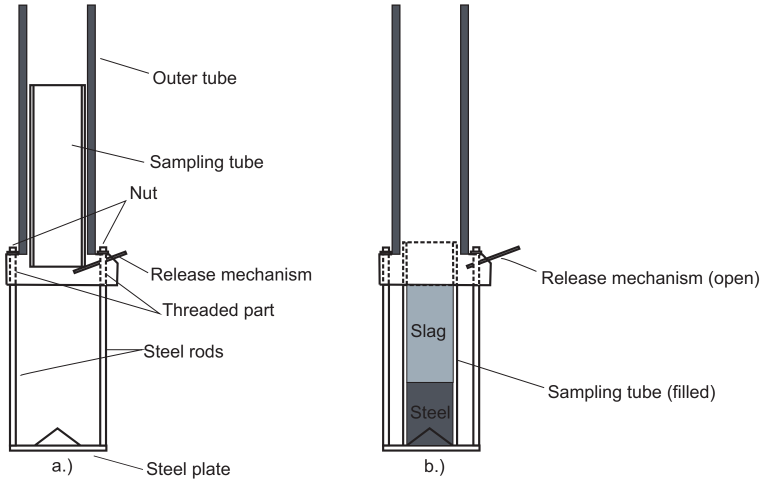

Figure 2.17: Schematic diagram of the sampler, a.) when the sampling tube is empty b.) when the sampling tube is filled with metal and slag [64].

Dayal *et al.* [65] also collected samples of medium and high carbon tool steels from a 65 *t* ladle using the same sample technique as described above. Different stirring conditions and sample positions were investigated in order to get an insight into the mixing behaviour of steel and slag. Based on their results, Dayal *et al.* [65] suggested that the shear force is one of the major influencing factors for slag/metal mixing. Moreover, the evaluation of a cold model study showed that the slag/metal system behaves very similar to the system oil/water. On the basis of the experimental results, the authors established preliminary mathematical models in order to describe the rate of mass exchange at the steel/slag interface. Although first feasible results were gained with the new sampling technique, further experiments are now needed primarily with regard to a quantitative description of the interface in order to be able to fully assess the ongoing procedures.

2.2.4 Summary

The removal of inclusions is an important aim in steelmaking. Therefore, the approach of an inclusion in the liquid metal to the steel/slag interface and the subsequent separation at this interface was studied in detail by several research groups using mathematical models in combination with experimental methods. The aggregate which has been addressed most often in the literature in this context is the tundish in continuous casting [46–51].

Basically, the movement of a inclusion in liquid steel can be described by a simple force balance between the natural buoyancy force of the particle and the fluid drag on the rising particle. Next to flow phenomena, for example caused by thermal convection, which can strongly influence the particle movement, the particle size is regarded to be most decisive for inclusion transportation to the steel/slag interface [47]. Moreover, gas bubbling was stated to be an effective method in order to advance inclusion removal [45].

As far as the separation step at the steel/slag interface is concerned, interfacial energies and bulk properties are essential. The first mathematical approach was done by Kozakevitch and Lucas [56] who assumed a thin plate-like inclusion. Since this model was limited by several simplifications, Nakajima and Okamura [52] improved this basic idea for non-continuous liquids and a solid spherical inclusion also taking into account the formation of a steel film as well as the influence of slag viscosity and wettability. The *Re*-number in combination with particle size was found to significantly influence the situation of the inclusion at the interface. The authors concluded that the non-film case ($Re < 1$) is more relevant in practice. The results of this model showed that a low slag viscosity and a positive wettability are favourable for the separation of an inclusion at the interface.

Besides mathematical approaches, also experimental methods were used in order to study the separation process. In the last years mainly the Laser Scanning Confocal Microscope (LSCM) emerged as an effective method for in-situ studies of inclusion behaviour. One major aspect in this context was the agglomeration of solid and liquid inclusions. It was found that the bigger the inclusions are the easier it is for them to agglomerate [7, 54, 61].

A new sampling method was developed by Beskow *et al.* [64] which enables the direct observation of samples out of the steel/slag interface in industrial processes. Although the basic idea is very interesting, elaborate systematic test series need to be performed in order to get a reliable insight on the reactions taking part. As these series have only been performed to a limited extent, the value of this method cannot be fully appraised at present.

2.3 Dissolution of Oxides in Slags

Basically, the dissolution rate of particles in the slag is a function of slag chemistry and temperature. The kinetics of inclusions dissolution has to be fast enough in order to minimize the probability of re-entrainment of the inclusion in the steel melt. Furthermore, the slag has to be designed properly to dissolve the inclusion so that the particle is not able to act as an heterogeneous nucleation site for slag crystallization.

One of the first research groups who studied the dissolution process of oxides in slags were Taira *et al.* [66]. They performed laboratory experiments using the rotating cylinder method to investigate the influence of revolution speed, temperature and slag composition on the dissolution rate of sintered alumina in molten CaO-SiO_2-Al_2O_3 slags. The slags used in the described study consisted of 10 %Al_2O_3 and a basicity CaO/SiO_2 ranging between 0.64 to 1.25. The synthetic slags were premelted in a Tammann

Furnace using a graphite crucible. Afterwards, the sintered alumina cylinder was preheated above the slag surface for about 5 min, it was immersed in the slag bath and rotated at a fixed revolution speed. After the withdrawal of the cylinder from the slag bath, its diameter was measured and compared with the initial state. Moreover, the cross section of the cylinder after the experiment was analysed by EPMA.

It was concluded that the dissolution rate of Al_2O_3 in molten CaO-SiO_2-Al_2O_3 slags rises with increasing revolution speed and higher temperatures. Secondly, increasing the slag basicity effects a higher dissolution rate, whereby the dissolution rate at a ratio $CaO/SiO_2 = 1$ was observed to be especially large. This finding was attributed to the formation and mechanical separation of $CaOAl_2O_3$ particles.

Yu *et al.* [67] performed similar experiments also using the same method. They studied the dissolution of Al_2O_3 in mould slags (varying CaO/SiO_2 between 1 and 1.5 with 4 – 16 %Al_2O_3 and additions of Na_2O and CaF_2) and deduced that the solubility of Al_2O_3 in the stated slags is about 38 % regardless of the composition, for the varying studied basicity range. Additions of CaF_2 and Na_2O were observed to only have little effect on the solubility of Al_2O_3. Nonetheless, the dissolution rate is seen to be significantly influenced by slag viscosity.

Considering the large volume ratio between slag and inclusion in the referred works using the rotating cylinder method, Sridhar and Cramb [68] assessed the applicability of these methods (mainly considering refractory erosion) to the kinetics of inclusion dissolution as limited and proposed a novel technology for an in-situ study using a Laser Scanning Confocal Microscope (LSCM). Applying this method in combination with a hot stage it is possible to analyse the dissolution of particles in slags at steelmaking temperatures. Principally, these experiments are performed by placing oxide particles on the surface of slag samples, offering a composition comparable to industrial slags. In order to maintain slag transparency after melting, slight composition changes were necessary in some cases. When the slag melts, the change of inclusion size and shape with time can be studied through the microscope.

Sridhar and Cramb [68] analysed the dissolution behaviour of Al_2O_3 in synthetic 33 %CaO-7.3 %MgO-19.5 %Al_2O_3-39.5 %SiO_2 slags. For this purpose, Al_2O_3 particles (diameter 50 – 90 μm) were placed on the top of the slag in a Pt-crucible. The samples were heated under Ar-atmosphere; experiments were performed at four different temperatures between 1430 °C and 1550 °C. As a result, the dissolution rate was low and no shrinkage of the particles was observed below 1400 °C. Above this temperature the dissolution process seemed to occur topochemically down to a radius of 10 μm. Below this size, the particles tended to become porous and some of them would fall apart. Optically, the particles seemed to dissolve continuously and no indication of a solid reaction layer preventing further dissolution was found. At 1550 °C particles of 48 μm radius dissolved completely within 203 s.

Several further publications also using a LSCM in combination with a high-temperature chamber and comparable experimental conditions followed [69–73] focussing on dissolution time of different particles in varying slag compositions and the related influencing factors. They will now be described in more detail in the following subsection.

2.3.1 Estimation of the Dissolution Times for Inclusions in Slags

According to Tse *et al.* [74], the dissolution time for Al_2O_3 with a diameter of 50 – 100 μm in 50 %CaO-50 %Al_2O_3 slags is about 1 min at 1500 °C. Valdez *et al.* [69] performed experiments using a LSCM in order to estimate the dissolution time of Al_2O_3, MgO and $MgOAl_2O_3$ in a 36 %CaO-21 %Al_2O_3-42 %SiO_2 slag in the temperature range between 1470 – 1550 °C. Their results showed that the total dissolution times for all particles decreased with increasing temperature. The dissolution times for MgO and $MgOAl_2O_3$ (for particles with 150 μm diameter) were observed as almost identical for these two types at about 200 s at

1500 °C. This is explained by the formation of an $MgOAl_2O_3$ layer on the surface of the MgO inclusion during dissolution. The dissolution times of Al_2O_3 were slightly longer in this case (about 250 s for a 150 µm particle at 1500 °C). These results are in good agreement with [72], who also reported a slower dissolution rate for Al_2O_3 than for $MgOAl_2O_3$ in 16.3 %CaO-19.3 %Al_2O_3-64.5 %SiO_2 slags.

Furthermore, Fox *et al.* [75] investigated the dissolution rates of MgO and Al_2O_3, $MgOAl_2O_3$ and ZrO_2 in fluoride-free mould slags for continuous casting consisting of the components CaO-Al_2O_3-SiO_2-MgO with slight additions of Na_2O, Li_2O and B_2O_3. Given an initial particle size between 100 – 300 µm, the dissolution rates in the studied temperature range of 1300 – 1500 °C of MgO, Al_2O_3, $MgOAl_2O_3$ and ZrO_2 were comparable for all three types, whereby the dissolution rate of ZrO_2 was remarkably slower. Since the dissolution time was very low at any of the applied temperatures, the removal of this inclusion type by dissolution in the slag seems to be rather unlikely. Such ZrO_2 particles may for example be the result of erosion of ZrO_2 insert in the Submerged Entry Nozzle (SEN). In order to decrease the attack of ZrO_2-containing refractory and consequently to minimize the presence of these particles in the final product, the adjustment of the slag composition via a reduced solubility ZrO_2 of was suggested [75].

Lastly, a summary of dissolution times for different particles in various slag compositions is given in Tab. 2.1.

Table 2.1: Summary of typical dissolution times observed for various inclusion types [69, 70, 75].

Inclusion	Size	Slag	Temperature	Dissolution Time
Al_2O_3	110 µm	Tundish slag	1470 – 1530 °C	225 s at 1500 °C
Al_2O_3	110 µm	Tundish (with 7.3 %MgO)	1470 – 1530 °C	225 s at 1500 °C
Al_2O_3	90 µm	Ladle slag	1470 – 1530 °C	60 s at 1500 °C
Al_2O_3	150 µm	36 %CaO-21 %Al_2O_3-42 %SiO_2	1470 – 1550 °C	250 s at 1500 °C
Al_2O_3	150 µm	F-free mould flux	1300 – 1500 °C	1800 s at 1300 °C
ZrO_2	150 µm	F-free mould flux	1300 – 1500 °C	4000 s at 1300 °C
MgO	150 µm	F-free mould flux	1300 – 1500 °C	800 s at 1300 °C
$MgOAl_2O_3$	280 µm	F-free mould flux	1300 – 1500 °C	2800 s at 1300 °C
MgO	150 µm	36 %CaO-21 %Al_2O_3-42 %SiO_2	1470 – 1500 °C	200 s at 1500 °C
$MgOAl_2O_3$	150 µm	36 %CaO-21 %Al_2O_3-42 %SiO_2	1470 – 1500 °C	200 s at 1500 °C
Al_2O_3	150 µm	36 %CaO-21 %Al_2O_3-42 %SiO_2	1470 – 1500 °C	250 s at 1500 °C

2.3.2 Factors Influencing the Dissolution Process

In order to study the governing dissolution mechanism, Sridhar and Cramb [68] applied the classical shrinking core reaction model [76] considering reaction control (see Eqs. (2.40) and (2.41)) as well as boundary layer diffusion control (see Eqs. (2.42) and (2.42)) as rate-limiting steps, where r and r_0 symbolise the instant and initial radius, respectively, $c_I - c_S$ describe the concentration difference between the particle and the slag and t and τ are the current and total dissolution times:

$$r/r_0 = 1 - (t/\tau) \tag{2.39}$$

$$\tau = \frac{\varrho r_0}{\zeta\,(c_I - c_S)} \tag{2.40}$$

$$r/r_0 = 1 - (t/\tau)^{1/2} \tag{2.41}$$

$$\tau = \frac{\varrho r_0^2}{2D\,(c_I - c_S)} \tag{2.42}$$

The essential factors are the particle density ϱ, the driving force for the dissolution (difference in concentration between the saturated slag and the bulk concentration, as shown in Fig. 2.18), and depending on the controlling mechanism, the diffusion coefficient D of the controlling species or the kinetic constant ζ for the reaction.

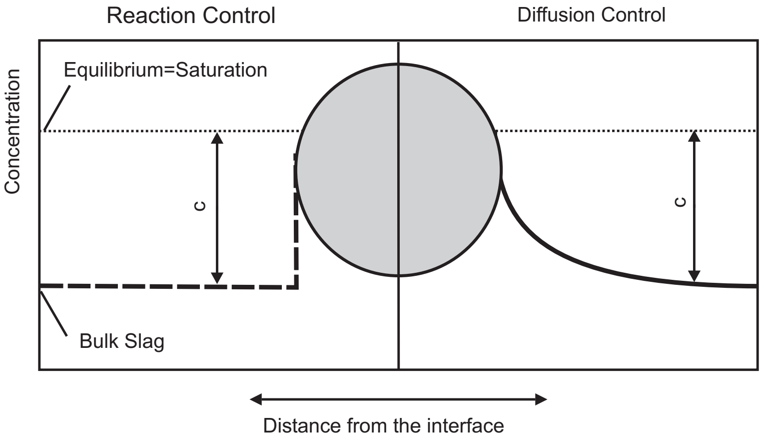

Figure 2.18: Schematics of the driving force for the case of reaction and diffusion control [77].

In the case of the dissolution of Al_2O_3 in 50 %CaO-50 %Al_2O_3 slags, boundary layer diffusion adjacent to the particle surface was reported to be the rate limiting mechanism [68].

As already mentioned beforehand, the dissolution behaviour of MgO, Al_2O_3 and $MgOAl_2O_3$ in CaO-SiO_2-Al_2O_3 slags was analysed by Valdez *et al.* [69, 70, 78]: During the dissolution process—while the surface of Al_2O_3 and $MgOAl_2O_3$ inclusions remains smooth—a dark reaction layer forms around the MgO particles. This layer consists of a slag with high MgO-content with spinel particles that have precipitated in the layer. Consequently, in contrast to MgO and $MgOAl_2O_3$, the dissolution of Al_2O_3 seems to follow the boundary layer mechanism in this case.

Temperature is one of the major aspects influencing the dissolution process. In general, increasing temperature leads to a decrease in dissolution time. Furthermore, a slight shift of the slag composition away from the level of MgO and Al_2O_3 saturation can result in a remarkable increase of dissolution rate according to Yi *et al.* [71], against what small additions of MgO into 40 %CaO-40 %SiO_2-20 %Al_2O_3 slags enhance the dissolution process significantly as stated by Tse *et al.* [74].

The dissolution behaviour of Al_2O_3 in CaO-SiO_2-Al_2O_3 slags (with varying CaO/SiO_2 ratio) in the temperature range between 1477 – 1577 °C was also studied by Monaghan and Chen [73]. The authors calculated the diffusion coefficients on the basis of the experimental results. A correlation of diffusion coefficients with slag viscosity was determined. Consequently, Monaghan and Chen [73] supposed that the dissolution process is at least partly controlled by mass transfer in the slag and the dissolution time seems to be inversely proportional to the ratio between super-saturation and slag viscosity ($\Delta c/\eta$). Additionally, an increasing dissolution rate of $MgOAl_2O_3$ with rising slag basicity was observed [77, 79].

Park *et al.* [80] connected the in-situ observation of the dissolution behaviour of inclusions using a LSCM with subsequent EPMA analyses. Through this combination of methods it was possible to study the dissolution paths of MgO and Al_2O_3 inclusions in various slags out of the system CaO-SiO_2-Al_2O_3. In these investigations the slag basicity was varied between 0.85 and 1.28 and the Al_2O_3 content was changed from 5 to 35 %. Next to temperature, slag viscosity and slag composition, the dissolution rate can also be influenced by the mechanism of reaction product formation during the dissolution. In order to prove the latter, the reaction product layers around the inclusions were analysed after each experiment. In the case of Al_2O_3 particles dissolving in the CaO-SiO_2-Al_2O_3 slags, reaction products such as $CaO\,6Al_2O_3$, $CaO\,2Al_2O_3$ and $Ca_2Al_2SiO_7$ formed on the surface of the inclusion. An almost constant dissolution rate was observed; the size of inclusions shrunk nearly linearly with the dissolution time. The same behaviour of dissolution rate was found for MgO particles in combination with the slag compositions, where no reaction product was formed (rather high content of SiO_2 and only very low Al_2O_3 contents).

On the contrary, in the case of MgO dissolution in slags featuring a higher Al_2O_3-content, the dissolution process was retarded. Only at the end of the dissolution reaction the inclusion size is reduced significantly. Detailed analyses showed that the core MgO continuously dissolved in the inner liquid phase, while the outer $MgOAl_2O_3$ or Ca_2SiO_4 phases kept their size and shape. After the complete dissolution of the core, the outer ring decomposed and was immediately dissolved in the bulk slag. As a result, Park *et al.* [80] concluded that the formation of this inner phase seems to be decisive for the differences in inclusion dissolution behaviour: It is assumed that once this phase forms, thermodynamically its composition should correspond to the co-saturation liquid composition with MgO and $MgOAl_2O_3$ phase. A schematic sequence for the dissolution mechanisms of MgO and Al_2O_3 in molten slags is illustrated in Fig. 2.19.

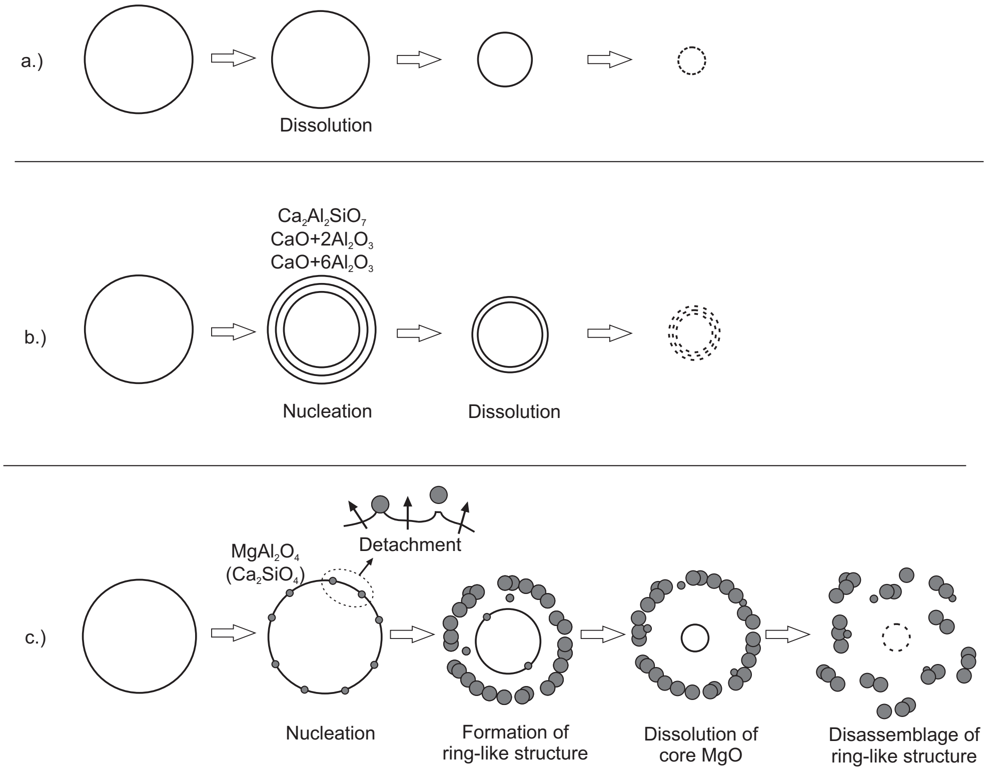

Figure 2.19: Schematic diagram for the dissolution mechanism of MgO and Al_2O_3 in molten slags: a.) when no reaction products form, b.) when reaction products are calcium aluminate phases and c.) when reaction products are $MgOAl_2O_3$ or Ca_2SiO_4 phases [80].

2.3.3 Summary

The two major factors influencing inclusion dissolution in slag are slag composition and temperature. In general, increasing temperature leads to a decrease in dissolution time.

From an experimental viewpoint, the Laser Scanning Confocal Microscope (LSCM) has become the outstanding method for in-situ observation of inclusion dissolution in different slags. For this purpose, oxide particles are placed on the surface of premelted slag samples and consequently the whole system is heated up to the desired observation temperature. Provided that the slag is transparent, the dissolution of the particles can be studied and the dissolution rates can be determined.

As far as the evaluated dissolution times are concerned, large differences were found in dependence of the used slag compositions. Comparing the dissolution of equal sized Al_2O_3, MgO and $MgOAl_2O_3$ in comparable slags (36 %CaO-21 %Al_2O_3-42 %SiO_2) and temperature conditions, a slower dissolution rate was observed for Al_2O_3 than for $MgOAl_2O_3$. The dissolution rate of ZrO_2 was found to be extremely low compared to other analysed oxides [69, 70, 72, 75].

Next to the mentioned experimental approaches, the governing dissolution mechanism was studied on the basis of the classical shrinking core reaction model. In the examined case, boundary layer diffusion adjacent to the particle surface was reported to be the rate limiting mechanism [68]. Moreover, the influence of slag basicity as well as slag viscosity on the dissolution behaviour of oxides were analysed. For the investigated conditions, the dissolution time seems to be inversely proportional to the ratio between super-saturation and slag viscosity ($\Delta c/\eta$). Also, an increasing dissolution rate of $MgOAl_2O_3$ with rising slag basicity was observed [77, 79].

Furthermore, it was found that the dissolution rate can also be influenced by the mechanism of reaction product formation during the dissolution. In the investigations by Park *et al.* [80] it was shown that for the assumed conditions, the dissolution can be retarded through the formation of reaction products during dissolution.

2.4 Steel/Slag Interfaces in Remelting Processes

In the following section the explanations concentrate on the Electroslag Remelting process, whereby especially the metal-slag reactions and the removal of inclusions at these interfaces are described in more detail. Special attention is also paid to the slag system used in the ESR process, since slag composition and the therewith related properties can significantly influence the removal and modification of inclusions.

2.4.1 Fundamentals about Remelting

In general, remelting processes are characterised by the melting and re-solidification of already solidified steel. Therefore, these processes—whose primary aim is metal refining—are ranked among secondary, respectively in recent years even tertiary, metallurgy. All remelting processes are continuous; a solid consumable electrode is transformed into an ingot. Depending on the reactive medium which is responsible for the refining effect, based on first developments going back to the late nineteenth century, two main processes have emerged over the years:

- Vacuum Arc Remelting (VAR)
- Electroslag Remelting (ESR)

While the VAR process experienced an intense growth in the USA, the initial use of the ESR process is rooted in the former USSR. Based on a patent by R. H. Hopkins following preliminary work of Armstrong, the ESR process was first applied on industrial scale in the 1940s by M. W. Kellog [81, 82]. A detailed historic review on the development of remelting processes can be found in [83].

The principles of the ESR and VAR process are schematically illustrated in Fig. 2.20. In both cases one end of the consumable steel electrode is heated above its liquidus temperature; in consequence liquid droplets form, fall down through the reactive medium and are subsequently collected in the liquid pool. This pool is bordered by a crystallizer, usually a water-cooled copper mould. Due to the heat removal the liquid metal solidifies directionally from the bottom to the top.

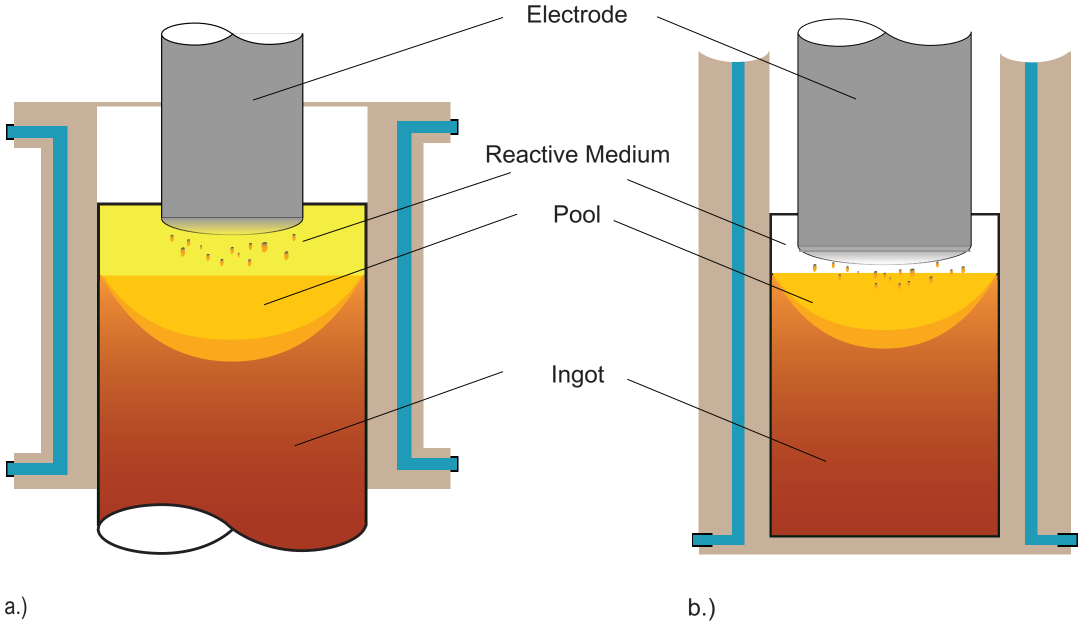

Figure 2.20: Schematic illustration of a.) the ESR process and b.) of the VAR process.

Assuming stationary conditions, a constant ingot growth rate leads to a constant displacement of the liquidus and solidus isotherms in axial direction. This results in an approximately constant volume of the liquid pool during the growth of the ingot. The solidification rate v_E is related to the ingot growth rate v_B via the relation,

$$v_E = v_B \cdot \cos\alpha. \tag{2.43}$$

The interrelationship between the ingot growth rate and the shape of the liquid pool is also explained in Fig. 2.21. Since the present thesis primarily concentrates on inclusion behaviour and modification in the liquid metal, the solidification during remelting processes is not treated in more detail. A comprehensive summary on solidification in remelting processes is for example given by Mitchell [84].

While the heart of the ESR process consists of the liquid slag bath, the refining in the VAR process is performed by the presence of a vacuum. This difference also has a significant impact on the refining of non-metallic inclusions. The gas content as well as the oxide inclusion content are generally lower in ingots remelted under vacuum. Furthermore, trace elements can be removed easily [86, 87]. For more details on the VAR process the reader is referred to literature [83, 88–93].

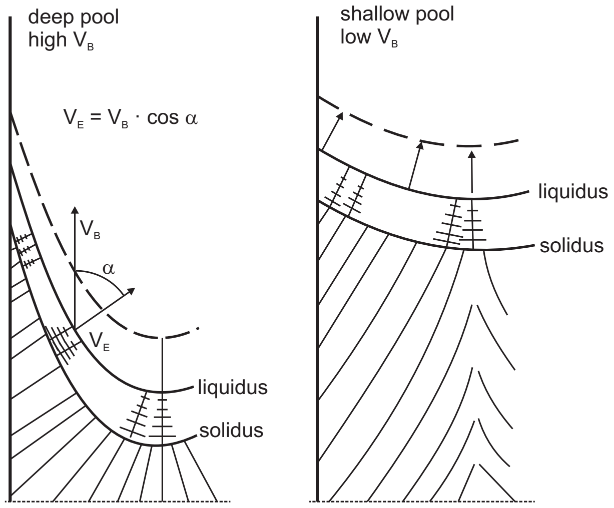

Figure 2.21: Schematic representation of the effect of the ingot growth rate on the shape of the liquid metal pool [85].

As the name of the ESR technology already implies, the slag fulfils several important functions [94, 95]:

- Control of the solidification structure of the remelted ingot via the liquid pool depth (slag temperature);
- Absorption of non-metallic inclusions and detrimental tramp elements;
- Protection of the mould against the liquid metal;
- Protection of the liquid metal against the atmosphere (only limited);
- Transformation of electrical energy into thermal energy.

The heat required for melting is generated by the electrical current passing the liquid slag acting as ohmic resistance. ESR plants can be operated with a static or a collar mould as well as direct or alternating current, whereby in the majority of industrial plants alternating current with 50 – 60 Hz is used. During the process the slag bath moves up according to the ingot growth rate and a thin slag skin is formed between ingot and mould wall. This film protects the mould on the one hand, and avoids a radial heat removal and—as already mentioned—mainly influences the quality of the ingot surface on the other hand. Figure 2.22 gives an insight on the temperature gradient from the slag region to the mould wall.

More information regarding the ESR system engineering and plant design can be found in [83, 88, 96–98]. Based on the ESR process further developments have been done. The Pressure-Electroslag Remelting process for example not only allows the remelting under inert atmosphere but also provides the possibility of nitrogen alloying, for example facilitating the use of stainless steels in medical science due to the replacement of Nickel [99–102]. Another special technology is Electroslag Rapid Remelting, which combines the advantages of the well known continuous casting process with the standard Electroslag Remelting [103].

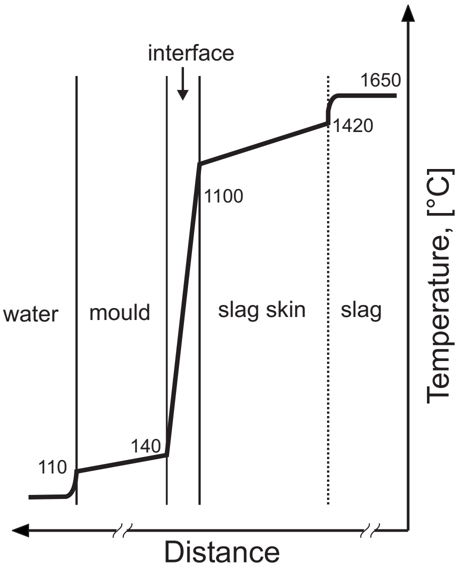

Figure 2.22: Thermal gradients from the slag region to the mould wall [88].

2.4.2 The Slag System CaO-Al_2O_3-CaF_2

The basic components of ESR slags are CaO, Al_2O_3, CaF_2 with additions of other oxides like MgO or SiO_2. Other compounds such as TiO_2 or MgF_2 may be present in small quantities. An overview on common industrial ESR slags is shown in Tab. 2.2. The slag composition most commonly applied consists of approximately equal fractions of CaO, Al_2O_3 and CaF_2.

Table 2.2: Composition of some common ESR slags in *wt.*-% according to [97].

CaF_2	CaO	MgO	Al_2O_3	SiO_2	Comments
100					Electrically inefficient, used where oxides are not permissible
34	33		33		Most commonly applied slag
70	30				Difficult starting, high conductivity, used where Al_2O_3 not allowed, risk of H_2 pick-up
70	20		10		Good, all-round slag, medium resistivity
70	15		15		Good, all-round slag, medium resistivity
50	20		30		Good, all-round slag, higher resistivity
70			30		Some risk of Al pick-up, good for avoidance of H_2 pick-up, higher resistivity
40	30		30		Good, general purpose slag
60	20		20		Good, general purpose slag
80		10	10		Moderate resistivity, relatively inert
60	10	10	10	10	Low melting point, "long" slag
	50		50		Difficult starting, efficient electrically

In order to fulfil the metallurgical demands, the slag must have certain well-defined properties. A very important aspect for slag selection is its liquidus temperature. It should be approximately 100 °C lower than the melting point of the steel. Thereby, an adequate energy efficiency is guaranteed. Furthermore, several technological as well as metallurgical demands are set to slags used in remelting processes [97]:

- Sufficient electrical conductivity for easy process start-up, but not too high energy consumption;

- Use of thermodynamically stable components for process stability;
- Low viscose and homogeneously liquid slags for a clean ingot surface;
- Low oxidation potential;
- Low solubility for gases;
- Maximum desulfurisation ability and absorption of non-metallic inclusions.

2.4.2.1 The Phase Diagram CaO-Al_2O_3-CaF_2

CaO, Al_2O_3 and CaF_2 represent the most important components for slags used for remelting processes. The ternary phase diagram of these components is composed of three two-phase diagrams, one of them—the system CaF_2-Al_2O_3—characterized as unstable due to the evaporation of AlF_3 respectively HF according to the reactions described in Eqs. (2.45) and (2.45) under open conditions or the presence of humidity.

$$(CaF_2) + (Al_2O_3) = 3(CaO) + 2\{AlF_3\} \tag{2.44}$$

$$(CaF_2) + \{H_2O\} = (CaO) + \{HF\} \tag{2.45}$$

Next to Al_2O_3, also other oxides such as SiO_2, TiO_2 or V_2O_5 react in a similar way with CaF_2. Consequently, the slag composition changes continuously. Basically, for experiments these changes can be minimized by the use of a sealed cell avoiding the reaction in Eq. (2.45), because the partial pressure of AlF_3 reaches equilibrium. Since the reaction product CaO formed by Eqs. (2.45) and (2.46) reacts to Calcium Aluminates in the melt according to Eq. (2.46), the compositional changes in practice may not be as large as estimated, caused by a progressive decrease of $a_{Al_2O_3}$ [104].

$$(CaO) + 6(Al_2O_3) = (CaOAl_2O_3) \tag{2.46}$$

For the determination of the phase diagram, experiments under open and closed conditions were carried out. An overview on the different approaches can be found in [104]. Over the years, two controversial ideas of the system CaO-Al_2O_3-CaF_2 were developed: The system after Nafziger [105] determined in open cells and displayed in Fig. 2.23 and the phase diagram according to Chatterjee and Zhmoidin [106] shown in Fig. 2.24, which was established for sealed cells.

The most significant difference between the two phase diagrams is that in one case a miscibility gap is observed. In contrast to the results of Nafziger [105], the findings of Chatterjee and Zhmoidin [106] have been approved by several research groups. Ries and Schwerdtfeger [107] as well as Mitchell [108] observed a phase separation, performing experiments under open and closed conditions. The isothermal cross section of the system CaO-Al_2O_3-CaF_2 at 1600 °C according to Ries and Schwerdtfeger [107] is illustrated in Fig. 2.25. According to Mills and Keene [104], it is therefore obvious that independent of the environmental conditions the phase system with miscibility gap is more likely and therefore recommendable for further investigations.

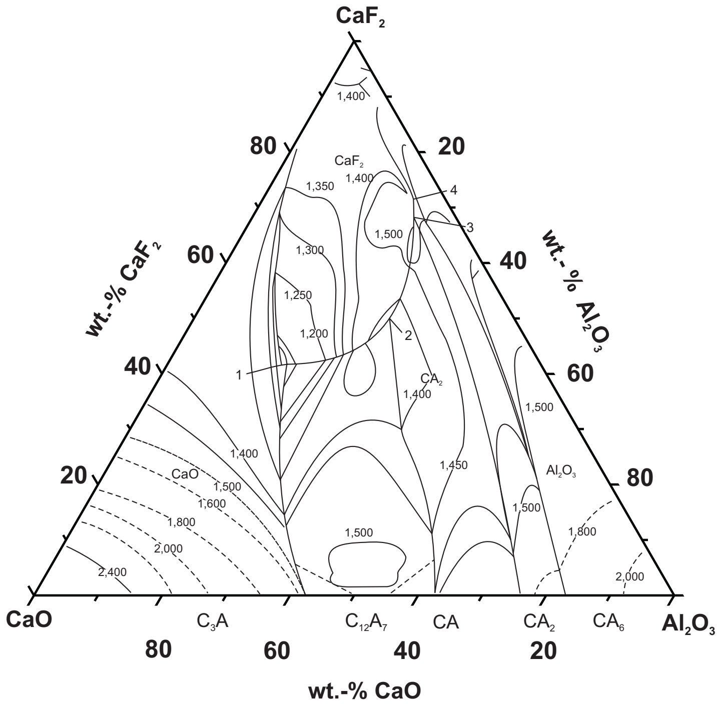

Figure 2.23: Phase diagram $CaO\text{-}Al_2O_3\text{-}CaF_2$ according to Nafziger [105].

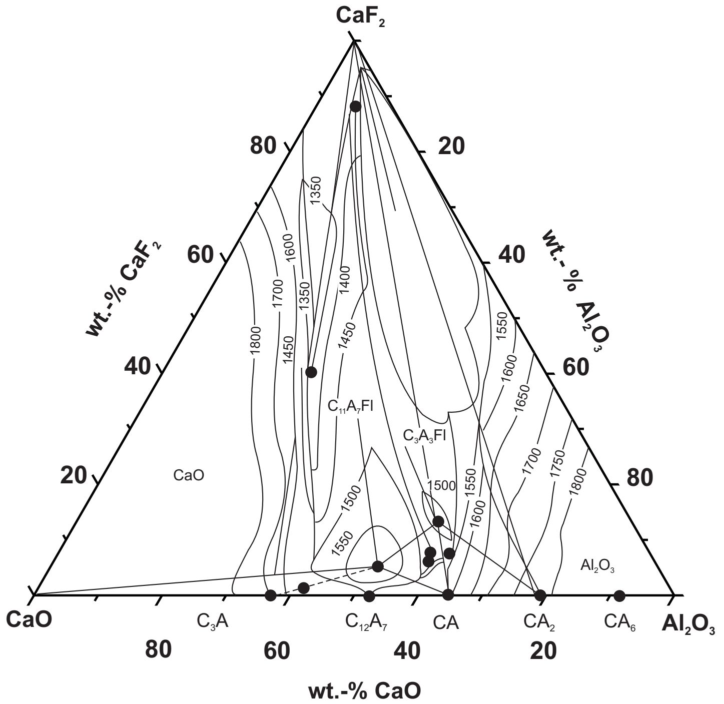

Figure 2.24: Phase diagram $CaO\text{-}Al_2O_3\text{-}CaF_2$ according to Chatterjee and Zhmoidin [106].

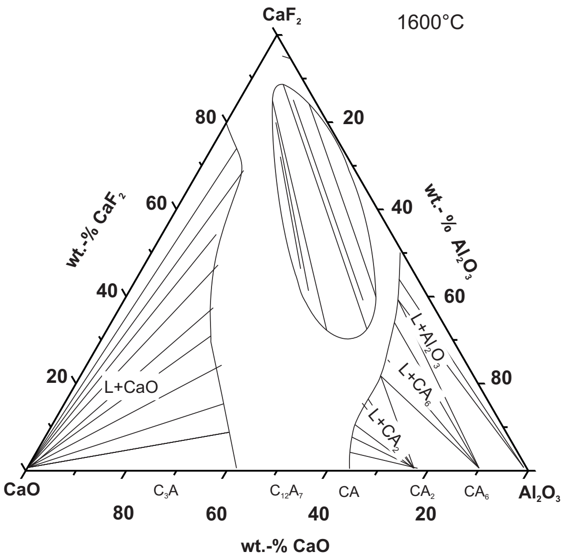

Figure 2.25: Isothermal cross section of the system $CaO\text{-}Al_2O_3\text{-}CaF_2$ at 1600 °C according to Ries and Schwerdtfeger [107].

2.4.2.2 Physical Properties

The physical properties of the slag have a great impact on the remelting process itself as well as on the final ingot quality. A summary of the physical properties within the system $CaO\text{-}Al_2O_3\text{-}CaF_2$ is given in Tab. 2.3. Since the viscosity and the density as well as the surface and interfacial tension are most relevant for the behaviour of non-metallic inclusions during remelting they will be explained in more detail in the following.

Viscosity The slag flow as well as the dwell time of droplets in the slag is influenced by the slag viscosity. Increasing temperatures decrease the viscosity. A low viscose slag results in a more intense stirring and is therefore favourable for metallurgical reactions at the steel/slag interface, whereas an increasing slag viscosity reduces the velocity of descenting droplets and consequently increases the residence time of droplets in the slag according to

$$t = \frac{k\eta}{r^2 \left(\varrho_M - \varrho_S\right)}. \tag{2.47}$$

Mills and Keene [104] indicate that it is very difficult to recommend any set of viscosity values, because large discrepancies are observed between the reported values [109, 110]. However, there are some meaningful values summarized in Tab. 2.3, whereof the following conclusions can be drawn [94]:

- CaF_2 additions decrease the slag viscosity;
- Al_2O_3 additions increase the slag viscosity;
- CaO additions slightly increase the slag viscosity.

Table 2.3: Overview on the physical properties of slags within the system CaO-Al_2O_3-CaF_2 (slag compositions illustrated in Fig. 2.26 [94, 104].

		Values for 1600 °C		
Slag	Viscosity η $[10^{-1}\ Nsm^{-2}]$	Density ϱ $[gcm^{-3}]$	Surface Tension σ $[10^{-3}Nm^{-1}]$	Electrical Conductivity κ $[\Omega^{-1}cm^{-1}]$
A	0.15	2.47	285	6.0
B	0.20	2.48	300	5.0
C	0.25	2.49	310	4.0
D	0.30	2.50	320	3.5
E	0.40	2.55	335	3.0
F	0.60	2.60	350	2.5
G	0.80	2.70	400	2.0
H	1.00	2.80	450	1.0

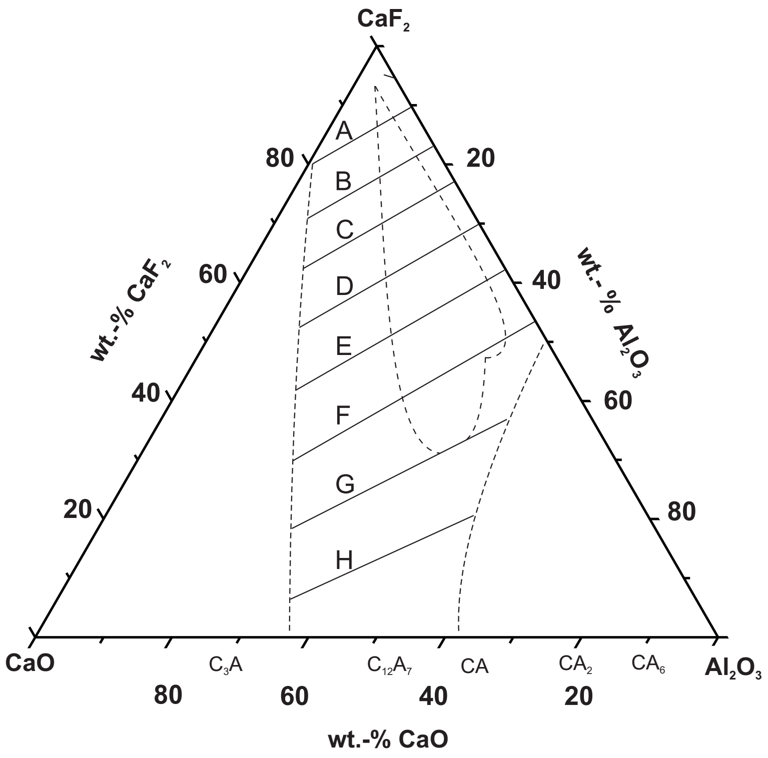

Figure 2.26: Composition of slags within the system CaO-Al_2O_3-CaF_2 described in Tab. 2.3 according to [94].

Furthermore, the electrical conductivity is important for process control and directly influences the slag temperature and consequently the melt rate of the metal to be refined. The addition of oxide components decreases the electrical conductivity, whereby Al_2O_3 acts stronger than MgO; CaO only has a marginal influence. According to Mills and Keene [104], this aspect can be explained in the following context: Oxides with partial polar bonding, like Al_2O_3 have a higher impact on the decrease of the electrical conductivity than oxides with purely ionic bonds (CaO, MgO) because of their tendency to form aggregates of complex ions (*e. g.*, $Al_3O_7^{5-}$) resulting in a lower mobility due to their larger dimensions. Further information about the significance of the electrical conductivity for the process as well as detailed values for the electrical conductivity can be found in [104, 111–116].

Surface Tension and Interfacial Tension Basically, the surface tension decreases with increasing temperature. A low interfacial tension is favourable for the mass transfer and the formation of small droplets, but also encourages slag reentrainment and the adhesion between the ingot and the slag. Thus, the interfacial tension should meet a compromise between the two described extremes. The interfacial and surface tension are linked according to

$$\sigma_{MS} = \sqrt{\sigma_M^2 + \sigma_S^2 - 2\sigma_S \cos\theta}. \tag{2.48}$$

For a detailed description of the correlation reference is made to [94]. Detailed investigations on surface tension in this system have been done by [117–120], a summary of reference values for the surface tension is given in Tab. 2.3. Additions of CaO, Al_2O_3 and MgO reduce the surface tension of CaF_2-based slags [94].

Density This physical property decreases with increasing temperature and influences the size of the droplets and their residence time in the liquid slag. In general, the larger the slag density the smaller the metal droplets and the longer the dwell time of the droplets in the slag. Several works giving data for slag densities within the system CaO-Al_2O_3-CaF_2 have been published [117–119, 121]. A summary of densities in dependence of slag composition is shown in Tab. 2.3. Additions of Al_2O_3, MgO and CaO cause a density increase, whereas SiO_2 decreases the density.

Short Summary Summing up, the advantages and disadvantages of the individual slag components can be descried as follows [122]:

- CaF_2 lowers the melting point and the viscosity of the slag, but on the contrary can be harmful to the environment because of the release of fluoride fumes at high temperatures according to

  $$(CaF_2) + \{H_2O\} = (CaO) + 2\{HF\}. \tag{2.49}$$

- Al_2O_3 increases the electrical resistance of the slag consequently allowing higher voltages and increased electrical input for the same current setting.

- CaO is favourable for a good desulfurisation, but is however hygroscopic and can consequently have a negative effect on the hydrogen content of the ingot.

2.4.2.3 Alternative Slag Systems

Especially because of the considerable danger to health and environment several efforts have been made, to use CaF_2-free slags in the ESR process. Generally, the use of CaF_2-free slags is difficult, because of the high specific electrical resistivity resulting in a problematic control of melting rate. Gammal and Hajduk [122] and Pateisky [123] carried out measurements of the specific electrical conductivity of fluoride and fluoride-free slags as a function of temperature in a Tammann furnace. The authors concluded that the specific electrical conductivity at constant temperatures is at least four times higher for slags containing CaF_2 than for fluoride-free slags. Regarding the desulfurisation potential as well as concerning the hydrogen content of the remelted ingot no significant difference between the slags was found.

Similar results were reported by J.Medved *et al.* [124], who also indicated the higher viscosity and density of fluoride-free slags. Nonetheless, the successful use of slags with less than 5 %CaF_2 for ESR was reported through the decrease of SiO_2 mass fraction. This measure increases electrical conductivity and is advantageous for the fluidity of slags. Results published by Brückmann and Schwerdtfeger [125] are in good agreement with previous works [122, 123] as far as the energy consumption and the ingot surface quality is concerned.

Besides the conventional slag components used in the ESR process, there are several other systems offering the same range of chemical and physical properties as already industrial used slags. Most remarkably in this context is the application of rare earth oxides in the system $CaO\text{-}Al_2O_3\text{-}CaF_2\text{-}RE_2O_3$[‡], whereby La_2O_3 is the most important and therefore most extensively treated oxide. Although La_2O_3 in general has a similar electrical behaviour as Al_2O_3, La^{3+} appears to strongly complex O^{2-} and F^-; the presence of $(RE - O - S)^{n-}$ complexes results in a strongly basic behaviour with respect to sulfur reactions. Hence, this systems allows a low conductivity, basic slag, which is a desirable process component in terms of metallurgical and thermal efficiency.

Another non-conventional slag component is LiF, which causes a great liquidus depression. In consequence, this system retains the approximate phase behaviour of undiluted slags, but offers liquidus temperatures depressed by up to 200 °C through the addition of 5 – 10 %LiF. The main advantage of these slags is an excellent surface quality in ingots where the alloy additions are not compatible with low melting point slags in the $CaO\text{-}Al_2O_3\text{-}CaF_2\text{-}SiO_2$ system. This is mainly the case for stainless steels alloyed with Ti, which could react with the SiO_2 of the slag. Through the use of LiF a low melting point in combination with a highly basic slag can be achieved [108].

2.4.3 Reactions Sites in the ESR Process

As shown in Fig. 2.27, there are seven possible reaction sites in the ESR process. Among them, the three metal/slag interfaces (1–3) which are characterised to be the most important in matters of inclusion removal and modification and therefore will be described in more detail in the following subdivisions [97, 126]:

1. Electrode/Slag
2. Droplet/Slag
3. Metal Pool/Slag
4. Electrode/Atmosphere: Oxides and nitrides may be formed, when the preheated electrode approaching to the slag reacts with air.

[‡] RE signifies *rare earth*

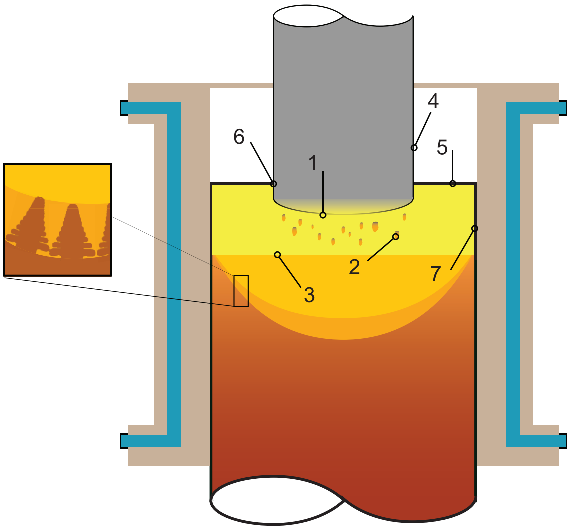

Figure 2.27: ESR reaction sites according to Cooper *et al.* [126].

5. Slag/Atmosphere: At this interface the removal of sulphur from the slag by oxidation as well as the transfer of oxygen in the slag are possible reactions. Moreover, moisture can enter the slag resulting in an increased hydrogen content in the metal.

6. Electrode/Slag/Atmosphere: At this reaction site the solution of scale, like FeO, is possible. This reaction is undesirable in assisting the loss of certain elements, but also may contribute to the removal of sulfur from the slag.

7. Slag/Mould Wall: The temperatures at this reaction site are significantly lower than at the pool/slag interface and the turbulence is much lower. Consequently, decisive reactions are rather unlikely.

Since the oxygen pick-up at the reaction sites 3 and 4 is not negligible, the use of Ar-atmospheres has become state-of-the-art in the industrial practice. This in turn constrains the removal of sulfur.

2.4.3.1 Electrode/Slag Interface

The temperature at the electrode tip is rising to the liquidus temperature of the alloy. The metal collects, forms a droplet and is detached. Basically, the geometry and the location of the electrode tip strongly influence the remelting process. In dependence of remelting parameters the shape of the electrode tip can vary between two extremes: From a nearly flat surface on the one hand, to an apex on the other hand.

The heat distribution in the slag bath is very complex. A typical temperature distribution in the slag determined by Kreyenberg and Schwerdtfeger [127] is shown in Fig. 2.28. The authors established a mathematical model which describes the fluid flow as well as the temperature distribution in the slag during the ESR process. For this purpose, the electromagnetic force and the weight force were inserted as driving forces into the Navier-Stokes Equation, assuming a turbulent flow. This flow is directed towards the electrode at the free surface of the slag, downwards at the centre, outwards in the lower region of the slag and upwards to the mould wall. The natural convection vortex due to density gradients is directed in the opposite direction. Their calculation results showed that assuming a low superheat of the pool, the weight force does not considerably influence the flow pattern. In contrast to this, assuming a high superheat the weight force can enable the formation of a second vortex which is located below the electrode.

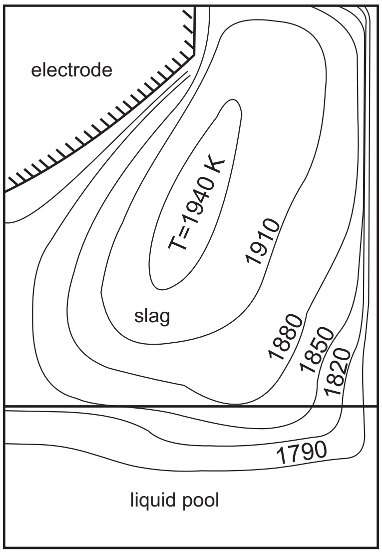

Figure 2.28: Temperature distribution in the slag and metal bath in an ESR system [83, 127].

A detailed study on the thermal characteristics of the ESR-process is also given by Mitchell and Joshi [128]. The authors examined the heat balance of a laboratory scale ESR-furnace working in quasi-steady state. The investigations were performed with a 40NiCrMo6 steel and a CaF_2-25 %Al_2O_3 slag. The temperature distribution in the slag was measured with a thermocouple coated with Borium-Nitride. Both results—measured and calculated—show a temperature gradient from the centre of the electrode to the mould wall as well as over the slag height. In a second step, the temperature and potential fields of the slag were determined. Out of their examinations, Mitchell and Joshi [128] concluded that the most important factors in order to control heat generation are the immersion depth of the electrode as well as the slag resistivity.

Choudhary and Szekely [129] developed a mathematical model for the description of the temperature fields in an industrial ESR unit. Therefore, the Lorentz force field and the spatial distribution of the Joule heating rate were calculated by solving the magneto-hydrodynamic form of Maxwell's equations. The turbulent fluid motion in the slag was calculated by solving the vorticity transport equation in conjunction with the $K-\varepsilon$ model of turbulence. Electromagnetic and buoyancy forces were considered. In a second step, the calculated results have been compared with measurements on an industrial-scale system. The authors determined that the temperature field is relatively uniform, but that large temperature gradients are established in the vicinity of the bounding surfaces. Additionally, as already described by Kreyenberg and Schwerdtfeger [127], Choudhary and Szekely [129] pointed out the flow field is definitely turbulent and the principal effect of this turbulence is to produce a significant enhancement in the diffusive transport of the thermal energy in the system. A good agreement between calculated results and experimental measurements was achieved.

The authors also [129] investigated the difference between an industrial ESR unit and one on laboratory scale: It was found out that the large scale system has a more uniform temperature field, while the maximum temperature in the both units was determined to be nearly the same, although the rate of heat generation per unit volume was substantially higher in the laboratory scale unit. Concerning the velocity field, a relatively uniform distribution was found for the laboratory scale. In contrast to this, in the industrial scale unit a very intense circulation was observed in the region between the mould and the electrode, while the region below the electrode was relatively quiescent.

Korousic [130] experimentally analysed the influence of technological parameters such as slag composition and amount, steel composition, applied energy and filling factor on the shape of the electrode tip as well as droplet formation. The authors performed experiments using an ESR-facility on laboratory scale. Other criteria like mould geometry, atmosphere and immersion depth of the electrode were kept constant. Different steel grades were analysed, primarily differing in carbon content (0.19 – 1.54 %) as well as in the content of overall alloying elements, since these parameters significantly influence the liquidus temperature as well as the thermal conductivity of the steel. The investigated steel grades were 16MnCr5, X30WCrV9-3, S6-5-2, X155CrVMo12-1; three different slag compositions out of the system CaO-Al_2O_3-CaF_2-MgO were applied (CaO/Al_2O_3 ranging between 0.011 and 1.24, CaF_2-content always < 30 %, MgO between 0.4 and 4.4 %). Al and Si were added continuously for deoxidation.

The results of Korousic [130] demonstrated that the slag amount is the major influencing factor for the shape of the electrode tip: Assuming a low slag amount, the heat quantity transferred to the mould wall is significantly smaller than for major slag amounts. The resulting temperature field causes a uniform melting of the electrode. Consequently a nearly flat interface between electrode and slag is observed. In contrast, an increasing slag amount implies a lower temperature directly beneath the electrode due to an increased heat transfer via the mould wall. Hence, the edges of the electrode are melted more rapidly and a cone-shaped electrode tip forms. The effect of the varied parameter on droplet formation will be discussed in the next subsection.

Already Holzgruber and Plöckinger [131] pointed out that the electrode/slag interface seems to be controlling reaction site concerning an effective procedure of metallurgical reactions. On the one hand because of the large slag/metal surface area and the therewith connected short diffusion distances; on the other hand because of the comparatively high temperatures at the interface. This idea was confirmed by Cooper *et al.* [126] and Zhengbang [132]. The latter did experiments on laboratory scale remelting electrodes of a 100Cr6 steel with a CaF_2-30 %Al_2O_3 slag. The refining effect of the different metal/slag reaction sites was evaluated by the use of an oscilloscope that measured the droplet frequency (drops/second). Combined with the melting rate, the droplet weight and metal/slag contacting specific area were calculated and compared. Their results showed that the specific contacting between metal and slag phase at the electrode tip is about 10 times larger than at the droplet/slag interface. Moreover, the time for formation of a droplet on the electrode tip was demonstrated to be 2.27 times longer as that of the droplet falling through the slag bath.

A comparison of relative reaction rates between the reaction sites electrode/slag and slag/pool focusing on sulfur transfer was performed by Cooper *et al.* [126]. The authors examined the remelting on laboratory scale of a C1117 free-cutting carburised steel (0.136 %S) with three different CaO-CaF_2 slags (compositions shown in Fig. 2.29). Steel and slag samples were taken continuously from different positions; subsequently the S-content was measured with LECO-analysis. Tungsten was used in order to outline the pool profile. A summary of their results is shown in Fig. 2.29, the corresponding mass balance equations are given in Eqs. (2.51) and (2.51), where $[S]_E$, $[S]_D$, $[S]_P$, $[S]_I$ are the S-contents of the electrode, droplet, pool and ingot, respectively; m and f are the melt and freezing rate in gram per seconds and M_P is the mass of the metal pool in grams.

$$E_{rate} = ([S]_E - [S]_D)m/100 \tag{2.50}$$

$$P_{rate} = m[S]_D/100 - f[S]_I/100 - \frac{d}{dt}\left(M_P[S]_P/100\right) \tag{2.51}$$

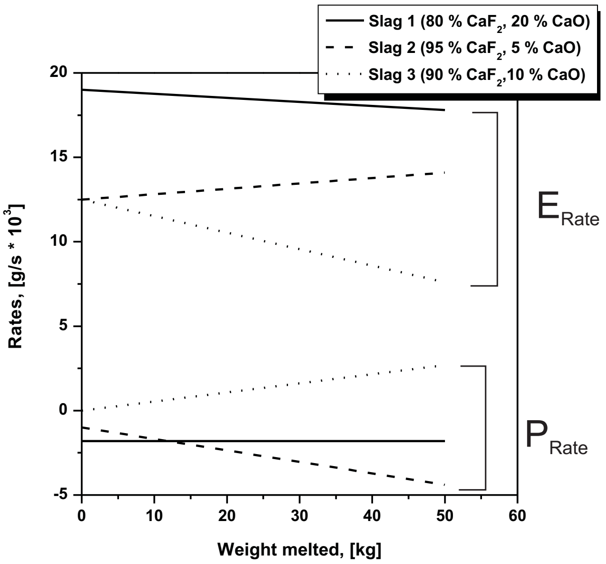

Figure 2.29: Comparison of reaction rates for sulfur removal at the electrode/slag and the slag/pool interface [97, 126].

Based on their investigations, Cooper *et al.* [126] stated that the rate of sulfur removal is clearly the greatest at the electrode/slag interface. Moreover, their results showed, that the reaction occurring at the metal/pool interface could be a reversion reaction. This assumption could have important consequences, especially concerning inclusion formation.

Fraser and Mitchell [133, 134] evaluated the significance of the three metal/slag interface by the use of a mathematical mass-transfer model. They described the kinetics of *Mn* oxidation by *FeO* at the phase boundary metal/slag under controlled conditions. No single transport process was considered as a possible rate-controlling step. Hence, the description of the entire-mass transfer process is permitted by the use of phenomenological flux equations. In the investigations the nature of mass-transfer processes involved at each reaction site was considered. This was complicated due to the dependency of mass-transfer coefficients on flow conditions at the interfaces. The theoretic considerations were coupled with laboratory experiments using an ESR-furnace with a mould diameter of 76 mm. In the experiments the low-carbon steel C 1018 and CaF_2-20 %CaO slags were used. Table 2.4 gives an overview on the calculated mass-transfer coefficients and the hence estimated area/volume ratios for the different considered interfaces as well as on the determined residence times. It can be seen that the residence times at the electrode/slag and the pool/slag interface are approximately the same, while the residence time of the droplet in the slag is significantly lower. These results are in good agreement with the considerations of Cooper *et al.* [126] and Zhengbang [132].

Although most authors [126, 131–133, 135] agree that the kinetic conditions are very favourable for metallurgical reactions at the electrode/slag interface, there is no consistent opinion as far as the attainment of the equilibrium at this interface is concerned: While Miska and Wahlster [136] supposed that intense stirring could assist in equilibration, Fraser and Mitchell [133] do not observe that equilibrium conditions will be attained because of the temperature variations in the slag. Then again, Kljuev and Spicberg [135] estimate that at every metal/slag interface in the ESR process equilibrium conditions are reached.

In sum, the following factors are concluded by a couple of researchers [130, 131, 135, 137, 138] to significantly influence the shape of the electrode tip:

Table 2.4: Summary of theoretical mass-transfer coefficients, average area/volume ratios and approximate residence time (for a 76 mm ESR furnace) [133].

Parameter	Electrode/Slag	Droplet/Slag	Pool/Slag
k_{Mn}, [cm/s]	0.012	0.112	0.016
$k_{Mn^{2+}}$, [cm/s]	0.018	0.023	0.013
$k_{Fe^{2+}}$, [cm/s]	0.018	0.023	0.013
Area/Volume, [cm^{-1}]	103	24	0.67
Residence time, [s]	0.95	0.12	0.80

- Temperature distribution in the slag;
- Immersion depth of the electrode in the slag as well as slag height;
- Electrical parameters;
- Physical-chemical properties system steel-slag.

An important aspect regarding the possible reactions taking place at the electrode/slag interface is the liquid film formed at the electrode tip. As far as this film is concerned, different estimations can be found in literature: While Klujev and Mironov [139] quoted thicknesses of 1000 – 2500 µm for ingots remelted on laboratory scale and values of 30 – 100 µm for industrial size ingots, Fraser and Mitchell [133] determined in their calculations an average film thickness between 50 – 200 µm. Due to the manifold influencing parameters like steel composition, electrode and mould geometries, slag amount and composition, it is very difficult to determine general reliable values for film thicknesses at the electrode tip.

Nevertheless, according to Klujev and Mironov [139] the influencing factors on the film thickness can be summarized as follows:

- The film thickness depends on steel and slag composition.
- Increasing electrode diameter and mould dimensions reduce the liquid film thickness.
- The film thickness is slightly decreased by increasing melting rate.
- The film thickness is enlarged by the intermixture of slag and metal phase.

2.4.3.2 Droplet/Slag Interface

The shape of the electrode tip significantly influences the droplet size and frequency. According to Korousic [130], a higher slag amount—equal melting rate and filling factor provided—results in an increased number of droplets but smaller droplet size. As given in Eq. (2.53), for larger slag amounts, the droplet size should increase with the third root of the electrode radius. For smaller slag amounts and a therefore nearly flat interface, the influence of the electrode radius minimizes (see Eq. (2.53), whereby b is a constant value between 2.04 ± 0.02):

$$r_D = \sqrt[3]{\frac{3\sigma_{MS}R_E}{2g\Delta\varrho}} \tag{2.52}$$

$$r_D = \frac{b\sigma_{MS}}{g\Delta\varrho} \tag{2.53}$$

Next to the slag amount, mainly current and voltage as well as the steel composition have an impact on droplet formation. Basically, the mean melting rate is proportional to the frequency of droplet formation. The influence of steel composition was studied by Korousic [130] who performed laboratory experiments with steels of different carbon contents between 0.19 – 1.54 %[§]. In the results, for low-alloyed steels a considerable influence of deoxidant addition like *Al* or *Ti* on droplet formation was observed: Increasing the *Al*-addition to the slag leads to an instantaneous minimization of the droplet number as well as to a higher melting rate. The droplet weight was not influenced by the addition of *Al*. In contrast to this, for high-alloyed steel like the X155CrVMo12-1 no influence of the *Al*-addition neither on the droplet number nor on the droplet size could be found.

On the basis of mathematical approaches calculating fluid flow, heat transfer as well as mass transfer in the ESR process [140–144], different data concerning the typical droplet size are found in literature. Typically, droplet sizes ranging between 1 – 20 mm in diameter are reported. Kharicha *et al.* [144] performed a numerical study concerning the droplet formation from a flat melting electrode for a DC system. Thereto, the VOF (Volume of Fluid) method in combination with the transient three-dimensional conservation equations for the metal and the slag momentum was applied. This method was designed for two or more immiscible fluids where the position of the interface between the fluids is of interest. In their considerations, the calculated droplet size was in the range of 0.7 – 20 mm continuously decreasing with the magnitude of the imposed DC current. Furthermore, a more uniform droplet distribution was found at higher current densities. The authors indicated that the presented results are only valid for a DC system, since the electric current distribution is not uniform along the radius of the electrode for a AC system. Caused by the skin effect, the electric current density is much higher at the electrode boundary compared to the centre region.

As far as the relationship between droplet size and their flow behaviour is concerned, numerical simulations showed a significant influence. Kharicha *et al.* [145] used an Euler-Euler approach in order to examine the interaction of steel droplets and the slag phase. Numerical simulations with two different droplet diameters (1 and 7.5 mm) showed remarkable differences in the results. While the larger droplets are only slightly deviated by the slag flow, small droplets are much more diverted by slag vortices. Consequently, they are not falling straightly in the pool. In the case of a droplet diameter of 7.5 mm only one clockwise rotating vortex was observed. For the smaller diameter, two vortices are present, one rotating clockwise at the vicinity of the mould and the exposed slag surface, the second rotating anticlockwise directly under the electrode. In addition, more concentrated current paths were observed for small droplets than for large ones. As far as temperature distribution is concerned, for both cases the coldest areas are located at the vicinity of the mould and just beneath the electrode Kharicha *et al.* [145].

Summing up, the following conclusions on the formation of droplets at the electrode tip can be drawn [130, 134]:

[§] Details on the experimental set-up of these experiments as well as used steels and slags have been explained in the last subsection

- The number of droplets per time unit is indirectly proportional to the slag amount.
- The mean melting rate is a linear function of droplet frequency.
- The residence time of a droplet in the slag increases with increasing viscosity of the slag and small differences between the density of the slag and metal phase.

2.4.3.3 Pool/Slag Interface

The dwell time of the metal at this reaction site is comparable to the electrode/slag interphase and therefore significantly longer than at the droplet/slag interphase. According to the mathematical considerations of Fraser and Mitchell [133, 134] it is about 80 s. As far as the temperature is concerned, different estimations are proposed by various researchers: While Holzgruber and Plöckinger [131] states an appreciably lower temperature at the pool/slag than at the electrode/slag interface due to the cooling effect of the mould, Hoyle [97] argues contrarily. The latter suggested that the metal entering the pool is superheated after passing the slag phase and consequently the temperature at this point is higher than at the electrode tip.

Numerical simulations using CFD-analysis to investigate the influence of electromagnetic parameters onto the shape and stability of the pool/slag interface were performed by Kharicha *et al.* [146]. It was found that the interface which is initially flat gets curved by the strong slag flow. This curvature affects the electric current path and induces a strong horizontal component to the current. Consequently, nearly all current coming from the electrode penetrates into the liquid steel at the top of the interface creating a new zone of high current density near the mould. In consequence, the total amount of released heat through joule heating is much higher than for a flat interface [146–148].

A comparison between the reaction rates of these two interfaces in dependence of the slag composition has already been shown in Fig. 2.29 and described in Section 2.4.3.1. The presented results demonstrated that the reaction occurring at the metal/pool interface could also be a reversion reaction which might significantly contribute to inclusion formation at this interface.

2.4.4 Behaviour of Elements in the ESR process

In order to understand the modification behaviour of oxide inclusions through remelting, the behaviour of sulfur and oxygen in the ESR process is of special importance. In the following section the reactions of these elements, their interaction with deoxidation elements like Al, Si or Ti and their impact on steel and slag composition are discussed. For the behaviour of nitrogen, hydrogen and other elements which are not directly connected to the oxide cleanness level, reference is made to literature [83, 97].

2.4.4.1 Sulfur

Through remelting a remarkable desulfurisation can be achieved. Equations (2.54) and (2.55) influence the desulfurisation process significantly:

- Metal-Slag Reaction:

$$[S] + (O^{2-}) \rightarrow [O] + (S^{2-}) \tag{2.54}$$

- Slag-Gas Reaction:

$$2(S^{2-}) + 3\{O_2\} \rightarrow 2\{SO_2\} + 2[O] \tag{2.55}$$

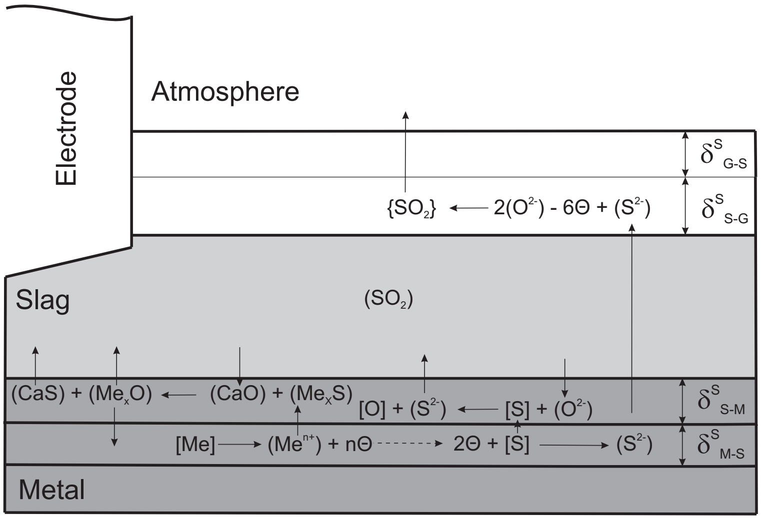

Figure 2.30: Reaction mechanisms of sulfur during Electroslag Remelting according to [150].

According to Eq. (2.56), the removal of sulfur is promoted by an increased oxygen partial pressure of the atmosphere as well as a reduced content of oxygen ions in the slag. Since the decrease of oxygen ions involves an higher sulfur activity in the slag, the oxidation of sulfur during remelting under air is advanced with increasing sulfur activity [149]:

$$\frac{p_{SO_2}}{a(S^{2-})} = K\frac{p_{O_2}^{3/2}}{a(O^{2-})} \tag{2.56}$$

Figure 2.30 demonstrates the reaction mechanisms for desulfurisation in the ESR process. After the diffusion of sulfur from the melt through the boundary layer δ^S_{M-S}, the transport of sulfur in the slag takes places according to Eq. (2.58), where a metal atom that is moved to the slag acts as electron supplier (see Eq. (2.58)). Desulfurisation is advantaged with increasing oxygen activity of elements dissolved in the melt.

$$[S] \rightleftharpoons (S^{2-}) - 2\Theta \tag{2.57}$$

$$[Me] \rightleftharpoons (Me^{n+}) + n\Theta \tag{2.58}$$

From the metal-slag interface the sulfur ion diffuses through the boundary layer δ^S_{S-M} in the slag, from where it is transported to the boundary layer δ^S_{S-G} through convection. Followed by the diffusion through the boundary layer δ^S_{S-G} the sulfur ion reacts with oxygen to SO_2 according to Eq. (2.55).

The more sulfur is transferred from the metal to the slag, the higher the content of oxygen ions of the slag and the lower the activity of oxygen in the steel melt. Assuming that the oxygen in the steel melt is continuously decreased through the reaction with deoxidation elements, the sulfur transport is also determined by the slag basicity. Klingelhöfer *et al.* [149] investigated the behaviour of sulfur during the ESR process through a continuous sampling from pool and slag out of an industrial ESR unit, especially focussing on the influence of slag basicity and as well as of Al and Si. For all experiments slags out of the system $CaO\text{-}Al_2O_3\text{-}CaF_2$ offering a liquidus temperature < 1500 °C were used. The remelted steel was composed of 0.13 – 0.16 %C, 0.30 – 0.40 %Si, 1.20 – 1.50 %Mn, 0.02 – 0.04 %S and 0.02 – 0.05 %Al.

Figure 2.31 visualises the relationship between the sulfur distribution (S)/[S] and the slag basicity. It is shown that a sufficient slag basicity is necessary for an effectual removal of sulfur. For Al_2O_3-free slags an increase of the sulfur distribution is observed with higher basicity. Against that, Al_2O_3-amounts in the slag higher than 15 % cause a significant decrease of the absorption capability for sulfur at the same basicity level [149].

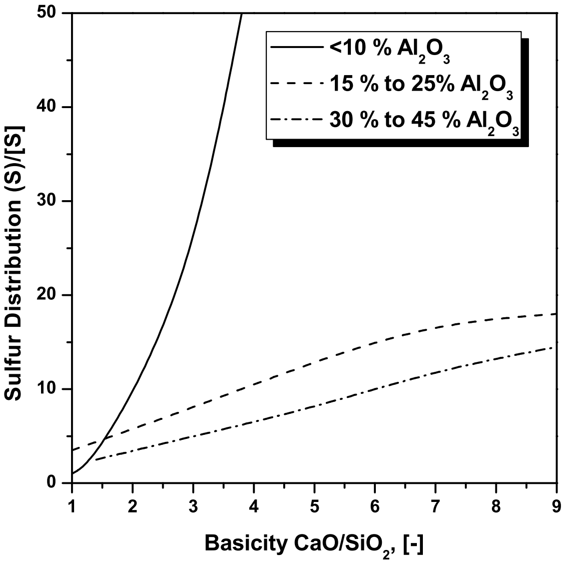

Figure 2.31: Influence of slag composition on sulfur distribution between steel and slag during remelting according to [149].

Figure 2.32 illustrates the influence of slag composition on desulfurisation rate during remelting. The desulfurisation rate is enhanced with increasing slag basicity and reaches a maximum at a basicity level of approximately 5. As already mentioned, increasing Al_2O_3-contents downgrade the sulfur removal, but not in the same extent as it is observed for sulfur distribution between slag and steel shown in Fig. 2.31 [149].

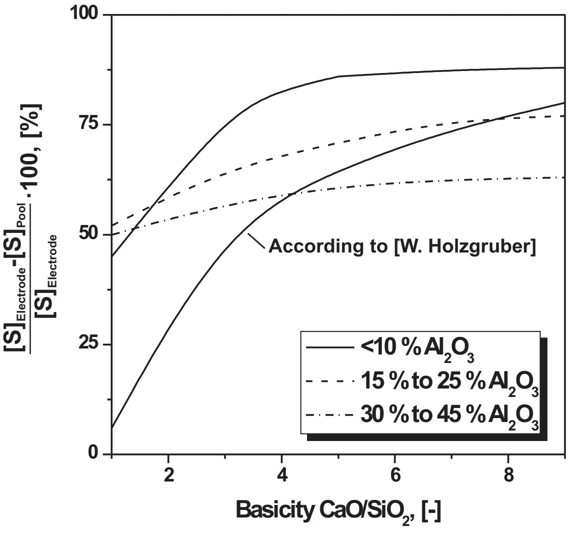

Figure 2.32: Influence of slag composition on desulfurisation during remelting according to [149].

Furthermore, investigations regarding the desulfurisation capability of different slags within the system CaO-Al_2O_3-CaF_2 showed that in the two phase region CaO-Al_2O_3, slags with a good desulfurisation capability are very close to others with a minor desulfurisation capability. Thus, already small changes in slag composition may have an essential influence on sulfur removal. The addition of CaF_2 enlarges the range of good desulfurisation remarkably; above 20 %CaF_2 a sufficiently broad concentration range with equal desulfurisation capability is reached. Besides the slag composition also the sulfur content of the electrode influences the sulfur removal rate. The final sulfur content in the remelted ingot was observed to be the larger, the higher the initial amount of sulfur in the electrode [131, 149, 151].

2.4.4.2 Oxygen

Basically, a decrease of the oxygen content is achieved through remelting. Both the slag and the steel are able to adjust oxygen while remelting. Next to the transfer of the oxygen dissolved in the electrode, the oxidation of the electrode surface directly above the slag bath and the subsequent dissolution of this oxide layer in the slag are known as a possible reaction mechanism. Finally, the transfer of oxygen from the gas phase in the slag through adsorption at the interface slag-gas has to be considered [136]. The latter instance is schematically shown in Fig. 2.33. Molecular oxygen diffuses from the gas phase through the boundary layer δ^O_{G-S} to the interface gas-slag, where the molecular oxygen is adsorbed. The released electrons are affiliated to the adsorbed oxygen during the oxidation of cations at the slag surface. In consequence, the oxygen ion diffuses through the boundary layer δ^O_{S-G} in the slag, where it is further moved to the boundary layer δ^O_{S-M} together with the $Me^{(n+1)+}$ ion. After this diffusion process, the O^{2-}-ion dispenses its electrons to the reduced metal ion Me^{n+} and diffuses in the steel melt as an oxygen atom. In the melt, the oxygen can react with the solved oxygen affine elements and merges as an anion together with the original cation in the slag.

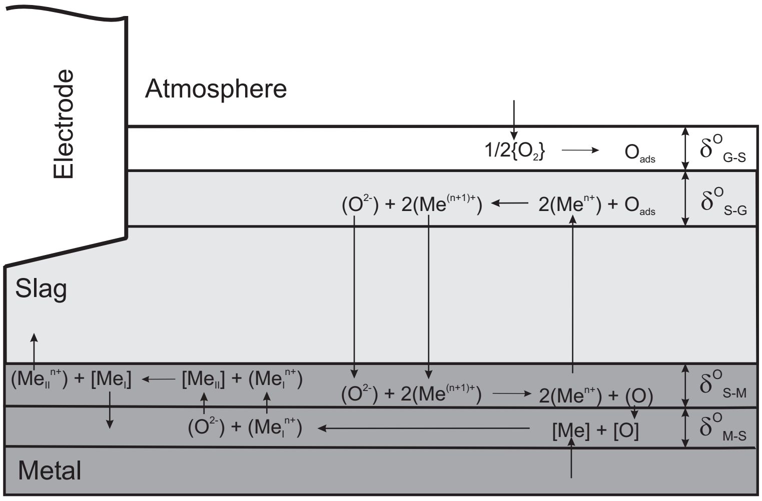

Figure 2.33: Reaction mechanisms of oxygen during Electroslag Remelting according to [150].

Thus, the final oxygen content in the remelted ingot is influenced by two competing reactions during remelting:

- Absorption of oxygen from the slag in the liquid melt;
- Absorption of inclusions from the electrode through the slag.

Miska and Wahlster [136] studied the influence of slag composition on the behaviour of oxygen during remelting of electrodes of low-alloyed carbon steels (Al-killed and unkilled) in a laboratory ESR-unit using different slag compositions out of the system CaO-Al_2O_3-CaF_2-SiO_2. The authors concluded that the Al_2O_3-saturation of the slag does not significantly influence the solubility product $[Al]^2 \cdot [O]^3$. The oxygen-content in the remelted ingot is first and foremost dependent on the activity of the oxygen affine element featuring the lowest oxygen activity according to

$$a_{[O]} = K\frac{a(Me_xO)}{a^x[Me]}. \tag{2.59}$$

Consequently, the slag composition only has an indirect influence on the oxygen content by determining the activity of deoxidation products and their precipitation velocity from the steel melt. The activity of deoxidation products as well as the absorbability of the slag for this deoxidation products is seen to be decisive for the upper limit of the total oxygen content in the remelted ingot. The lowest achievable oxygen limit is defined by the oxygen-potential of oxidic slag components. If the O-content of the steel melt lies beneath the equilibrium content, the oxidic slag components were reduced as long as equilibrium conditions between steel and slag are reached.

According to Klingelhöfer *et al.* [149], the velocity of oxygen transfer and therefore the rate of melting loss depends on the slag composition. Figure 2.34 illustrates the influence of slag composition on the final O-content in the remelted ingots. Although a light decrease of the O-content with increasing slag basicity can be noticed, the Al_2O_3-content of the slag seems to be primarily important: At the same basicity, the final O-content can further be reduced through Al_2O_3-addition. In contrast to this, Korousic and Holzgruber [138] did not ascertain a clear influence of Al_2O_3-content of the slag (between 20 and 35 %) on the oxygen content of the remelted ingot.

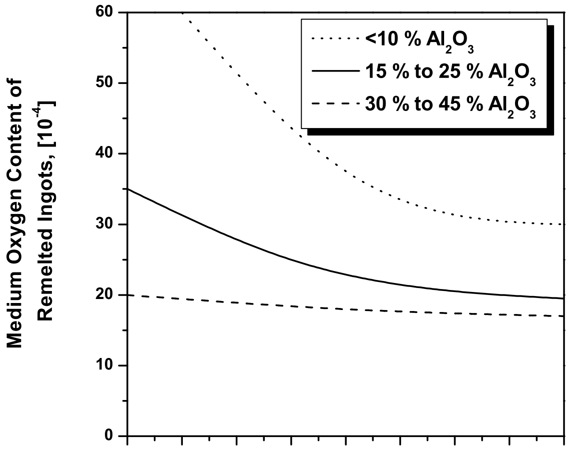

Figure 2.34: Influence of slag composition on oxygen contents of remelted ingots according to [149].

Referring to the results of Miska [150], the Al-content of the remelted ingot is influenced by the Al_2O_3-activity in the slag and the Al-content of the electrode. The loss of Al in the steel takes place according to

$$2[Al] + 3[O] \leftrightarrows (Al_2O_3). \tag{2.60}$$

If the Al_2O_3-content of the slag is reduced—provided the Al-activity of the metal remains unmodified—the oxygen activity of the metal will be decreased. An increase of the Al_2O_3-content of the slag will cause a pick-up of either aluminium or oxygen according to the conditions. Since the deoxidation potential of silicon is significantly increased if highly basic slags are used for remelting [150] (see Fig. 2.35), Si can act as a strong reducing agent when present in SiO_2-free slags according to Eq. (2.61), which would result in an increased content of Al.

$$3[Si] + 2(Al_2O_3) \rightarrow 3(SiO_2) + 4[Al] \tag{2.61}$$

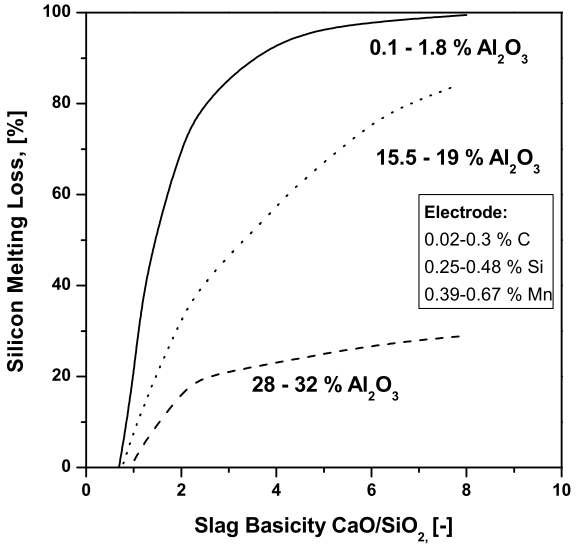

Figure 2.35: Influence of slag basicity on the melting loss of Si [150].

If a sufficient concentration of titanium is present, the same reaction as described for silicon can proceed. In this relation it is important to control the ratio of TiO_2 and Al_2O_3 in the slag in order to obtain the required contents of Ti and Al in the steel melt [83, 97, 152].

Holzgruber and Plöckinger [131] examined the influence of slag basicity on the oxygen-content in remelted ingots also considering the effect of steel composition in more detail. As shown in Fig. 2.36 the lowest oxygen-contents were observed for high carbon-alloyed steels as exemplified for the X210Cr12 and 100Cr6 due to the increased deoxidation effect of silicon in presence of dissolved carbon in the steel melt.

Another aspect determining the behaviour of oxygen is the partial pressure of the gas phase. The higher the partial pressure of oxygen, the larger the amount of oxygen that is absorbed from the slag and transferred to the metal/slag interface. There, again reactions with oxygen affine elements such as Si or Al in the steel can occur. The deoxidation product is removed to the slag and consequently a decrease of slag basicity is observed which finally would result in a higher O-content in the remelted ingot [131].

Generally, the following measures can be taken in order to decrease oxidation procedures [83, 97, 149, 150, 152]:

- Avoidance of air admission in the mould;
- Remelting under protective atmosphere;
- Use of FeO- and MnO-depleted slags;

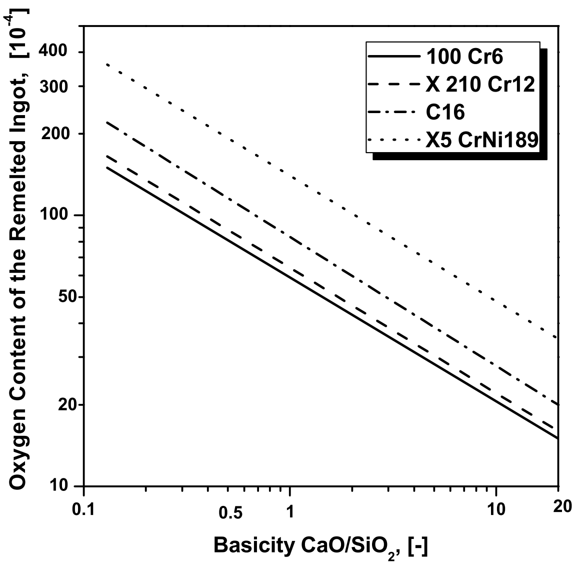

Figure 2.36: Influence of basicity on the oxygen content of different remelted steel grades [131].

- Use of scale-free electrodes;
- Continuous deoxidation.

2.4.5 Inclusion Removal and Modification during Remelting

In general, a significant improvement of the cleanness is reached through remelting. One of the first systematic investigations concerning the decrease of the inclusion content through remelting was performed by Klingelhöfer *et al.* [149]. The authors made a comparison between the cleanness levels of conventionally manufactured and Electroslag Remelted ingots (steel composition: 0.13 – 0.16 %C, 0.30 – 0.40 %Si, 1.20 – 1.50 %Mn, 0.02 – 0.04 %S and 0.02 – 0.05 %Al). As shown in Fig. 2.37 not only a remarkable difference in the overall inclusion content was observed, but also a lower scattering was found due to a more homogeneous distribution of the final inclusion size and significantly smaller inclusions.

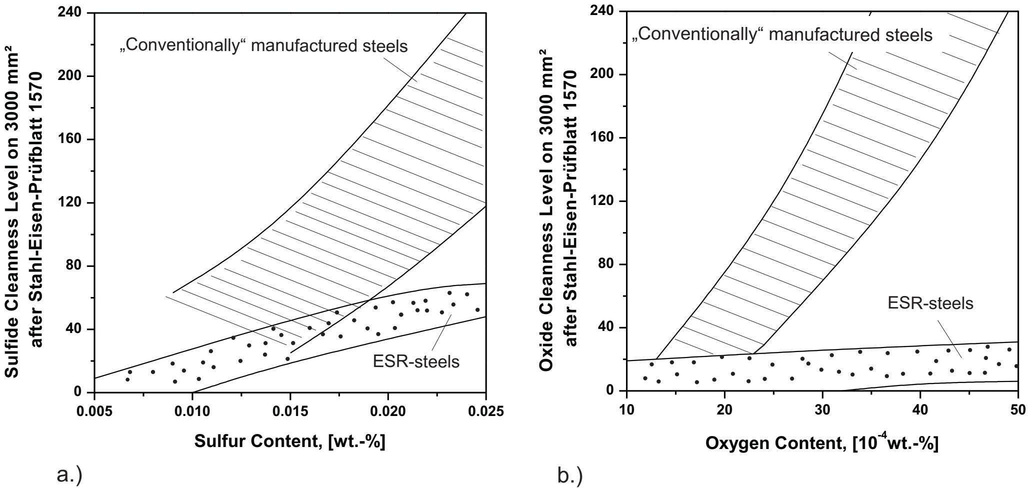

Figure 2.37: Relationship between a.) oxygen and b.) sulfur content and the respective cleanness level [149].

Basically, three potential sources for non-metallic inclusions present in the remelted ingot exist [153]:

- Non-metallic inclusions from the electrode;
- Oxygen or deoxidation elements dissolved in the electrode;
- Reactions between slag and metal during the remelting process.

In principle three major mechanisms which may be responsible for the refining effect in the ESR process are described in literature [135, 154]:

1. Refining through flotation (loss of gravitational potential energy);
2. Refining through adhesion (loss of surface energy);
3. Refining through chemical reactions (loss of chemical free energy).

While the first assumption primarily applies to the liquid pool, the second and third may occur at all present existing metal/slag interfaces. Lloyd *et al.* [155] classified the inclusions present in the ESR process in two categories: Inclusions which do not react with the slag and are immiscible with steel and those which do react with the slag and are in solution at refining temperatures. While the first type is removed by flotation into or adhesion to the slag, the second type is most efficiently removed by chemical reactions and the use of basic slags. Inclusions being part of the first type are for example silicates and oxides, while sulfides are part of the second type. The removal rate for the first type is the greater, the larger the size of the particle.

The first item, the separation of non-metallic inclusions through flotation in the liquid pool is approximated by Stokes' Law,

$$v = \frac{2}{9} g\, r^2 \frac{d_M - d_E}{n}, \tag{2.62}$$

whereby the flotation velocity depends on the particle size, the density difference between metal and slag as well as on the viscosity. Figure 2.38 demonstrates the relationship between the density of the inclusions, which have the chance to float, and the particle diameter. However, the physical-chemical interaction between the inclusion and the liquid metal is not considered in Eq. (2.62).

Gammal and Denkhaus [156] described the influence of pool geometry on the final inclusion landscape as follows: The final inclusion size is strongly determined by the local solidification rate and the geometry of the liquid pool. While a comparatively deep pool offers a longer period for possible flotation, a more shallow pool does not provide most favourable conditions for inclusion precipitation and growth. However, existing oxide inclusions in the pool can act as heterogeneous nuclei for further precipitation reactions if there is enough time for reaction.

The second assumption for the separation of non-metallic inclusions by Electroslag Remelting is based on the physical-chemical interactions between the inclusion, the metal and the slag. The driving force for this reaction is the minimization of the interfacial energy. The energy change of an inclusion with the radius r which is transferred from the metal to the slag phase is described by

$$\Delta G = -4\pi r^2 j(\sigma_{IM} + \sigma_{MS} + \sigma_{IS}), \tag{2.63}$$

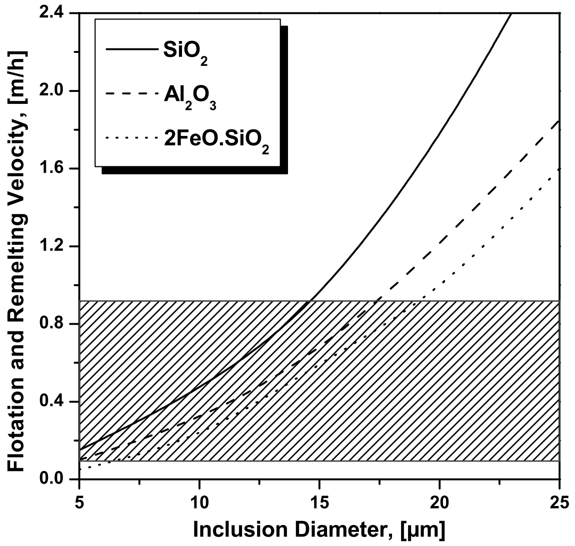

Figure 2.38: Relationship between the particle size and and their flotation velocity (dashed area illustrates the typical range of remelting rate in the ESR process) [97, 135].

where σ_{IS}, σ_{IM} and σ_{SM} are the interfacial tensions between the phases inclusion, metal and slag, respectively, and *j* represents the percentage of inclusion surface which is contact with the slag. The separation process at the interface is successful if the condition

$$\sigma_{IS} < \sigma_{IM} + \sigma_{SM} \tag{2.64}$$

is fulfilled [135, 157].

The third assumption, which states that the refining effect is based on chemical reactions, is influenced by several metallurgical as well as procedural factors. Here, on the one hand the size of specific reactive surface, and time and temperature at this surface on the other hand are essential for the effective procedure of refining processes. Non-metallic inclusions can be absorbed from the slag at the three metal/slag reaction sites present in the ESR process (see Section 2.4.3). One proposed mechanism is that inclusions dissolve in the molten metal at the electrode tip and the oxygen and the deoxidant are transferred to the slag by slag-metal reactions like exemplarily given in Eqs. (2.66)–(2.68). Inclusions which are not dissolved in the slag, may be eroded from the liquid film by the slag. For this mechanism the thickness of the liquid film, the interfacial tension and the size and shape of the inclusions are essential [156].

$$\langle SiO_2 \rangle = [Si] + 2[O] \tag{2.65}$$
$$[Si] + 2[O] = (SiO_2) \tag{2.66}$$
$$\langle Al_2O_3 \rangle = 2[Al] + 3[O] \tag{2.67}$$
$$2[Al] + 3[O] = (Al_2O_3) \tag{2.68}$$

Although these reactions theoretically can take place at every of the three possible reaction sites, the electrode/slag interface is supposed to be the most efficient for the removal of non-metallic inclusions by a couple of researchers [131, 132, 135, 155–157] because of the comparatively high temperatures and the residence time of the inclusions at this site which is remarkably higher than at the droplet/slag interface (details given in section 2.4.3).

Paton *et al.* [158] studied the transformation and removal of non-metallic inclusions during remelting on industrial scale. For this purpose the size distributions of oxides in the electrode (diameter of 1200 mm, in the droplet and in the remelted ingot (0.18 – 0.26 %C, 0.17 – 0.4 %Si, 0.7 – 1 %Mn and 0.4 %Cr) were recorded with the use of an optical microscope. The comparison of determined size distribution of inclusions is demonstrated in Fig. 2.39. Based on these results, Paton *et al.* [158] concluded that the majority of inclusions is already removed at the liquid film at the electrode tip. The inclusions detected in the droplet in this case were very different regarding their shape and size in comparison with the electrode and were rather similar to the inclusions in the final ingot. However, the droplets are undergoing a relatively strong mixing and the probability of the inclusions getting in contact with the slag is therefore high. Hence, a certain decrease of oxide inclusion content is expected at this reaction site too [153].

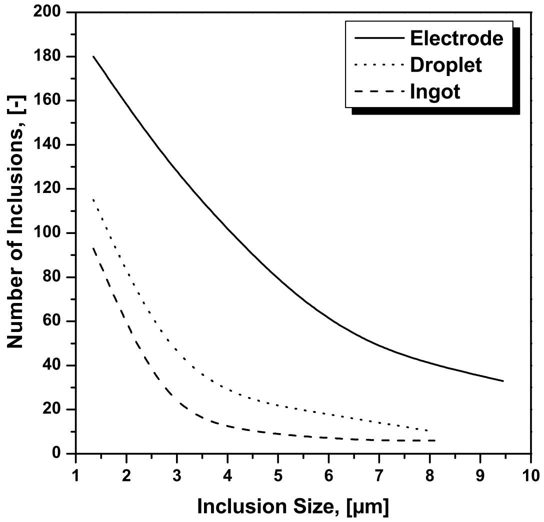

Figure 2.39: Comparison of size distribution of inclusions in the electrode, the droplet and the remelted ingot according to [158].

Kay and Pomfret [157] tried to answer the question whether the liquid metal leaving the electrode still contains non-metallic inclusions which are of the same characteristic as those of the solid electrode or not. They performed experiments in a small ESR-furnace using electrodes deoxidised with Si and Al (0.02 %C, 0.08 %Mn, 0.07 %Si and 0.015 %O). The electrode tip was rapidly retrieved from the slag and analysed metallographically. In their experiments a significant change of inclusion size distribution was observed when approaching the electrode tip. This modification was attributed to the time-temperature history of the metal during heating and melting. Thus, these findings accord with the assumption of Paton *et al.* [158].

Povolotskii *et al.* [159] studied the transfer conditions of inclusions across the metal/slag interface theoretically as well as with experiments on a laboratory ESR-furnace where electrodes of 100CrMn6 were remelted using different slags composed of CaO, Al_2O_3 and CaF_2. Their results showed that when the fluoride-slag is diluted with Calcium-Aluminates up to 15 %, the rate of solution of Al_2O_3 particles is diminished. The higher the slag basicity, the more significant this effect. An increase of the $(CaO+Al_2O_3)$-content of the slag to 35 %, provokes the converse effect. Out of their calculations considering interfacial tensions of metal, slag and inclusions, the authors concluded that inclusions may not be completely transferred to the slag at the electrode/slag interface but tend to accumulate at the interphase boundary. In contrast to this, Mitchell and Burel [160] suggests that once the inclusion is in contact with the slag, the solution rate should be high enough for all common inclusion-slag combinations.

The relationship between removal rate of inclusions and the particle size was studied by Zhengbang [132]. They performed laboratory tests remelting electrodes of a 100Cr6 steel with a CaF_2-30 %Al_2O_3 slag. As illustrated in Fig. 2.40, it was shown that the removal rate increased obviously with enlarging particle volume of the original inclusions in the electrode.

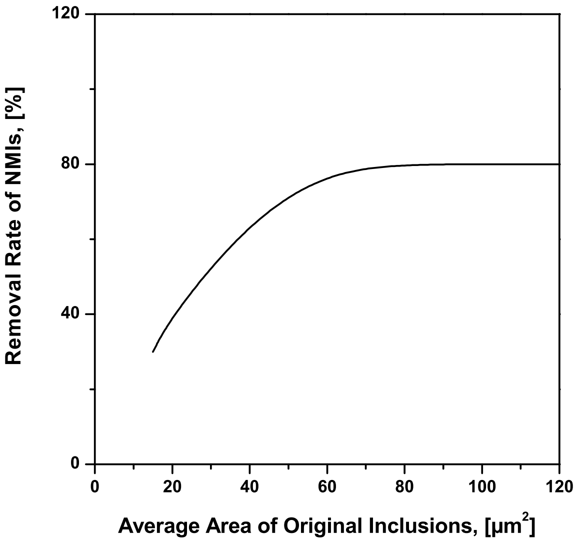

Figure 2.40: The effect of the average size of original inclusions on removal rate of inclusions during remelting [132].

Mitchell [153] contributed fundamental studies on the behaviour of inclusions during remelting with his experiments in an ESR-furnace, remelting oxygen-containing iron with CaF_2-20 %Al_2O_3 and CaF_2-20 %CaO slags. Samples were taken from the electrode tip (after withdrawn from the slag) as well as from the liquid pool providing a very rapid quench of a liquid volume withdrawn from the pool. Subsequently, the samples were analysed using SEM/EDS. According to his results, physical solution only seems to have a small impact on the final inclusion landscape and the majority of inclusions present in the final ingot might have nucleated and grown in the mushy zone of the ingot. In the performed experiments no ingot inclusions could clearly be identified as relics of the electrode. This estimation was also approved through laboratory tests performed by Kljuev and Spicberg [135].

Liddle [154] encourages this theory analysing the inclusions size distribution before and after remelting. For this purpose, an iron-alloy doped with Al_2O_3 inclusions was cast and rolled half-inch diameter rods. These rods were used as electrodes and were melted into a slag consisting of 70 %CaF_2, 20 %Al_2O_3 and 10 %CaO. Samples from the initial electrode and the remelted ingot were then analysed metallographically. As displayed in Fig. 2.41, it is obvious that two size classes were reduced significantly in the ingot: Inclusions with a diameter of 1 μm and inclusions larger than 4 μm in diameter. This would be a strong indicator that the inclusion population present in the electrode is going into solution and is reduced in quantity by the diffusion into the slag. A second population is formed during cooling.

Another aspect is the change in composition between inclusions in the electrode and in the ingot. According to Liddle [154], if the composition of inclusions is different between the electrode and the ingot,

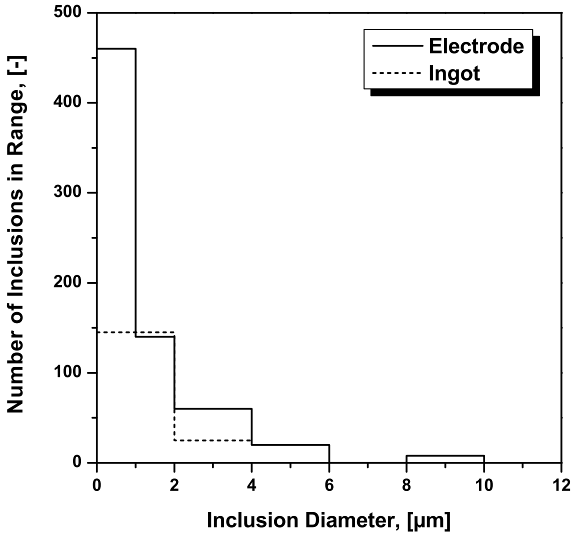

Figure 2.41: Comparison of inclusion size distribution in the electrode and in the ingot [154].

solution and re-precipitation has taken place. In their point of view, the converse argument however is not acceptable: An inclusion in the ingot with the same composition as an inclusion in the electrode could have got there by different means, solution included. One criterion that might provide useful information about the history of an inclusion is its shape. An inclusion grown in the ingot will be rather smooth in appearance, while inclusions which were partially eroded by solution in the metal might rather show a ragged form [154]. In contrast to the conclusions above that no relics of the electrode are present in the remelted ingot, Paton *et al.* [158] detected a noticeable number of inclusions with matchable properties as in the electrode, in the liquid film, in the forming drop as well as in the ingot.

In contrast to many other works described beforehand, Mitchell [153] expects that inclusion solution at the electrode tip is not the decisive removal mechanism. In the author's opinion the rejection of large inclusions to the slag/metal interface might probably be more important to the overall reaction. The behaviour of inclusions at the electrode/slag interface has also been extensively examined by Roshchin *et al.* [161], who studied the behaviour of oxides, nitrides and sulfides at the electrode tip of the stainless steel Cr23Ni18 during high-temperature heating with an optical microscope. As far as sulfides are concerned, a significant reduction in number was already observed at the incipient melting stage. Regarding oxides, Roshchin *et al.* [161] detected a remarkable increase of their size in the liquid electrode film. Furthermore, they were found to concentrate at the interface, begin to accumulate and enlarge as a result of coalescence and coagulation. These findings support the theory of Mitchell [153].

Mitchell [153] also pointed out that considering their experimental results, the electrode deoxidation practice influences the final inclusions in the ingot the following: Deoxidation changes the liquid metal composition due to reactions with the slag which consequently influence the subsequent precipitation of oxides. All modifications of inclusion composition are addressed to slag/metal reactions. The use of slags with a high content of Al_2O_3 will lead to an increase of pure Al_2O_3 inclusions in the remelted ingot.

On the basis of the accomplished experiments, Mitchell [153] proposes the following conditions for reaching the smallest amount of inclusions in ingots remelted via ESR:

- Maximum amount of deoxidant added to the liquid pool;
- Maximum residence time of liquid metal in the pool, in order to achieve the deoxidation equilibrium;
- Slag composition having the smallest tendency towards dissociation into the liquid metal.

Rehak *et al.* [162] also affirmed the significant influence of slag/metal interactions on the final inclusions in the remelted ingot by the observations of inclusion modification in field tests. The authors concluded that the inclusion composition in the ingot is defined by the activity of the deoxidising elements which are present in the metal. The final amount of oxides inclusions in the ingot is at a lower level if the relationship between the activities of the elements in the metal and of the oxides in the slag permit reactions due to which the element passes into the slag. While sulfide inclusions tend to get finer through remelting more or less independent of the used slag composition, the refining effect for the reduction of oxides is higher if this particular oxide component is not part of the slag phase.

2.4.6 Summary

Electroslag Remelting (ESR) is a process often used in stainless steelmaking in order to optimise ingot structure and steel cleanness. The basic principle consists of the remelting of a so-called consumable electrode, which is the product of a precedent casting process. This electrode is heated above its liquidus temperature; in consequence liquid droplets are formed, fall down through the reactive medium and are subsequently collected in the liquid pool. This pool is bordered by a crystallizer, usually a water-cooled copper mould. Due to the heat removal the liquid metal solidifies directionally from the bottom to the top. The heart of the ESR process is a reactive slag bath which not only significantly influences the overall process control, but also is responsible for the achieved refining effect.

CaO, Al_2O_3 and CaF_2 are the basic components of ESR-slags. Over the years two different approaches describing this ternary system were reported in literature. The system published by Nafziger [105] does not show a miscibility gap at higher CaF_2-contents, while the ternary phase diagram demonstrated by Chatterjee and Zhmoidin [106] does. The latter subsequently was confirmed by several researchers [104, 107, 108] and has therefore become widely accepted.

An essential aspect for the behaviour of non-metallic inclusions in the ESR process are slag properties. Next to the electrical conductivity which mainly influences the slag temperature and therefore process control, the slag viscosity is of importance. On the one hand, increasing temperature effects decreasing viscosity which results in a more intense stirring and is therefore regarded to be more favourable for metallurgical reactions at the steel/slag interface. On the other hand, an increasing slag viscosity reduces the velocity of descenting droplets and consequently increases the residence time of droplets in the slag. Slag viscosity decreases with higher CaF_2-contents; Al_2O_3-additions act contrariwise. Additionally, a low interfacial tension between slag and metal is favourable for the mass transfer and the formation of small droplets, but also encourages slag reentrainment and the adhesion between the ingot and the slag. Finally, slag density has to be considered: The larger the slag density the smaller the metal droplets and the longer the dwell time of the droplets in the slag.

In the ESR process three metal/slag reaction sites exist that considerably influence inclusion removal and modification:

1. Electrode/Slag Interface: Here, the major aspect is the shape of the electrode tip which can very between a rather flat interface and a coned shape. This geometry primarily depends on temperature distribution in the slag, slag height and immersion depth of the electrode in the slag as well as on the physico-chemical properties of the steel/slag system. In this relation also the thickness of the liquid film at the electrode tip is of major importance, since it significantly influences the behaviour of inclusions at this reaction site. Although there is no consistent opinion about the film thickness in literature (ranging between $30 - 2500\ \mu m$) [133, 135, 136], steel and slag composition as well as mould geometry and melting rate are concluded to be decisive.
2. Droplet/Slag Interface: Typical droplet sizes between $1 - 20\ \mu m$ in diameter are found in literature [140–144]. The droplet frequency is described as a linear function of melting rate and the number of droplets per time unit is indirectly proportional to the slag amount. Droplet size also remarkably influences the flow behaviour and consequently their residence time in the slag. The residence time of a droplet in the slag also increases with increasing viscosity of the slag and small density differences between slag and metal phase [130, 134, 144, 145].
3. Pool/Slag Interface: The dwell time of the metal at this reaction site is comparable to the electrode/slag interphase and is therefore significantly longer than at the droplet/slag interphase. It was demonstrated that the reaction occurring at the metal/pool interface could also be a reversion reaction which might significantly contribute to inclusion formation at this interface [126, 132–134].

Principally, a significant desulfurisation is achieved by Electroslag Remelting based on metal/slag and slag/gas reaction. The removal of sulfur is advantaged through an increased oxygen partial pressure of the atmosphere as well as a reduced content of oxygen ions in the slag. The more sulfur is transferred from the metal to the slag, the lower the activity of oxygen in the steel melt. Desulfurisation is enhanced with increasing slag basicity, whereas increasing Al_2O_3-contents downgrade the rate of sulfur removal. Besides the slag composition, the final sulfur content in the remelted ingot is the larger, the higher the initial amount of sulfur in the electrode [131, 149–151].

As far as oxygen is concerned, the final O-content in the remelted ingot is influenced by the absorption of oxygen from the slag in the liquid melt and the absorption of inclusions from the electrode through the slag. Additionally, according to Miska and Wahlster [136] the oxygen-content in the remelted ingot is a function of the activity of the oxygen affine elements. Consequently, the slag composition is seen to only have an indirect influence on the O-content by determining the activity of deoxidation products and their precipitation velocity from the steel melt. On the contrary, Klingelhöfer *et al.* [149] demonstrated that influence of slag composition on the final O-content. Although a light decrease of the O-content with increasing slag basicity was observed, the Al_2O_3-content of the slag seems to be primarily important.

Three major mechanisms which may be responsible for the refining effect in the ESR process are found in literature [135, 154]. Next to flotation which mainly is addressed to the liquid pool, refining through adhesion can take place if the condition $\sigma_{IS} < \sigma_{IM} + \sigma_{SM}$ is fulfilled [135, 157]. Lastly, refining can take place through chemical reactions between steel and slag.

Although the decisive refining effect theoretically can take place at every of the three mentioned reaction sites, the electrode/slag interface is supposed to be the most efficient for the removal of non-metallic inclusions by a couple of researchers [131, 132, 135, 155–157] because of the comparatively high temperatures and the residence time of the inclusions at this site which is remarkably higher than at the droplet/slag interface. This relationship is visualized in Fig. 2.42.

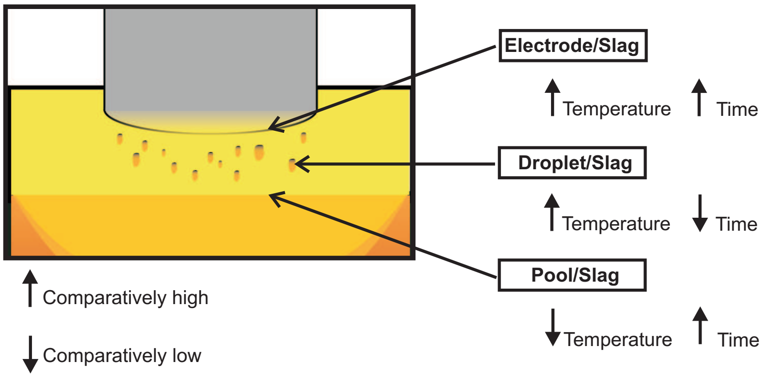

Figure 2.42: Comparison of time and temperature conditions at the three metal/slag interfaces in ESR process according to [131].

As far as the relation between inclusions in the electrode and inclusions in the remelted ingot is concerned, mainly three potential sources for inclusions in the ingot exist: First, non-metallic inclusions may be a relic of the electrode; secondly, oxygen or deoxidation elements dissolved in the electrode may react with other elements in the liquid melt; finally, reactions between steel and slag during remelting may form or modify inclusions.

There is no clear opinion in literature about the question whether inclusions from the electrode may survive until the remelted ingot. In the investigations by Kljuev and Spicberg [135] and Mitchell [153] the majority of inclusions present in the final ingot was supposed to have nucleated and grown in the mushy zone of the ingot and no ingot inclusions could clearly be identified as relics of the electrode. Although Liddle [154] supports this thesis, the problems of getting a reliable answer to this questions are highlighted and the inclusion shape was proposed as an important indicator whether an inclusion has precipitated in the liquid pool or may be a relic from the electrode.

As far as the decisive influencing factors on an effective removal of inclusions are concerned, Zhengbang [132] concluded that the removal rate increases obviously with enlarging particle volume of the original inclusions in the electrode, while Povolotskii *et al.* [159] and Mitchell and Burel [160] demonstrated that foremost the chemical composition of inclusions in relation to slag composition is essential for inclusion removal.

Both—deoxidation practice and slag composition—are stated to have a major influence on the modification of non-metallic inclusions during remelting. The use of slags with a high content of Al_2O_3 is seen to cause an increase of pure Al_2O_3 inclusions in the remelted ingot. Deoxidation changes the liquid metal composition due to reactions with the slag which consequently influence the subsequent precipitation of oxides in the pool Mitchell [153]. Rehak *et al.* [162] found that the final amount of oxides inclusions in the ingot is at a lower level if the relationship between the activities of the elements in the metal and of the oxides in the slag permit reactions due to which the element passes into the slag. While sulfide inclusions tend to get finer through remelting more or less independent of the used slag composition, the refining effect for the reduction of oxides is higher if this particular oxide component is not part of the slag phase.

3 Key Aspects of Inclusion Characterisation

In order to verify and improve the cleanness of steels continuously, the reliable characterisation of non-metallic inclusions is inevitable. For this purpose, a broad palette of different analysing methods exists, each of them featuring specific pros, but also none of them providing the overall solution for the large spectrum of cleanness information. Thus, a general assessment of characterisation methods is rather difficult, owing to the large amount of appraisal factors: Next to the information content of the results (chemical and/or morphological data), the detectable range of inclusion sizes as well as the analysed sample volume—respectively area—are fundamental points of interest. Although the more information can be gained the better, the complexity of analysis and the related time effort must be considered in practice. As far as the representativeness of each method is concerned, it must be well understood which conclusions can be drawn out of the obtained results. And, probably even more important, which questions may not be answered based on the available information.

The macro cleanness has reached a quite high level over the years. Thus, the detection of macro-inclusions is rather difficult, because they are infrequent and also distributed irregularly in steel. In consequence, conclusions about the maximum inclusion diameter in a defined sample volume based on measured results has to be questioned critically. Micro-inclusions are arbitrarily frequent. One limitation might be seen in the detection of submicro-inclusions, which cannot be analysed due to the detection limit of most commonly applied methods.

The present chapter summarises the state of the art concerning inclusion characterisation and compares the advantages as well as disadvantages of the individual methods, especially focusing on the methods also applied in the present thesis. Moreover, the differences and challenges in the determination of the medium and maximum inclusion diameter in a defined sample volume are discussed. Based on literature considerations, a new approach combining statistics with automated SEM/EDS analyses is introduced providing important information as far as the representativeness of automated SEM/EDS analyses is concerned. Moreover, the electrolytic extraction is described as one used approach for getting an three-dimensional insight into the inclusion landscape.

3.1 What does the Measurement Result Really Tell Us?

Although a significant progress regarding inclusion characterisation was achieved in the last 20 years, the statement “Clean Steel is Harder to Measure than Produce” by the British steel industry in 1989 [163] still has some truth. Especially as far as the determination of inclusion size is concerned, it has always to be considered that most analysing methods only show a two-dimensional view of the inclusions distributed in space. While this reduction of dimensions brings along a substantial facilitation for the measuring process, the severe question of the measurements’ representativeness arises: The cleanness level is often described by a size distribution of the detected particles. Considering the fact that a particle is not cut at its maximum diameter necessarily, it must be kept in mind that, as shown in Fig. 3.1, a metallographic specimen only gives an apparent distribution of the inclusion diameters. Moreover, the cleanness assessment can be rather difficult based on a size distribution, since every method only covers a certain inclusion size range. Figure 3.2 exemplarily shows two size distributions: Steel A has a lower mean inclusion size than steel B and therefore mostly is regarded to be *cleaner* according to most analysing methods. However, the probability of finding a large inclusion is higher in steel A than in steel B and therefore steel B should be regarded as *cleaner* than steel A for most applications. This example points out the diversity of the term *cleanness* on the one hand and on the other hand, how complex the reliable determination of inclusion sizes can be [1].

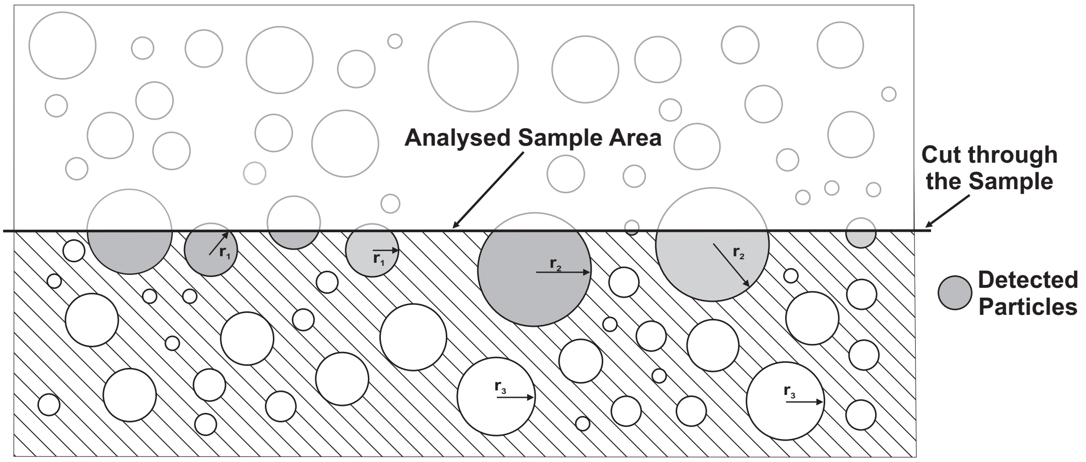

Figure 3.1: Scheme of an apparent size distribution of non-metallic inclusions on a metallographic specimen, acoording to [164].

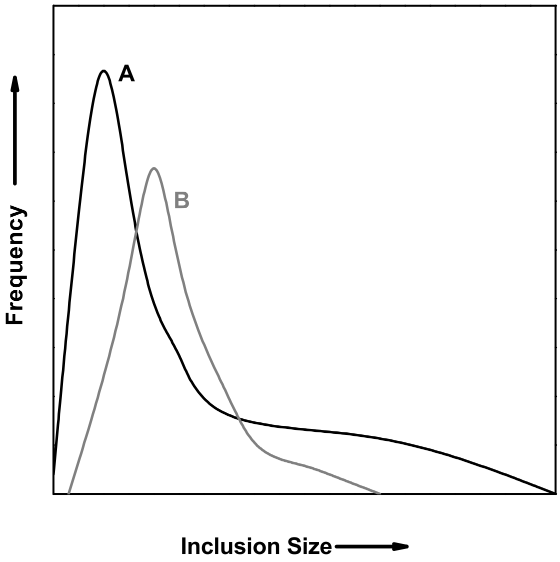

Figure 3.2: Comparison of two inclusion size distributions illustrating the difficulty of defining steel cleanness [1].

Basically, the number, size and size distribution as well as their position are important parameters of the cleanness. Table 3.1 clarifies the importance of a reliable characterisation of inclusion size: Here, the effect of size on the number of oxides is given for a hypothetical steel with 100 *ppm* oxygen, distributed as equally sized Al_2O_3 inclusions [1].

Table 3.1: Influence of size of oxides (All inclusions are supposed to be spherical and equal in size; oxygen content of steel is 100 *ppm*) [1].

Diameter μm	Number per ton	Steel volume per inclusion	Mean inclusion distance
10^3	10^5	1300 mm^3	11 mm
10^2	10^8	1.3 mm^3	1.1 mm
10^1	10^{11}	$1.3 \cdot 10^6$ μm^3	110 µm
10^0	10^{14}	1300 μm^3	11 µm
10^{-1}	10^{17}	1.3 μm^3	1.1 µm
10^{-2}	10^{20}	$1.3 \cdot 10^{-3}$ mm^3	0.11 µm
10^{-3}	10^{23}	$1.3 \cdot 10^6$ Å	110 Å

Consequently, for a meaningful interpretation of measurement results of inclusion analysis, an overall view of the following questions is very important:

- Which analysing method was used for inclusion characterisation?
- Which size spectrum of particles can be covered by the used method?
- How large was the analysed sample volume/area?
- Where was the sample taken and what kind of sample is it?
- What steel grade has been analysed?

3.2 Comparison of Analytical Methods

In general, a distinction between standardised and non-standardised methods for inclusion analysis has to be made. One of the most traditional standardised approaches for the determination of inclusion contents in steel is the Standard Chart Comparison. The identification and classification of inclusions is done by comparison of image sections from samples under the optical microscope with charts. Two of the most commonly applied methods in practice are DIN 50602 and ASTM E45. It must be noted that these methods are only based on a visual comparison of the operators and therefore can easily susceptible for mistakes. Moreover, only oxides and sulfides, differentiated only by their shape, are considered for evaluation. No detailed information about the chemical composition of inclusions is gained. The basic result consists of a so-called K-value, defining the medium inclusion content present in the analysed sample. Depending on the analysed steel grade, this K-value can contain inclusions of different size index numbers, relevant for the product. For steel grades produced under vacuum for example, a K1-value, evaluating all inclusion sizes down to size index one, is applied, whereas for most other steels an examination starting with K4 is sufficient [165, 166]. Due to the described restrictions of the mentioned methods, another standardised method developed in the last few years. The EN 10247 is principally based on the same concept as DIN 50602 and ASTM E45. The big advantage of this standard is that the comparison between the image of the optical microscope and the chart can be done automatically using defined mathematical vicinity relations. Therefore, the obtained results have physical dimensions like length in $\mu m/ mm^2$, area in $\mu m^2/ mm^2$ or number per mm^2 [167]. These standardised methods are often used as acceptance criteria between the steel producer and the customer. In the present thesis these methods have not been applied, since the chemical composition of inclusions is one of the major information needed for the investigations of steel-slag interactions. Therefore, they will not be treated in more detail.

For research purposes, mainly as far as the understanding of the modification behaviour of inclusions is concerned, mostly non-standardized methods are applied. These methods often are connected with an increased time effort, but in return provide a lot of information on the morphology as well as the chemical composition of non-metallic inclusions. Zhang and Thomas [168] give a comprehensive review on the state of the art of inclusions characterisation. The authors differ between direct and indirect methods: While indirect methods, like for example Total Oxygen Measurement, Nitrogen Pickup or Dissolved Aluminium Loss Measurement, are only reliable as relative indicators for steel cleanness, direct methods enable a concrete analysis of non-metallic inclusions in a defined steel sample. Some of the most common direct methods for inclusion analysis are:

- Automated SEM/EDS Analysis (Scanning Electron Microscope with Energy-Dispersive X-ray Spectroscopy),
- OES/PDA (Optical Emission Spectrometry with Pulse Discrimination Analysis),
- Electrolytic Extraction,
- Image Analysis,
- Ultrasonic Analysis.

All these mentioned methods are able to represent different size ranges of inclusions and provide different limitations regarding the analysed sample area/volume. Consequently, each of them offers certain advantages and disadvantages. For a detailed description of the physical principles of the methods references is made to literature [4, 169–177]. Regarding the general significance and the reproducibility of results from different analysing methods, from the authors' point of view [168], a comprehensive inclusion characterisation is most effectively achieved by a sensible combination of several methods. Figures 3.3 and 3.4 summarise and compare some non-standardised analysing methods for inclusion characterisation based on literature data.

In general, a distinction between methods that give a three-dimensional view of the inclusion landscape on the one hand and on the other hand those, which only offer a two-dimensional perspective of the non-metallic inclusions, has to be made. As already mentioned beforehand, based on results of two-dimensional analyses, conclusions concerning morphology and size of the particles may be inaccurate. Out of this reason, the electrolytic extraction, based on the dissolution of the steel matrix and the remaining of inclusions in the residue, is a very useful tool in order to study the morphology of inclusions in detail. Since OES/PDA is a very rapid method compared to the others mentioned, it is also applied for direct process control in the melt shop. All the other methods are rather used for quality control of the semifinished products as well as research purposes. In contrast to all other methods, ultrasonic analysis offers the advantage of being a non-destructive investigation method. While ultrasonic analysis and chemical extraction offer the possibility of considering a relatively large sample volume, the automated SEM/EDS analysis provides the highest information content compared to the other listed methods, although only a rather small sample area is scanned. In spite of the considerable effort related to automated SEM/EDS analyses, this method has become state of the art [178–180] not only in the field of material characterisation but also concerning metallurgical process control and optimisation.

In the present thesis the automated SEM/EDS analysis is primarily used for the determination of inclusion landscape. Knowing about the limitations of this method, it was combined with electrolytic extraction as well as statistical considerations. The next section concentrates on the representativeness of automated SEM/EDS analyses. The answer to this question is sought through a combination of experimental data with statistic considerations.

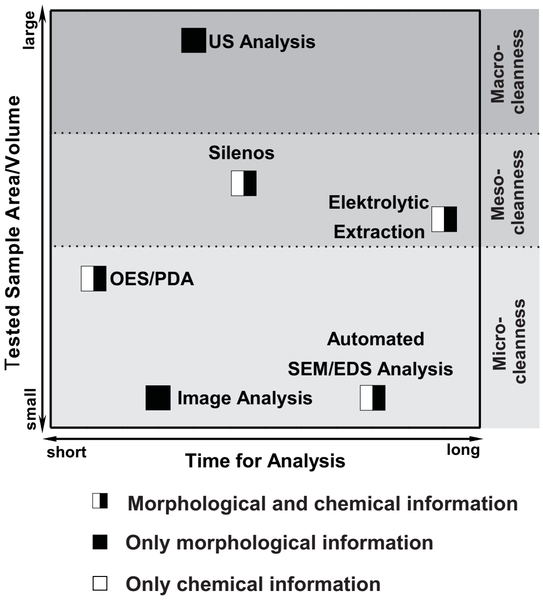

Figure 3.3: Comparison of some current methods for inclusion analysis regarding time effort and analysed sample volume according to data from [4, 169–177].

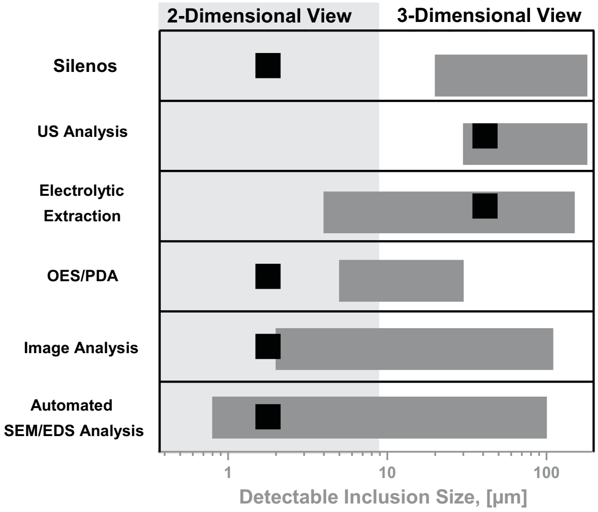

Figure 3.4: Comparison of some current methods for inclusion analysis regarding the detectable inclusion size spectrum according to data from [4, 169–177].

3.3 Representativeness of Automated SEM/EDS Analyses

Due to the combination of low occurrence of inclusions in clean steels and the practically limited testing volumes of most cleanness assessment methods, the significance of the results strongly depends on the size of the analysed area. Thus, for two-dimensional inclusion analyses using the automated SEM/EDS analysis two decisive questions arise: Firstly, whether the sample area is sufficient to determine large, however stochastically rare inclusions. Secondly, if the analysis of a defined sample area is adequate to give an impression of the global cleanness (also involving the influence of smaller inclusions) of a whole volume. The first question has extensively been treated in the last years by different theoretical approaches, which will be summarised in the following. The second question of general representativeness of a defined sample area has not been addressed precisely so far. In order to answer the question of the representative sample area and its impact on the inclusion size distribution, within this work experimental measurements are coupled with a statistical-geometric model of the problem.

3.3.1 Basics of Inclusion Analysis with SEM/EDS

By using the automated SEM/EDS analysis for the characterisation of cleanness in steels, inclusions are detected due to material contrast differences in the backscattered electron (BSE) image. The contrast of the BSE image is significantly dependent on the atomic number of the element. This circumstance facilitates the distinction between different phases. Generally, points of high atomic number are shown brightly, points of low atomic number are displayed darkly; usually non-metallic inclusions have much lower atomic numbers than the steel matrix. The output consists of the position and the morphological data of every detected particle as well as its chemical composition. In addition, in order to get an impression of the sample homogeneity, the distribution of the non-metallic inclusions over the whole sample area is registered. Essential advantages of the automated SEM/EDS analysis compared to a manual analysis are:

- Simultaneous analysis of inclusions of all possible size classes;
- Higher overall number of detectable inclusions;
- Possibility of relocating interesting particles and re-processing.

When interpreting the results the truncation of data must be considered, since a lower measuring limit exists: For every analysis, the minimum number of pixels which is needed to identify a particle has to be defined. In the present study a resolution of $1\,024 px \times 960 px$ is used. In order to be identified as a particle, at least 4 connected pixels have to show a greyscale value different to the matrix. Depending on the magnification and the resolution, the area of each included particle is measured; out of it, the so-called Equivalent Circle Diameter (ECD) is calculated,

$$\mathrm{ECD} = \sqrt{\frac{4A}{\pi}}. \tag{3.1}$$

For the SEM/EDS device employed for the present thesis, the practical limit lies at an ECD of 0.6 μm. Usually, a limit of 1.1 μm is used, achieving an acceptable compromise between measuring time and obtained results. Consequently, not the whole size spectrum of inclusions is analysed. An typical example of a size distribution measured with SEM/EDS is given in Fig. 3.5.

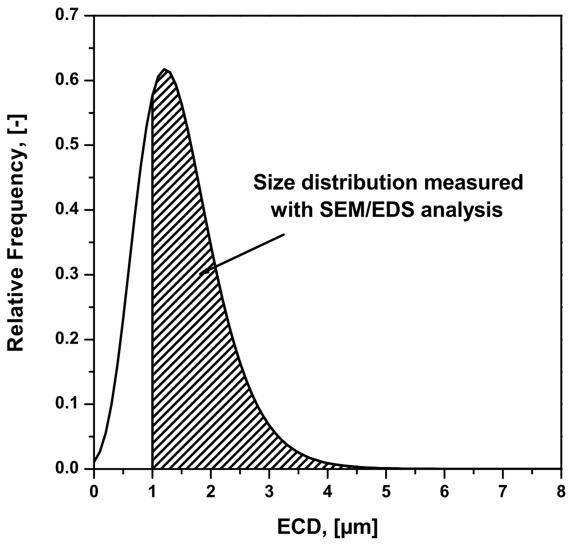

Figure 3.5: Typical truncated size distribution of particles measured with SEM/EDS analysis.

Furthermore, the determination of the ECD can be difficult for several fine agglomerated inclusions, appearing as one large particle for the system and hence presenting an inaccurate ECD. In the case of the used settings, two particles are detected separately, if at least two connected pixels between them have a grey scale value different to the defined threshold. In order to avoid such incorrect measurements, a subsequent manual verification of the results is advisable. Within the present work, a Scanning Electron Microscope manufactured by Fei (Quanta 200 MK2) is used in combination with an EDS system of Oxford Instruments (INCA). The settings applied for the automated SEM/EDS analysis for all measurements presented in this thesis are summarised in Tab. 3.2.

Table 3.2: Experimental settings.

Beam energy	15 *keV*
Working distance	10 mm
Resolution	1 024 *px* × 960 *px*
Magnification	600×
Minimum particle size	4 *px*
EDS evaluation time for one particle	3 s

Concerning the measured chemical composition the following relation has to be taken into account: The particle size also affects the detected EDS spectrum. Depending on the chosen accelerating voltage a certain sample volume is activated and the detected elements are displayed in the resulting EDS spectrum. As shown in Fig. 3.6 for compact samples the interaction volume (depth and width) changes directly with accelerating voltage and contrariwise with atomic number. Further details on the SEM in combination with an EDS system, also pointing out all interactions as well as applications, can be found in [181, 182].

In general, the larger the particle, the smaller the amount of measured matrix around the inclusion is. Two examples of SEM-images of Al_2O_3 inclusions detected on a measured sample area (steel composition see Tab. 3.3) are displayed in Fig. 3.7. Both particles show a very globular shape, whereat one is significantly smaller than the other. Looking at the corresponding EDS analyses in Fig. 3.8, the effect

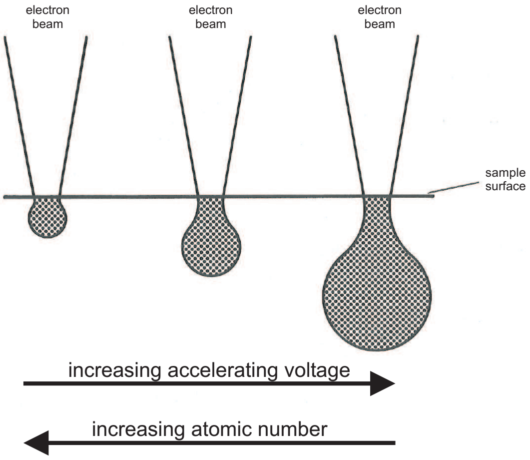

Figure 3.6: Dependence of accelerating voltage and atomic number on the interaction volume [181].

of particle size on the measured spectrum for the used settings can be seen: While due to an ECD of the particle of < 2 µm, in the case of spectrum 1 several matrix elements are detected, spectrum 2 only shows the elements the measured inclusion is composed of. This effect always has to be considered when dealing with the chemical composition of non-metallic inclusions. Thus, in many cases a matrix correction of the raw data gained of the SEM/EDS analysis is recommended.

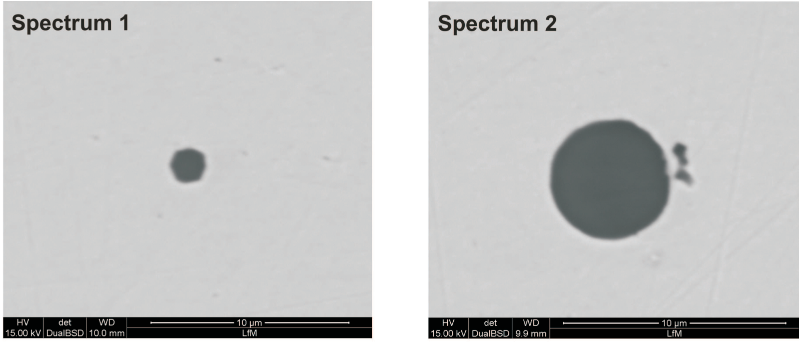

a.) b.)

Figure 3.7: Exemplary SEM-images of detected Al_2O_3 particles on the analysed sample area.

Within the present work, the automated SEM/EDS analysis is the predominant method for inclusion analysis. For all measurements the same settings were used an a matrix correction of raw data has been performed. The analysed sample area was defined based on the results of the model described in section 3.3.3.1. In general, a sample area of 100 mm² was investigated.

3.3.2 Statistic Approaches for the Determination of the Maximum Inclusion Diameter

As stated beforehand, it is very difficult to find the few large inclusions in clean steel because of their low incidence and the small examined sample volumes. Thus, the size of the maximum inclusion in a large volume has to be estimated from data from a very small volume of steel. Moreover, most methods only offer a limited range of detectable inclusion size. Thus, statistical approaches are used to estimate the maximum inclusion diameter. The size distribution of inclusions in steel is often found to have a log-normal form [175, 183]. One method of predicting the maximum inclusion size in a defined steel volume is the extrapolation of the log-normal distribution.

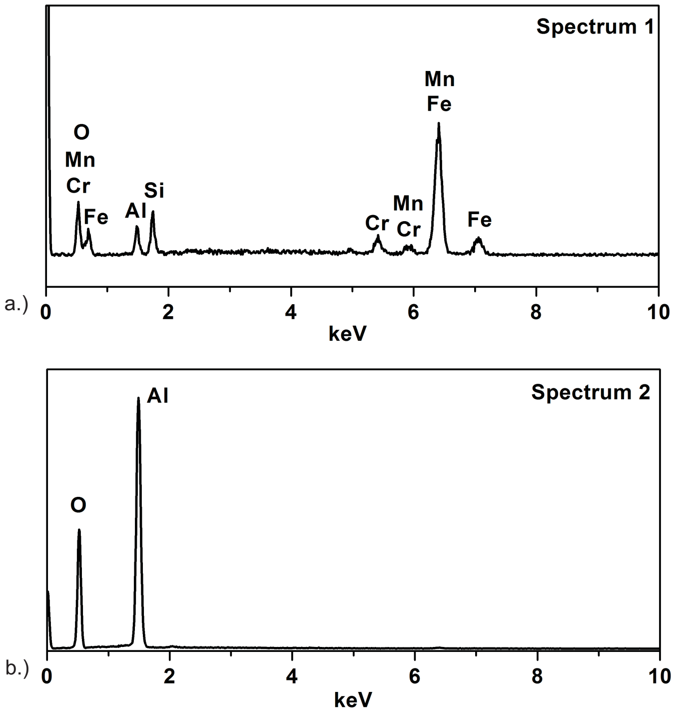

Figure 3.8: Corresponding EDS analyses to Al_2O_3 particles shown in Fig. 3.7.

Using this approach, two problems arise [4, 184]:

1. The estimated characteristic size of the maximum inclusion increases with the increase of the logarithm of the volume of steel and there is no upper limit for the estimated inclusion size. The width of the confidence intervals also increases with increasing extrapolated steel volume.
2. Quantitative data is required for the standard method of fitting the log-normal distribution. For feasible data a large size spectrum of inclusions has to be measured, also including very small inclusions on the one hand but also rather large inclusions on the other hand, in order to get a representative distribution. Usually, only inclusions situated in the central part of the distribution can easily be measured.

Even if reasonable data could be provided, the assumption that a log-normal distribution for the middle range of inclusions implies that the same distribution can be applied for large particles, is neither testable nor logically inevitable. The mentioned problems can be avoided by the use of prediction methods based on the extreme value theory. Two methods have been developed for the estimation of the maximum inclusion size:

- Statistics of Extreme Values (SEV);
- General Pareto Distribution (GPD).

The SEV is based on the measurement of the maximum inclusion size in randomly chosen areas or volumes. For calculations with the GPD only measurements of inclusions larger than a threshold value are needed. The essential advantage of both methods is that they allow data on inclusion sizes in small samples to be used for the prediction of the maximum inclusion size in a large steel volume. A comprehensive comparison of SEV and GPD methods regarding their similarities as well as distinctions is given by Anderson *et al.* [185].

3.3.2.1 Statistics of Extreme Values (SEV)

The first method—SEV—was originally applied for other questions out of the field of material science such as the estimation of the pit depth of the localised corrosion or the estimation of grain size during recrystallization. Murakami *et al.* [186] first applied this concept for the estimation of the maximum inclusion size. The basic idea of SEV is that when a fixed number of data points are collected that follow a basic distribution, the maximum and minimum of each of these sets also follows a distribution which is different from the basic distributions such as normal, exponential or log-normal. In the work of Uemura and Murakami [187] the Gumbel-Distribution was used,

$$G(z) = \exp\left[-\exp\left(-\frac{z-\lambda}{\alpha}\right)\right], \tag{3.2}$$

where $G(z)$ represents the probability that the largest inclusion is not larger than size z. α and λ are the scale and the location parameters. A standard measuring area S_0 is defined and the area of the maximum inclusion in S_0 is measured. In a next step, the square root of the area

$$z = \sqrt{\mathrm{Area}_{\mathrm{max}}} \tag{3.3}$$

of the maximum inclusion is calculated. This procedure is repeated for N areas S_0. The cumulative probability $G(z_{(i)})$ of the i^{th} largest maximum inclusion size $z_{(i)}$ can then be calculated by

$$G\left(z_{(i)}\right) = \frac{i}{N+1} = \exp\left[-\exp\left(-\frac{z_{(i)}-\lambda}{\alpha}\right)\right], \tag{3.4}$$

where $z_{(i)}$ is the i^{th} in the ordered series of $\sqrt{\mathrm{Area}_{\mathrm{max},i}}$. If the distribution of Eq. (3.2) is correct and if inclusion size $z_{(i)}$ is plotted against $-\ln\left[-\ln\left(\frac{i}{(N+1)}\right)\right]$ an approximately straight line of slope α and intercept λ on the vertical axis is obtained:

$$\sqrt{\mathrm{Area}_{\mathrm{max}}} = \alpha. \tag{3.5}$$

In order to estimate the distribution of inclusion size in a large volume of steel V, the return period T is defined as

$$T = \frac{V}{V_0}, \tag{3.6}$$

where V_0 is the analysed volume of a single sample area. By solving Eq. (3.7) the characteristic size of the maximum inclusion in volume V, which is denoted by z_v can be calculated,

$$G(z_v) = 1 - \frac{1}{T}, \tag{3.7}$$

hence resulting in

$$\frac{(z_v-\lambda)}{\alpha} = -\ln\left[-\ln\left(\frac{(T-1)}{T}\right)\right]. \tag{3.8}$$

The standard inspection volume V_0 is defined by

$$V_0 = hS_0, \tag{3.9}$$

where h is given by

$$h = \frac{\sum \sqrt{\text{Area}_{(\max,i)}}}{N}. \tag{3.10}$$

Hence, Eq. (3.8) can be used to calculate the maximum inclusion diameter, once α and λ have been estimated [4, 188, 189]. For this estimation the maximum likelihood method is used. The detailed calculation procedure of these parameters can be found in Atkinson *et al.* [188, 189].

Murakami and co-workers also investigated the correlation between the fatigue strength and the maximum inclusion size [187, 190–193]. The SEV method proposes a prediction of the lower band of the fatigue limit. This predicted fatigue limit can be standardised to each type of specimen. In their investigations a good agreement between calculations and results of fatigue tests could be observed.

Zhou *et al.* [194] upgraded the method for the case that the SEV distribution is not described by a single straight line, but becomes bilinear. This case may appear, if multiple inclusion types of inclusions with different chemical compositions are contained in the steel.

3.3.2.2 General Pareto Distribution (GPD)

The second method—GPD—was developed by Shi and co-workers [195]. In contrast to the approach of Murakami *et al.* [186], the GPD predicts an upper limit to the inclusion size, which seems to be more realistic regarding practical aspects. GPD is the standard family of statistical distributions used for modeling data with values over a threshold: Assuming u is the threshold size and x is the size of inclusions larger than the threshold, the probability of an inclusion not larger than x, $F(x)$ (given that it exceeds u) is approximated by the GPD with the distribution function given in Eq. (3.11), [184, 195, 196].

$$F(x) = 1 - (1 + \xi(x-u)/\sigma')^{-\frac{1}{\xi}} \tag{3.11}$$

In this case σ' is a scale parameter and ξ ($-\infty < \xi < +\infty$) is a shape parameter. The characteristic size of the maximum inclusion x_v in a large volume V is estimated using

$$x_v = u - \frac{\sigma'}{\xi}\left[1 - [N_v(u)V]^{\xi}\right], \tag{3.12}$$

where $N_v(u)$ indicates the expected numbers of exceedances of u in unit volume. The number of inclusions per unit volume $N_v(i)$ in size group i is calculated by

$$N_v(i) = \frac{N_{A(i)}}{\overline{D_i}}, \tag{3.13}$$

where $N_A(i)$ is the number of intercepted inclusions in size group i per unit area on the polished surface and $\overline{D_i}$ is the mean of the inclusion size in the group i. This approximation is qualified when u is substantially greater than the modal value of the distribution. The number of inclusions per unit volume larger than a critical size $N_v(u)$ is then determined by summing up all the $N_v(i)$ of inclusions larger than u. For the use of this method, three parameters in the GPD function have to be estimated. u can be estimated by plotting the mean observed excess of the inclusion size above the threshold against u. ξ and σ are evaluated by the maximum likelihood method. A description of the estimation of these parameters as well as more details on the GPD method can be found in [188, 197, 198].

Shi *et al.* [198] compared multiple steel types and used diverse experimental methods for obtaining inclusion data, among others cold crucible remelted samples. Additionally, Beretta *et al.* [199] and Beretta and Murakami [200] especially concentrated on the behaviour of different inclusion types in this context. The authors developed a new approach for the statistical analysis of extreme defects, which allows to choose the relevant control areas for extreme value sampling.

3.3.3 Representative Determination of the Medium Inclusion Content

Since the considerations in the practical part of this thesis are significantly based on results out of automated SEM/EDS analysis, the representativeness of this method is of major importance. In the following, a statistic-geometric model is described which is used for the calculation of the error of area ratio. The calculations are compared to experimental results and a critical evaluation of the required sample area is accomplished, appraising the significance but also demonstrating the limitations of automated SEM/EDS analysis.

3.3.3.1 Model Formulation

For inclusion characterisation using the SEM/EDS method, a planar metallographic specimen is necessary. In order to describe the representative sample area in dependence of sample volume and inclusion content, the following model was formulated: A defined number of inclusions was distributed in a cube. Although inclusions can show very complex geometries in reality, the model is currently based on the assumption of spherical shapes only. As illustrated in Fig. 3.9a, the individual spheres with the centre coordinates $S_i = (s_{x,i}, s_{y,i}, s_{z,i})$ are randomly distributed in the cube, with the diameters of the spheres d_i according to a log-normal distribution $\aleph(\mu, \sigma)$. Thus,

$$\frac{1}{\sqrt{2\pi\sigma}} \sum_{0}^{N_V} \frac{1}{d_i} \exp(-\frac{\ln(d_i - \mu)}{2\sigma^2}) \cong 1, \tag{3.14}$$

where μ and σ are the mean and the standard deviation of the applied log-normal distribution, respectively; N_V is the amount of distributed spheres per mm^3. Upon initialisation, the positions of the spheres are arbitrarily determined. The required input parameters, *i. e.*N_V, μ and σ are chosen according to the experimental results (see subsequent section). Since these parameters depend on the inclusion content N_A on the sample area, they are varying for every steel grade.

Hence, the cube is numerically intersected m times with the intersection plane parallel to the cube base. The position of the plane is termed z_m with $0 < z_m < z_0$ where $x_0 = y_0 = z_0$ is the cube side length. The set of spheres $\overline{S_m}$ cut by the plane m, schematically illustrated in Fig. 3.9b, is determined by

$$\overline{S_m} = \{s_{z,i} - d_i/2 \leq z_m \leq s_{z,i} + d_i/2 \mid 0 < i < N_V\} \tag{3.15}$$

Since the spheres of each set $\overline{S_m}$ are actually cut at different distances from their centre points, the diameters of the resulting intersections (circles) needs to be determined individually. Evidently, their calculation results from

$$d^c_{i,m} = 2\sqrt{\left(\frac{d_i}{2}\right)^2 - \mid z_m - s_{z,i} \mid^2} \tag{3.16}$$

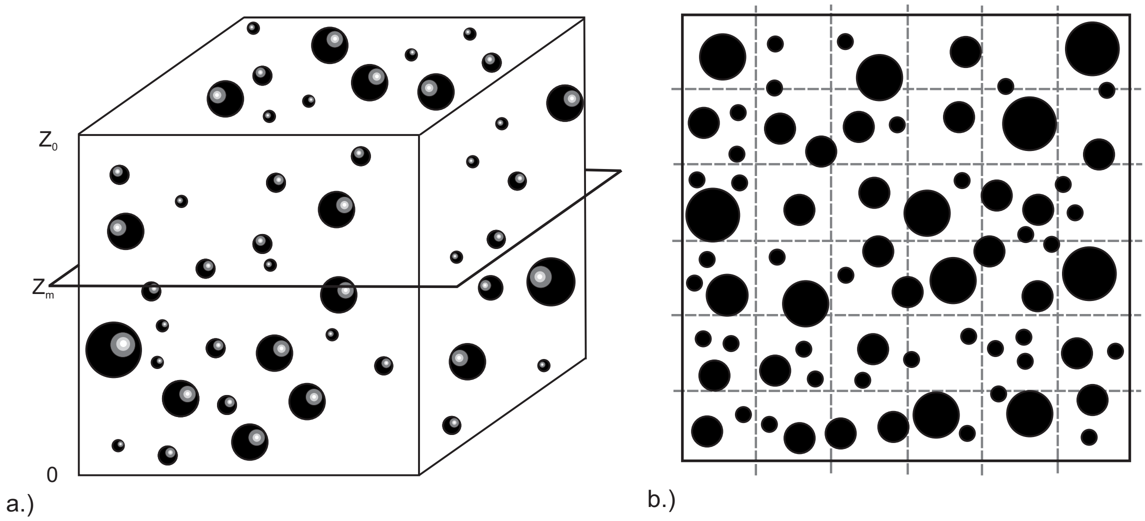

Figure 3.9: a.) Schematic illustration of a cube with distributed spheres and b.) Schematic cut through the cube plane parallel to the cube base.

where $d^c_{i,m}$ are the diameters of the respective intersection circles. Hence, the total area of all intersected circles $\overline{A}$ is given by

$$\overline{A} = \frac{\pi}{4} \sum_m \sum_i (d^c_{i,m})^2. \tag{3.17}$$

In the present model $m = 5$, therefore the maximum virtual analysed sample area is 2000 mm^2 since each intersection plane has an area of 400 mm^2. Evidently, the maximum sample area thus exceeds virtually any practically employed experimental analysing area (typically < 400 mm^2). Thus, the high ratio between analysed sample area and total sample volume ensures an unbiased, stochastic distribution of the particles. By numerically limiting the single intersection place, the influence of the minimisation of analysed sample area could be studied. The error in analysed sample area is finally determined by

$$\text{Error} = \frac{\overline{A} - A_T}{A_T} \times 100\% \tag{3.18}$$

where A_T is the area of all intersected circles at the maximum intersection area of 2000 mm^2. Moreover, in difference to the results of the automated SEM/EDS analyses, there is no truncation limit for the circle diameter in the model. Hence, the sum of all intersected spheres equals entirety. In order to analyse the influence of this truncation, the truncation limit from the practical observations 1.1 µm is also introduced numerically. Given that the diameters in $d^c_{i,m}$ follow the log-normal distribution $\aleph(\mu^\star, \sigma^\star)$, the distribution parameters could further be obtained.

3.3.3.2 Experimental SEM/EDS Analyses

In order to get input parameters for the model and to compare the calculated results with practical measurements, systematic automated SEM/EDS analyses were performed. Although this method also provides information about the chemical composition of inclusions, this data was not considered for the study of representativeness, because this consideration primarily concentrates on the overall inclusion content and therefore the morphological properties of inclusions. Thus, only one inclusion type, namely Al_2O_3, (offering a mostly spherical inclusion shape and therefore adequate for comparison) has been used for evaluation in this case. Consequently, the theoretical results are also only valid for the defined inclusion content.

All measurements were carried out on a metallographic specimen of a stainless steel sample. The steel was melted in an induction furnace; its composition is shown in Tab. 3.3. Out of the cast steel ingot a cuboid with the dimensions 49 × 49 × 65 mm^3 was formed at 1200 °C with a deformation degree of $\varphi = 0.7$. In order to study the influence of the measurement area, three different sizes of sample areas were analysed. For this purpose an area of 50 mm^2 was enlarged continuously (see Fig. 3.10), always using the identical SEM/EDS settings and a minimum feature diameter of 1.1 µm. When superimposing the three reiterations for the results of 50 mm^2, an accordance of 99 % is observed. Consequently, variations resulting out of measurement influences are negligible.

Table 3.3: Chemical composition of the steel used in the experimental investigations.

%C	%Cr	%Si	%Mn	%Mo	%V
0.34	5.02	1.57	0.53	1.28	0.49

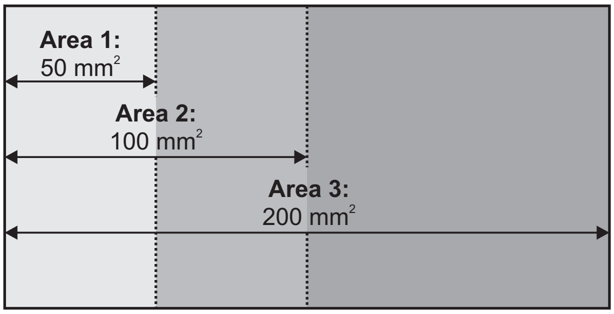

Figure 3.10: Schematic illustration of the arrangement of the different used measuring areas.

Figure 3.11 shows the positions of detected Al_2O_3 inclusions on the measured sample area of 200 mm^2. The inclusions are scaled in four size classes ranging between 1 µm and 20 µm ECD. In the present case, the particles are distributed very homogenously and the majority of inclusions is smaller than 10 µm.

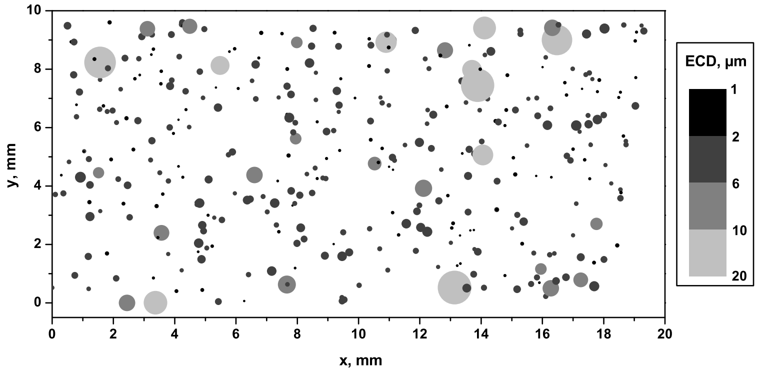

Figure 3.11: Illustration of the distribution of detected Al_2O_3 inclusions on a measured sample area of 200 mm^2 scaled in different size classes.

Figure 3.12a demonstrates the percentage of inlcusions with an ECD < 5 µm as a function of the measured area. In all cases more than 87 % of all Al_2O_3 particles have an ECD < 5 µm; the medium

ECD amounts to app. 3 µm for all analysed areas. Although slight variations are found in the results for the maximum ECD (see Fig. 3.12b) there is no significant increase of the maximum detected inclusion size with larger measuring area; no outlier can be observed. Theoretically it is also imaginable that in spite of increasing the measuring area, the largest inclusion is detected in the smallest analysing field. Therefore, locating a larger particle is not only difficult even on a larger analysing area, but foremost varies considerably.

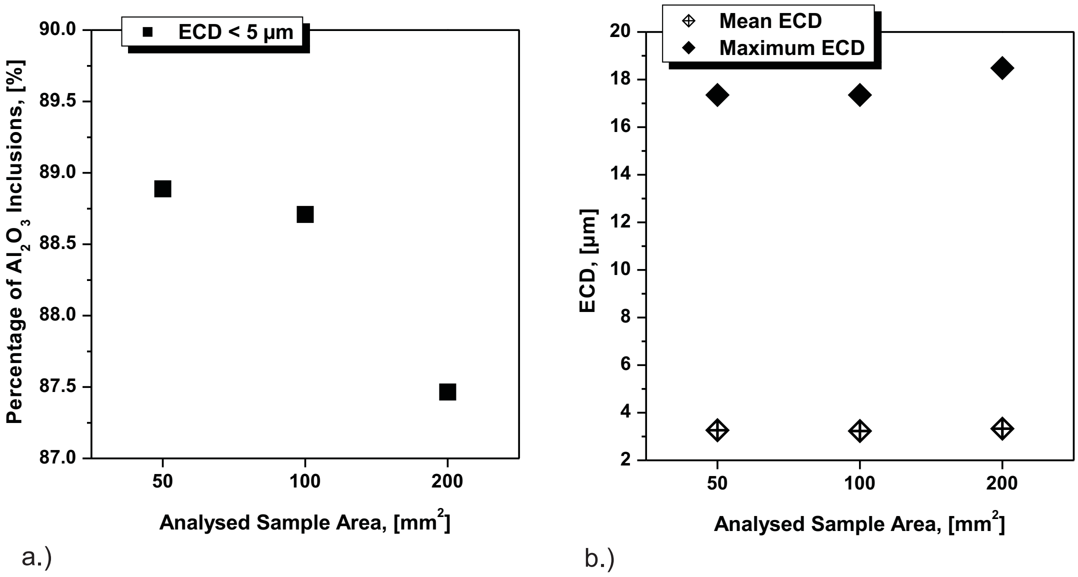

Figure 3.12: a.) Percentage of NMIs with an ECD < 5 µm as a function of the analysed sample area. b.) Experimental results for the mean and maximum ECD for different sample areas.

A typical output of automated SEM/EDS analyses is illustrated in Fig. 3.13. Evidently, the overall number of detected particles increases with larger measuring area. The overall inclusion content amounts to app. 2 Al_2O_3 per mm^2 in all three cases and the maximum lies in the class between 1 µm and 2 µm ECD. Out of this illustration no considerable disparities can be found. Table 3.4 summarises the results for μ_A, σ_A and the inclusion content N_A for the three different measured area sizes. A reasonable consistency is achieved for these values. Anyhow, neither the size distribution nor the values in Tab. 3.4 give a concrete conclusion regarding the maximum particle diameter.

Table 3.4: Values of µ and σ and the inclusion content N_A for different measured area sizes.

Truncation Limit 1.1 µm			
Area, mm²	μ_A, µm	σ_A, µm	N_A, mm²
50	3.27	2.38	1.98
100	3.23	2.13	1.86
200	3.33	2.45	1.83

With the aid of the practical results from the measurements of 200 mm², the input parameters for the statistical-geometric model were defined. Therefore, in a first step, it was necessary to estimate values for the medium sphere diameter µ, the standard deviation σ and the number of distributed spheres per

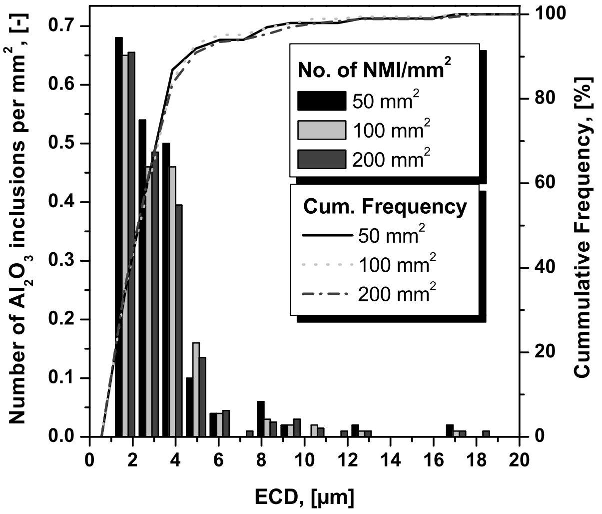

Figure 3.13: Number of Al_2O_3 inclusions per mm^2 between 1 µm and 20 µm ECD on the different analysed area sizes.

volume unit, N_V. For this purpose the following approach was employed, where n_{dA} is the harmonic mean of all measured particle diameters on the area 200 mm^2 [201]:

$$\mu = \frac{\pi}{2} \cdot n_{dA} \tag{3.19}$$

$$\sigma = \frac{1}{2}\sqrt{n_{dA} \mid 8\mu_A - \pi^2 n_{dA} \mid} \tag{3.20}$$

$$N_V = \frac{2}{\pi}\frac{N_A}{n_{dA}} \tag{3.21}$$

Although a useful estimation basis, the values gained by this approach are not definite, owing to the fact that they are based on truncated data. Therefore, in a subsequent optimisation step, the final input parameters for the statistical-geometric model were gained by iterations over N_V, μ and σ until convergence with the experimental results was achieved; the results of this additional iteration can be found in Tab. 3.5. The maximum sphere diameter distributed in the cube was defined with 110 µm.

Table 3.5: Constant simulation parameters.

Cube Side Length	20 mm
N_V	1217 mm^{-3}
μ	1.88 µm
σ	1.69 µm

3.3.3.3 Representative Sample Area as a Function of the Inclusion Content

Table 3.6 summarises the calculated results for μ^* and σ^* of the circles as well as the inclusion content N_A^*, for the two different truncation limits for 10 intersections, each with an area of 200 mm^2. It is obvious that the number of inclusions per mm^2 increases with decreasing truncation limit. Evidently, μ^* is smaller for 0 µm than 1.1 µm, against what σ^* is smallest for a truncation limit of 1.1 µm. In difference to the results of the automated SEM/EDS analyses, there is no bottom limit for the circle diameter in the calculations. The mean value and the standard deviation of the error of the area ratio of the NMIs are displayed in dependence of the measuring area in Fig. 3.14. The indicated error is displayed with a negative algebraic sign; since in practice usually a lower number of particles—resulting in a smaller area ratio—is detected during the measurement.

The values of the error of area ratio resulting from the experimental data are also displayed for the truncation limit of 1.1 µm. In contrast to calculations where the reference area is 2000 mm², the evaluation basis for the experimentally determined values was 200 mm², due to the mentioned practical limitations. Therefore, it is comprehensible that these are found outside of the calculated range. Nonetheless, comparative results could be obtained. In case of the truncation of 0.0 µm, no sensible experimental points can be plotted in the diagram.

Table 3.6: Values of μ^* and σ^* and the inclusion content N_A^* for different truncation limits.

	Truncation Limit 0.0 µm			Truncation Limit 1.1 µm		
Section	μ^*, µm	σ^*, µm	N_A^*, mm^{-2}	μ^*, µm	σ^*, µm	N_A^*, mm^{-2}
1	2.76	2.75	2.36	3.52	2.86	1.73
2	2.61	2.38	2.34	3.33	2.41	1.71
3	2.55	2.65	2.34	3.38	2.79	1.63
4	2.80	2.90	2.44	3.42	3.02	1.89
5	2.72	2.62	2.26	3.52	2.68	1.62
6	2.84	5.20	2.30	3.46	5.76	1.79
7	2.67	2.89	2.19	3.34	3.06	1.64
8	2.75	2.46	2.26	3.43	2.49	1.70
9	2.62	2.67	2.37	3.31	2.80	1.75
10	2.56	2.54	2.42	3.35	2.66	1.70

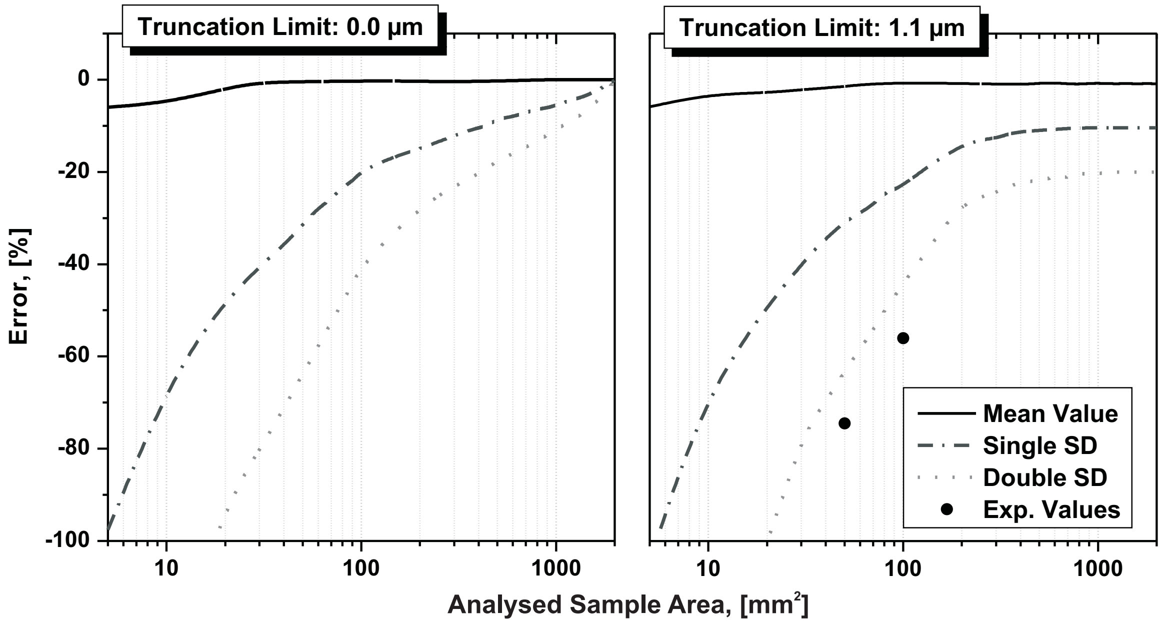

Figure 3.14: Error of area ratio in dependence of the analysed sample area for different truncation limits (SD: Standard Deviation).

Out of the results in Fig. 3.14 the following conclusions can be drawn for the application of automated SEM/EDS analyses for the defined conditions:

- If an area of 200 mm^2—a defined number of inclusions per mm^2 provided—is measured by presetting a minimum particle diameter of 1.1 µm, the mean error of the measured area ratio lies approximately at 2 %. Looking at the standard deviation, in the worst case the error can amount to nearly 30 %. It must be noticed that in this case relatively low inclusion content was assumed, since all the practical examinations were done for a single inclusion type in the steel matrix.
- Pertaining to the data truncated at 1.1 µm, it can be concluded that an increase of the analysed sample area above 200 mm^2 would not effectively ameliorate the results, as there is no noticeable influence on the resulting error due to the truncation of the data. A comparison between the two truncation limits in Fig. 3.14 shows that the truncation of the experimental data implies a certain systematic error, independent of the analysed area.
- In contrast to this, reducing the measured area causes a rapid and significant increase of the error. An area of 100 mm^2-200 mm^2 seems to be a reasonable compromise under the given parameters.
- Regarding the only theoretical possibility that particles of all size classes could be detected, it is shown that the error is clearly smaller. In this case, a reduction in analysed area will inevitably lead to a remarkably broader scattering of the values, indicated by the increasing standard deviation.

3.3.3.4 Comparison between Size Distributions of Calculated and Measured Particles

Figure 3.15 shows the size distributions between 0 – 9.9 µm ECD for all sections of the calculations compared to the measured values resulting from the analysis of 200 mm^2. Considering that this is a comparison of absolute values, the results show good agreement. The variation of single calculated planes shows the effect of the probability of intersection mentioned in the introduction. In Fig. 3.16 the results of calculated and experimental outputs are compared in a Box-Whisker-Plot. It can be seen that the interquartile ranges yield roughly equivalent results. Regarding the range in between of which 90 % of the values are located, a higher scattering is observed. However, extreme outliers cannot be found.

3.3.3.5 Comparison between Maximum and Medium Diameter of Calculated and Measured Particles

An overview on the medium and maximum particle diameters for the 10 sections in comparison to the measured results is given in Fig. 3.17. In this case, large variations are obtained primarily for the maximum ECD. The largest particle in the model had an ECD of 110 µm. In one section, the maximum diameter is 102 µm, against what the majority—also the experimental value—lies in a range between 20 µm and 30 µm ECD. This reflects the randomness regarding the maximum ECD–also a very large measuring area is not a warranty for the detecting the largest particle for the reasons mentioned beforehand.

3.3.3.6 Conclusions

It was concluded that the analysis of an area of 100 – 200 mm^2 offers a valuable basis for the analysis under the assumed conditions. Owing to the truncation of data, a significant increase of analysing area, also resulting in a considerable increase of measuring time, would not result in a more representative output in this case. In contrast, only a slightly smaller measuring area provokes a substantial increase of the error and is therefore not recommended to get a good impression on the inclusion landscape.

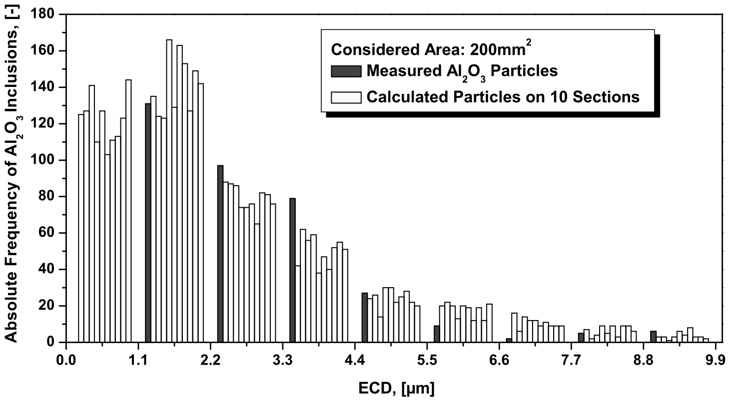

Figure 3.15: Size distribution of particles for the 10 sections of the calculations compared to the measured values of Al_2O_3 resulting from the analysis of 200 mm^2.

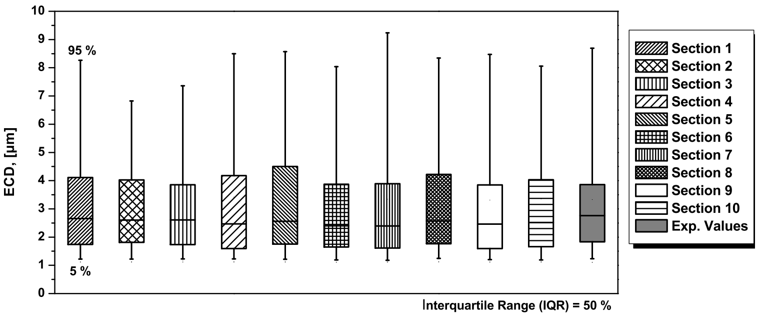

Figure 3.16: Box Plot of particles for the 10 sections of the calculations compared to the measured values of Al_2O_3 resulting from the analysis of 200 mm^2.

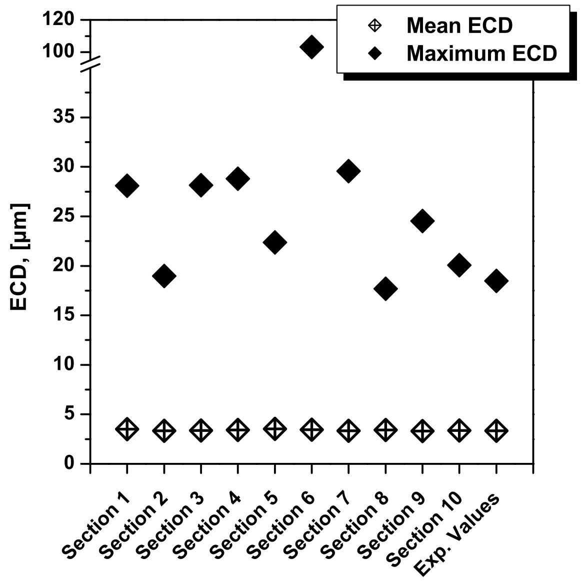

Figure 3.17: Medium and maximum particle diameters for the 10 sections of the calculations compared to the measured values of Al_2O_3 resulting from the analysis of 200 mm^2.

Regarding the maximum inclusion diameter, it has been shown that substantial differences are observed for various calculated and experimental sections. While the maximum sphere diameter distributed in space was defined with 110 mm², only in one calculated section, a circle diameter > 100 mm² was found. Consequently, the significance of automated SEM/EDS analysis regarding the maximum diameter in a defined sample volume is very limited. By the presented model, a quantification of the error that is made for defined analysing conditions is available. Thus, conclusions on the representative sample area for steels with a comparable size distribution and inclusion content can be made.

3.4 Electrolytic Extraction as a Tool for Three-Dimensional Inclusion Analysis

In order to get a three dimensional image of non-metallic inclusions and therefore a more detailed information regarding inclusion morphology, the electrolytic extraction method is applied. Here, the steel matrix is dissolved in a galvanic cell and the inclusions remain in the residue. In a second step, the residue is filtrated and the NMIs on the filter can subsequently be analysed in the SEM. This method has a very long tradition: Already Klinger and Koch [202] dealt with similar questions in the year 1938 and can therefore be seen as precursors concerning the extraction method. In the following 40 years, several researcher picked up this topic: Different electrolytes and cells were tested regarding their applicability for varying steel grades [203–206]. Based on numerous test series with a number of electrolytes described in literature (see Tab. 3.7), this method was continuously optimised at the Chair of Metallurgy in the last 4 years.

Table 3.7: Applied electrolytes for the extraction of NMIs from literature [205, 206].

Artner Electrolyte	
Amount, [*wt.*-%]	Component
5.0	$C_6H_5O_7 \cdot 3Na$
1.2	KBr
0.6	KI
1.0	$C_6H_8O_6$
92.2	H_2O
10% AA Electrolyte	
Amount, [*wt.*-%]	Component
1.0	$[(CH_3)_4N]Cl$
10.0	$C_5H_8O_2$
89.0	CH_4O

The schematic experimental set-up is illustrated in Fig. 3.18. By means of systematic parameter studies, optimal experimental conditions were defined. Figure 3.19 displays the weight reduction of steel in dependence of test duration and varying applied currents. Out of the performed experiments, a test duration of max. 1 hour is seen as adequate. As a function of the analysed steel grade slight adaption concerning test parameters have to be made. Basically, the higher alloyed the steel, the shorter the test duration in the analysis.

In addition to the already well known electrolytes from literature, a new concept is applied for extraction experiments: Ionic liquids were used as electrolytes. These are organic salts, which melt at ambient

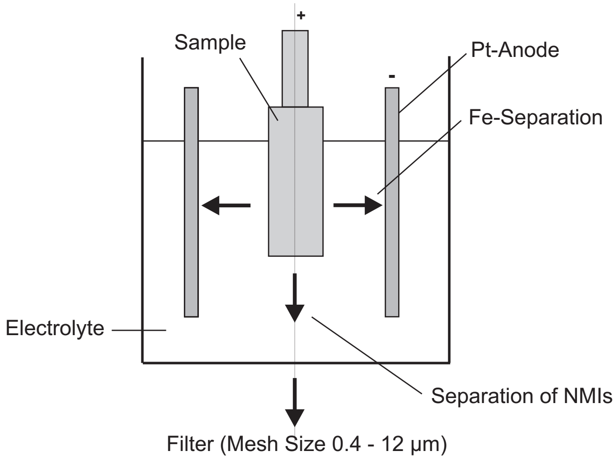

Figure 3.18: Schematic experimental set-up of the electrolytic extraction method.

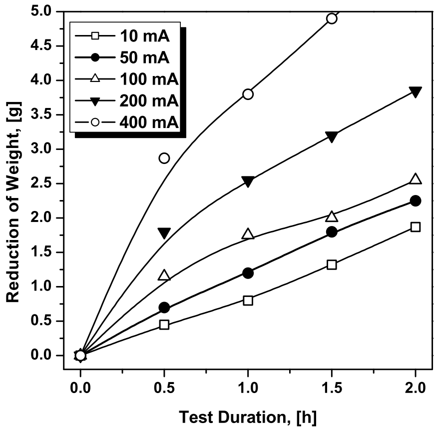

Figure 3.19: Weight loss as a function of applied current and test duration.

temperature. The chemical composition of the used ionic liquid, consisting of Cholinchloride and Urea, is given in Tab. 3.8 [207].

Table 3.8: Composition of the used ionic liquid for electrolytic extraction.

Amount, [*wt.*-%]	Component
53.57	$C_5H_{14}ClNO$
46.25	CH_4N_2O

Ionic liquids offer some advantages: they are thermally stable, have a very low, practically non-measurable, vapour pressure and offer very good solution properties for numerous substances. Furthermore, due to their solely ionic composition, ionic liquids possess interesting electrochemical properties, as for example electrical conductivity and high electrochemical stability [207].

After extraction, the solution is filtrated and the residue is analysed with the SEM. Extraction experiments have been performed for different steel grades, starting with low-alloyed carbon steels. Figure 3.20 shows three examples of inclusions extracted from the mentioned low-alloyed carbon steel. Figure 3.20a gives an overview on numerous Al_2O_3 inclusions in different size ranges. Two globular agglomerated inclusions are illustrated in Fig. 3.20b. In order to enable a simultaneous extraction of ox-

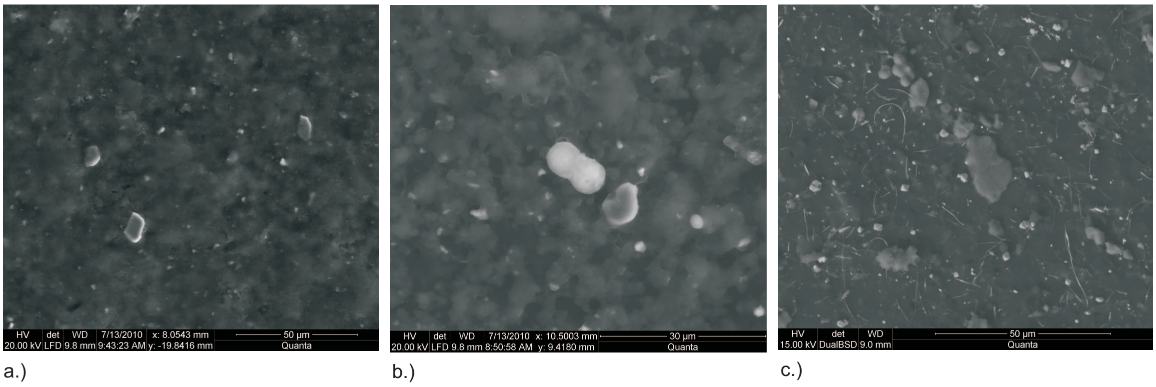

Figure 3.20: SEM-images of inclusions on filter residue isolated with electrolytic extraction.

ides and sulfides, the test parameters have to be adjusted very carefully; the test duration must be limited in order to not dissolve sulfides. One example of oxides and sulfides is shown in Fig. 3.20c. Examples of isolated inclusions from residual electrode material from the ESR process will be given in Chapter 5.

Currently, electrolytic extraction is only used for qualitative analysis of inclusions. Regarding these results, it is shown that this method is very useful for a detailed study of inclusion morphology, mainly as far as complex or agglomerated inclusions are concerned. Thus, it is intended to upgrade the method, in order to also get a quantitative information on the three-dimensional inclusion distribution.

3.5 Summary

Since inclusion analysis is a very broad and manifold topic with numerous influencing aspects, a general appraisal of methods is very difficult. In this chapter the general problems and challenges concerning a reliable characterisation of non-metallic inclusions are discussed and commonly used analysing methods are compared. One of the most frequently applied methods for cleanness measurements of steels is the automated SEM/EDS analysis. This method provides a large information content and is therefore often applied for research purposes. One major aspect dealing with this method is its representativeness with special regard to the measured sample area. Different sizes of sample areas were investigated experimentally focussing on the size distributions of the non-metallic inclusions as well as the medium and the maximum diameter of the particles.

Based on experimental investigations a statistical-geometric model was formulated giving the chance of getting an impression of the whole size distribution. A practical analysing limit inflicts a lower bound for experimental measurements, which therefore always yields truncated data. In dependence of the analysed area and the inclusion content, it is possible to calculate the error of the area ratio. These result also have recently been published by the author of this thesis [208]. The used model input parameters have been chosen consciously, in order to get an impression of the lower limit of sample area for the analysis of clean steel with very low inclusion content. Consequently, the calculations are also representative for the steel analysed in the practical part of this thesis. Therefore the obtained results provide the fundamental basis for evaluation and interpretation of the changes in inclusion landscape especially as far as the modification behaviour of oxides is concerned.

Furthermore, the electrolytic extraction method is demonstrated, which gives a three-dimensional view on inclusions and consequently provides important information concerning inclusion morphology. Summing up, a significant characterisation of inclusion landscape can be assured by the combination of different methods, profiting of their individual advantages and also being aware of their limitations. An overview of the used characterisation methods in order to get a qualitative as well as quantitative analysis of steel cleanness is published by Michelic *et al.* [209].

4 Applied Tools and Experimental Methods for the Description of Inclusion Modification

The present chapter describes the methods which were used to study the modification behaviour of non-metallic inclusions through the interaction with different slags. Next to an overview on the analysed steel and used slag compositions, the basic procedure of thermodynamic modelling is demonstrated and the kinetic approach for the evaluation of dissolution of oxides in steel is presented. Secondly, the used laboratory set-up and the employed test parameters are described. A Tammann Furnace has been applied to investigate the influence of different slag compositions on the resulting inclusion landscape. A Laser Scanning Electron Microscope (LSCM) offers the possibility of in-situ observation of dissolution of inclusions in steel and slag. Its fundamental principle as well as the used experimental conditions are explained. Next to a general description of the applied experimental methods as well as calculation procedures, some fundamental results are shown, providing the basis for the performed investigations as well as the results given in Chapter 5.

4.1 The Analysed Material

In the present thesis, the hot-work tool steel X38CrMoV5-1 manufactured at Böhler Edelstahl GmbH & Co KG was used for all calculations as well as in the experimental part. Its basic composition is shown in Tab. 4.1.

Table 4.1: Chemical composition of the steel used for thermodynamic calculations as well as in the experimental part.

wt.-%C	*wt.-%Cr*	*wt.-%Si*	*wt.-%Mn*	*wt.-%Mo*	*wt.-%V*
0.38	5.00	1.10	0.40	1.30	0.40

In a first step, the changes in inclusion landscape between electrodes and corresponding ingots remelted at Böhler Edelstahl GmbH & Co KG were analysed. For this purpose it was also necessary to examine the representativeness and reproducibility of different sampling positions in the electrode as well as in the ingot. In a second step, material of the same electrodes was used for laboratory experiments, where the samples were remelted in a Tammann Furnace using different slag compositions. A flow chart of the experimental procedure is shown in Fig. 4.1.

4.1.1 Properties of X38CrMoV5-1

Basically hot-work tool steels are stainless steels, belonging to the group of tool steels, and are used for non-cutting deformation of steels and other alloys. Generally, hot-work tool steels were applied for processes at which the surface temperature of the tool continuously exceeds 200 °C. Depending on the process, the temperatures of the work piece can lie between 400 °C and 1200 °C and contact

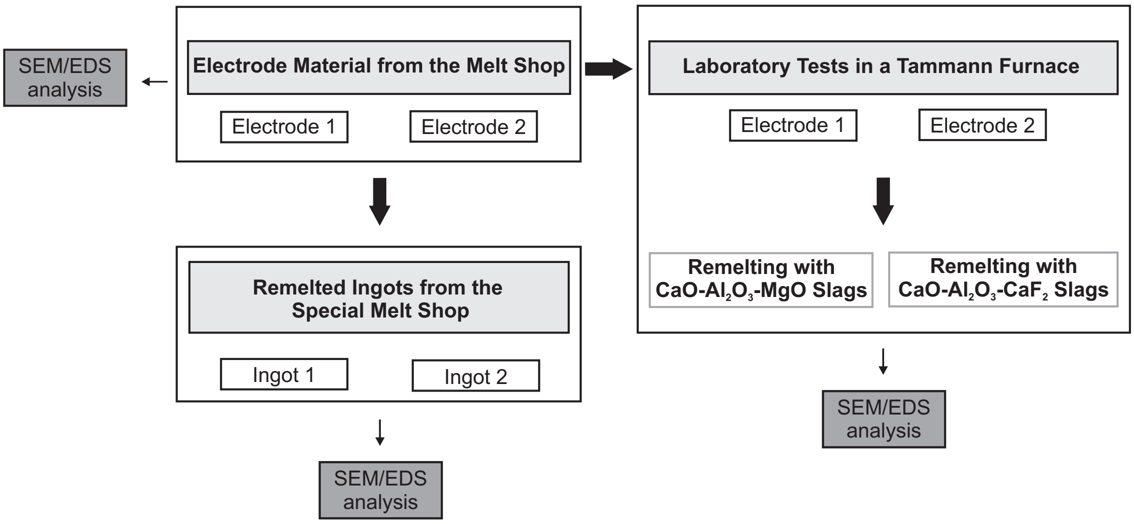

Figure 4.1: Flow chart of experimental procedure.

times between tool and work piece vary between fractions of a seconds and several minutes. Typical examples for the application of hot-work tool steels are die-casting or extrusion. Consequently, the essential required properties may be summarised as follows:

- Tempering resistance;
- High temperature strength;
- Hot hardness;
- Thermal shock resistance;
- Creep strength;
- Hot ductility.

In order to fulfil these requirements, *Cr*, *Mo* and *V* are the essential alloying elements of hot-work tool steels. They highly influence tempering resistance as well as high temperature strength. Due to their ability of carbide formation, *Mo* and *V* also increase hardness and wear resistance. The relatively high *Si*-content primarily improves impact properties and is therefore responsible for a longer period of use [210]. Tables 4.2 and 4.3 give an overview on the mechanical and physical properties of the X38CrMoV5-1.

4.1.2 Production at Böhler Edelstahl GmbH & Co KG

Basically, at Böhler Edelstahl GmbH & Co KG, the hot-work tool steel X38CrMoV5-1 is manufactured on a scrap basis. After melting in the electric arc furnace, most metallurgical work and the refining is done in the AOD converter. Since the *Cr*-content of this steel is relatively low compared to other stainless steels, the use of an AOD converter is not essentially required, but offers some advantages as far as decarburisation velocity, the recovery of alloying elements and degassing are concerned. Furthermore, the possibility of alloying elements in an oxidic form decreases the overall production costs [212]. The fine adjustment of alloying elements as well as temperature adaptation for the subsequent casting is

Table 4.2: Mechanical properties of the X38CrMoV5-1 for a working temperature of 500 °C [211].

Hardness after tempering at 600 °C [HRC]	Tensile strength [Nmm^{-2}]	Yield strength [Nmm^{-2}]
48	1100	900

Table 4.3: Physical properties of the X38CrMoV5-1 for a working temperature of 500 °C [211].

Elastic modulus [$kNmm^{-2}$]	Density [gcm^{-3}]	Thermal conductivity [$W(mK)^{-1}$]	Thermal extension between 20 – 500 °C [10^{-6} $m(mK)^{-1}$]
176	7.64	29.5	12.9

done in secondary metallurgy. For casting, both, continuous casting as well as ingot casting, can be used. The cast product provides the input material for remelting processes, the so-called electrodes. All electrodes used in the present study are products of ingot casting and have been remelted via ESR in the special melt shop. The slag composition used for remelting via ESR is given in Tab. 4.4. This standard slag primarily consists of CaO, Al_2O_3 and CaF_2 with slight additions of MgO and SiO_2.

Table 4.4: Basic slag composition used for remelting the two electrodes in the special melt shop at Böhler Edelstahl GmbH & Co KG.

$wt.\text{-}\%CaO$	$wt.\text{-}\%Al_2O_3$	$wt.\text{-}\%CaF_2$	$wt.\text{-}\%SiO_2$	$wt.\text{-}\%MgO$
23.0	34.0	35.0	5.0	3.0

In order to investigate the influence of the electrode composition on the inclusion landscape in the final ingot, two different initial electrode conditions have been examined in the present work. These two electrodes had the same basic composition but were treated differently in the melt shop at Böhler Edelstahl GmbH & Co KG, resulting in varying contents of Al, Mg and O. A comparison between the two electrode conditions is given in Tab. 4.5. The oxygen content was measured using LECO-analysis. The contents of Al, Mg, Ca and O have been determined via Inductively Coupled Plasma Mass Spectrometry (ICP-MS).

Table 4.5: Contents of Al, Mg, Ca and O of the electrodes used for thermodynamic calculations as well as in the experimental part.

	$wt.\text{-}\%Al$	$wt.\text{-}\%Mg$	$wt.\text{-}\%Ca$	$wt.\text{-}\%O$
Electrode 1	0.0200	0.0003	0.0055	0.0060
Electrode 2	0.0110	0.0007	0.0050	0.0130

4.1.3 Sampling of Electrodes and Ingots

For the comparison of the inclusion modification between electrode and ingot due to steel-slag interactions, samples out of two residual electrodes (compositions given in Tab. 4.5) and the corresponding ingots were taken. These samples were then prepared metallographically and analysed with automated SEM/EDS analyses (the used settings are listed in Tab. 3.2), measuring a sample area of 100 mm^2 in each case.

4.1.3.1 Comparison of Different Sampling Positions on the Electrode

A schematic illustration of the residual electrode and the sampling positions is given in Fig. 4.2. Since the electrode is a cast product, inhomogeneities in inclusion distribution have to be considered. Furthermore, the reliable characterisation of the initial state is very important for the subsequent observation of changes in inclusion landscape. For this purpose, in order to get representative information on the inclusion landscape, samples over the cross section as well as over the height of the residual electrodes have been compared. All following figures comparing different sample positions in the electrodes as well as in the ingots show the overall number of inclusions including oxides, sulfides, oxisulfides as well as nitrides.

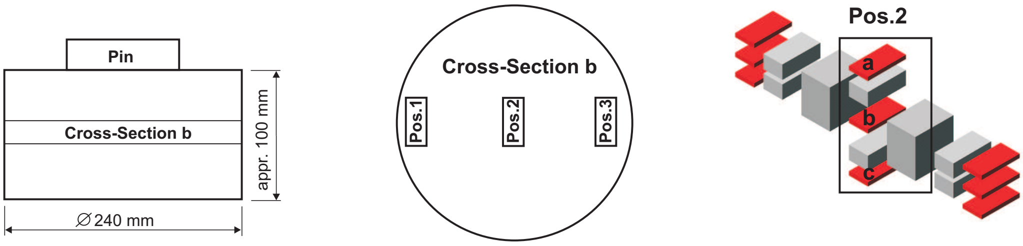

Figure 4.2: Schematic illustration of sampling positions in the analysed electrodes.

Figures 4.3 and 4.4 exemplarily show and compare the results of different sampling positions of electrode 1. It can be seen that—considering that the electrode is a cast product— a relatively high concordance in the number of NMIs as well as the medium ECD of the inclusions over the analysed cross section exists. The higher amount of NMIs in the centre position may be explained by the solidification conditions in ingot casting. Expectedly, as far as the maximum inclusion diameter is concerned, large difference are observed. This fact—as already explained in Chapter 3—is a result of the high level of macro-cleanness and the therewith connected accidental distribution of large inclusions. Secondly, results of the automated SEM/EDS analysis only have a limited significance regarding the maximum inclusion diameter, as explained in the last chapter. Nevertheless, a representative conclusion for the medium inclusion content in the electrode is gained. Regarding different sample positions over the height, a slight increase of the mean inclusion diameter is observed from the top to the bottom of the residual electrode. Since the bottom end of the residual electrode was in direct contact with the slag during the process, consequently a certain heat affected zone exists, which may influence the inclusion landscape. All in all, similar trends have been observed for electrode 2. In sum, the changes of inclusions number as well as medium diameter over the cross section as well as over the height of the residual electrode are marginal when considering that this is an cast product. Consequently, a sample from the centre is used in order to describe the initial state of inclusion landscape and also for comparisons with the inclusion landscape in the ingot as well as with laboratory experiments. Moreover, all samples for laboratory experiments have also been taken from the centre range of the two residual electrodes.

4.1.3.2 Comparison of Different Sampling Positions on the Ingot

Figure 4.5 shows the dimensions of the remelted ingots as well as the used sampling positions. In both cases, samples out of a cross section at the bottom (termed cross section B) of the ingot and out of a cross section at the medium ingot height (termed cross section M) have been analysed. A comparison of number of inclusions per mm^2 and the mean and maximum inclusion diameter of different sample positions on the two ingot cross sections exemplarily shown for ingot 1 is given in Figs. 4.6 and 4.7.

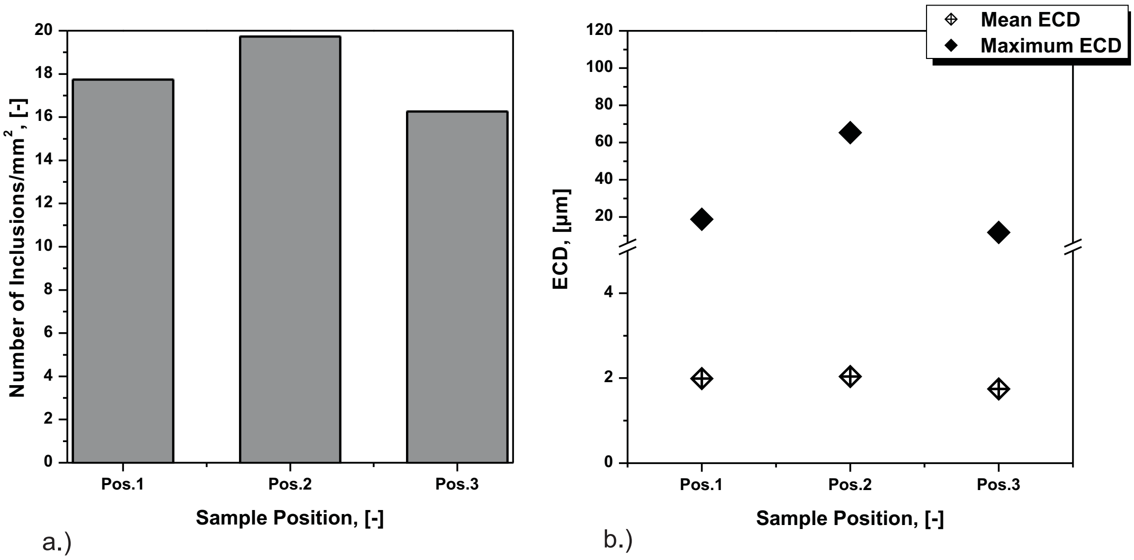

Figure 4.3: Comparison of a.) number of inclusions per mm² and b.) mean and maximum ECD on different positions on the cross section of the residual electrode 1.

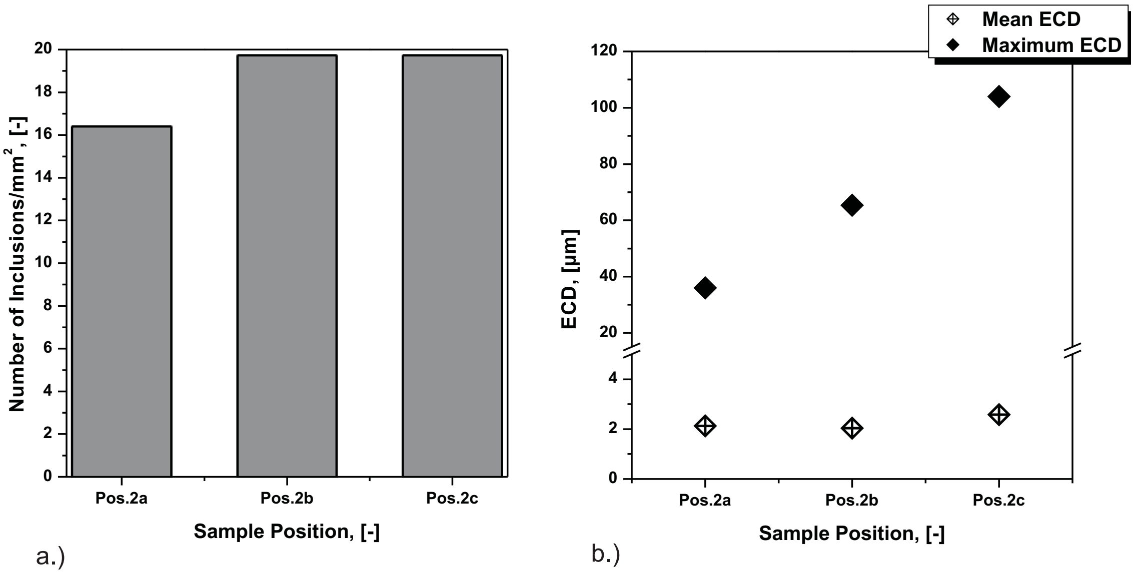

Figure 4.4: Comparison of a.) number of inclusions per mm² and b.) mean and maximum ECD on different positions over the height of the residual electrode 1.

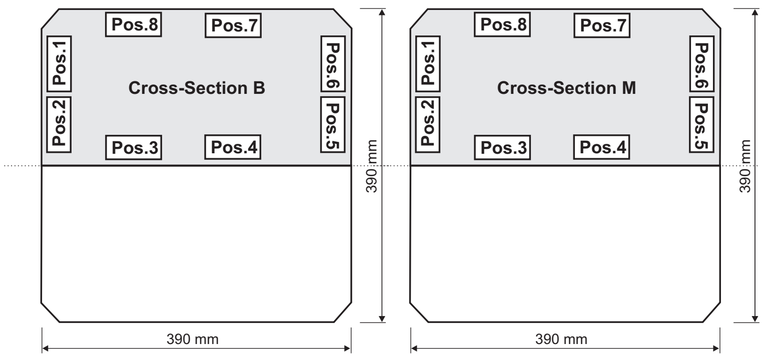

Figure 4.5: Schematic illustration of sampling positions in the analysed ingots.

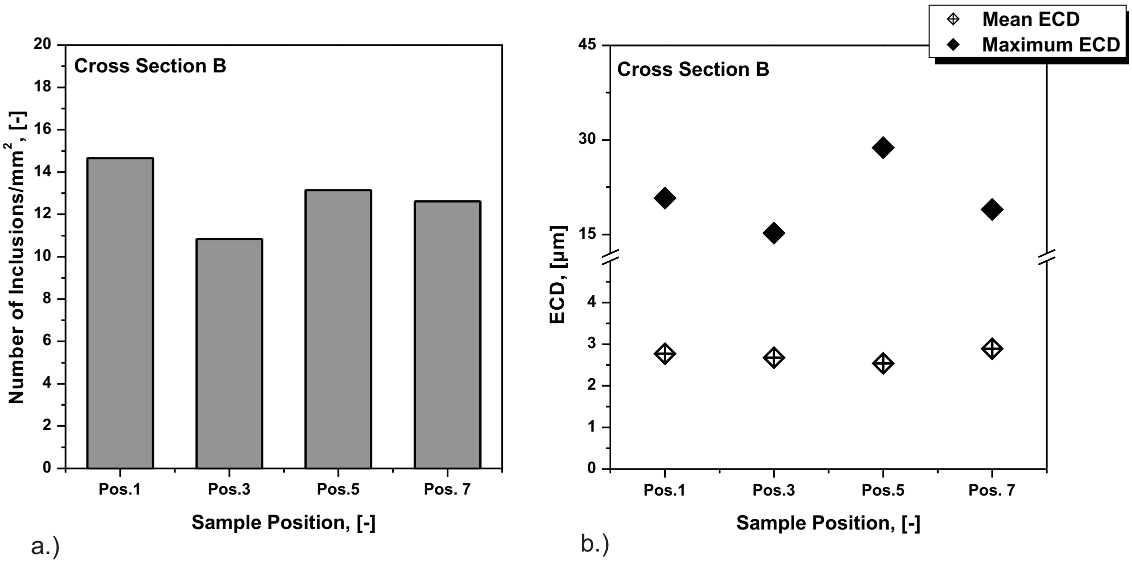

Figure 4.6: Comparison of a.) number of inclusions per mm² and b.) mean and maximum ECD on different positions over the cross section B of ingot 1.

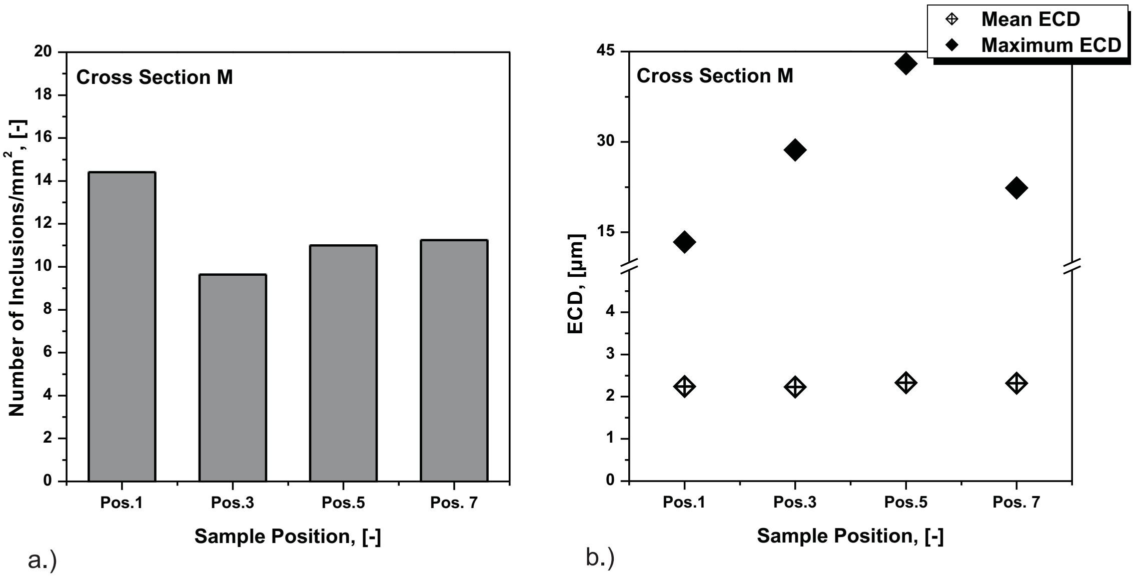

Figure 4.7: Comparison of a.) number of inclusions per mm² and b.) mean and maximum ECD on different positions over the cross section M of ingot 1.

Regarding the different sample positions, on both cross sections the lowest number of inclusions is detected in the centre of the remelted ingot. No significant difference between the two cross sections concerning number of inclusions per mm² is observed. In sum, a significant decrease of the number of inclusions compared to the electrode is observed. Moreover, the maximum detected inclusions diameters are much lower than those in the electrode. In case of ingot 1 no inclusions larger than 45 µm have been detected. It is worth noting that the overall mean ECD does not decrease considerably between electrode and ingot. This can be explained as follows: In this evaluation all inclusion types are considered. Generally, sulfide inclusions are smaller than oxide inclusions in this type of steel. Since the sulfide content is decreased the most via Electroslag remelting and the remaining ingot inclusions are primarily oxides, the mean ECD is apparently unchanged or even slightly increased. In fact, generally a decrease of the mean inclusion diameter between electrode and ingot is observed for oxides as well as sulfides. More details on the change of the mean ECD through remelting will be given in Chapter 5. In sum, a good comparability between the single sample positions on the ingot cross sections has been determined. For the comparison with samples from the electrode as well as with laboratory experiments, the results out of the center range of the individual cross sections of the ingots were used.

4.2 Thermodynamic Calculations

The different reactions between steel, slag and NMIs under equilibrium conditions were calculated with the *Equilib* tool of *FactSage 6.1* using the databases *FToxid*, *FSstel* and *FACT 53*. In a first step, equilibrium calculations of the single components steel, slag and NMI were performed with varying temperature conditions. In a second step, non-metallic inclusions were combined with a steel or slag phase in order to get an impression of their influence on the modification of the NMIs. Finally, all components were put together to a complex system. As a result a thermodynamic description of the system steel-slag-inclusion for the defined conditions was gained. In order to consider the influence of the electrode composition as well as the modification through slag composition in the calculations, several successive calculation steps had to be performed. The calculations presented in this work refer to the combination of 100 g steel with 5 g slag. In the diagrams presented in Chapter 5 all components have been normalized.

Since the slag is the essential element concerning the modification of NMIs during remelting, an adequate description of the phase diagram $CaO\text{-}Al_2O_3\text{-}CaF_2$ is indispensable. Figure 4.8 shows the phase diagram for 1600 °C calculated with the *Phase Diagram* tool of *FactSage 6.1*. Comparing this diagram with well-established systems published in literature [106, 107], it is obvious that the miscibility gap cannot be simulated with the available databases*.

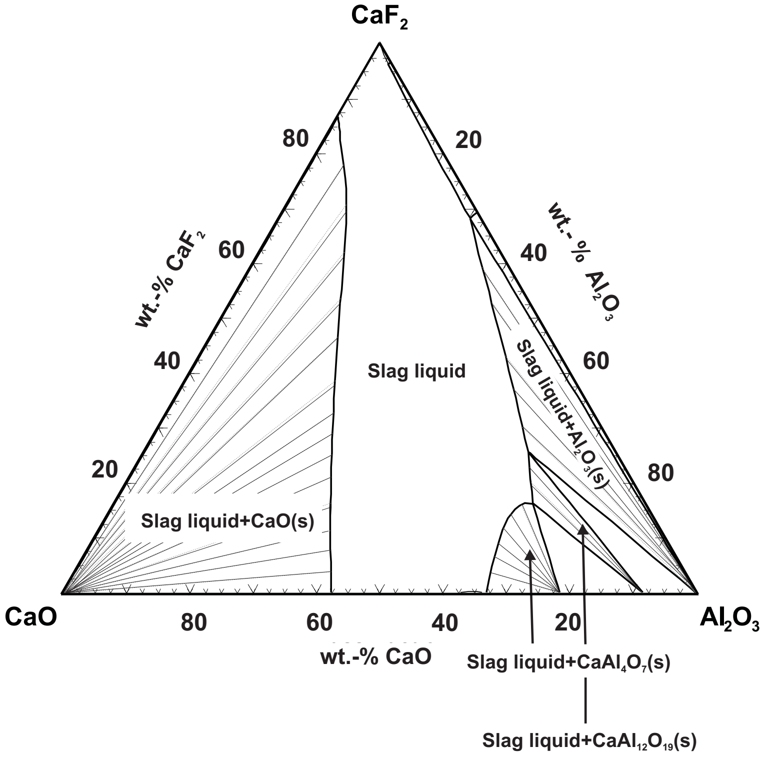

Figure 4.8: The phase diagram $CaO\text{-}Al_2O_3\text{-}CaF_2$ calculated with *FactSage*.

---

[*] See phase diagrams from literature in Section 2.4.2.1 on pages 38ff.

The data provided for this system by *FactSage* is currently limited to relatively low contents of CaF_2. Consequently the calculation of slag compositions containing amounts > 35 *wt.-%*CaF_2 may be problematic. Nevertheless, a good compromise was reached for CaF_2-contents used in standard ESR slags. Comparing the activity data between literature [9] and calculations performed with *FactSage* a good concordance was achieved. Figure 4.9 exemplarily shows the Al_2O_3 activity for a standard ESR slag consisting of approximately equal parts of CaO, Al_2O_3 and CaF_2 as a function of temperature. Comparing the value at 1600 °C with data from literature shown in Fig. 4.10, equal results were obtained. Thus, in spite of the described limitations, *FactSage* offers a valuable basis concerning the slag compositions examined in the present study. The calculation results for electrode conditions as well as the effect of remelting with different slag compositions will be discussed in Chapter 5.

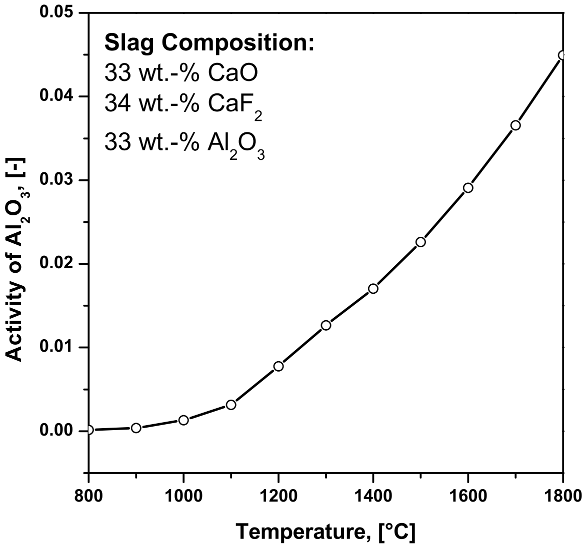

Figure 4.9: Activity of Al_2O_3 in a standard ESR slag as a function of temperature calculated with *FactSage*.

Furthermore, the phase stability diagram published by Itoh *et al.* [21] was recalculated also considering the interaction coefficients of alloying elements of the X38CrMoV5-1. The interaction coefficients of Al, Mg and O which have been considered temperature dependent; C, Si, Mn, Cr and Mo were taken into consideration without temperature dependence. Thermodynamic data for this calculations were taken from literature [21, 213, 214]. The transitions between $MgO - MgOAl_2O_3$ and $MgOAl_2O_3 - Al_2O_3$, each consisting of a non-linear equation matrix with three unknown variables were solved using the Levenberg-Marquardt algorithm. Equations (4.1) and (4.2) show the equations for the transition between $MgO - MgOAl_2O_3$; the transition $MgOAl_2O_3 - Al_2O_3$ is shown in Eqs. (4.3) and (4.4). The calculated diagram will be shown in Chapter 5.

$$3\left(\log K_{MgO} + \log f_{Mg} + \log m_{Mg}\right) - \left[\log K_{M-MA} + 2\left(\log f_{Al} + \log m_{Al}\right)\right] = 0 \tag{4.1}$$

$$\log K_{MgO} + \log f_{Mg} + \log m_{Mg} + \log f_O + \log m_O = 0 \tag{4.2}$$

$$3\left(\log K_{MA-A} + \log f_{Mg} + \log m_{Mg}\right) - \left[\log K_{Al_2O_3} + 2\left(\log f_{Al} + \log m_{Al}\right)\right] = 0 \tag{4.3}$$

$$\log K_{Al_2O_3} + \log f_{Al} + \log m_{Al} + \log f_O + \log m_O = 0 \tag{4.4}$$

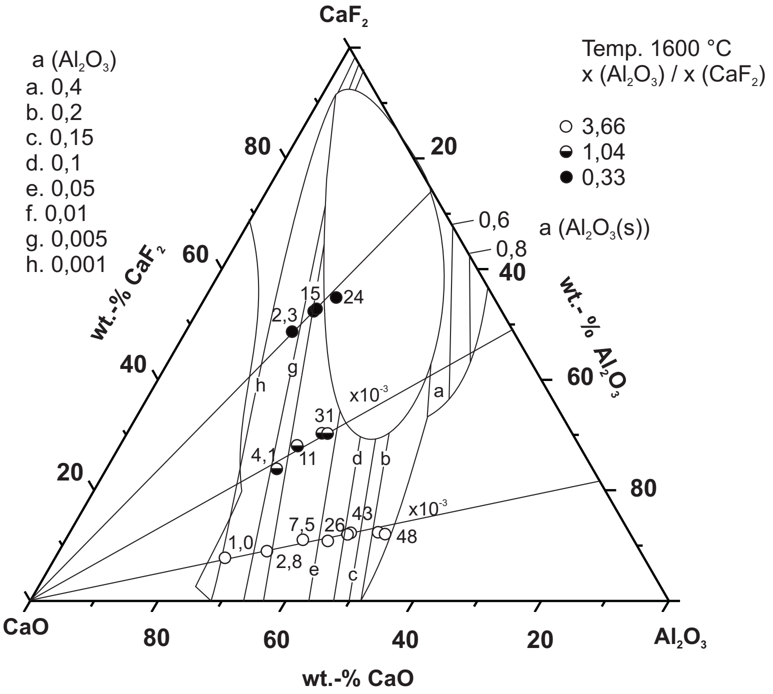

Figure 4.10: Activity data of Al_2O_3 within the system CaO-Al_2O_3-CaF_2 according to [9].

4.3 Kinetic Considerations

In order to consider and compare the dissolution times for non-metallic inclusions in the hot-work tool steel X38CrMoV5-1, a tool developed by Hong and Debroy [215] was extended for the inclusion types most relevant in the present thesis. In [215] the authors present a formalism that describes the effects of time and temperature on the diffusion controlled growth and dissolution kinetics of inclusions in different steel compositions. For reasons of simplification, the following assumptions are made:

- Constant concentration field near each inclusion during growth and dissolution;
- Heterogeneous nucleation;
- Unity of the activities of liquid iron and all solid compounds;
- Only the concentrations of those elements that make up the inclusion were calculated at the interface between the inclusion and the liquid steel. The concentrations of other elements were assumed to be the same as in the bulk metal.

The dissolution rates of small spherical inclusions are assumed to be limited by the transport of non-metallic elements in the alloy. For the dissolution of the inclusions, the solution of the diffusion equation with stationary interface approximation was considered. By considering the Laplace approximation for short times, [216] derived

$$r_{i+1} - r_i = -\frac{k}{2}\left[\frac{D_0}{r} + \sqrt{\frac{D_0}{\pi t}}\right]\Delta t, \tag{4.5}$$

where r_{i+1} and r_i are the inclusion radii before and after the i^{th} time step, t is the dissolution time, D_0 is the diffusion coefficient, Δr is the change of inclusion radius, Δt is the time step and k is defined as $k = -2c^\star$. Thus, using Eq. (4.5) the time needed to decrease the particle size to a certain value, for example, 1% of the initial radius at different temperatures can be calculated. For dissolution calculations within this thesis usually a final inclusion radius of 0.001 µm was applied.

The original program by Hong and Debroy [215] provides data to calculate oxides, sulfides, nitrides as well as some complex oxides [213, 217, 218], but does not include thermodynamic data for Mg-containing inclusions. Thus, the data basis of the program has been extended with literature values for the calculation of $MgOAl_2O_3$ [19–23]. The modified program was used to calculate the dissolution times of Al_2O_3 and $MgOAl_2O_3$ in X38CrMoV5-1 (composition given in Tab. 4.1) as a function of temperature for different initial inclusion radii. This approach was used in order to examine the dissolution time of Al_2O_3 and $MgOAl_2O_3$ in the liquid film at the electrode tip and therefore gain important information concerning the behaviour of these inclusions in the remelting process. Calculation results will be shown in Chapter 5.

4.4 Laboratory Experiments

In order to analyse the modification of inclusions in more detail and to be able to assess the different modification mechanisms and influencing factors, experiments on laboratory scale were performed. A Tammann Furnace was used for the remelting samples of electrode material with varying parameters under defined conditions. Additionally, the dissolution behaviour of inclusions in X38CrMoV5-1 as well as in CaF_2-containing slags was examined using a Laser Scanning Confocal Microscope (LSCM). In the following, the experimental set-up as well as the used test parameters are described.

4.4.1 Remelting Experiments in a Tammann Furnace

Samples of the two residual electrodes of X38CrMoV5-1 were taken for laboratory tests in the Tammann Furnace. Different compositions out of the following two basic slag systems have been used:

1. CaO-Al_2O_3-MgO
2. CaO-Al_2O_3-CaF_2

Since laboratory experiments using CaF_2 containing slags are rather complex with the available experimental set-up, slags of the system CaO-Al_2O_3-MgO were used in a first approach for reasons of simplicity. Furthermore, using these slags also the influence of CaF_2 on the inclusion modification could be studied in more detail. For this purposes, in order to establish a comparable reaction system, the activities of Al_2O_3 and CaO have been calculated for both slag systems. As illustrated in Fig. 4.11, comparable Al_2O_3 activities are obtained. Regarding the activity of CaO, higher values are observed for the system CaO-Al_2O_3-CaF_2 which seems logical due to the presence of CaF_2. Thus, laboratory experiments were used to study the influence of activity relations on the resulting inclusion landscape.

Next to the influence of slag composition also different crucible materials were tested. Additionally, the slag amount as well as the duration time within the experiments have been varied. Figure 4.12 demonstrates the basic test sequence of laboratory experiments in the Tammann furnace. In the following the used experimental set-up as well as the test conditions and used slag compositions are explained in detail.

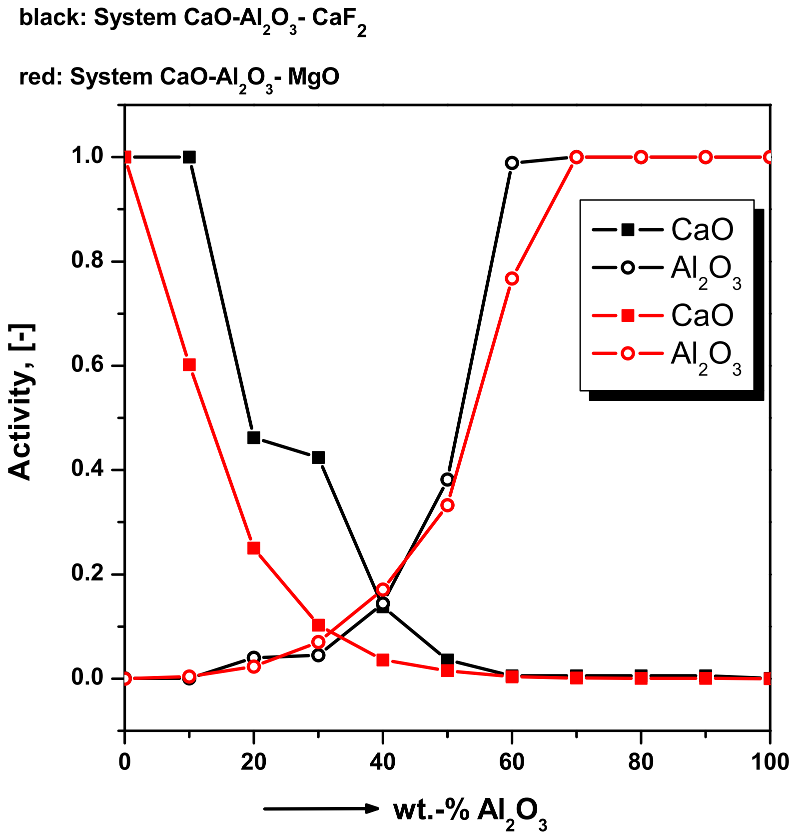

Figure 4.11: Comparison of Al_2O_3 and CaO activities in the two slag systems CaO-Al_2O_3-MgO and CaO-Al_2O_3-CaF_2 as a function of Al_2O_3-content.

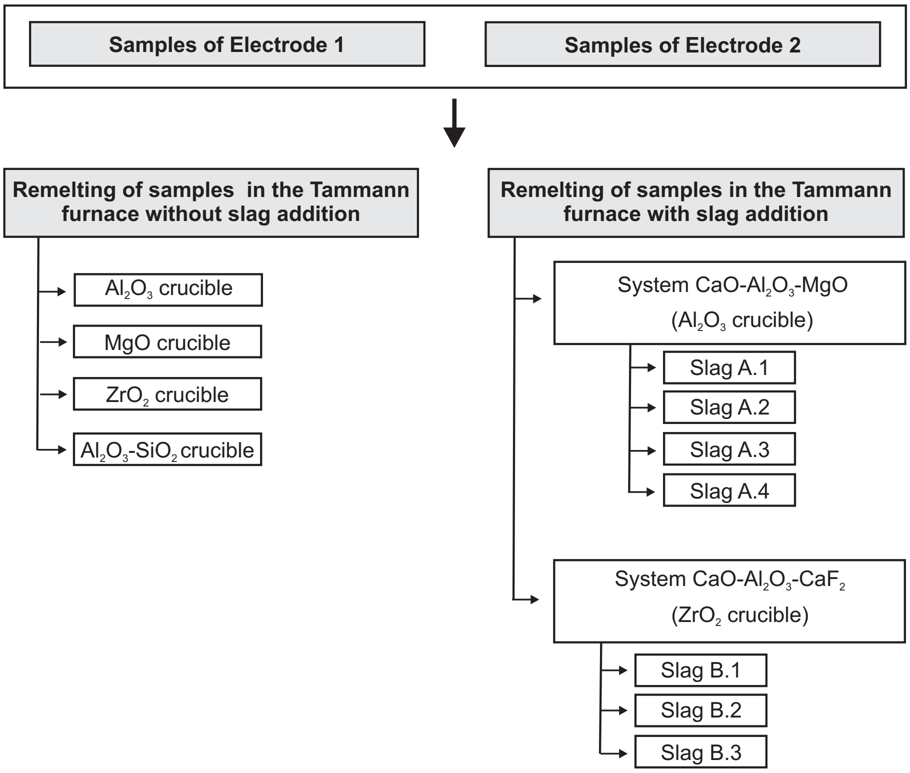

Figure 4.12: Illustration of test sequences for laboratory experiments in the Tammann Furnace.

4.4.1.1 Experimental Set-Up

The Tammann furnace is a high-temperature electric resistance furnace, which can be heated up to 2000 °C. Due to the carbon heating tubes inside the furnace and their reaction with the residual oxygen, the final oxygen content in the furnace vessel is extremely low (0.001 *ppm*). The schematic experimental set-up for the remelting experiments as well as the furnace itself is shown in Fig. 4.13. All experiments in the Tammann furnace were carried out under *Ar*-atmosphere (Argon 5.0), using a sample weight of appr. 100 g steel. The samples were heated up to 1600 °C; this temperature was usually held for 10 min. After this duration time, the sample was cooled as fast as possible under controlled conditions and *Ar*-atmosphere inside the furnace. Although the possible reaction time in the experiments is comparatively long, only near-equilibrium conditions are obtained. Furthermore, the separation and agglomeration of NMIs—which are not considered in the calculations—influence the resulting inclusion landscape.

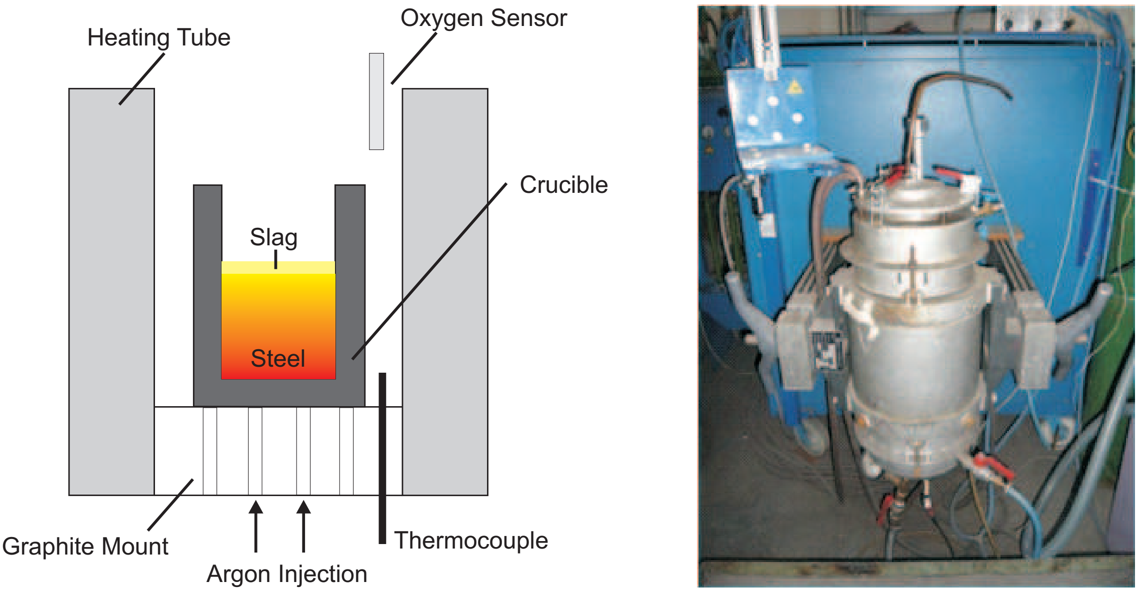

a.) b.)

Figure 4.13: a.) Schematic illustration of the test arrangement and b.) photograph of the Tammann furnace used for laboratory experiments.

In a first phase, the experiments were carried out without slag addition to study the influence of the crucible on the modification of the NMIs. For all experiments without slag addition a holding time of 10 min was applied. In the second phase, different compositions of the described slag systems were added to the crucible covering the whole steel bath surface (the slag mass equals appr. 5 % of the steel mass). Details on the experimental variations are given in the next subsections. After the experiments the steel samples were prepared metallographically and investigated by automated SEM/EDS analyses for the characterisation of non-metallic inclusions. Figure 4.14 exemplarily shows a section through the crucible with the sample and two pictures of a vertical section of the remelted sample as well as the corresponding metallographic specimen which was subsequently analysed using SEM/EDS.

4.4.1.2 Used Slag Compositions

All used slags are mixtures out of their pure substances which were premelted in the induction furnace. Hence, the premelted slags were fractured and ground. Tables 4.6 and 4.7 summarise the different slag

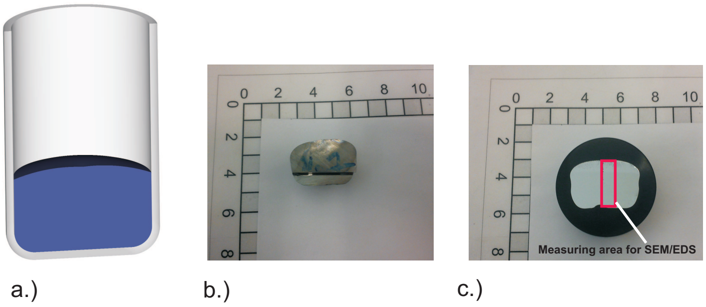

Figure 4.14: a.) Schematic section through the crucible and the sample b.) photograph of the vertical section of the remelted sample and c.) the corresponding metallographic specimen (with SEM/EDS analysed sample area marked in red).

compositions used for laboratory experiments. Within each slag system different compositions were used, continuously increasing the CaO/Al_2O_3 ratio in both cases. In terms of the CaO/Al_2O_3 ratio, slag A.2 out of the system $CaO\text{-}Al_2O_3\text{-}MgO$ fits the ESR process slag composition most closely. Regarding slags out of the system $CaO\text{-}Al_2O_3\text{-}CaF_2$, the used ESR slag lies between slag B.1 and slag B.2.

Table 4.6: Slag compositions of the system $CaO\text{-}Al_2O_3\text{-}MgO$ used for laboratory tests.

	wt.-%CaO	wt.-%Al_2O_3	wt.-%MgO	wt.-%SiO_2
Slag A.1	46.0	46.0	3.0	5.0
Slag A.2	36.8	55.2	3.0	5.0
Slag A.3	30.7	61.3	3.0	5.0
Slag A.4	15.4	76.6	3.0	5.0

Table 4.7: Slag compositions of the system $CaO\text{-}Al_2O_3\text{-}CaF_2$ used for laboratory tests.

	wt.-%CaO	wt.-%Al_2O_3	wt.-%CaF_2	wt.-%MgO	wt.-%SiO_2
Slag B.1	28.5	28.5	35.0	3.0	5.0
Slag B.2	19.0	38.0	35.0	3.0	5.0
Slag B.3	9.5	47.5	35.0	3.0	5.0

In order to ensure effective interactions between steel and slag, the presence of a fully liquid slag at reaction temperatures is essential. The liquid slag projections of the two analysed slag systems calculated with the *PhaseDiagram* Tool of *FactSage 6.1* are shown in Figs. 4.15 and 4.16. In these figures, also the used slag compositions are plotted. It can be seen that in the case of slags containing CaF_2 all of them are fully liquid at 1600 °C. In the case of the slag system $CaO\text{-}Al_2O_3\text{-}MgO$, slag A.1 to slag A.3 are also fully liquid at this temperature, while slag A.4 is not melted until nearly 1700 °C. Experiments with slags out of the system $CaO\text{-}Al_2O_3\text{-}MgO$ which are not fully liquid at experimental temperatures, but saturated with MgO or $MgOAl_2O_3$ have also been performed by the author of this thesis, in order to study the reaction behaviour of these slags with special regard to the formation and modification of $MgOAl_2O_3$. Details to these investigations have recently been published [219, 220].

The applied test conditions and parameter variations for the performed laboratory tests with slag addition are summarised in Tab. 4.8.

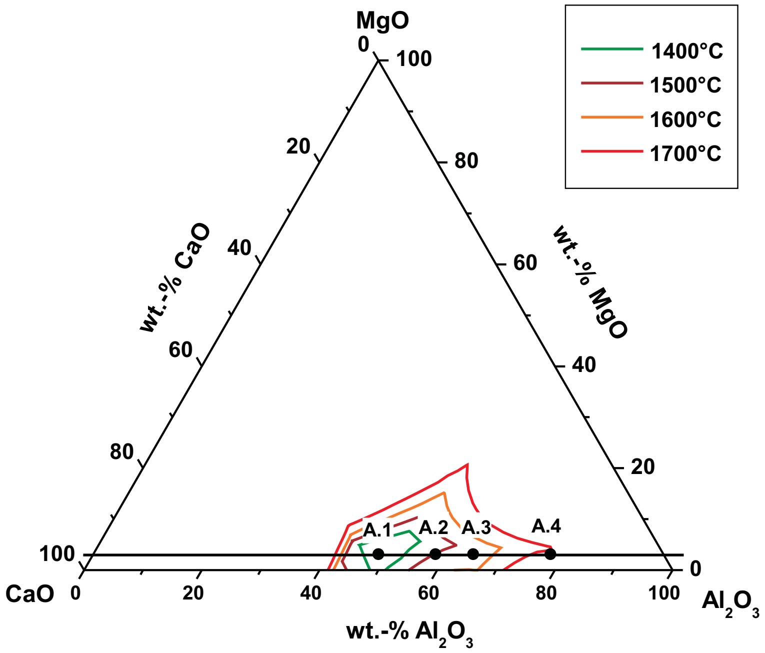

Figure 4.15: Liquid slag projection of the system CaO-Al_2O_3-MgO with the slag compositions used for laboratory tests.

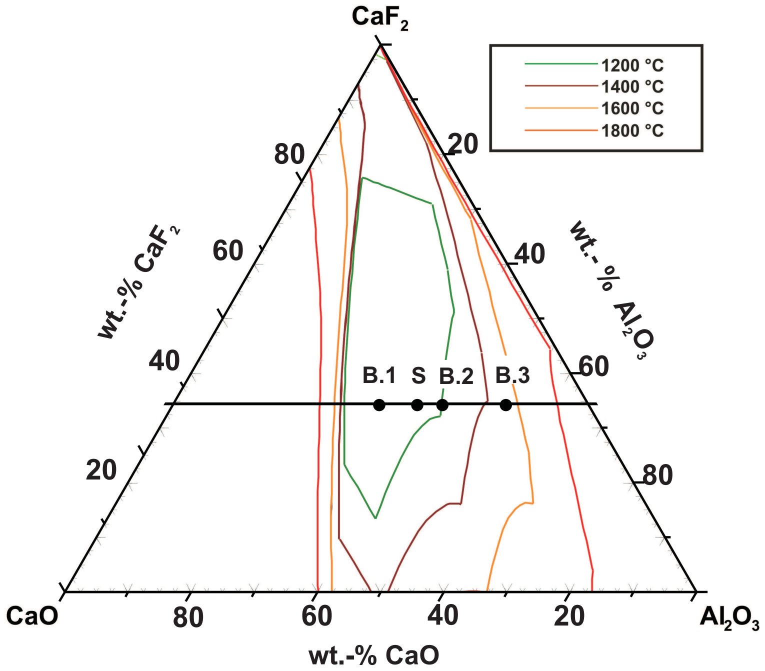

Figure 4.16: Liquid slag projection of the system CaO-Al_2O_3-CaF_2 with the slag compositions used for laboratory tests.

Table 4.8: Test conditions and parameter variations in the laboratory tests.

Tests with slags out of the system CaO-Al_2O_3-MgO

No.	Crucible material	Slag composition	Slag amount	Duration time
1	Al_2O_3	Slag A.1	5%	10 min
2	Al_2O_3	Slag A.2	5%	10 min
3	Al_2O_3	Slag A.3	5%	10 min
4	Al_2O_3	Slag A.4	5%	10 min
5	Al_2O_3	Slag A.2	5%	20 min
6	Al_2O_3	Slag A.2	5%	30 min

Tests with slags out of the system CaO-Al_2O_3-CaF_2

No.	Crucible material	Slag composition	Slag amount	Duration time
1	ZrO_2	Slag B.1	5%	10 min
3	ZrO_2	Slag B.2	5%	10 min
4	ZrO_2	Slag B.3	5%	10 min
5	ZrO_2	Slag B.1	5%	20 min
6	ZrO_2	Slag B.1	5%	30 min
7	ZrO_2	Slag B.1	10%	10 min
8	ZrO_2	Slag B.1	10%	20 min

4.4.2 Experiments with the Laser Scanning Confocal Microscope

In order to study the dissolution behaviour of inclusions in a standard slag used in ESR as well as the dissolution of inclusions in the X38CrMoV5-1, experiments were carried out in the LSCM permitting an in-situ observation of the dissolution process.

4.4.2.1 Experimental Set-Up

The experimental set-up consists of a LSCM attached to a high temperature furnace. The LSCM is equipped with extra long distance lenses. In order to be out of the characteristic spectrum of samples with temperatures up to 1600 °C, the wavelength of the laser is 405 nm. As illustrated in Fig. 4.17, the gold coated chamber of the infrared furnace has the shape of a symmetric ellipse where the halogen lamp is in the bottom focal point; the crucible is in the upper focal point. It is possible to use oxidizing or reducing atmosphere and vacuum down to 10^{-8} bar, the highest temperature is 1700 °C (short time) with a maximum heating rate of 1000 $°Cmin^{-1}$. Cooling rates are temperature-dependent between 1000 $°Cmin^{-1}$ down to 800 $°Cmin^{-1}$ without quenching. For more details to the experimental set-up as well as the investigation possibilities, reference is made to literature [221].

4.4.2.2 Test Procedure

Two different experiments were performed with the LSCM:

1. Dissolution of Al_2O_3 particles in a CaO-Al_2O_3-CaF_2 slag;
2. Dissolution of inclusions in electrode material of X38CrMoV5-1.

The used experimental set-up as well as the time-temperature profiles of the experiments are shown in Figs. 4.18 and 4.19. The analysed sample weight was in every case about 2 – 3 g. In the case of in-situ observation of Al_2O_3 particles in a CaF_2-containing slag, the Al_2O_3 particles with a grain size of appr.100 µm were added to the cold pre-fused cylinder of CaO-Al_2O_3-CaF_2 slag. The sample was rapidly heated to 1200 °C under Ar-Atmosphere with heating rate of 440 $°Cmin^{-1}$. The heating rate to 1400 °C was 120 $°Cmin^{-1}$, after that the temperature was controlled manually stepwise up to 1450 °C, where the temperature was held until complete dissolution of the particles was observed. Similar experiments using a well-known CaO-Al_2O_3 slag have also been performed. For details regarding the dissolution of Al_2O_3 particles in this slag reference is made to a recent publication [220].

In the case of the analysis of electrode material, a sample of electrode 1 was taken. A metallographic specimen of the sample was first studied under the SEM in order to mark a region with a very large inclusion conglomerate. A small sample containing this region was then extracted from the whole sample and subsequently investigated in the LSCM.

The results of the laboratory tests in the Tammann Furnace as well as of the in-situ study of inclusion dissolution with the use of the LSCM will be illustrated in Chapter 5.

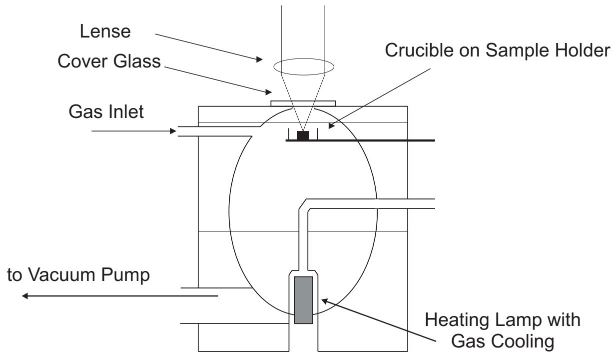

Figure 4.17: Schematic illustration of the Laser Scanning Electron Microscope with the attached high-temperature furnace [221].

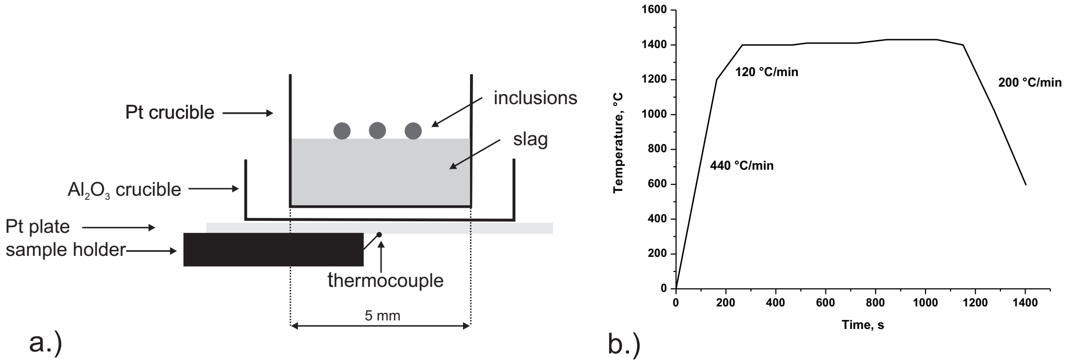

Figure 4.18: a.) Schematic illustration of sample and crucible configuration in the experiment with slag b.) Time-temperature profile used in the experiments.

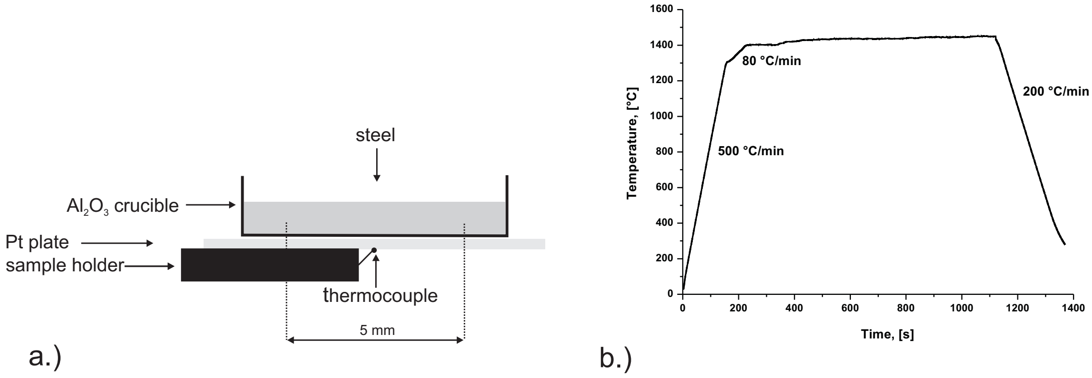

Figure 4.19: a.) Schematic illustration of sample and crucible configuration in the experiment with steel b.) Time-temperature profile used in the experiments.

5 Results and Discussion

This chapter concentrates on the results gained by experiments and calculations described in Chapter 4 concerning the modification of oxides due to steel-slag interactions. All samples from the ESR process as well as from laboratory tests have been analysed using manual and automated SEM/EDS analyses. Therefore, the representativeness of this method has been examined in Chapter 3. The findings affirm the suitability of this methods for the performed investigations and are the basis for a reliable characterisation of NMIs within the present thesis. In the course of this chapter firstly, the changes in inclusion landscape through Electroslag Remelting are explained, considering the initial state in the electrode, the procedures in the liquid film at the electrode tip as well as the behaviour of inclusions in droplets, and comparing these situations to the inclusion landscape in the remelted ingots. Only one sample position of each electrode and ingot cross section has been used for further analyses and comparisons, since the representativeness of these positions has already been investigated and confirmed in Chapter 4.

Secondly, the results of laboratory tests using the Tammann Furnace are described, focussing on the changes in chemical composition through remelting with various slags out of the systems CaO-Al_2O_3-MgO and CaO-Al_2O_3-CaF_2. Moreover, the influence of the used crucible material as well as duration time of the experiments and the applied slag amount are discussed. Details concerning the experimental set-up as well as used steel and slag compositions and test conditions were already given in the previous Chapter 4. Special attention is paid to the changes in inclusion morphology through remelting, because these modifications may permit conclusions about the history of an inclusion during remelting and therefore the decisive reaction mechanisms. The morphologies of inclusions remelted via ESR as well as in laboratory tests are analysed and compared. Moreover, the results of laboratory tests are compared to the behaviour inclusions in the ESR process as well as to thermodynamic calculations. Finally, results of the Laser Scanning Electron Microscope give insight to the dissolution behaviour of oxides in the analysed steel as well as in an applied slag composition.

5.1 Changes in Inclusion Landscape through Electroslag Remelting

As already described in the literature part (see Section 2.4), a significant decrease in the number of nonmetallic inclusions is reached through Electroslag Remelting. Figure 5.1 exemplarily demonstrates the changes of inclusion content as well as the mean ECD between electrode 2 and ingot 2. Considering all inclusion types, in this case a decrease of the overall inclusion content of over 80 % is observed. The most significant diminution is found for oxisulfides and sulfides. However, also for oxides a substantial reduction of the inclusion content of over 70 % is determined. Regarding the mean ECD before and after remelting, the most noticeable difference is observed for oxide inclusions, where the mean ECD in the ingot lies at appr. 2.5 μm compared to more than 3 μm in the electrode.

The ESR-process does not only effect a decrease of the overall inclusion content as well as a more homogeneous distribution of NMIs, but also leads to a modification of the inclusions due to reactions between steel and slag. In the following, the focus lies on the changes in chemical composition and morphology of oxide inclusions, in order to understand the decisive reaction mechanisms for inclusion

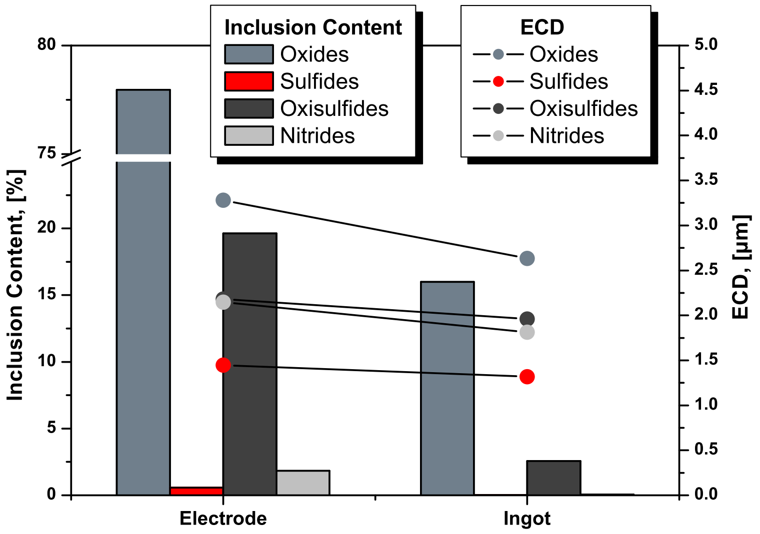

Figure 5.1: Change of inclusion content through Electroslag Remelting exemplified on a comparison between inclusions in electrode 2 and ingot 2.

modification under these conditions. Al_2O_3 and $MgOAl_2O_3$ are the two most frequent inclusion types. Consequently, especially the changes within the system CaO-Al_2O_3-MgO are examined and described, in order to better understand the formation and modification of spinel inclusions such as $MgOAl_2O_3$. Since *Ca* is strongly participating at the decisive reactions and is also known to be a preferred reaction partner with sulfur, sulfides and oxisulfides are considered in the evaluation out of this viewpoint. Nitrides will not be treated in more detail. Next to a description of the initial inclusion landscape in the electrodes, these findings are compared to the inclusions in the two ingots. Moreover, the liquid film at the electrode tip as well as the droplets are analysed. Since the representativeness of samples from the electrodes and ingots has already been investigated and proved in Chapter 4, in every case the results are only shown exemplarily for one characteristic sample. In the case of the electrodes, a sampling position at the centre was selected, for the ingots a centre sample of each cross section has been chosen.

5.1.1 Initial Inclusion State in the Electrodes

5.1.1.1 Comparison of Predominant Inclusion Types

The two electrodes have been treated differently in the melt shop. Consequently, as shown in Fig. 5.2 differences are detected regarding the inclusion types present within the system CaO-Al_2O_3-MgO: While the predominant inclusion type in electrode 1 is Al_2O_3, electrode 2 exhibits mainly $MgOAl_2O_3$ inclusions. Furthermore, a considerable amount of MgO is observed in electrode 1. Comparing the presence of complex inclusions, consisting of Al_2O_3, MgO as well as contents of CaO a slight majority of this type is detected in electrode 1. Moreover, several inclusions of the two phase system CaO-Al_2O_3 are observed in both cases, whereby the overall percentage of these inclusions is slightly higher in electrode 1 than in electrode 2.

Principally, the sulfur limit for oxide inclusions was defined with 3 *wt.-%* in the present study. This means that inclusions with an appropriate *O*-content and a *S*-content $<$ 3 *wt.-%* were treated as pure oxide inclusions, against what inclusions with a *S*-content $>$ 3 *wt.-%* in combination with the presence of a corresponding *O*-content were assigned to the group of oxisulfides. All oxides containing *Mg* and *Al* (a *Ca*-content $<$ 2 *wt.-%* provided) are ranked among the group $MgOAl_2O_3$. In equal measure, oxides

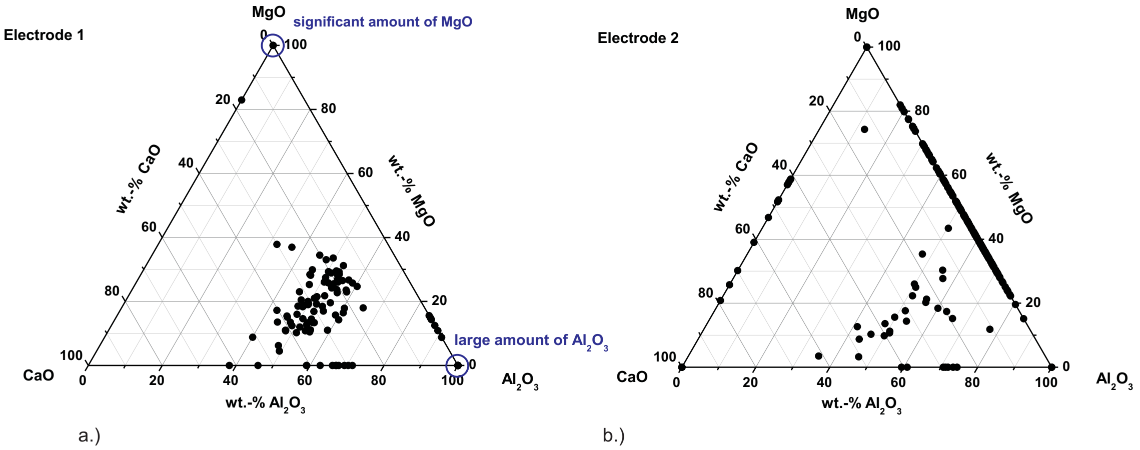

Figure 5.2: Initial compositions of oxides in the ternary system CaO-Al_2O_3-MgO in the two electrodes.

containing *Al* are classified as Al_2O_3, if the *Mg*- and *Ca*-contents were < 2 *wt.*-% each. Of course also *Si* is present in a certain number of oxides. Since this study mainly focuses on the behaviour of Al_2O_3 and $MgOAl_2O_3$, the effect and change of *Si* over the ESR process will not treated in further detail.

As stated beforehand, next to the large amount of oxides a significant number of oxisulfides was detected in the electrode samples, at which the majority is composed of *Ca*, *Mg* and *Al*. Oxisulfides containing *Mn* were hardly observed. Figure 5.3 displays the composition of these inclusions within the ternary system CaS-MgO-Al_2O_3, assuming that the available *Ca*-content primarily reacts with sulfur. Considering the detected S-level of these oxisulfides, practically no *Ca* would be available for the subsequent reaction with oxygen in this case. Comparing the compositions of oxisulfides between electrode 1 and 2 it is obvious that in electrode 2 the mean *MgO*-percentage of inclusions is higher. This is in good agreement with the composition of oxides shown in Fig. 5.2 where also an increased *MgO*-content was observed in electrode 2. Beside oxisulfides consisting of *MgO*, Al_2O_3 and *CaS*, also inclusions in the phase system CaS-Al_2O_3 were observed.

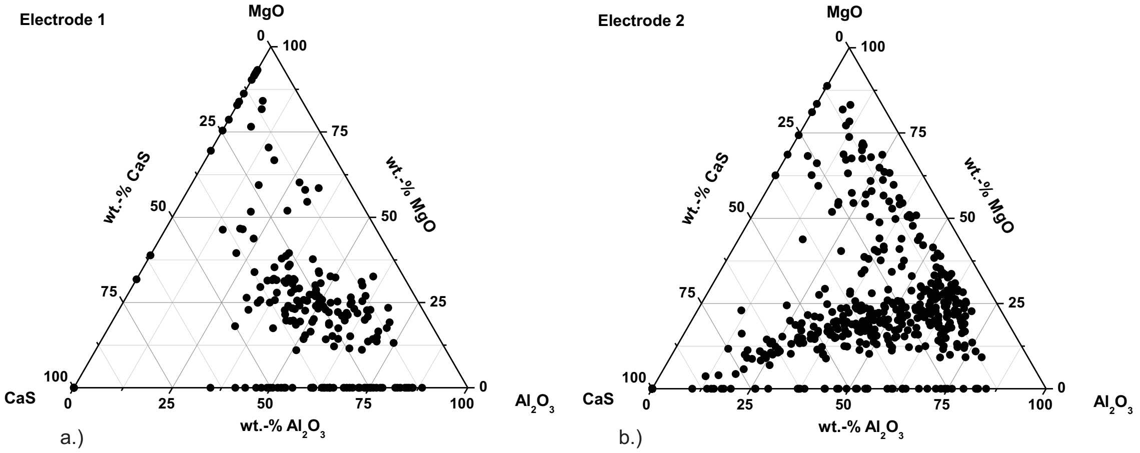

Figure 5.3: Initial compositions of oxisulfides in the ternary system CaS-Al_2O_3-MgO in the two electrodes.

Figure 5.4 illustrates the size distributions of Al_2O_3 and $MgOAl_2O_3$ in the two investigated electrodes. It is obvious that the Al_2O_3 inclusions in electrode 1 show a significantly larger mean ECD than the $MgOAl_2O_3$ in electrode 2: While the Al_2O_3 inclusions in electrode 1 are distributed between 1 – 10 μm, hardly any $MgOAl_2O_3 > 4$ µm are observed in electrode 2. In sum, the $MgOAl_2O_3$ are remarkably smaller than the Al_2O_3 inclusions in both electrodes.

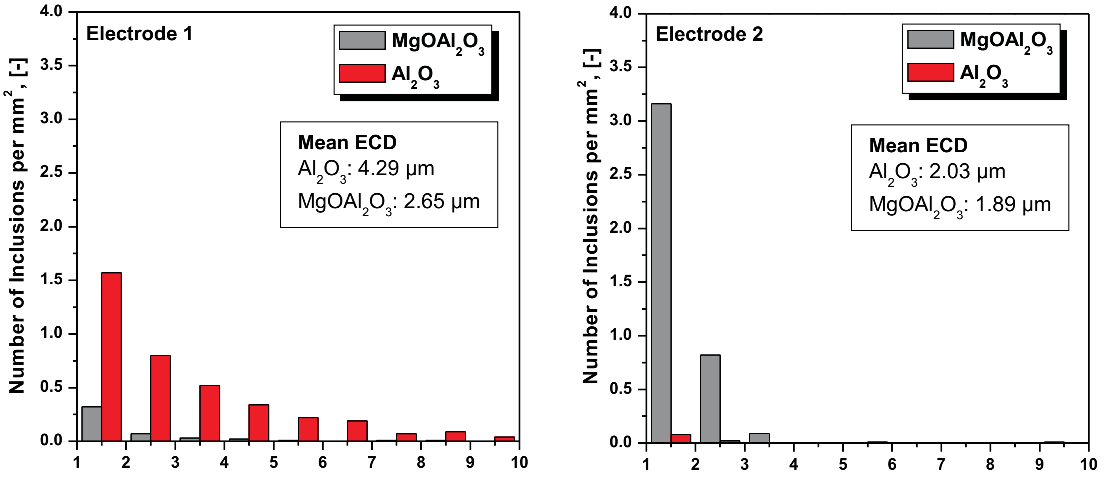

a.) b.)

Figure 5.4: Size distributions of Al_2O_3 and $MgOAl_2O_3$ in the two electrodes.

Comparing the inclusion types detected with automated SEM/EDS analyses with the results of thermodynamic calculations with *FactSage* (see Fig. 5.5), a good accordance can be noticed as far as the presence of $MgOAl_2O_3$ in electrode 2 as well as the formation of CaS in both cases is concerned. But, in both calculated cases, the primarily formed oxide is $CaAl_2O_4$. Although some of these inclusions have been detected analytically in both electrodes, the calculation results does not really reflect the analytic examinations in this case. Since nearly all available Al is used for the formation of $CaAl_2O_4$, the calculation does not yield a stable Al_2O_3 phase.

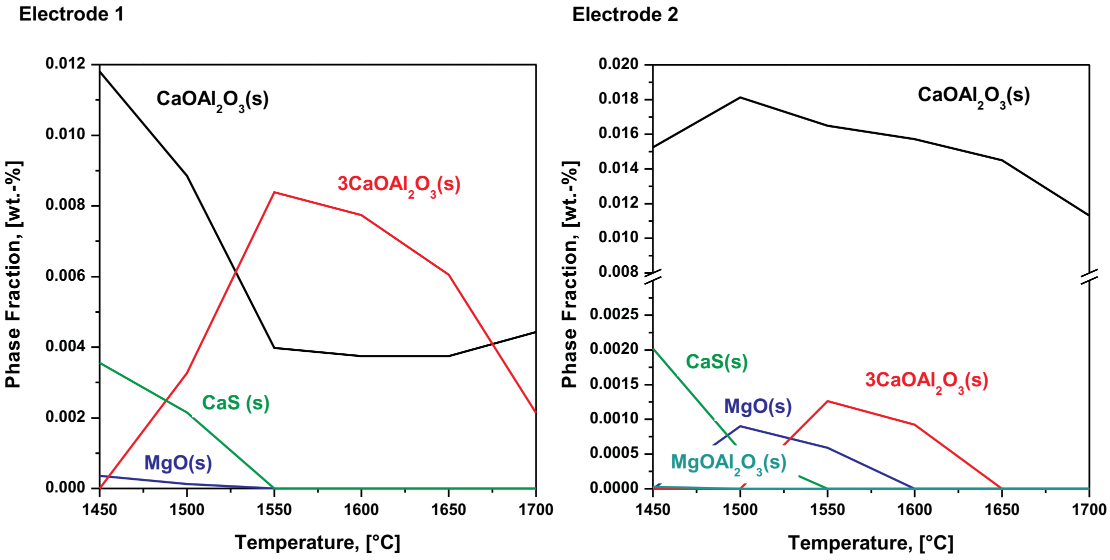

a.) b.)

Figure 5.5: Results of thermodynamic calculations with *FactSage* for the stable phases in the two electrode compositions.

In order to follow up this discrepancy, the influence of *Ca*-concentration in the electrode on the Al_2O_3 activity was calculated. The result is given in Fig. 5.6. The *Ca*-concentration measured via ICP-MS is comparable for both electrodes and lies at appr. 50 *ppm*. Under consideration of the calculation result for 1600 °C, it can be seen that under the assumption that all *Ca* would react with *O*, not until a *Ca*-concentration of $<$ 10 *ppm* the activity of Al_2O_3 becomes 1. Taking additionally the formation of *CaS* into account will change this value towards a slightly higher *Ca*-concentration. However, this fact also excludes possible measurement errors, since this difference substantially exceeds the detection limit of ICP-MS (which lies in the range of a few *ppm*). Even though a total accordance cannot be expected due to the assumption of equilibrium conditions in the calculations as well as due to disregarded kinetic aspects, this difference is not negligible and the sensitivity of *FactSage* calculations to *Ca*-concentrations must be kept in mind.

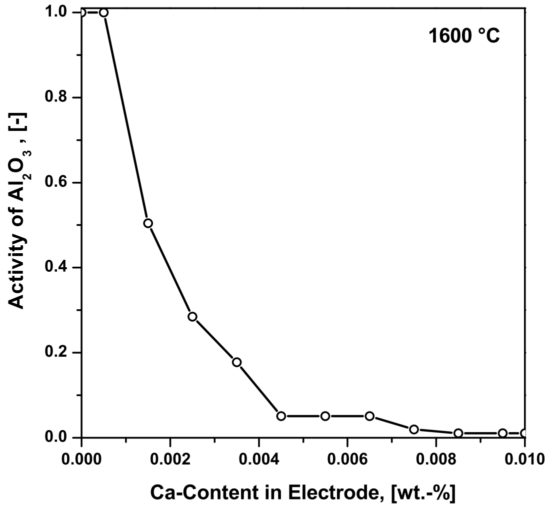

Figure 5.6: Activity of Al_2O_3 in the X38CrMoV5-1 as a function of the *Ca*-content in the electrode calculated with *FactSage*.

Furthermore, although the two analysed electrodes offer different contents of *Al* and *Mg*, regarding the detected inclusion types, both combinations should in fact lie in the stability range of $MgOAl_2O_3$, even if one electrode has a significantly higher percentage of $MgOAl_2O_3$ than the other one. As already described in Chapter 2, varying stability ranged for this inclusion type are found in literature [21, 29]. Figure 5.7 illustrates the calculation result for the stability range of $MgOAl_2O_3$ pertaining to the composition of X38CrMoV5-1 using thermodynamic data from literature (see Chapter 4). While one of the electrodes would not lie in the $MgOAl_2O_3$ stability range without considering the interaction parameters of alloying elements—which shows a good agreement to the stability diagram published by Itoh *et al.* [21]—, both electrodes are situated within this range when taking these interactions into account which cause a shift to lower *Al*-contents.

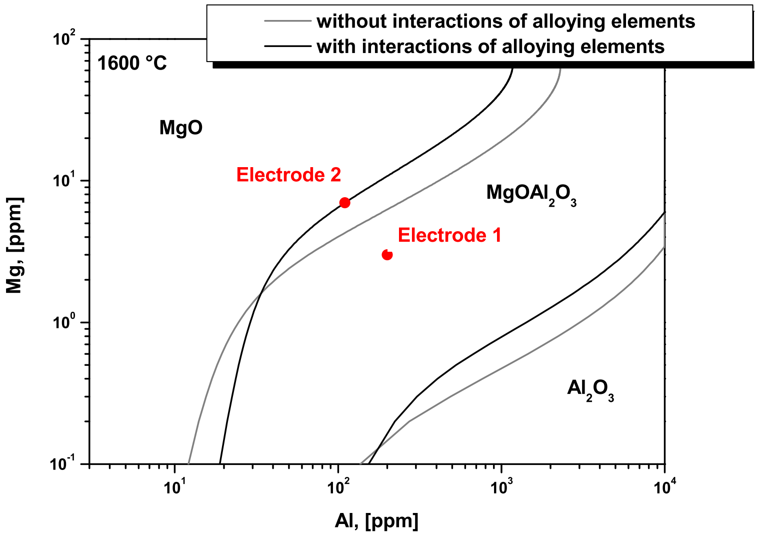

Figure 5.7: Calculated stability diagram of $MgOAl_2O_3$ on the basis of literature data.

5.1.2 Procedures in the Liquid Film at the Electrode Tip

The electrode/slag interface is supposed to be the controlling reaction site in the ESR process by a couple of researchers [126, 131, 132] due to the comparatively high temperature as well as the significantly longer dwell time of inclusions. However, there is no consistent opinion as far as the thickness of the liquid film at this reaction site is concerned. The microstructure of several positions of the residual electrodes has been examined in the course of this study. Depending on the used remelting parameters in the final phase of the process, different shapes of the bottom end of the electrodes were observed, from rather waved to almost linear. Despite certain differences in external appearance, the determined film thickness was comparable in all cases. Figure 5.8 shows one representative section of the bottom end of an analysed residual electrode. Referring to the orientation of dendrites at the bottom end, a characteristic re-solidified range of about 500 µm is observed. These values are in-between the thicknesses stated by other authors [133, 139]. A meaningful detailed comparison is rather difficult, because the thickness is strongly influenced by electrode dimensions as well as steel and slag compositions. Nevertheless, an important statement can be proved by these investigations, since all thicknesses between 100 – 1000 µm provide a significant higher dwell time for inclusions in the film than in the droplets. In the course of droplet formation the profile of the electrode tip changes in microscopic scale. Figure 5.9 shows a position at the electrode tip shortly before droplet detachment. The metal collects in order to form a droplet; consequently the liquid range is enlarged in comparison to Fig. 5.8.

Since Al_2O_3 and $MgOAl_2O_4$ are the predominant inclusion types in the electrodes, their dissolution time in X38CrMoV5-1 has been calculated using an approach by Hong and Debroy [215] (see Chapter 4). This information provides important knowledge regarding the modification of inclusions due to remelting as well as concerning the appreciation of the decisive metal/slag reaction site in the ESR process. Comparing the results in Fig. 5.10 shows that basically—assuming an equal initial ECD and a temperature of 1600 °C—Al_2O_3 is dissolved much faster in electrode material than $MgOAl_2O_3$. Then again, the performed automated SEM/EDS analyses of the electrodes indicated a significantly higher mean ECD of Al_2O_3 than of $MgOAl_2O_3$ inclusions. However, even when considering these differences in initial ECD, an Al_2O_3 inclusion (assuming a mean ECD of 4 µm) dissolves nearly twice as fast as a $MgOAl_2O_3$ with a mean ECD of 2 µm.

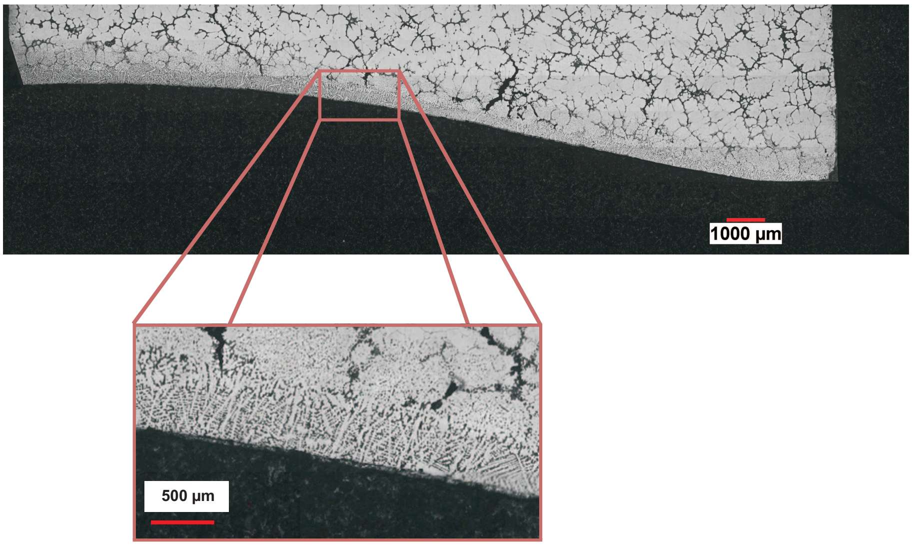

Figure 5.8: Image of microstructure at the bottom end of the electrode (etched with chromic acid).

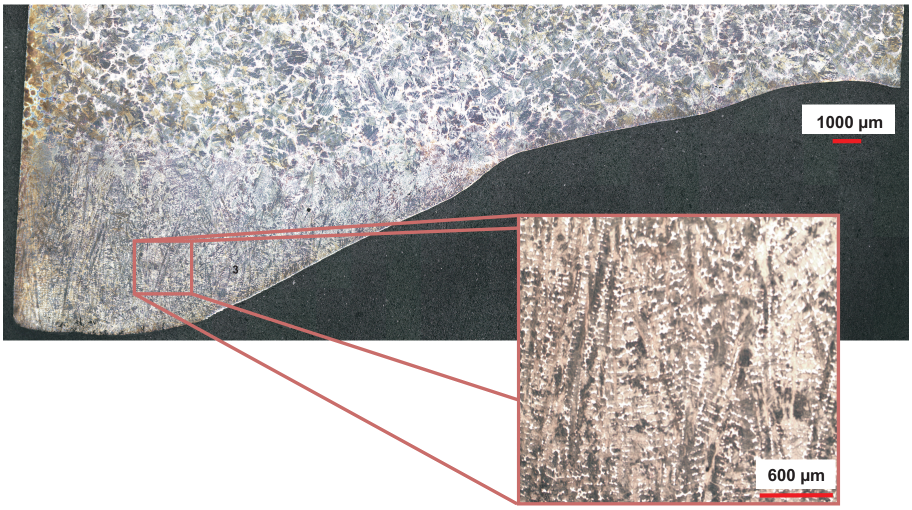

Figure 5.9: Image of microstructure at the bottom end of the electrode, beginning of droplet formation (etched with Beraha II).

Table 5.1 summarises the percentaged distribution of inclusion sizes of Al_2O_3 and $MgOAl_2O_3$ between 1 – 10 µm for the two examined electrodes. It can be seen that while the majority of $MgOAl_2O_3$ inclusions in both electrodes is smaller than 2 µm, the percentage of Al_2O_3 > 4 µm is remarkably increased, primarily in electrode 1. Under the assumption of this initial conditions the dissolution rates for both inclusion types were calculated for different estimated dwell times of NMIs in the liquid film. The results given in Tab. 5.2 clarify the significance of the initial inclusion types in the electrode regarding the final inclusion landscape in the ingot: Assuming an available dwell time of 20 s, 75 % of Al_2O_3 inclusion would be dissolved (although their mean ECD is considerably larger), while virtually the time would not be sufficient to dissolve any $MgOAl_2O_3$. Moreover, already after a dwell time of 5 s, all Al_2O_3 inclusions < 2 µm would have dissolved.

For all calculations shown in Fig. 5.10, a final ECD of 0.002 µm was assumed as a lower limit for complete dissolution of the particle. In order to evaluate the sensitivity of the calculations on the chosen final ECD, additional calculations have been performed.

Table 5.1: Percentaged distribution of inclusion sizes between 1 – 10 μm for electrodes 1 and 2.

	Electrode 1		Electrode 2	
Size class	Al_2O_3	$MgOAl_2O_3$	Al_2O_3	$MgOAl_2O_3$
< 2 μm	41 %	68 %	72 %	77 %
2 – 4 μm	34 %	21 %	18 %	23 %
> 4 – 10 μm	25 %	11 %	10 %	0 %

Table 5.2: Comparison of percentaged dissolution rates for Al_2O_3 and $MgOAl_2O_3$ in dependence of the available dwell time in the liquid film and the inclusion sizes for electrodes 1 and 2 at 1600 °C.

	Electrode 1		Electrode 2	
Dwell time of NMI in the liquid film	Dissolved Al_2O_3	Dissolved $MgOAl_2O_3$	Dissolved Al_2O_3	Dissolved $MgOAl_2O_3$
5 s	41 %	0 %	72 %	0 %
10 s	75 %	0 %	90 %	0 %
20 s	75 %	0 %	90 %	0 %
50 s	100 %	68 %	100 %	77 %
100 s	100 %	89 %	100 %	100 %

As demonstrated in Fig. 5.11a no significant influence of the final ECD (as long as it is smaller than 1 μm) can be observed for small particles. Nonetheless, since the available time might not be sufficient in the liquid electrode film for a complete dissolution of inclusions with an ECD > 10 μm, also the time for a certain reduction of ECD was in the focus of interest. It can be seen in Fig. 5.11b and c that the dissolution time obviously increases with increasing initial ECD and that the reduction of a 40 μm Al_2O_3 inclusion to half its size at 1600 °C would take longer than 500 s. Consequently, the complete dissolution of meso- and macro-inclusions in the liquid film seems to be practically impossible. The only way to remove such large inclusions is for them to get into contact with the slag.

The formation of Ca-containing oxides seems to be closely related with the desulfurisation at this steel/slag interface. Fig. 5.13 summarises the change of inclusion types between the initial electrode and the liquid film at the electrode tip and the related chemical reactions. As the amount of oxisulfides significantly decreases between the initial electrode state and the liquid film, the dissolution of CaS is assumed. The dissolved Ca is supplied to the melt, the Ca-activity in liquid steel increases and CaO can form. Al_2O_3 dissolves, and the dissolved Al can subsequently react with Ca or CaO to form $CaOAl_2O_3$. The dissolution of $MgOAl_2O_3$ is comparably marginal, which is in good agreement with the kinetic considerations. Not only the microstructure of the electrode tip was studied, but also SEM/EDS analyses were used in order to investigate which inclusions are present in this region. Since the electrode tip of residual electrodes out of the ESR process gets in contact with air during the withdrawal from the slag, which might result in a modification of inclusions originally existent in the electrode tip as well as scale formation, electrodes from the PESR process (which is done under protective atmosphere) have been used for the purpose of comparison. The analyses of both—residual electrodes from ESR as well as PESR—showed the same results. The predominant inclusion types in this region are CaO and $CaOAl_2O_3$. A SEM-image of an inclusion at the bottom end of a residual electrode as well as the corresponding EDS spectrum is exemplarily shown in Fig. 5.12. Only a little fraction of pure Al_2O_3 inclusions has been detected. Since these Ca-containing inclusions are rather small, have a quite globular shape and are definitely located in the re-solidified region, they are supposed to have been freshly formed in the liquid film.

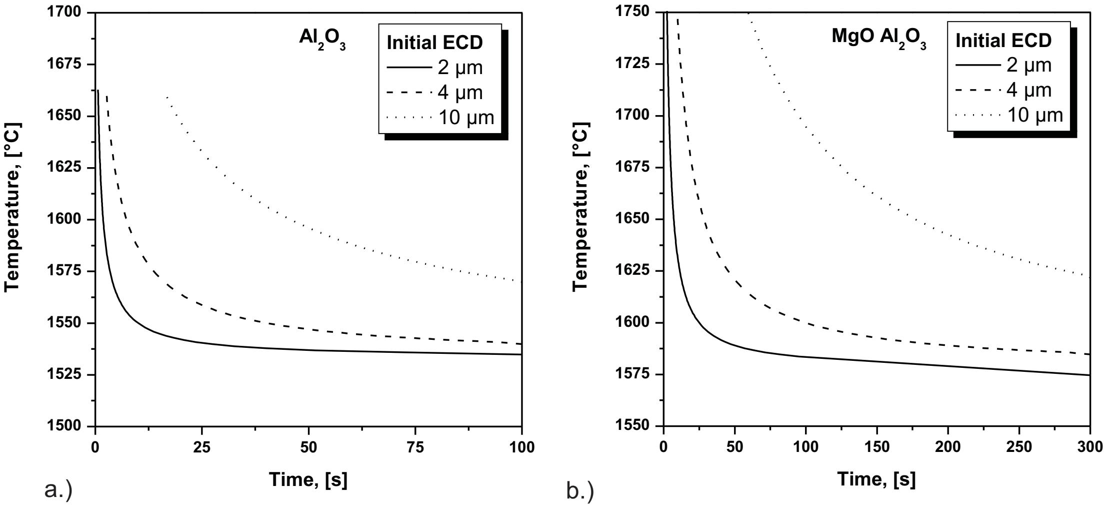

Figure 5.10: Comparison of dissolution times of a.) Al_2O_3 and b.) $MgOAl_2O_3$ in X38CrMoV5-1 for different initial ECDs.

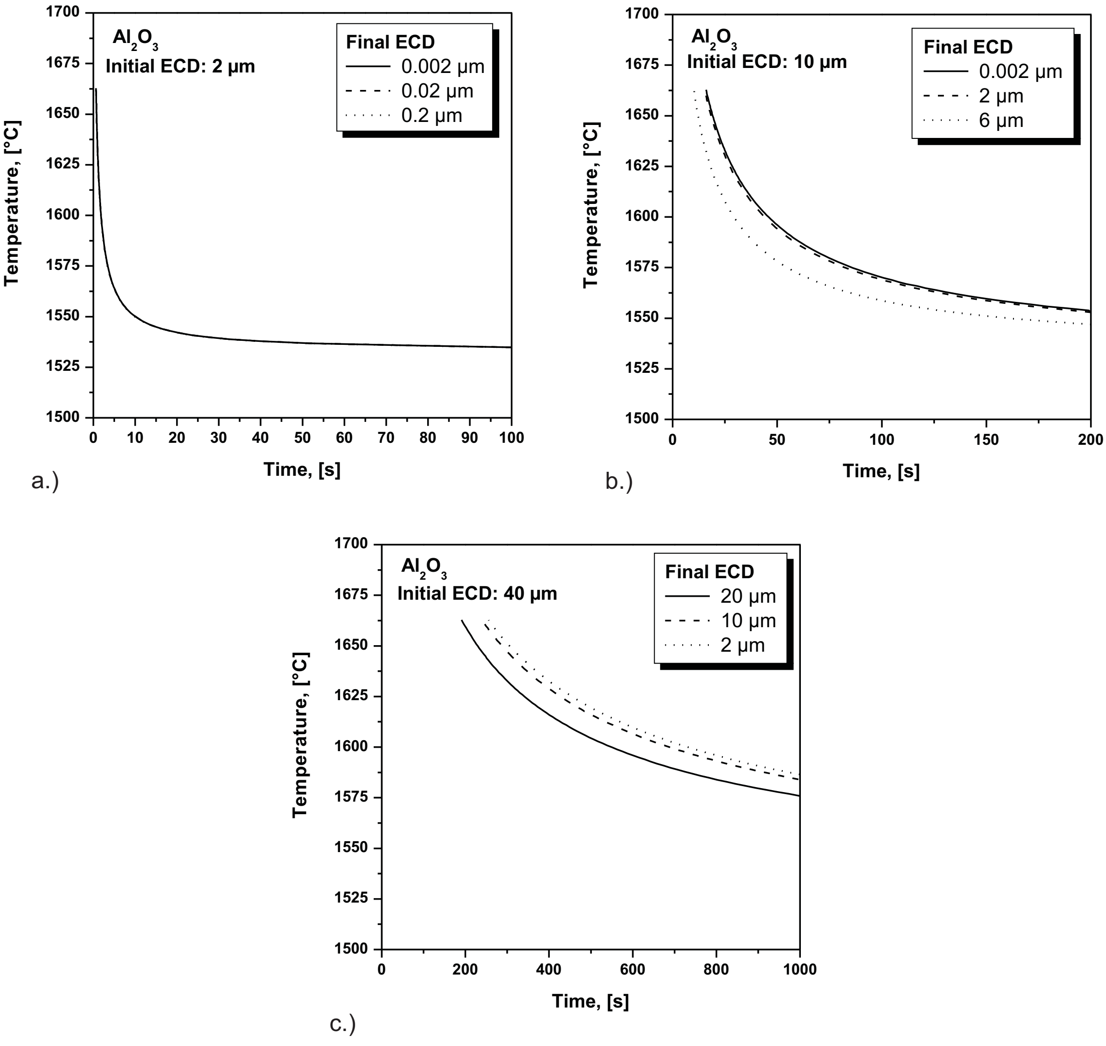

Figure 5.11: Comparison of dissolution time of Al_2O_3 in dependence of the final ECD for varying initial ECDs.

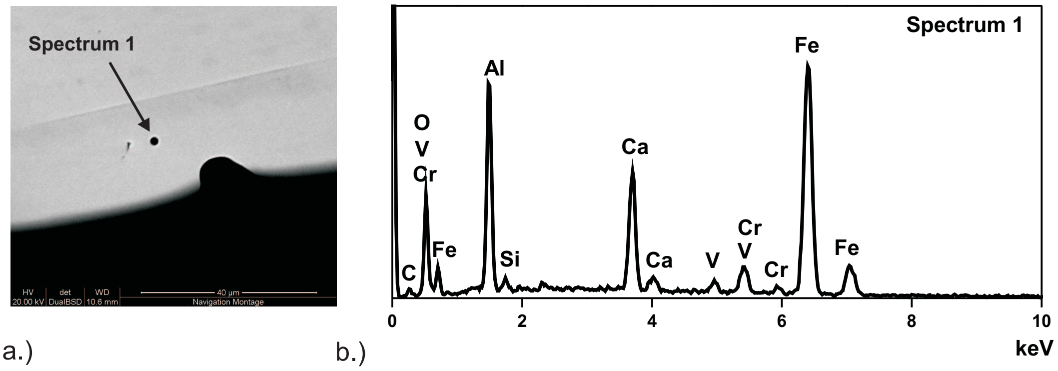

a.) b.)

Figure 5.12: a.) SEM-image of an inclusion at the bottom end of a residual electrode and b.) the corresponding EDS spectrum

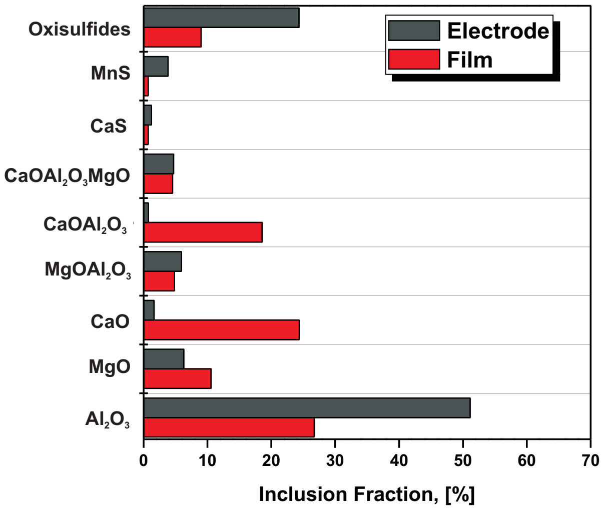

Essential Reactions:

$\langle MgOAl_2O_3CaS\rangle \longrightarrow \langle MgOAl_2O_3\rangle + [Ca]+[S]$

$\langle Al_2O_3CaS\rangle \longrightarrow \langle Al_2O_3\rangle + [Ca]+[S]$

$\langle Al_2O_3\rangle \longrightarrow 2[Al]+3[O]$

$\langle MgOAl_2O_3\rangle \longrightarrow [Mg]+2[Al]+4[O]$

$\langle CaS\rangle \longrightarrow [Ca]+[S]$

$[Ca]+[O] \longrightarrow \langle CaO\rangle$

$[Ca]+4[O]+2[Al] \longrightarrow \langle CaOAl_2O_3\rangle$

$[S]+(O^{2-}) \longrightarrow [O]+(S^{2-})$

$2(S^{2-})+3\{O_2\} \longrightarrow 2\{SO_2\}+2[O]$

Figure 5.13: Overview on the change of inclusion type distribution between initial electrode state and liquid film at the electrode tip (exemplified for electrode 1) with the related chemical reactions.

5.1.3 Procedures during the Falling of the Droplet through the Slag

A typical droplet, taken from the tip of the residual electrode 1 just before detachment, is illustrated in Fig. 5.14. Comparing this droplet size with values of mathematical models for the calculation of droplet size [140–144] a good agreement is achieved. Although it must be kept in mind that this droplet size does not necessarily represent the absolute size of droplets falling through the slag, because the withdrawal of the electrode from the slag may influence the droplet geometry, a reference value is gained for the estimation of dwell time of inclusions.

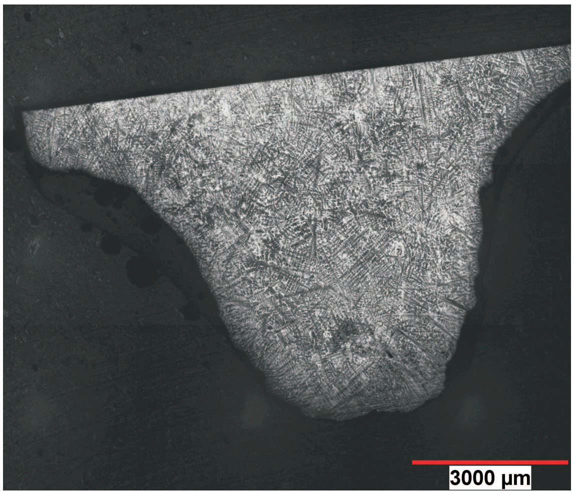

Figure 5.14: SEM-image of a droplet formed at the bottom of the residual electrode 1 (etched according to Kane).

Comparing this droplet size with the thickness of the liquid film stated in the last subsection, the most common idea published in literature [126, 131, 132] that the electrode/slag interface is more decisive than the droplet/slag interface, is affirmed. This idea is further approved when regarding the changes in size distribution of oxides from electrode to droplet and to the final ingot shown in Fig. 5.15. Comparing the three size distributions, it is obvious that the one of the droplet is already very similar to the one of the remelted ingot and that their mean ECD is significantly lower than for the electrode distribution. Consequently, a large percentage of inclusions coming from the electrode should already have been dissolved or removed at the electrode/slag interface in this case. An interesting detail is the slight increase of oxides between electrode and ingot which might be an indication for the precipitation of new inclusions in the mushy zone.

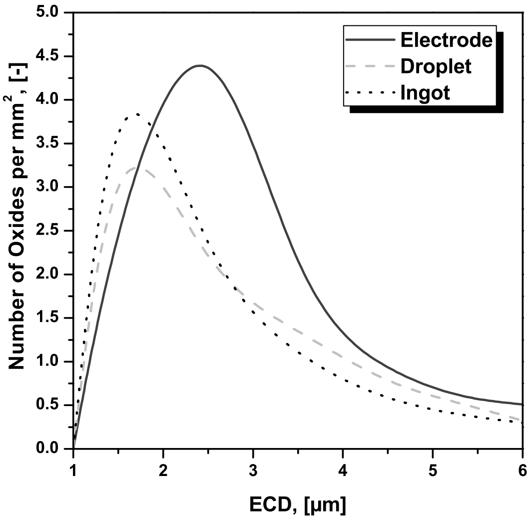

Figure 5.15: Comparison of size distributions of oxides between 1 – 6 µm in the electrode 1, the droplet and the remelted ingot 1.

Regarding the droplet tip in Fig. 5.16, the position of non-metallic inclusions inside the droplet can be analysed in more detail. It is shown that the majority of inclusions is located at the boundaries of the droplet; the number of inclusions detected in the centre region of the droplet is significantly lower. As far as the detected inclusion types are concerned, the shape and composition of inclusions in the boundary region is very similar to inclusions in the bottom end of the electrode, while inclusions in the centre tend to be remarkably larger. Figure 5.17 shows a SEM-image and the corresponding EDS spectrum of an inclusion from the centre of the droplet shown in Figure 5.16. Figure 5.18 exemplifies an inclusion in the boundary area of the same droplet. While the latter looks very similar to the one shown in Fig. 5.12, the first is significantly larger and also shows some differences regarding its chemical composition. Consequently, it is supposed to be an inclusion which already existed in the electrode that has neither come in contact with slag nor has enough time to dissolve.

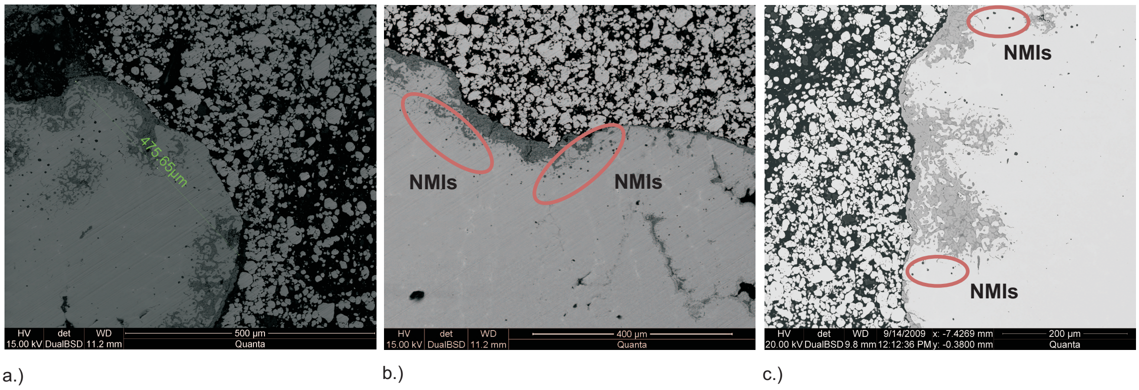

Figure 5.16: SEM-images of a droplet in electrode 2 showing a.) the droplet tip as well as the position of inclusions in the droplet in b.) and c.).

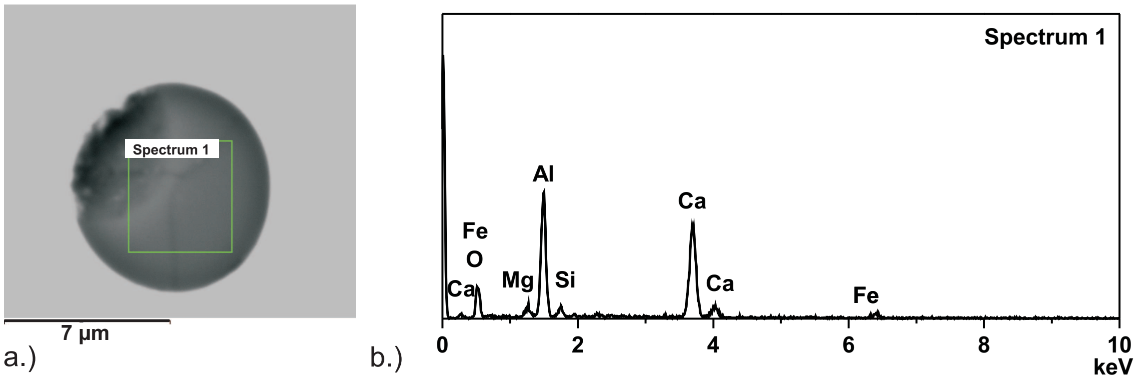

Figure 5.17: a.) SEM-image of inclusion in the centre of the droplet and b.) corresponding EDS spectrum.

Calculation results of *FactSage* show that once an inclusion gets in contact with the slag, it is dissolved completely in the slag. Figure 5.19 exemplarily demonstrates the increase of phase fraction of liquid slag components caused by an addition of solid fraction at 1600 °C. Solid fraction in this context means the sum of stable oxide inclusion phases calculated for the two different electrode conditions (shown in Fig. 5.5). So, assuming only the theoretically possible case that all inclusions from the electrode get in contact with the slag phase, all of them would be gathered and dissolved in the slag.

Figure 5.20 summarises the described procedures at the droplet/slag interface. As already observed at the electrode/slag interface, the percentage of oxisulfides as well as Al_2O_3 of the overall amount of considered inclusions is smaller compared to the initial electrode state, although the change of the latter between film and droplet is by far not so distinct. Consequently, a significant dissolution and removal of inclusions is already attributed to the electrode/slag interface. At the droplet/slag interface, the percentage of $CaOAl_2O_3$ is further increased due to the reaction of Ca with dissolved Al. Next to the desulfurisation reaction, also the slag may act as a Ca-supplier for the formation of $CaOAl_2O_3$. Additionally, new $MgOAl_2O_3$ can be formed due to the reaction of MgO or Mg with dissolved Al and O based on the reaction with slag components.

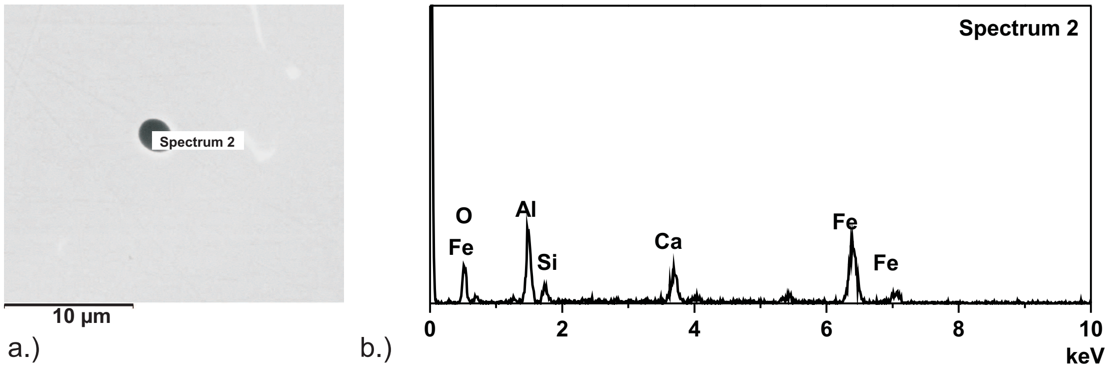

a.) b.)

Figure 5.18: a.) SEM-image of inclusion in the boundary region of the droplet and b.) corresponding EDS spectrum.

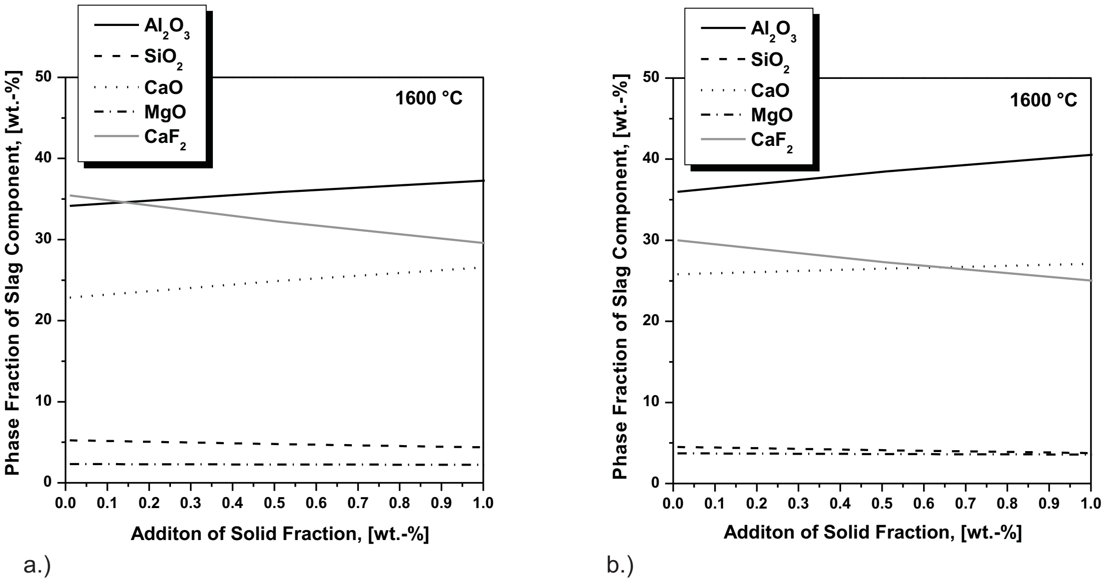

a.) b.)

Figure 5.19: Increase of phase fraction of slag components through the dissolution of inclusions in the slag: a.) Inclusion phases from electrode 1 and b.) Inclusion phases from electrode 2.

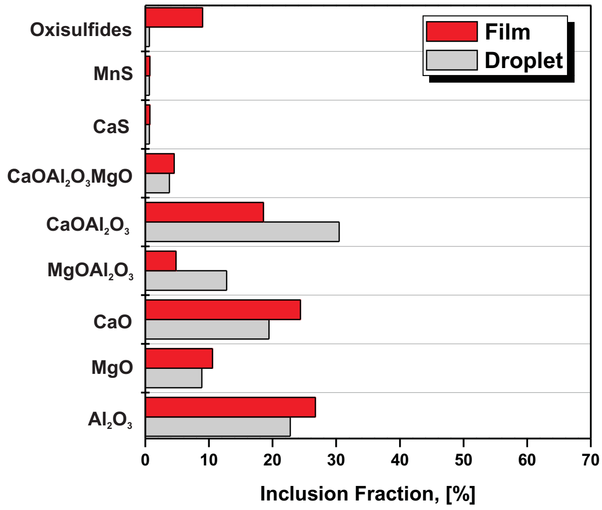

Essential Reactions:

$\langle MgOAl_2O_3CaS\rangle \longrightarrow \langle MgOAl_2O_3\rangle + [Ca]+[S]$

$\langle Al_2O_3CaS\rangle \longrightarrow \langle Al_2O_3\rangle + [Ca]+[S]$

$\langle MgO\rangle+2[Al]+3[O] \longrightarrow \langle MgOAl_2O_3\rangle$

$[Mg]+2[Al]+4[O] \longrightarrow \langle MgOAl_2O_3\rangle$

$[Ca]+4[O]+2[Al] \longrightarrow \langle CaOAl_2O_3\rangle$

$\langle CaO\rangle+3[O]+2[Al] \longrightarrow \langle CaOAl_2O_3\rangle$

$[S]+(O^{2-}) \longrightarrow [O]+(S^{2-})$

$2(S^{2-})+3\{O_2\} \longrightarrow 2\{SO_2\}+2[O]$

Figure 5.20: Overview of the change of inclusion type distribution between the liquid film at the electrode tip and the droplet (exemplified for electrode 1) with the related chemical reactions.

5.1.4 Inclusion Landscape in the Remelted Ingots

Substantial differences are found when comparing the inclusion landscape in the remelted ingots with that of the initial electrodes. The predominant inclusion type in both ingots is $MgOAl_2O_3$ in contrast to the electrode conditions, where electrode 1 was mainly dominated by pure Al_2O_3. The composition of NMIs within the ternary system CaO-Al_2O_3-MgO is shown in Figs. 5.21 and 5.22; each for two different cross sections: Cross section B from the bottom area of the remelted ingot and cross section M from the medium ingot height. It is obvious that the composition of NMIs in the two remelted ingots is relatively similar, although the original states before remelting were very different. Moreover, a higher consistency with regards to their composition within the ternary system CaO-Al_2O_3-MgO is noticed after Electroslag Remelting. In both cases, most of the inclusions are situated in two phase system MgO-Al_2O_3, shifted to slightly higher contents of MgO in the case of ingot 2. Differences between the two ingots are observed concerning inclusions within the two phase system CaO-Al_2O_3; the detected percentage of these inclusions is raised in ingot 1.

Regarding the two cross sections of ingot 1 and 2, a considerable shift of inclusions towards the *Al*-rich corner within the ternary system CaO-Al_2O_3-MgO is observed between the bottom and the medium ingot height. This is the result of a slightly increasing Al_2O_3-content of the slag over the process due to continuous deoxidation. Thus, it can be said that already small changes in slag composition can significantly influence the final inclusion landscape in the ingot.

When comparing the experimental results to calculations with *FactSage* a good concordance is observed. Fig. 5.23 summarises the results of thermodynamic calculations for the two ingots. The primarily predicted inclusion type for both ingots is $MgOAl_2O_3$, together with some percentages of Al_2O_3 and $CaO2MgO8Al_2O_3$. It must be mentioned that these calculations assume that all inclusions from the electrode are dissolved in the slag and therefore do not consider the possible survival of inclusions from the electrode to the ingot. The results only show the stable inclusion phases according to *FactSage* for the instant steel compositions in the ingot and also consider the change in *Al*, *Mg*, *Ca* and *O* concentration due to the reaction between steel and slag.

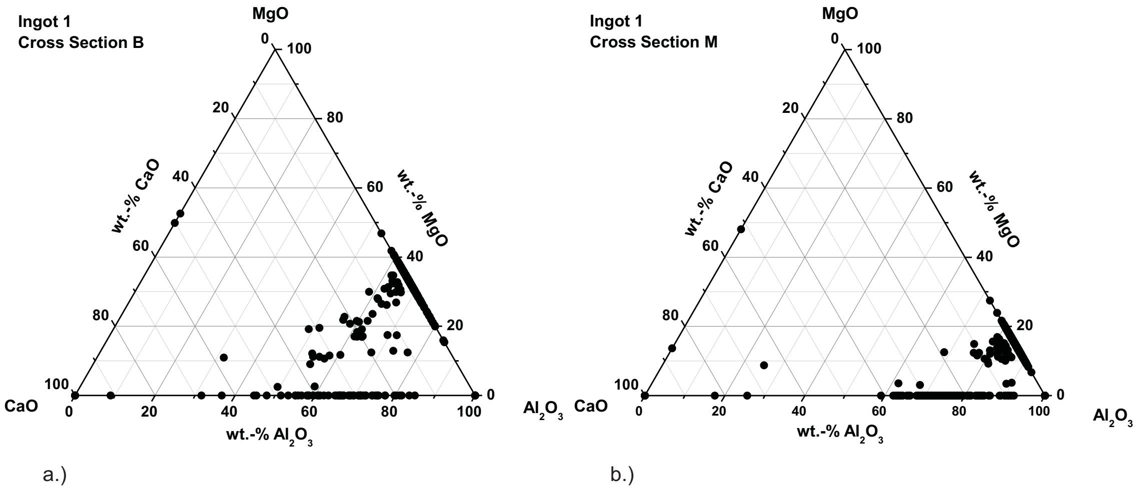

a.)

b.)

Figure 5.21: Compositions of NMIs in the ternary system *CaO-Al_2O_3-MgO* in the remelted ingot 1: a.) on the cross section B and b.) on the cross section M.

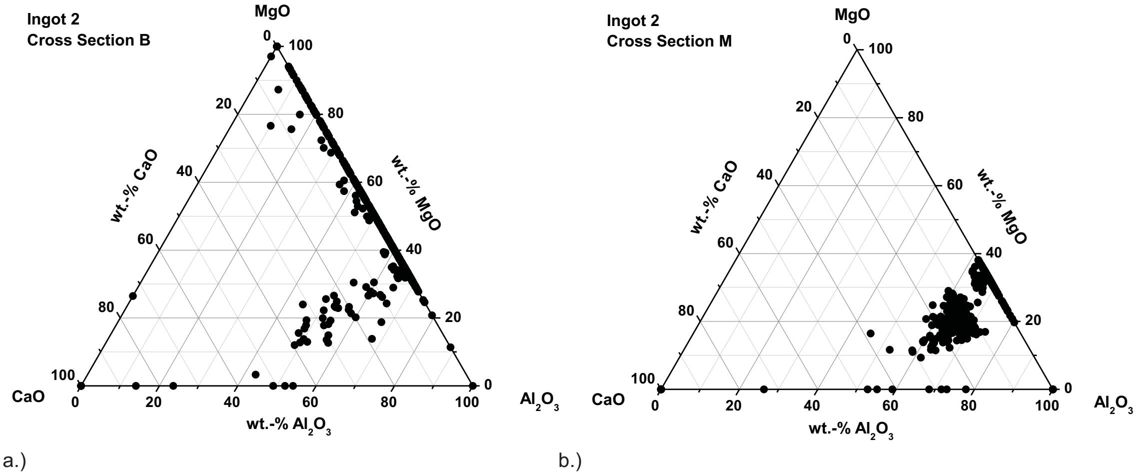

a.)

b.)

Figure 5.22: Compositions of NMIs in the ternary system *CaO-Al_2O_3-MgO* in the remelted ingot 2: a.) on the cross section B and b.) on the cross section M.

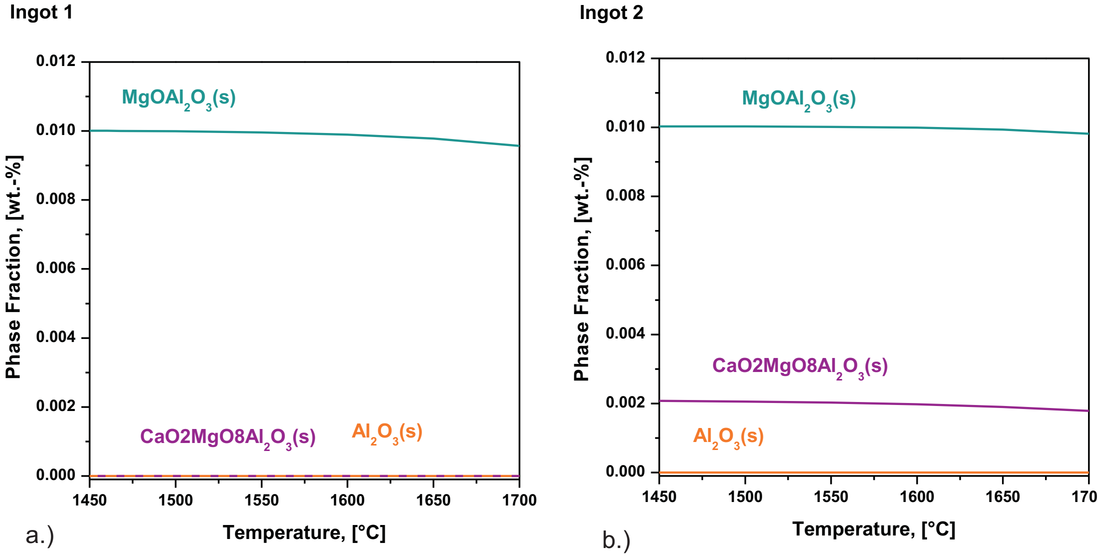

a.)

b.)

Figure 5.23: Results of thermodynamic calculations with *FactSage* for the stable inclusion phases in the two remelted ingots.

Figures 5.24 and 5.25 demonstrate the size distributions of Al_2O_3 and $MgOAl_2O_3$ in ingot 1 and 2 for two different cross sections of the ingot heights. In the case of ingot 1—illustrated in Fig. 5.24—a remarkable decrease of the mean ECD of Al_2O_3 is noticed in comparison to the electrode. Nevertheless, the remaining Al_2O_3 are considerably larger than the detected $MgOAl_2O_3$ in cross section B. Comparing both cross sections a significant increase of the mean ECD of $MgOAl_2O_3$ is observed with increasing ingot height, resulting in a mean ECD of > 3 µm in the medium area. In fact, the mean ECD of $MgOAl_2O_3$ inclusions in ingot 1 is slightly higher than in the corresponding electrode. Regarding the size distributions of Al_2O_3 and $MgOAl_2O_3$ in ingot 2 shown in Fig. 5.25 similar results as for ingot 1 are obtained: In the bottom area the mean ECD of $MgOAl_2O_3$ is lower than of Al_2O_3, but considerably rising with increasing ingot height. Al_2O_3 inclusions in ingot 2 tend to be smaller than in ingot 1.

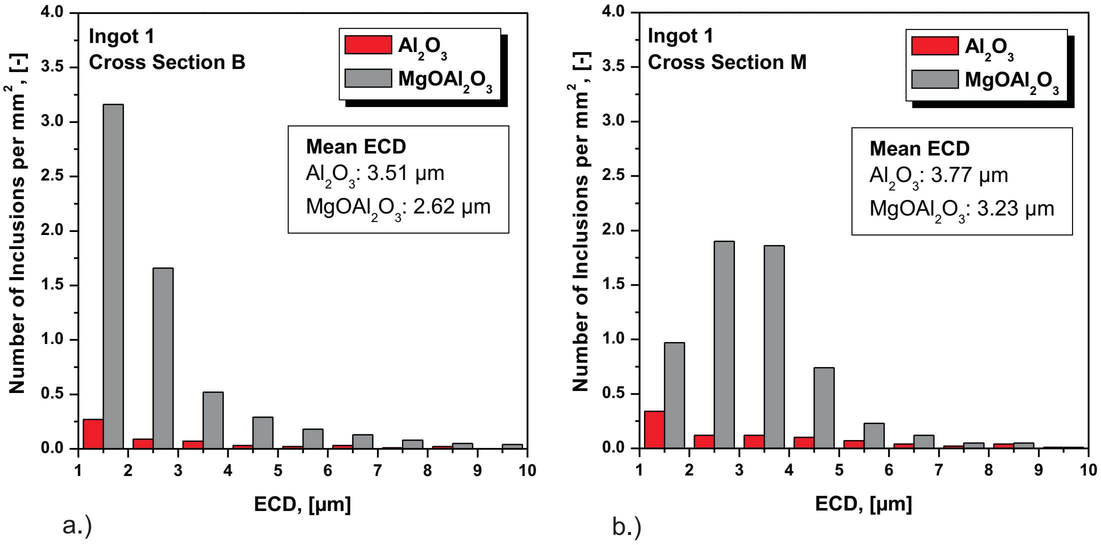

Figure 5.24: Size distributions of Al_2O_3 and $MgOAl_2O_3$ in ingot 1: a.) on the cross section B and b.) on the cross section M.

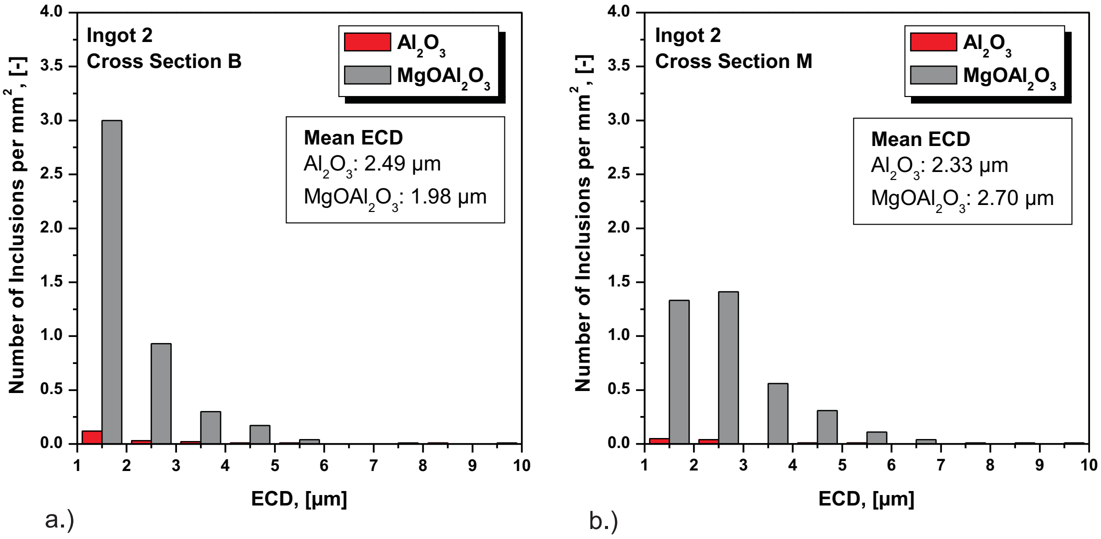

Figure 5.25: Size distributions of Al_2O_3 and $MgOAl_2O_3$ in ingot 2: a.) on the cross section B and b.) on the cross section M.

The essential changes in inclusion landscape between the droplet and the ingot are illustrated in Fig. 5.26. Next to an increase of oxisulfides due to solidification, primarily the percentage of $MgOAl_2O_3$ increases significantly. The latter is related to reactions at the pool/slag interface which are also summarised in Fig. 5.26.

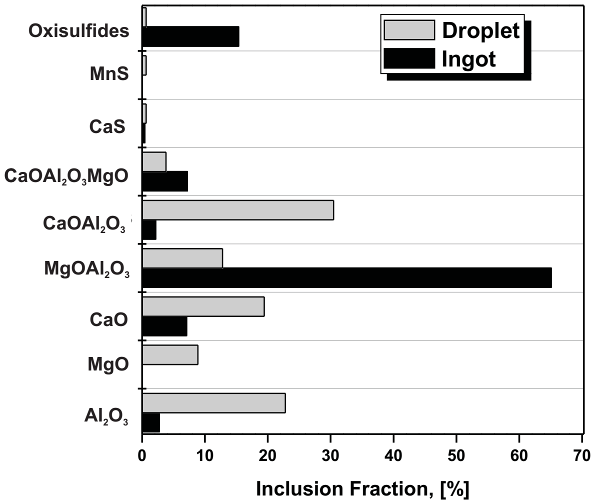

Essential Reactions:

$\langle MgO\rangle + 2[Al] + 3[O] \longrightarrow \langle MgOAl_2O_3\rangle$

$[Mg] + 4[O] + 2[Al] \longrightarrow \langle MgOAl_2O_3\rangle$

$\langle MgO\rangle + [Ca] + 4[O] + 2[Al] \longrightarrow \langle CaOAl_2O_3MgO\rangle$

$[Mg] + [Ca] + 5[O] + 2[Al] \longrightarrow \langle CaOAl_2O_3MgO\rangle$

$\langle MgOAl_2O_3\rangle + [S] + [Ca] \longrightarrow \langle MgOAl_2O_3CaS\rangle$

Figure 5.26: Overview on the change of inclusion type distribution between the droplet and the ingot (exemplified for electrode 1) with the related chemical reactions.

5.1.5 Modification of Inclusion Morphology

So far, mostly the chemical composition as well as the mean ECDs of the detected inclusions were in the focus of interest. In order to characterise the modification of NMIs in greater detail, also the morphology of inclusions is an important aspect. Figure 5.27 exemplarily shows three SEM-images of typical inclusions in the two electrodes. While Al_2O_3 and $MgOAl_2O_3$ have a rather globular shape, MgO inclusions are polygonal. This difference in morphology has also been proven using electrolytic extraction offering a three-dimensional view on the inclusions. Figure 5.28 shows SEM-images of inclusions on the filter after extraction from the matrix of electrode 1.

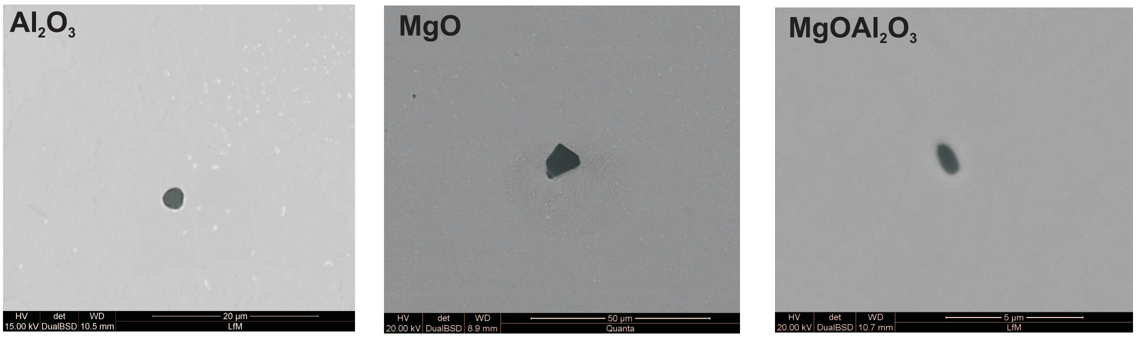

a.) b.) c.)

Figure 5.27: Typical oxide inclusions in electrodes: a.) Al_2O_3 in electrode 1, b). MgO in electrode 1 and c.) $MgOAl_2O_3$ in electrode 2.

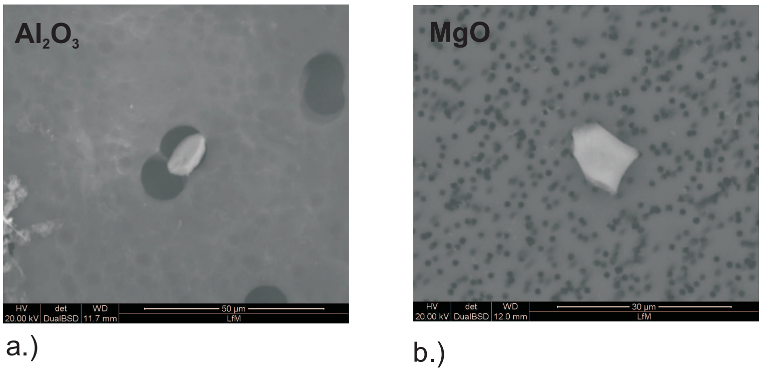

a.) b.)

Figure 5.28: Typical oxide inclusions in electrode 1 on the filter after electrolytic extraction (dark areas are filter porosities).

The comparison between the inclusion landscape in the electrodes and in the ingots showed a comparable modification of inclusion composition within the system $CaO\text{-}Al_2O_3\text{-}MgO$—despite the different initial conditions. The majority of inclusions is situated in the two phase region $Al_2O_3\text{-}MgO$ in both cases and $MgOAl_2O_3$ is also predicted to be the predominant inclusion type in the remelted ingots by thermodynamic calculations. However, comparing the morphology of the inclusions, significant differences between the two ingots are observed. Typical examples for the morphology of oxides in ingot 1 and 2 are given in Figs. 5.29 and 5.30. Inclusions in ingot 1 often consist of two or more oxide phases which can clearly be separated from each other, where mostly the core is surrounded by an Al-rich layer. An example of a SEM-mapping of a multi-phase oxide inclusion from ingot 1 is demonstrated in Fig. 5.31. It shows an oxide inclusion formed around a pore, surrounded by an Al_2O_3-layer. The light dots inside the oxide are carbides. Regarding a typical inclusion in ingot 2, the oxide mostly consists of a single phase, but is surrounded by a (Ti, V)-nitride (see Fig. 5.32). In these cases, the darker part of the inclusion is the oxide phase, against what the lighter areas represent the carbonitrides. Next to these described multi-phase types, also ordinary single-phase $MgOAl_2O_3$ are found in both ingots, although the number of these single-phase $MgOAl_2O_3$ is considerably higher in ingot 1 than in ingot 2. These described morphologies also give an indication of the reaction mechanisms in ESR for the different inclusion types and a possible answer to the question, whether the inclusion in the ingot may be a relic from the electrode or not. Both inclusions presented in Figs. 5.31 and 5.32 are assumed to be inclusions which were not in contact with the slag, therefore are relics from the electrode and had enough time to

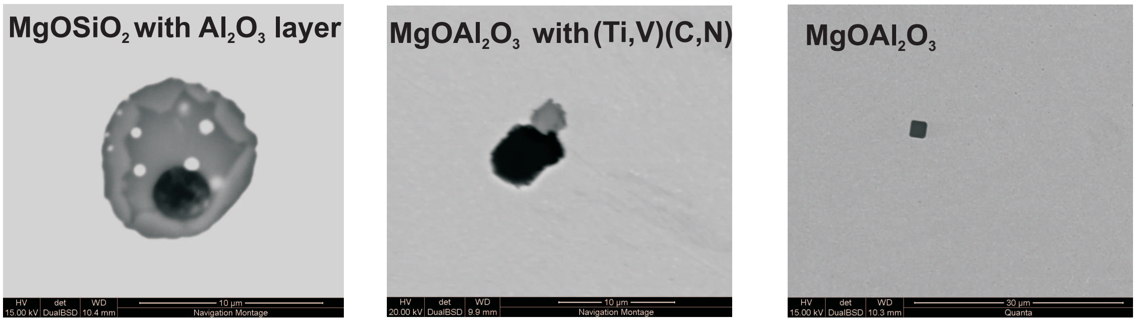

a.) b.) c.)

Figure 5.29: Typical oxide inclusions in ingot 1.

be modified in the liquid pool. For the inclusion shown in Fig. 5.31 this assumption is affirmed by the size of the inclusion. Since it offers an ECD > 10 µm, a dwell time of more than 50 s would have been necessary in the liquid electrode film in order to dissolve this inclusion. Thus, the dissolution of this particle at the electrode/slag interface is considered rather unlikely. Concerning the inclusion demonstrated in Fig. 5.32 this assumption is based on the fact that the oxide phase is completely surrounded by the $(Ti, V)(C, N)$. If the $MgOAl_2O_3$ precipitated at the pool/slag interface, the subsequent dwell time in the pool is not supposed to be sufficiently long for a complete surrounding of the oxides. Only a partial attachment of a $(Ti, V)(C, N)$ would rather argue for initial precipitation of the $MgOAl_2O_3$ in the pool.

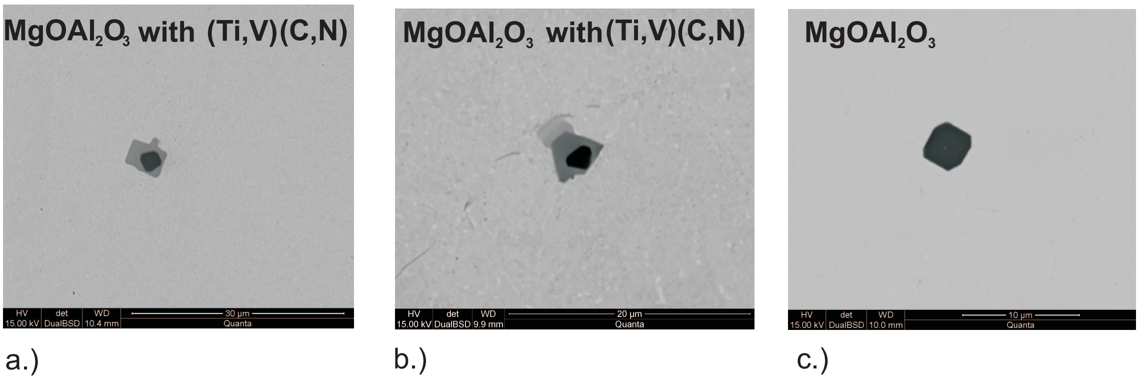

Figure 5.30: Typical oxide inclusions in ingot 2.

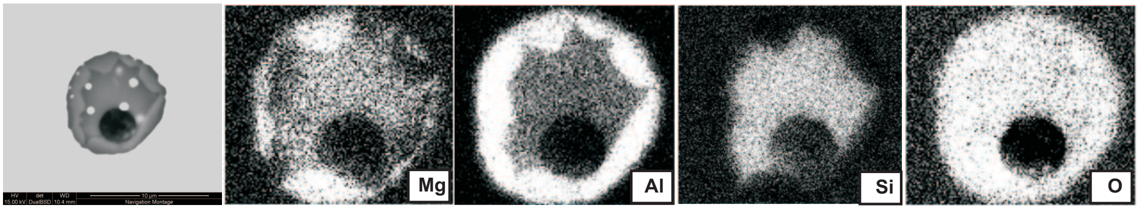

Figure 5.31: SEM-mapping of a typical multi-phase inclusion in ingot 1 formed around a pore: A core consisting of MgO and SiO_2, surrounded by an Al_2O_3-layer (light dots representing Cr-carbides).

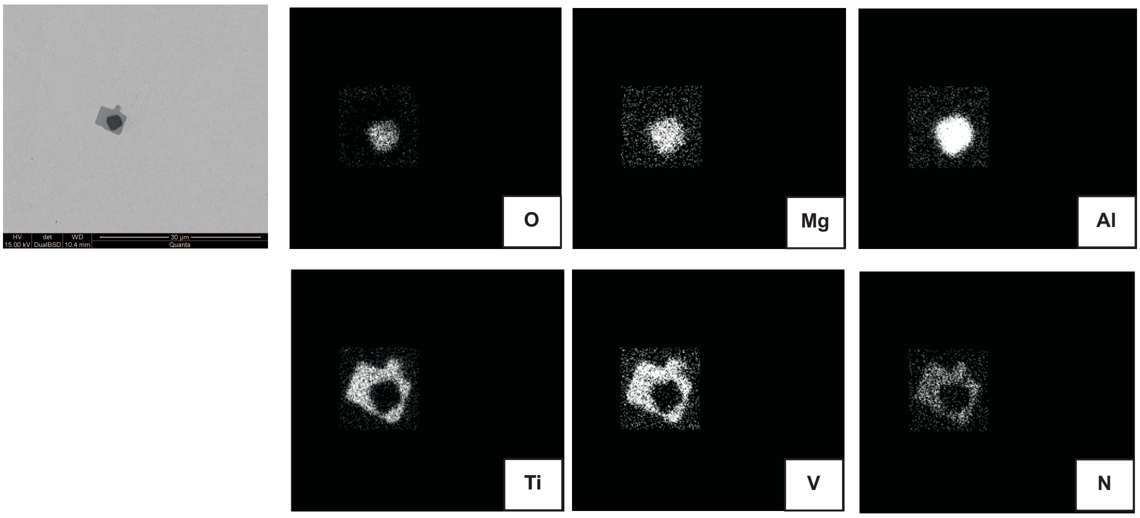

Figure 5.32: SEM-mapping of a typical multi-phase inclusion in ingot 2, consisting of an oxide surrounded by a (Ti, V)-nitride.

In contrast to this, single-phase $MgOAl_2O_3$ are supposed to have partially formed due to steel-slag reaction at the metal/slag interfaces, which would be in good agreement with the comparatively fast dissolution of Al_2O_3 in the liquid film at the electrode tip. Since $MgOAl_2O_3$ dissolve much slower, the possibility of surviving from the electrode to the remelted ingot is higher than for Al_2O_3.

Summing up, it can be stated that the initial inclusion landscape in the electrode does considerably influence the inclusions in the remelted ingot for the following reasons:

- Some inclusion types tend to dissolve much faster than others in the given steel composition. In the present case Al_2O_3 dissolves quicker than $MgOAl_2O_3$ in the liquid film at the electrode tip. Assuming a possible dwell time of NMIs in the liquid film of 10 s, more than 75 % of Al_2O_3 inclusion between 1 – 10 μm would already have dissolved, against what practically no dissolution of $MgOAl_2O_3$ would have taken place, although their mean ECD is significantly lower. In consequence of a longer dissolution time of $MgOAl_2O_3$ at the electrode tip, also the possibility of surviving the pass from the electrode to the ingot for this inclusion type—assuming that the inclusion does not get in contact with the slag—is increased.

- The presence of oxisulfides (containing Ca, Mg and Al) in the initial electrode also significantly influences the inclusions at the electrode tip and in the droplet. Caused by the dissolution of CaS, the Ca-activity in the liquid melt increases and Ca forms oxides in combination with the Al from the Al_2O_3-dissolution. This reaction is found at the electrode/slag as well as the droplet/slag interface. Sulfur is removed by the slag. If an inclusion gets in contact with the slag, it is dissolved independent of its composition.

- Comparing the inclusion size distributions between electrode, droplet and ingot, the interface electrode/slag seems to be the decisive reaction site for inclusion removal, since the inclusion size distribution in the droplet is already very similar to the final inclusion distribution in the remelted ingot. Moreover, in the droplet centre mostly complex $CaOMgOAl_2O_3$ inclusions were observed which are supposed to be initial $MgOAl_2O_3$ inclusions modified by Ca. Furthermore, considering the relation between droplet and inclusion size, a separation of an inclusion from the droplet centre is rather unlikely in the view of very short available reaction times.

- The dwell time of an inclusion in the liquid pool strongly influences its final morphology. Basically, if an inclusion re-precipitates at the pool/slag interface or in the liquid pool it is remarkably smaller than residual inclusions from the electrode which have much more time to grow or modify. In the present case, a modification was primarily observed for $MgOAl_2O_3$, acting as heterogeneous nuclei for divers carbides and nitrides, resulting in an considerably increased mean ECD. Consequently, on the hand a relatively short dwell time of inclusions in the pool seems to be advantageous for the stated reasons, but on the other hand a longer dwell time would increase the possibility of flotation and subsequent separation.

5.2 Modification of Inclusions in Laboratory Experiments

In the following, the results of the performed laboratory tests in the Tammann Furnace will be described. Next to the influence of the used crucible material, the change of inclusion landscape through remelting with different slag compositions is discussed. Furthermore, the influence of duration time and as well as slag amount will be explained. Special attention is paid to the changes in inclusion morphology.

5.2.1 Influence of the Crucible Material

In order to determine the influence of the used crucible material on the final inclusion landscape after remelting in the Tammann Furnace, experiments without slag addition using different crucible materials were done. Figure 5.33 exemplarily shows the results for the four examined crucible materials using samples of electrode 1. It can seen that also remelting without the addition of slag, changes the composition of inclusions within the system CaO-Al_2O_3-MgO. Remelting in an Al_2O_3 or an Al_2O_3-SiO_2 crucible leads to comparable results. Comparing them to the initial inclusion state in the electrode shown in Fig. 5.2, a shift of the inclusion via the Al_2O_3-rich corner is observed, accompanied by a noticeable increase of $MgOAl_2O_3$ in both cases. Regarding the composition of inclusions remelted with a MgO crucible, a tendency to higher contents of MgO in the inclusions is observed. While the three mentioned crucible types beforehand have a non-negligible influence on the inclusion composition within the system CaO-Al_2O_3-MgO, the use of a ZrO_2 crucible has the smallest influence on the compositions of inclusions within the displayed ternary system. Of course, due to the melting and re-solidification of the steel sample, a certain change of inclusion composition occurs, resulting in a slightly higher percentage of $MgOAl_2O_3$ inclusions than in the initial electrode material. But, as demonstrated by the described results, also the crucible interacts with the molten steel and has an impact on inclusion modification, which has to be considered when interpreting the results out of laboratory tests. In regards of Al_2O_3, MgO and Al_2O_3-SiO_2 crucibles it is difficult to evaluate the influence of the crucible exactly, because these elements are also part of the metal phase. This fact is different for the case of ZrO_2. If ZrO_2 is part of an inclusion as shown in Fig. 5.34, this modification can usually be clearly assigned to the used crucible. In the latter case a $CaOAl_2O_3$ with slight contents of MgO is surrounded by an ZrO_2-layer.

5.2.2 Variation of Slag Composition

Since the reaction between metal and slag is decisive for inclusion modification, the influence of different slag compositions on the changes of inclusion composition has been analysed. The used slag compositions as well as the applied test conditions are given in Section 4.4.

5.2.2.1 Slags of the System CaO-Al_2O_3-MgO

Figure 5.35 shows the results for remelting samples of electrode 1 and 2 with different slag compositions. The CaO/Al_2O_3 ratio has been decreased continuously from slag A.1 to A.4[*]. In can be seen that in both cases, a significant shift of the inclusion compositions towards the Al_2O_3-rich corner is observed with increasing Al_2O_3-content of the slag also resulting in a higher amount of pure Al_2O_3 inclusions primarily in samples remelted with slag A.4. Focussing on the modification of $MgOAl_2O3$ inclusions, not only an increase of the overall number of this inclusion type is observed with increasing Al_2O_3-content of the slag, but also a significant higher mean ECD is determined (see Fig. 5.36).

Comparing these results with the modification of inclusions in the ESR process described in the previous section, some parallels can be drawn. Firstly, concerning the composition of inclusions: The CaO/Al_2O_3 ratio of slag A.2 fits most closely to the one of the slag used for Electroslag Remelting. Comparing the compositions of inclusions within the system CaO-Al_2O_3-MgO in the cross sections B of remelted ingots 1 and 2 (see Figs. 5.21 and 5.22) with the laboratory results of slag A.2 in Fig. 5.35 a remarkable concordance is found, especially for samples of electrode 2. Moreover, the shift of inclusion composition due to higher Al_2O_3-contents in the slag can also be indicated in both—samples of the

---

[*] See Tab. 4.6 on page 100 for details

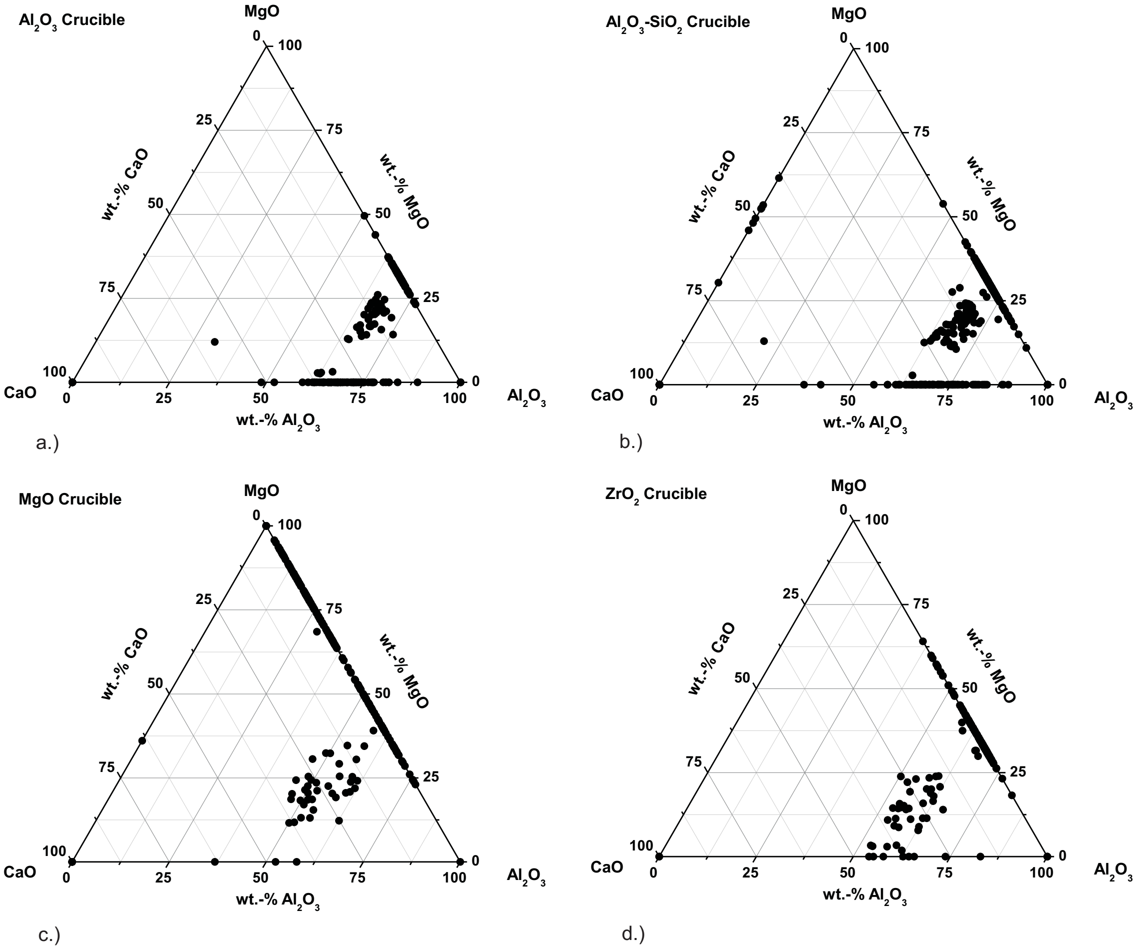

Figure 5.33: Compositions of NMIs in the ternary system CaO-Al_2O_3-MgO after remelting samples of electrode 1 without slag addition but using different crucible materials.

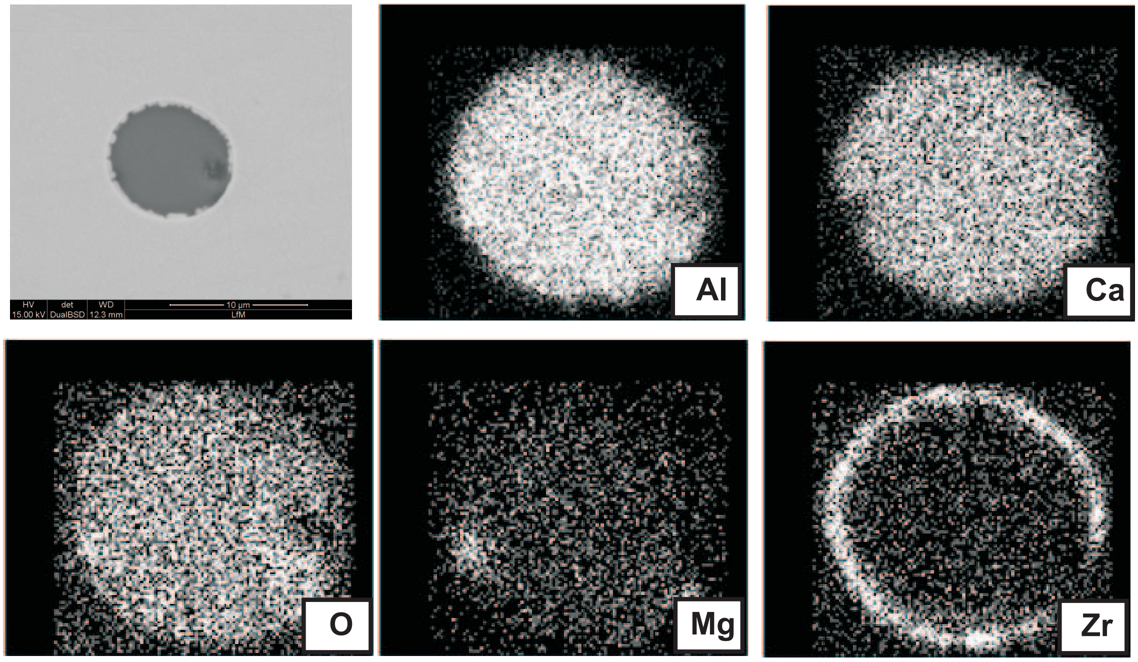

Figure 5.34: SEM-mapping of a typical inclusion from a sample of electrode 2 remelted in the Tammann Furnace without slag addition.

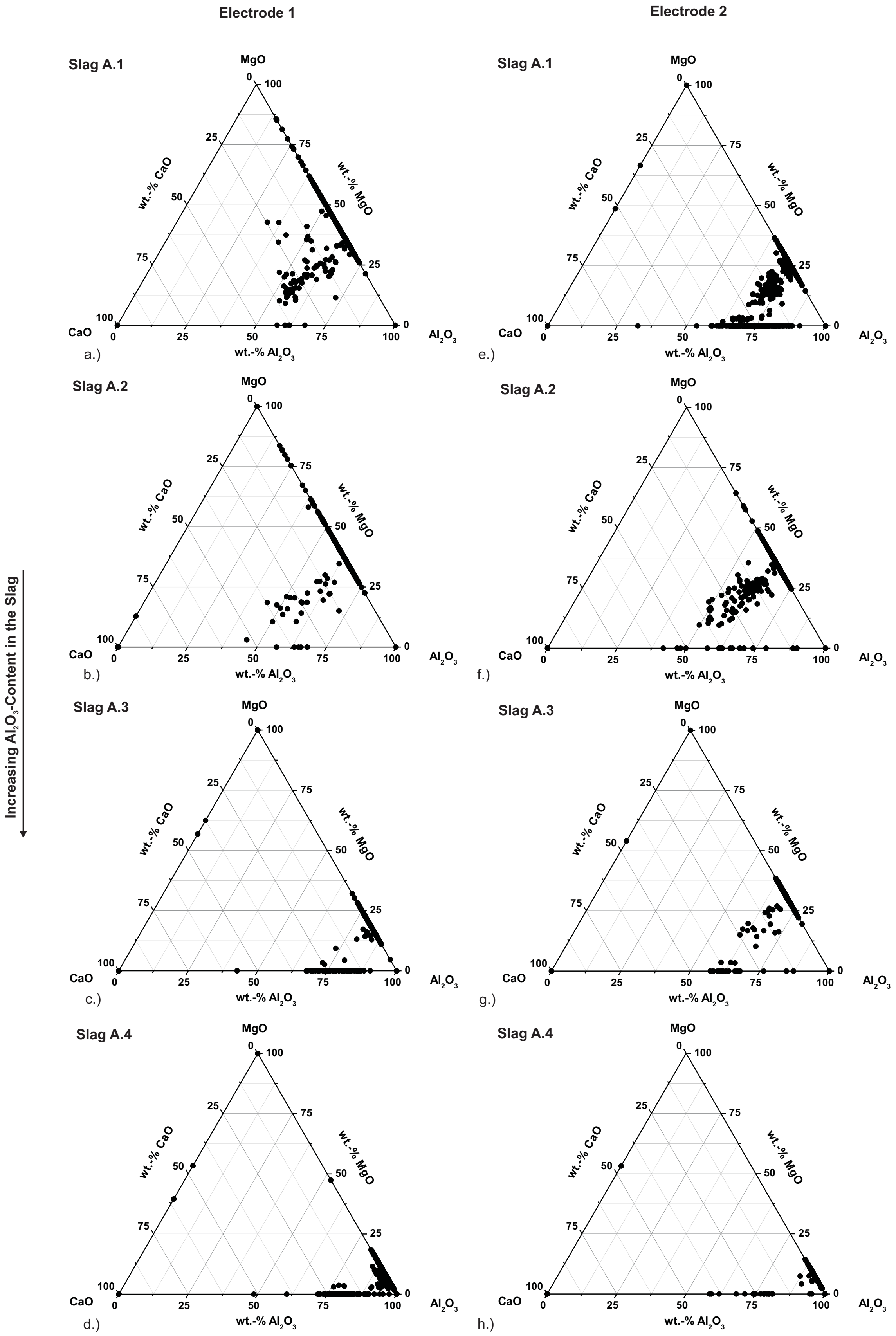

Figure 5.35: Composition of inclusions within the ternary system CaO-Al_2O_3-MgO after remelting with different slags. a.)–d.) showing the results for electrode 1, e.)–h.) showing the results for electrode 2.

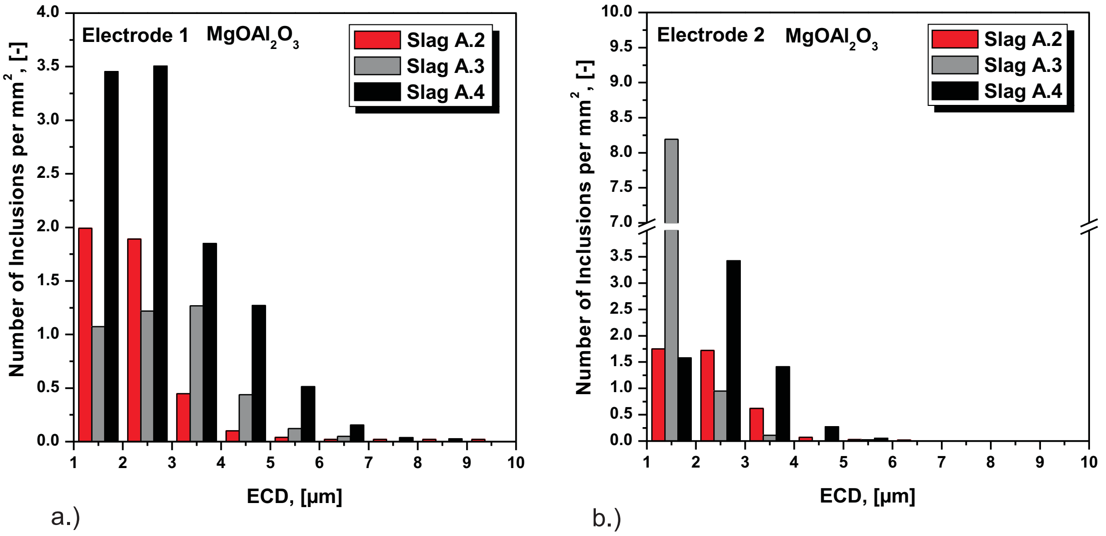

Figure 5.36: Comparison of size distributions of $MgOAl_2O_3$ in samples of electrode 1 and 2 remelted with different slag compositions out of the system CaO-Al_2O_3-MgO.

ESR process (cross sections M in Figs. 5.21 and 5.22) and samples remelted on laboratory scale. Thus, it can be concluded that already small changes in the Al_2O_3-content of the slag significantly influences the final inclusion landscape. The higher the Al_2O_3-content in the slag, the more considerably the shift of inclusion composition within the system CaO-Al_2O_3-MgO towards the Al_2O_3-corner. This effect was concordantly found in samples from the ESR process as well as in laboratory tests.

Secondly, as far as the change of $MgOAl_2O_3$ inclusions towards higher mean ECDs is concerned: As illustrated in Fig. 5.36, in laboratory experiments a shift to an increased mean ECD is observed from slag A.2 to slag A.4. Also in the samples from the ESR process, a noticeable increase of the mean ECD of $MgOAl_2O_3$ was found with increasing ingot height. The higher ECD of $MgOAl_2O_3$ in ingot cross sections M than in cross section B, may be related to different reasons. On the one hand, also a change of slag composition occurs caused by continuous deoxidation and a consequently increase of the Al_2O_3-content in the slag, on the other hand also the dwell time of inclusions in the pool might be higher resulting in longer time for growth and modification. The influence of dwell time on inclusion modification on laboratory scale will be explained in the next subsection.

Finally, also similar morphologies have been determined in the laboratory tests and the samples remelted via ESR. Inclusions detected in samples from both electrodes remelted with slag A.2 look very similar with those determined in the remelted ingots. Figure 5.37 shows examples for two $MgOAl_2O_3$ from a remelted sample of electrode 1 and Fig. 5.38 exemplifies inclusions in remelted samples of electrode 2. As already observed in the remelted ingot 2, $MgOAl_2O_3$ also tend to act as nuclei for carbides and nitrides in laboratory tests in samples of electrode 2 in contrast to samples of electrode 1. In a disadvantageous case, several $MgOAl_2O_3$ can agglomerate and—a sufficient dwell time in the liquid metal provided—may also act as nuclei for Mo-phases, as exemplarily shown in Fig. 5.39. In the presented case this results in an overall extension of the inclusions of more than 10 µm which can cause material failure if situated near the surface of the final product.

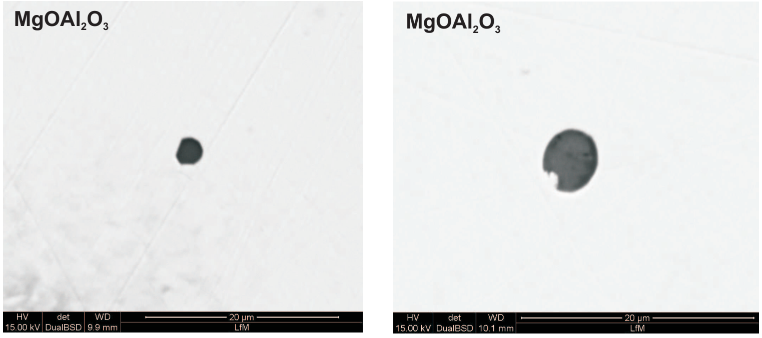

a.) b.)

Figure 5.37: SEM-images of typical $MgOAl_2O_3$ inclusions in the sample of electrode 1 remelted with slag A.2.

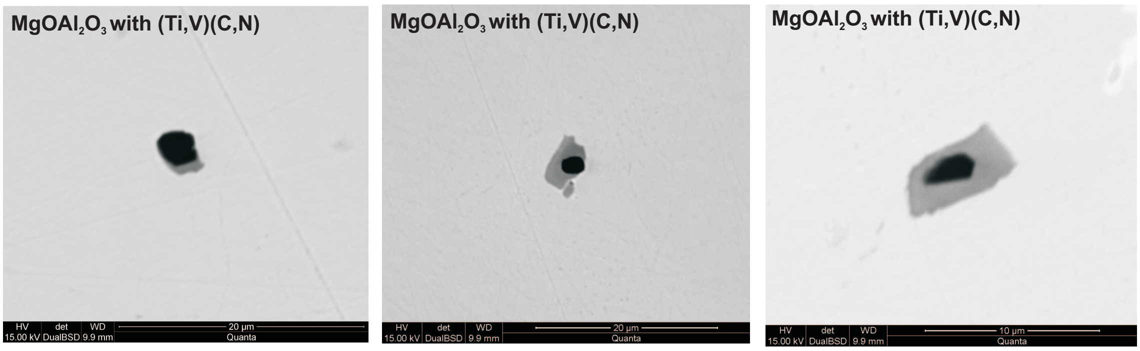

a.) b.) c.)

Figure 5.38: SEM-images of typical $MgOAl_2O_3$ inclusions in the sample of electrode 2 remelted with slag A.2.

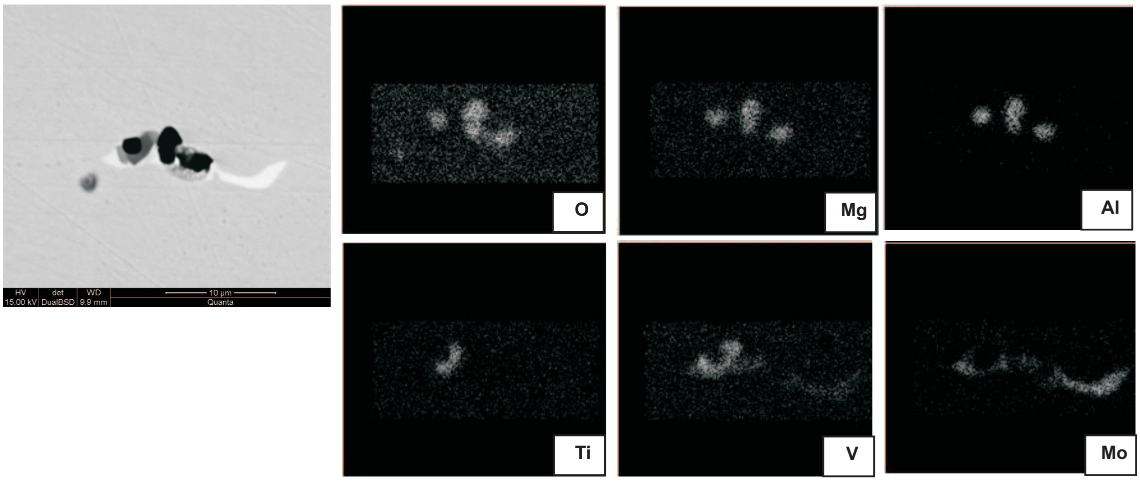

Figure 5.39: SEM-mapping of an inclusion conglomerate in the sample of electrode 1 remelted with slag A.2.

5.2.2.2 Slags of the System $CaO\text{-}Al_2O_3\text{-}CaF_2$

As already demonstrated for experiments using $CaO\text{-}Al_2O_3\text{-}MgO$ slags, the same scheme has been applied for slags primarily consisting of CaO, Al_2O_3 and CaF_2. Figure 5.40 illustrates the results for remelting samples of electrode 1 and 2 with the different slag compositions. Regarding the composition, the used ESR process slag is situated between slag B.1 and B.2[†]. As also observed previously for slags A, a continuous increase of the Al_2O_3-content of the slag causes a shift of the inclusion compositions towards the Al_2O_3 corner, although the shift is not as distinct for the samples remelted with slag B.3 as it has been for slag A.4. A possible reason for this might also lie in the different used crucible material, since for remelting with slags A an Al_2O_3 crucible was used and for the experiments with CaF_2-slags a ZrO_2 crucible was applied. Comparing the results in Fig 5.40 with the remelted ingots in Figs. 5.21 and 5.22 similar results are obtained concerning inclusion compositions.

In addition, attempts were undertaken to simulate these changes in inclusion composition through the contact of different slags with the use of *FactSage*. The calculation results for the two electrodes in combinations with slag B.1 to B.3 are illustrated in Figs. 5.41 and 5.42. The same calculation principle and assumptions as for the predictions of inclusion types in the remelted ingots (see Fig. 5.23) have been used. Thus, it is assumed that no solid inclusions from the electrode reach the remelted ingot. Principally, in all cases the predominantly predicted inclusion type is $MgOAl_2O_3$, which is in good agreement with the experimental results. Regarding the predicted phases in more detail, it is also obvious that for electrode 1 a significant increase of the phase fraction of Al_2O_3 is found with increasing Al_2O_3-content of the slag. Furthermore, an overall increase of the sum of calculated solid phase fractions is determined from slag B.1 to slag B.3. A similar tendency is observed for the calculation results of electrode 2 in combination with the three different slags. But in contrast to electrode 1, where the overall increase of solid fractions was based on the emergence of Al_2O_3, calculations with the composition of electrode 2 show a continuous increase of the $MgAl_2O_4$ fraction and only a slight augmentation of Al_2O_3.

In terms of the influence of slag composition on inclusion size, the same tendency is observed as already stated for the Electroslag Remelted ingots as well as for laboratory tests with slags A: The mean ECD of $MgOAl_2O_3$ rises with the Al_2O_3-content of the slag. The difference between the samples remelted with slags A and B lies in the final number of inclusions in the remelted samples. In the samples remelted with slags B, a considerably lower amount of $MgOAl_2O_3$ has been detected compared to samples remelted with slags A. This effect might be attributed to the presence of CaF_2 which—as shown in Tab. 2.3—significantly influences slag viscosity. Thus, the conditions for separation seem to be advantageous using $CaO\text{-}Al_2O_3\text{-}CaF_2$ slags, since all other parameters also including duration time of the experiments have been the same. The number of detected $MgOAl_2O_3$ inclusions in samples remelted with slag B.1 to B.3 also fits more closely to the ones in the remelted ingots.

As far as the morphology of inclusions is concerned, interesting parallels to the other laboratory tests as well as to the samples of the remelted ingots are observed. Figure 5.44 visualises a typical example of an multi-phase oxide inclusion in a sample remelted with slag B.1. As already observed for inclusions in ingot 1 (see Fig. 5.29), an oxide core is surrounded by an Al_2O_3-layer; in the present case forming an $MgOAl_2O_3$ consisting of two separate phases. On the contrary, as shown in Fig. 5.45 $MgOAl_2O_3$ in samples of electrode 2 often are accompanied by a nitride or carbide phase after remelting.

[†] See Tab. 4.7 on page 100 for details

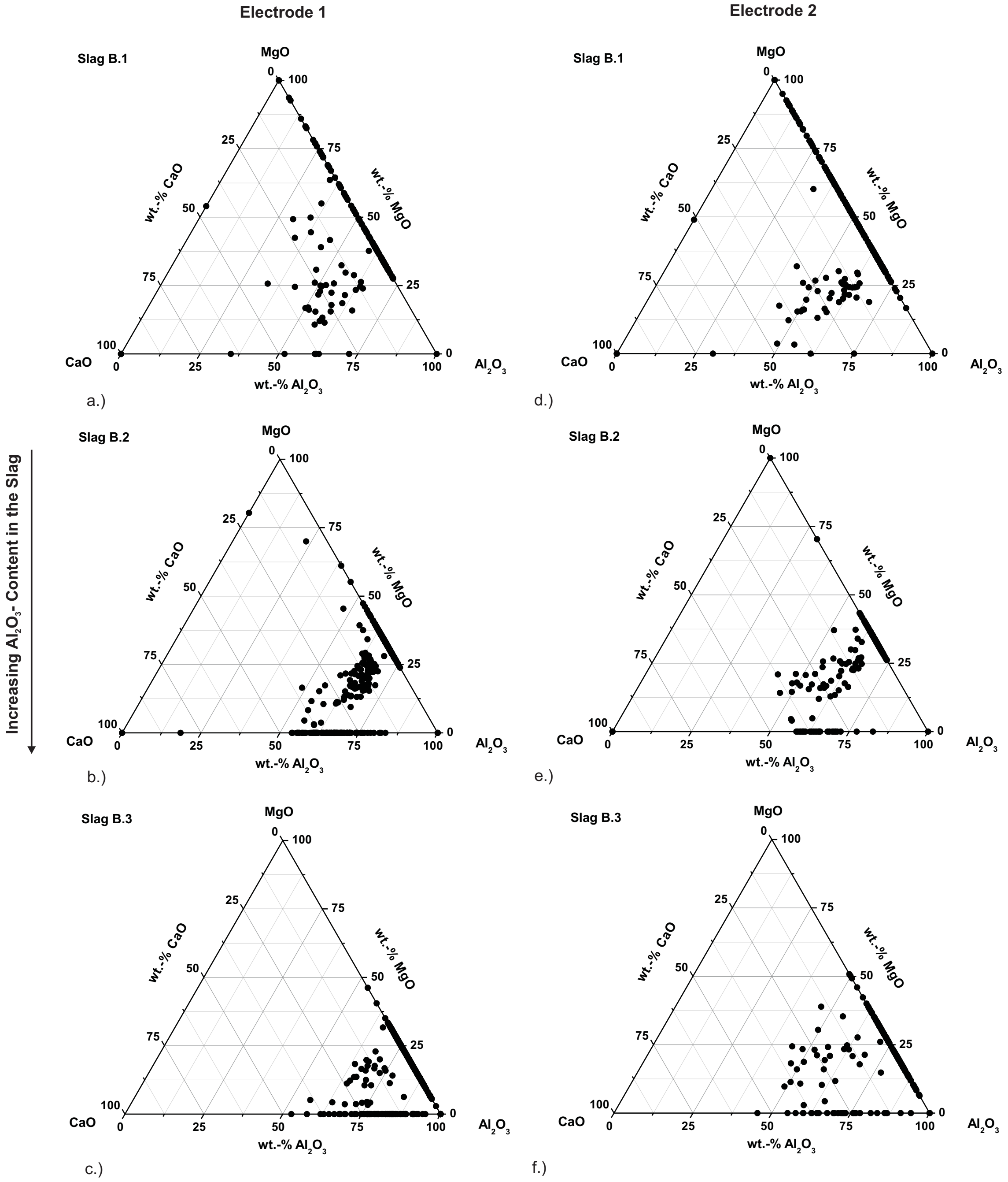

Figure 5.40: Composition of inclusions within the ternary system $CaO\text{-}Al_2O_3\text{-}MgO$ after remelting with different slags. a.)–c.) showing the results for electrode 1, d.)–f.) showing the results for electrode 2.

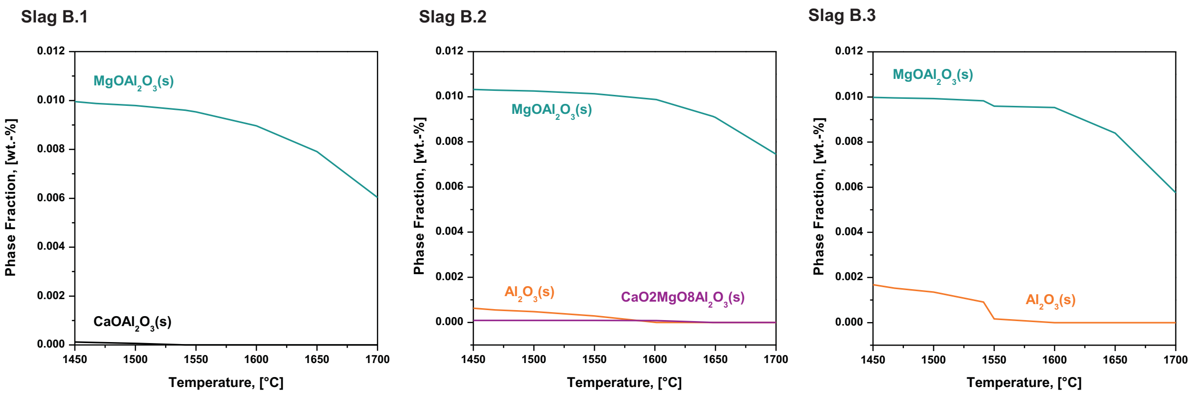

a.) b.) c.)

Figure 5.41: Results of thermodynamic calculations with *FactSage* for the stable phases after remelting samples of electrode 1 with the three different applied slag compositions out of the system $CaO\text{-}Al_2O_3\text{-}CaF_2$.

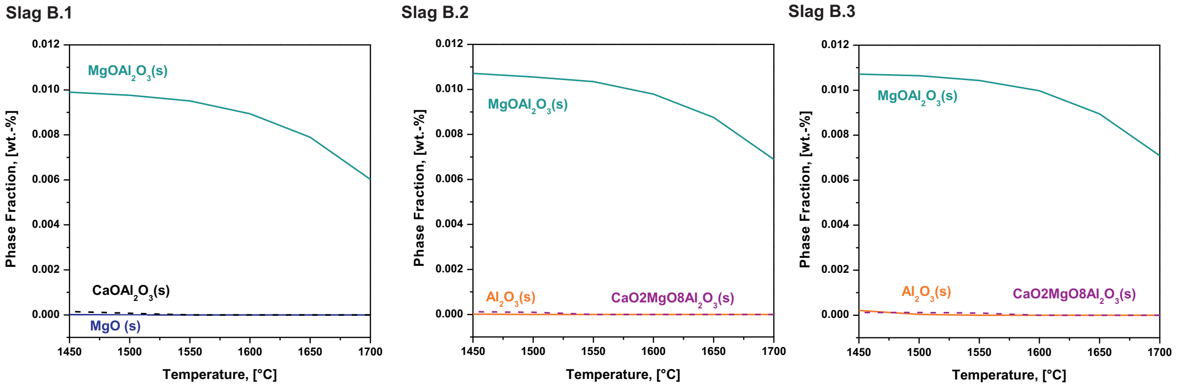

a.) b.) c.)

Figure 5.42: Results of thermodynamic calculations with *FactSage* for the stable phases after remelting samples of electrode 2 with the three different applied slag compositions out of the system $CaO\text{-}Al_2O_3\text{-}CaF_2$.

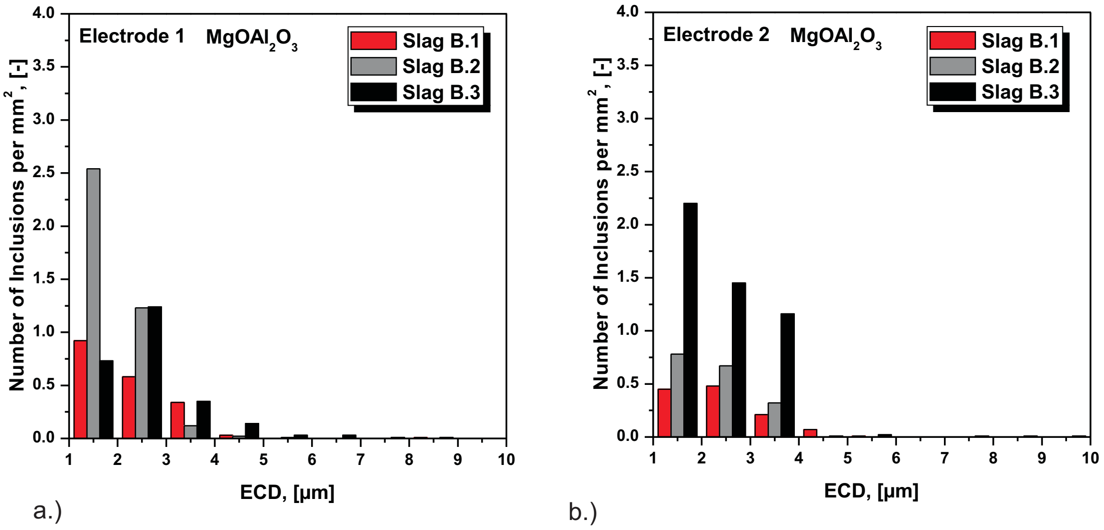

a.) b.)

Figure 5.43: Comparison of size distributions of $MgOAl_2O_3$ in samples of electrode 1 and 2 remelted with different slag compositions out of the system $CaO\text{-}Al_2O_3\text{-}CaF_2$.

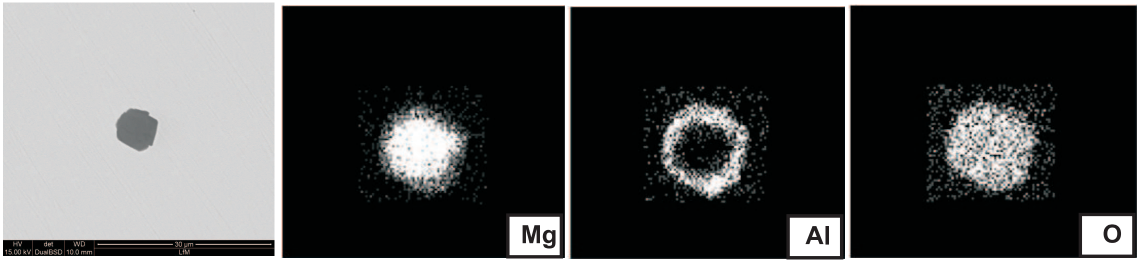

Figure 5.44: SEM-images of a $MgOAl_2O_3$ inclusions in the sample of electrode 1 remelted with slag B.1.

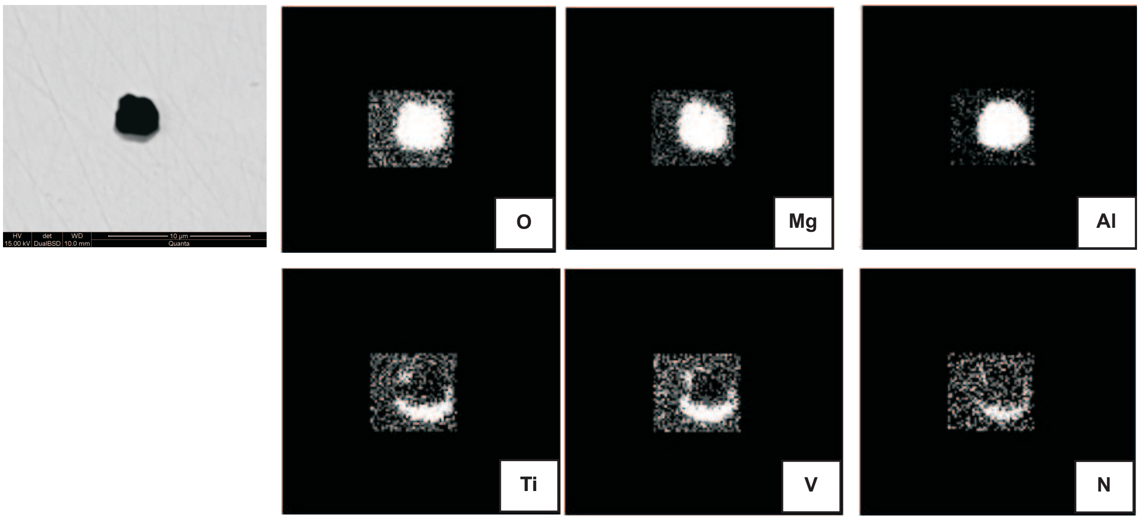

Figure 5.45: SEM-images of typical $MgOAl_2O_3$ inclusions in the sample of electrode 2 remelted with slag B.1.

Considering the results of remelting experiments with the Tammann Furnace, the influence of slag composition on the final inclusion landscape can be summarised as follows:

- Remelting experiments with both slag systems principally show similar trends as far as the change of inclusion composition within the system CaO-Al_2O_3-MgO is concerned as well as in inclusion morphology. The main detected inclusion type in all cases is $MgOAl_2O_3$. Consequently, CaF_2 does not seem to have a significant influence on the change of inclusion composition through remelting. Additionally, mainly $MgOAl_2O_3$ in samples of electrode 2 were found to act as heterogeneous nuclei for $(Ti, V)(C, N)$. This findings are in good agreement with the observations in the ESR process.

- An increasing Al_2O_3-content in the slag causes a remarkable shift of the inclusion composition towards the Al_2O_3-rich corner. This result also affirms the change of inclusion composition in the ESR process over the ingot height, since there also the Al_2O_3-content of the slag increases continuously due to deoxidation.

- Moreover, an increase of the mean ECD of $MgOAl_2O_3$ is observed with increasing Al_2O_3-content in the slag. In laboratory experiments this effect is also attributed to the change in slag composition. Although the mean ECD of $MgOAl_2O_3$ also increases with ingot height in the ESR process, here also the longer dwell time in the pool has to be taken into account. The influence of dwell time will be discussed in the next subsection more precisely.

- Differences between the two used slag systems were found concerning the number of $MgOAl_2O_3$ inclusions in the remelted samples. Samples remelted with CaF_2-containing slags show a noticeably lower number of remaining inclusions. Although—as stated above—CaF_2 does not seem to have a significant influence on the change of inclusion composition through remelting, CaF_2 highly influences the physical properties of the slag and therefore the separation process. CaF_2 decreases slag viscosity which results in a more intense stirring and is therefore regarded to be more favourable for metallurgical reactions at the steel/slag interface.

The effect of CaF_2 in slags on the modification of inclusion composition has also been examined by Andersson and Sichen [222]. They investigated the influence of CaF_2 in slags used for ladle refining by industrial trials. The authors also concluded that the absence of CaF_2 does only marginally affect the inclusion type as well as the number of inclusions. While the first conclusion is in good agreement with the instant results, the latter was not affirmed by the investigations in the present thesis.

5.2.3 Influence of Duration Time and Slag Amount

In order to study their influence on the inclusion modification, the duration time during the laboratory experiments as well as the used slag amount have been varied. Figure 5.46 summarises the effect of both mentioned parameters. The duration time at 1600 °C has been varied between 10 – 30 min for both electrode conditions and the two slag compositions fitting most closely to the ESR process slag composition. As illustrated in Fig. 5.46a primarily the mean ECD of samples from electrode 2 increases significantly with longer duration time, most effectively between 20 – 30 min. Nonetheless, the mean ECD of oxides after remelting with slag B.1 and a duration time of 30 min is smaller than for samples remelted with slag A.2. This may also be related to the more advantageous separation using CaF_2-slags as already mentioned beforehand. For samples of electrode 1 also a slight increase of the mean ECD is observed with longer duration time, but not as distinct as for electrode 2. Regarding the morphology of inclusions in remelted samples of electrode 2 with longer duration time in more detail, the following two cases were observed: In many cases the original $MgOAl_2O_3$ whether acts as heterogeneous nuclei for a $(Ti, V)(C, N)$ (see Fig. 5.47) and the longer the duration time the more likely also a Mo-rich phase is formed, or is surrounded by $CaOAl_2O_3$-layer as illustrated in Fig. 5.48. Usually, the latter ones are smaller than $MgOAl_2O_3$ combined with a $(Ti, V)(C, N)$.

Figure 5.49 illustrates a SEM-mapping of a typical inclusion detected in a sample of electrode 1 remelted with slag B.1. In principal, the same modification is observed as for electrode 2, an $MgOAl_2O_3$ is surrounded by a $CaOAl_2O_3$-layer. Additionally, a ZrO_2-layer resulting from reactions with the crucible material is formed. With increasing duration time reactions with the crucible material become more evident. Figure 5.50 shows some examples of inclusions detected in a sample remelted with a duration time of 30 min, where the dark parts represent the CaO-Al_2O_3-MgO phase and the light areas are ZrO_2. It contrast to shorter duration times, where the ZrO_2 mainly forms a layer around an existing oxide inclusion, an increasing duration time leads to an increased presence of ZrO_2 inside the inclusion.

Figure 5.46b demonstrates the influence of the used slag amount in combination with longer duration time for experiments with slag B.1. Comparing the results for different slag amounts for the particular duration time, no large differences are observed. A trend to a slight decrease of the mean oxide ECD is detected with increasing slag amount. However, the duration time within laboratory experiments at reaction temperature influences the final inclusion landscape more significantly.

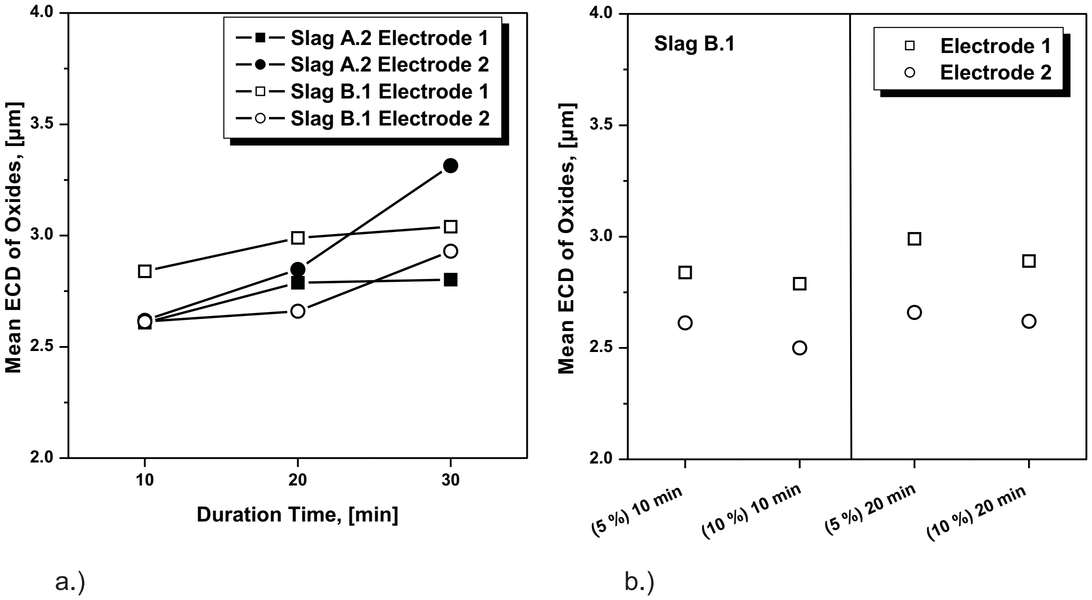

Figure 5.46: Influence of duration time and slag amount on the mean ECD of oxide inclusions in samples remelted with slag A.2 and B.1.

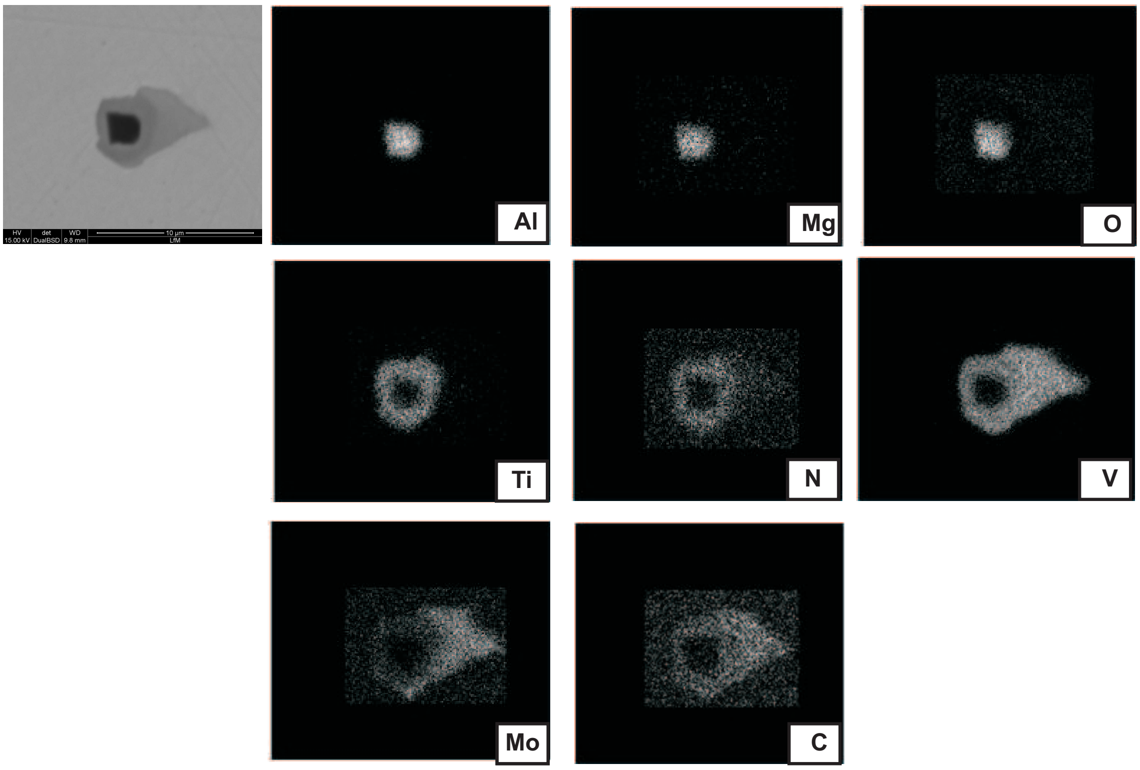

Figure 5.47: SEM-mapping of a typical inclusion in a sample remelted of electrode 2 remelted with slag A.2 and an duration time of 30 min.

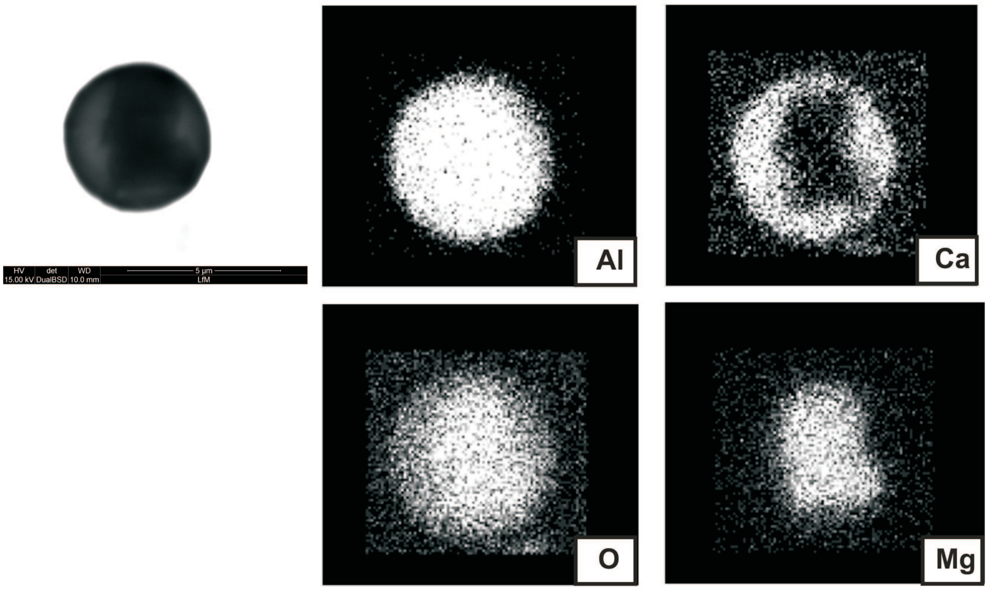

Figure 5.48: SEM-mapping of an inclusion in a sample remelted of electrode 2 remelted with slag A.2 and an duration time of 20 min.

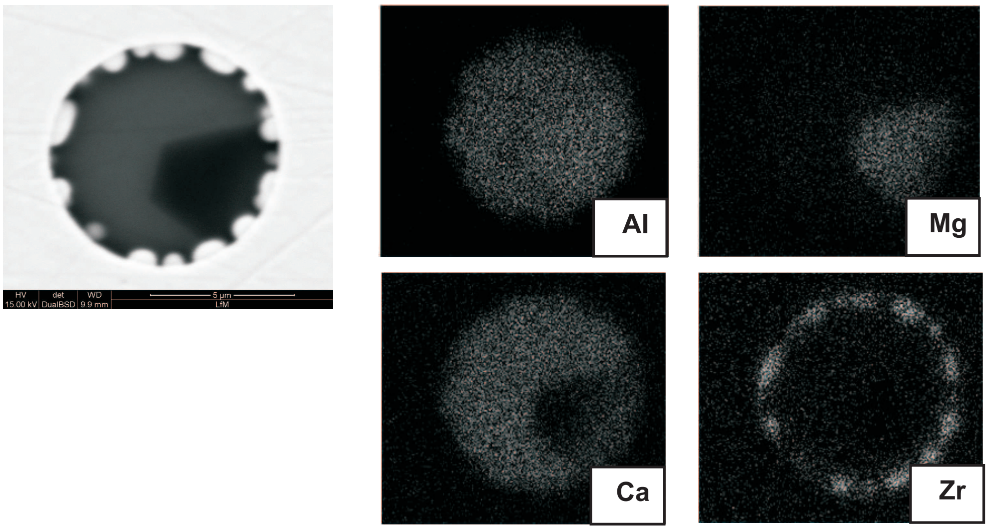

Figure 5.49: SEM-mapping of an inclusion in a sample remelted of electrode 1 remelted with slag B.1 and a duration time of 20 min.

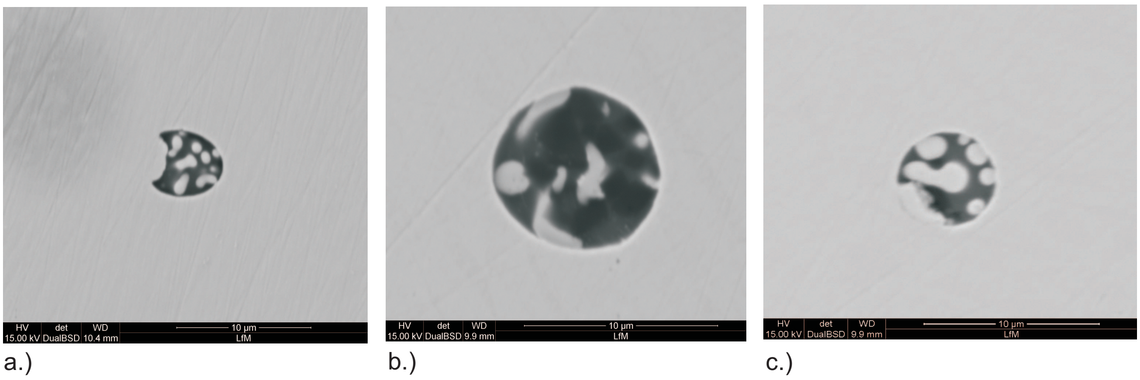

a.) b.) c.)

Figure 5.50: SEM-images of complex multi-phase inclusions in a sample remelted of electrode 1 remelted with slag B.1 and an duration time of 30 min.

The influence of duration time and slag amount on the final inclusion landscape in laboratory experiments can be summarised as follows:

- The mean ECD of $MgOAl_2O_3$ increases with longer duration time in the experiments. This is the result of inclusion modification, since $MgOAl_2O_3$ tends to act as heterogeneous nuclei for $(Ti,V)(C,N)$. Moreover, the longer the duration time, the more likely also a Mo-rich phase nucleates. Additionally, the formation of a CaO-Al_2O_3l-layer was observed in many cases. These findings conform with the observations from the ESR process, where also $MgOAl_2O_3$ was found to act as heterogeneous nucleus for $(Ti,V)(C,N)$ if the dwell time in the liquid pool is sufficiently long.

- The longer the duration time of the laboratory test, the more significant the influence of the crucible material on the final inclusion landscape becomes. For long duration times, a significant ZrO_2-content was found in the inclusions.

- As far as the slag amount is concerned, no noticeable influence on the final inclusion landscape was found. The duration time is therefore seen to be more essential for the behaviour of NMIs.

The laboratory tests with the Tammann Furnace were used to study the modification of non-metallic inclusions due to steel/slag interactions,as far as size, composition and morphology are concerned. For this purpose, the slag composition, the duration time as well as the slag amount have been varied. In a second step possible parallels to the ESR process were drawn and the decisive influencing parameters on inclusion modification were deduced. Summing up, the following main conclusions can be drawn on the basis of the performed laboratory experiments:

- Regarding the used slag composition, mainly Al_2O_3 was found to significantly influence inclusion composition as well as inclusion size. In contrast, CaF_2 does not seem to considerably affect inclusion composition, but has an important impact on physical slag properties and consequently codetermine the removal rate of inclusions.

- Longer experimental duration times cause longer dwell time of inclusions in the liquid metal. On the one hand, this increases the time for inclusion modification and especially $MgOAl_2O_3$ were found to act as heterogeneous nuclei for carbides and nitrides. On the other hand, longer dwell time also enhances the possibility of inclusion separation through flotation. Consequently, an agreement of an most adequate dwell time has to be defined weighing the involved advantages as well as disadvantages.

5.3 Dissolution Behaviour of Oxides in Steel and Slags

The dissolution behaviour of oxides in fluoride slags used in the ESR process as well as the dissolution of oxides in X38CrMoV5-1 was analysed with a Laser Scanning Confocal Microscope. The experimental setup and the applied test conditions are explained in Section 4.4.2. Figure 5.51 illustrates the behaviour of the distributed Al_2O_3 particles at different time steps and temperatures on slag B.1, which was also used for laboratory experiments in the Tammann Furnace. At about 1340 °C little pools of molten slag around the Al_2O_3 occurred and the particles started to dissolve. As soon as the slag phase was completely liquid, the particles tend to agglomerate and were continuously dissolved in the slag. The estimated dissolution time of the Al_2O_3 particles with an initial size of approximately 100 µm at 1450 °C is about 200 s.

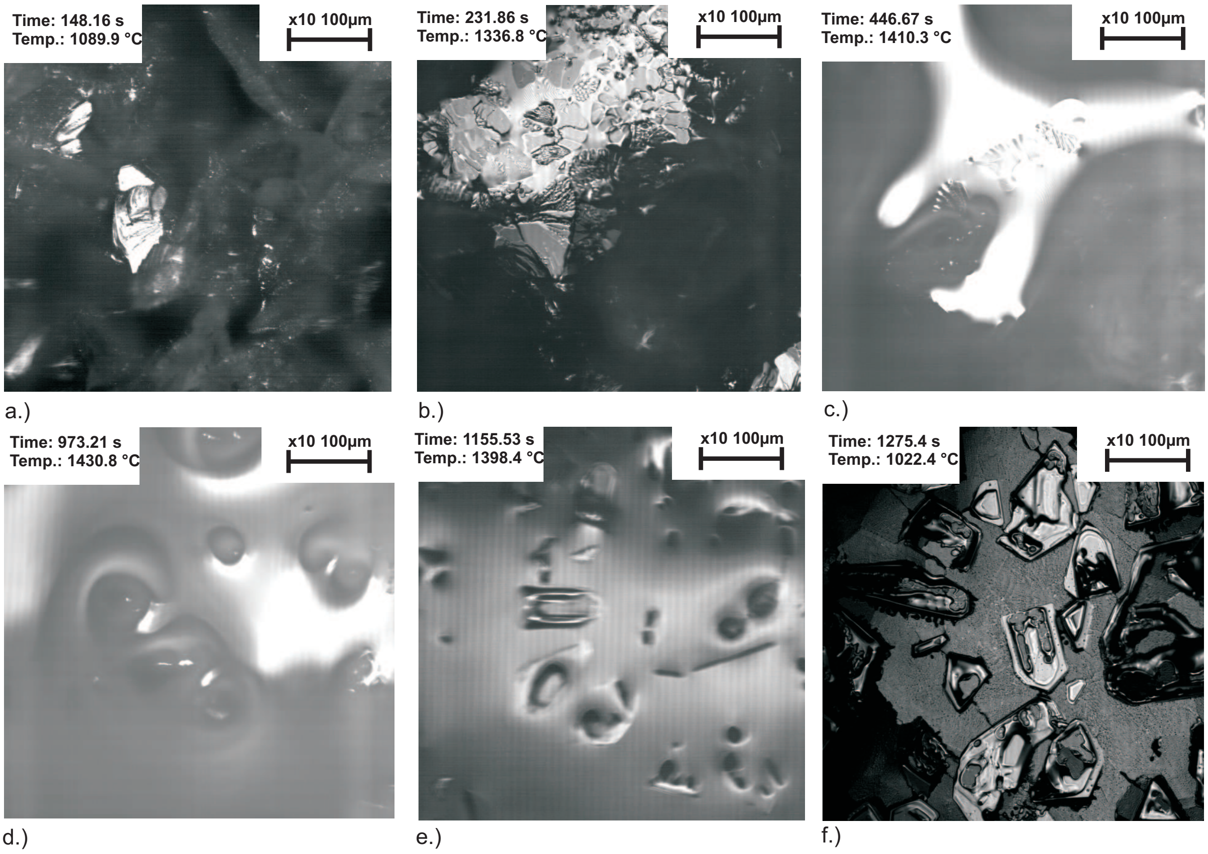

Figure 5.51: LSCM-images describing the dissolution of Al_2O_3 particles on slag B.1 at different time steps and temperatures.

Up to now, no experiments with slags containing such high contents of CaF_2 in the used slags have been published in literature. Thus, a comparison with results of other research is rather difficult. On the one hand, comparing the present results with experiments done with 36 %CaO-21 %Al_2O_3-42 %SiO_2 slags [69, 70], the dissolution times of Al_2O_3 particles of the mentioned size lie in a comparable range. On the other, calculating the dissolution time for Al_2O_3 based on the experimentally determined empirical rate equation by Fox *et al.* [75],

$$\ln \tau = -31.82 - 3.64 \ln R + 90\,523/T \tag{5.1}$$

no accordance is achieved. The relationship in Eq. (5.1) was established for a fluoride-free mould flux (20 %CaO-10 %Al_2O_3-40 %SiO_2-10 %MgO-20 %Na_2O). For an inclusion size of 100 µm, the calculated dissolution time at 1450 °C would be longer than 600 s, which is far away from the experimentally observed dissolution time of 200 s in fluoride-slags in the present study. Obviously, the CaF_2-content of the slag influences the dissolution behaviour of oxides considerably. Consequently, no reliable parallels to experiments performed with other slag compositions can be drawn.

Figure 5.52 shows the results for the observation of the dissolution of a large inclusion conglomerate in an electrode sample of X38CrMoV5-1. This inclusion conglomerate has been marked under the SEM before, in order to exactly observe this sample region. It can be seen that at a temperature of 1350 °C the metal around the inclusions starts melting, and a large percentage of the initially present inclusions has already dissolved at 1440 °C. But, as shown in Fig. 5.52b, the agglomerate at the right side of the

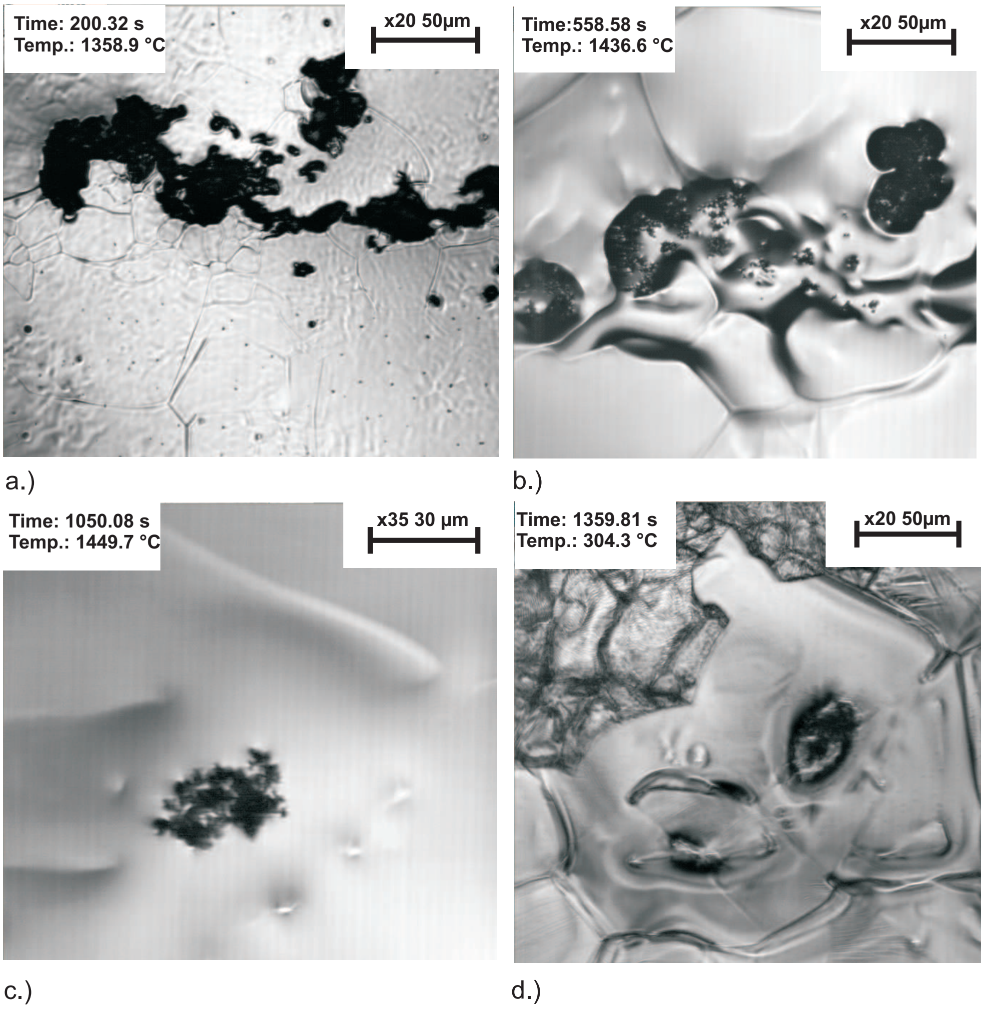

Figure 5.52: LSCM-images describing the dissolution of an inclusion conglomerate in electrode material of X38CrMoV5-1 at different time steps and temperatures.

picture seems to be almost unchanged compared to Fig. 5.52a. In addition, with continuous duration time at 1450 °C, the described inclusion agglomerate only started to dissolve very slowly. In order to examine this inclusion under the SEM, the temperature was not increased any more at this point of the experiment, in order to not completely dissolve the inclusion. Fig. 5.52c illustrates the re-solidifying sample with partial beginning of martensite formation and the inclusion situated in the centre of the picture. The analysis of the re-solidified sample under the SEM explains why this inclusion dissolved that slowly. As shown in Fig. 5.53 the analysed inclusion mostly consists of ZrO_2. This inclusion represents a very large agglomerate of smaller inclusions and therefore certainly would affect macro-cleanness if not separated during Electroslag Remelting.

Within the present thesis, only a qualitative analysis of the dissolution behaviour of oxides in steels and slags has been done with the LSCM. Since this method is a very useful tool for the in-situ observation of the proceeding reactions, in the future, also a quantitative determination of dissolution rates as a function of particle size would be an interesting aspect. Moreover, the further investigation of slags with high CaF_2-contents should be a primary aim in future, since the dissolution behaviour of inclusions in these slags is a decisive criterion for the overall refining effect through Electroslag Remelting.

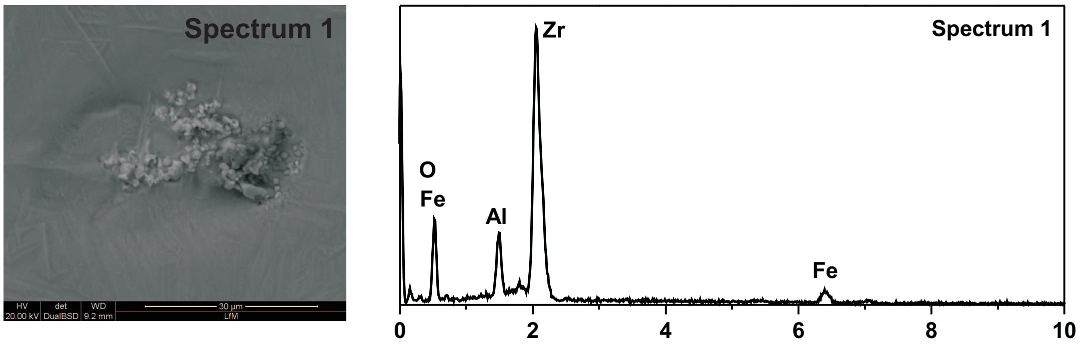

a.) b.)

Figure 5.53: a.) SEM-images of the inclusion conglomerate in the re-solidified sample and b.) the corresponding EDS spectrum.

5.4 Decisive Influences on Inclusion Modification

The modification behaviour of non-metallic inclusions in remelting processes has been analysed comparing results from industrial samples of the ESR process with the results of laboratory experiments in a Tammann Furnace. Additionally, thermodynamic and kinetic calculations were performed. It has been shown that the final inclusion landscape in a remelted sample is usually very different in comparison to the initial state. Due to reactions between steel and slag, the composition, the size and the morphology of the inclusions change significantly.

Based on the theoretic and experimental considerations within the present thesis, the modification of inclusions through remelting can be summarised as follows:

- Although the initial inclusion landscape (inclusion composition as well as inclusion size) in the investigated electrodes before remelting was very different, the final composition of inclusions within the ternary system CaO-Al_2O_3-MgO in the remelted ingots was similar.

- However, large differences concerning the inclusion morphology were determined between the ingots. One decisive factor influencing the final inclusion morphology is whether an inclusion from the electrode gets in contact with the slag or not.

- If an inclusion gets in contact with the slag during the ESR process, it is dissolved independent of its composition. In this case, inclusions may re-precipitate in the liquid pool, usually being smaller than relics from the electrode.

- If an inclusion does not get in contact with the slag, it is modified in the liquid pool. The modification is highly influenced by the available dwell time.

- The electrode/slag interface seems to be the decisive reaction site for inclusion removal, since the inclusion distribution in the droplet is already very similar to the final inclusion distribution in the remelted ingot and the number of inclusions in the droplet is significantly smaller than in the electrode. This conclusions is in good agreement with the majority of published literature [131, 132, 135, 155–157].

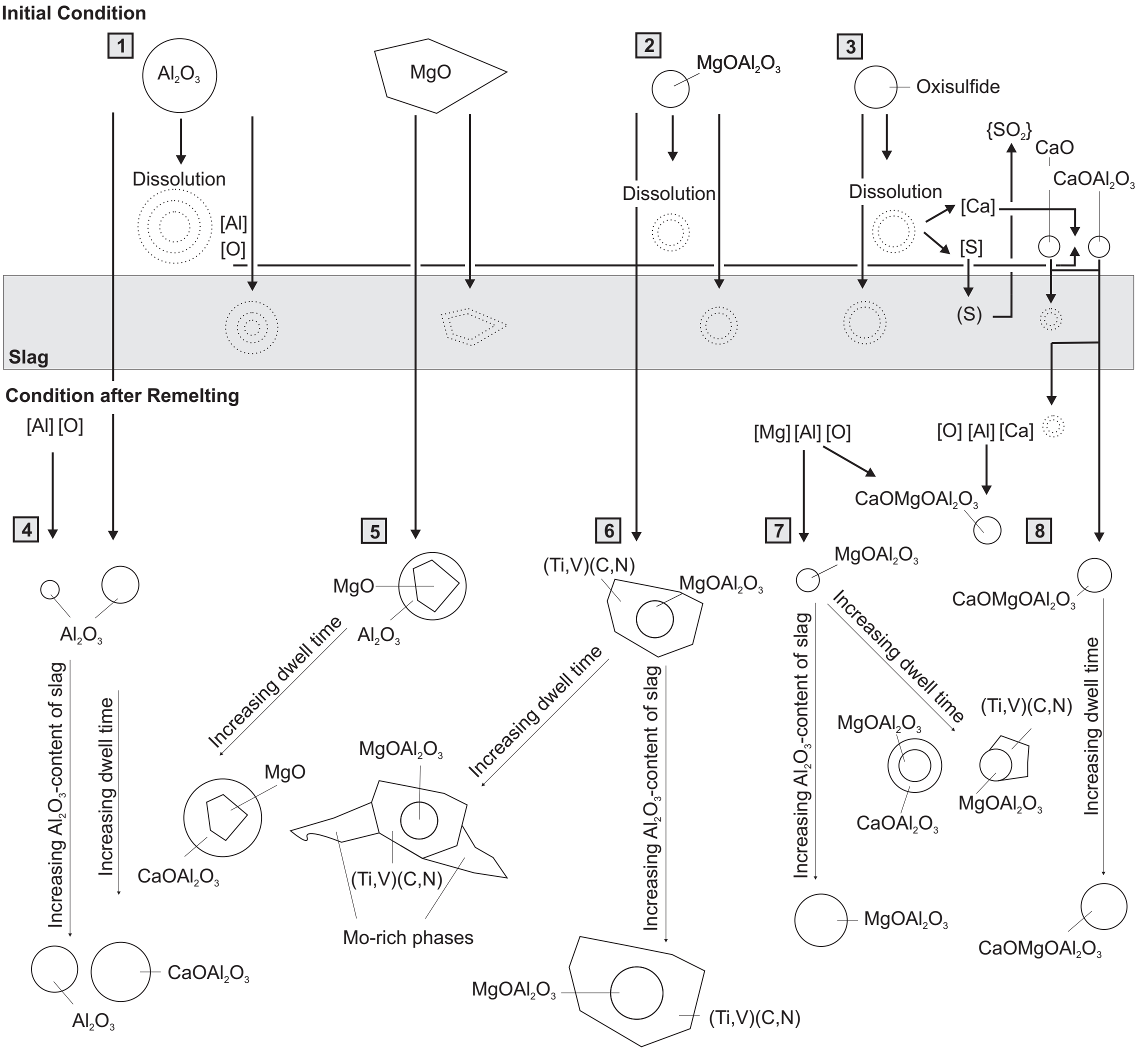

Figure 5.54: Schematic illustration of modification of inclusion morphology through remelting.

The different modification mechanisms are schematically given in Fig. 5.54. The subsequent explanations correspond to the numbering in this figure. Describing the different mechanisms in more detail, the following reaction and interactions steps are essential:

1. Al_2O_3 and $MgOAl_2O_3$ were the predominant oxides in the initial electrode conditions. Kinetic calculations for the defined conditions have shown that Al_2O_3 inclusions tend to dissolve much faster than $MgOAl_2O_3$ in the examined steel composition. Although the mean ECD of Al_2O_3 in the electrodes is remarkably higher than that of $MgOAl_2O_3$, assuming a dwell time of inclusions in the liquid electrode film of 10 s, more than 75 % of Al_2O_3 inclusion between 1 – 10 µm would already have been dissolved, against what practically no dissolution of $MgOAl_2O_3$ would have taken place.

2. Due to the significantly longer dissolution time in the liquid film, the possibility of surviving from the electrode to the ingot if not getting in contact with the slag is considerably higher for $MgOAl_2O_3$ than for Al_2O_3.

3. The presence of Ca-containing oxisulfides in the electrode has a great influence on the inclusion behaviour at the electrode/slag as well as at the droplet/slag interface. Due to the favourable conditions for desulfurisation, the content of oxisulfides is significantly decreased at these reaction

sites. The dissolved *Ca* is supplied to the slag and the *Ca*-activity in the liquid metal increases; CaO respectively $xCaO\ yAl_2O_3$ are formed.

4. As stated beforehand, the possibility for an Al_2O_3 to survive from the electrode to ingot is rather low due to the favourable dissolution conditions. If an Al_2O_3 precipitates at the pool/slag interface respectively in the pool it should be significantly smaller than a relic from the electrode. Increasing dwell time in the liquid pool would mainly effect inclusion composition and therefore would advantage the modification into $xCaO\ yAl_2O_3$. Increasing Al_2O_3-contents in the slag cause a shift towards an increased mean ECD of Al_2O_3 inclusions.

5. If an MgO (the most stable of the mentioned oxides under the assumed conditions) survives from the electrode to the ingot, it tends to be surrounded by an AL_2O_3-layer. Increasing dwell time would not only assist a possible growth of the inclusion, but also effects the modification of the Al_2O_3-layer to $xCaO\ yAl_2O_3$.

6. Since $MgOAl_2O_3$ are more likely to be relics from the electrode than Al_2O_3, also the final inclusion morphology is considerably influenced. These inclusions are often found to act as heterogeneous nuclei for various carbide and nitride phases and therefore mostly have a remarkably higher mean ECD than Al_2O_3 after remelting. In many cases a complete surrounding of the oxide phase by a $(Ti, V)(C, N)$ is observed. An increasing Al_2O_3-content of the slag leads to a further growth of these complex inclusions. An increasing dwell time in the liquid pool advantages the nucleation of *Mo*-rich phases, resulting a significantly increased inclusion size that may reach values > 50 µm.

7. If an $MgOAl_2O_3$ forms at the pool/slag interface respectively in the liquid pool its size is comparable to the sizes of initial $MgOAl_2O_3$ in the electrode. The longer the dwell time, the more likely $(Ti, V)(C, N)$ partly attach to the oxide inclusions. Moreover, the formation of a $xCaO\ yAl_2O_3$-layer around the $MgOAl_2O_3$ was observed with increasing dwell time. Higher Al_2O_3-contents in the slag tend to increase the mean ECD of $MgOAl_2O_3$.

8. The $xCaO\ yAl_2O_3$ formed due to the dissolution of CaS at the electrode/slag and the droplet/slag interface may dissolve in the pool. The dissolved elements can react with dissolved *Mg* or $MgOAl_2O_3$ to form complex CaO-Al_2O_3-MgO inclusions.

Summing up, the morphology of inclusions in remelted samples is seen to be a decisive indicator for the understanding of inclusion behaviour during remelting. Although most so far published works on this topic [135, 153, 154] concluded that no inclusions from the electrode are found in the remelted ingot, also due to the fact that a reliable distinction is really difficult, the present thesis demonstrates an approach to differentiate between inclusions which are relics from the electrode and those who have precipitated in the liquid pool, on the basis of the final inclusion morphology. Considerations dealing with inclusion modification through remelting, especially focussing on changes in inclusion morphology have been recently submitted for publication [223].

As shown by different examples beforehand, the dwell time of inclusions in the liquid pool considerably affects the final inclusion landscape. Although a longer dwell time also increases the possibility of separation of an inclusion at the metal/slag interface, a compromise between sufficient time for separation and limited time for modification has to be assessed. On the basis of the performed considerations, the effect of inclusion modification with longer dwell time in the pool, especially as far as $MgOAl_2O_3$

are concerned, is found to affect the final inclusion size much more negatively than the improvement achieved through longer time for possible flotation. This is concluded primarily due to the fact that the cleanness of the electrode already is comparably high and therefore the percentage of initial macro-inclusions is rather small. This conclusions has not been addressed precisely in literature so far.

Concerning the influence of slag compositions it is concluded that while Al_2O_3 significantly influences the final inclusion size and composition, the influence of CaF_2 on inclusion composition is marginal. An increased Al_2O_3-content of the slag leads to a significant shift of the inclusion composition towards the Al_2O_3-rich corner within the system CaO-Al_2O_3-MgO and an increased mean ECD of oxide inclusions, which agrees with the observations of Mitchell [153]. Thus, CaF_2 mainly affects slag viscosity and therefore the overall removal rate of inclusions. This was also confirmed by experiments with the Laser Scanning Electron Microscope, which showed much shorter dissolution times of oxides in fluoride-slags compared to dissolution times of oxides in fluoride-free slags given in literature [75].

Lastly, it has been found that the initial inclusion composition in the electrode significantly influence the final inclusion composition and inclusion size in the ingot. $MgOAl_2O_3$ inclusions in the electrode (case 6 in Fig. 5.54) are seen to be worst case and therefore the prevention of $MgOAl_2O_3$ already in the primary melting of the electrode is recommended. Against the findings in literature [132], the initial number and size of inclusions in the electrode are not seen to be the most decisive factor for the final overall inclusion content in the remelted ingot. The results of the present thesis affirm that the overall removal rate of inclusions through Electroslag Remelting is strongly dependent on the initial inclusion composition in the electrode. This is in partial agreement with the statements of Povolotskii *et al.* [159] and Mitchell and Burel [160] who ascertained that the chemical composition of inclusion in relation to slag composition is essential for inclusion removal. The negative effect of $MgOAl_2O_3$ during remelting mostly independent of the used slag composition (valid for the investigated ranges and the analysed steel grade) has not been described in literature so far.

6 Summary and Conclusion

The application of hot-work tool steels requires exactly defined properties due to the stresses and strains these steels are exposed to. Not least from an economic viewpoint, an essential criterion is their durability in use. In order to meet these requirements and to consequently produce a precise work piece, mechanical and physical properties of the applied tool steel as well as its surface condition are of special importance.

Since steel properties can be highly influenced by steel cleanness, the content of non-metallic inclusions in the steel matrix is desired to be as low as possible. However, the cleanness of steel cannot only be measured by the overall inclusion content. Several aspects of inclusions including their size and chemical composition as well as their distribution and morphology have to be considered. Electroslag Remelting (ESR), a process often used in stainless steelmaking, does not only enable a considerable decrease of the overall inclusion content but principally also causes a more uniform distribution of inclusions and a reduction of mean inclusion size.

The basic principle of the ESR process consists of the remelting of a so-called consumable electrode which is the product of a precedent casting process. The refining effect is achieved through the contact with a reactive slag bath. Due to steel-slag interactions, also a modification of inclusion composition is observed comparing the initial inclusion landscape in the electrode with the one in the remelted ingot. Within the ESR process three metal/slag reaction sites exist, each of them providing different conditions for inclusion separation and dissolution. In literature, there is neither a clear, consistent conclusion concerning the most decisive reaction site nor regarding the influence of the initial inclusion landscape of the electrode on the final refining effect and the related influencing aspects.

Within the present thesis, the modification of non-metallic inclusions in the steel grade X38CrMoV5-1 through Electroslag Remelting has been investigated in detail—especially focussing on oxides—studying different steps of the remelting process with the use of analytical methods as well as thermodynamic calculations combined with some kinetic considerations.

The main tool for inclusion characterisation within the present work was the automated SEM/EDS analysis, since this method provides a large spectrum of information regarding the number, size, distribution and composition of inclusions. Due to the limited analysed sample area, often the question of its representativeness arises. Consequently, this aspect has been examined in detail within this work coupling a geometric-statistical model with experimental analyses. Next to the determination of the representative sample area for the reliable determination of the mean inclusion size, also the limitations regarding the detection of the maximum inclusion diameter have been examined.

Moreover, in order to appraise the decisive reactions during remelting, laboratory tests in a Tammann Furnace were performed. Different influencing factors like slag composition and duration time were examined. The results of laboratory tests were compared to samples taken from the ESR process and conclusions on the decisive modification mechanisms were drawn. Especially the morphology of inclusions was found to be an important indication for the estimation of procedures during remelting.

6.1 Prospects and Limitations of Automated SEM/EDS Analyses

The expectations associated with methods for inclusion analyses are manifold. Next to a preferably high information content consisting of chemical as well as morphological information, also the necessary time effort, the complexity of analysis and the connected costs are essential and often decisive for the practical application. Moreover, each method offers differences regarding the detectable range of inclusion sizes as well as the analysed sample volume, respectively area.

Automated SEM/EDS analyses have become state of the art in inclusion analysis for research purposes in recent years. Since one analysis not only takes several hours (depending on the detected inclusion content) but also the costs per measuring time are comparatively high, this method has not yet been established for on-line analysis during steel making processes or process control. Moreover, the measured sample area is extremely small compared to the volume of typical aggregates used in steel making. Within the present work a geometric-statistical model was established, calculating the error of area ratio in dependence of a defined inclusion content. The calculation results were compared with experimentally determined data. Thus, the obtained new findings are:

- The defined measuring area of 100 mm^2 is adequate for the determination of the medium inclusion content in the investigated steel grade and therefore results of this methods are applicable and representative for the description of inclusion modification for the defined conditions.
- The inclusion content in the model was defined very base, imitating a very high cleanness level, in order to assess the lower limit for a measuring area under the assumed conditions. It was concluded that a larger measuring area would not essentially improve the results due to the truncation of data based on the detection limit of the analysing method. On the contrary, a reduction of the measuring area < 100 mm^2 would significantly increase the error.
- The stated results enable the determination of the minimal required measuring area depending on the expected inclusion content in order to obtain representative results. Thus, not only the representativeness of automated SEM/EDS analysis for the defined conditions has been proved within this study, but also the measuring area can now be adjusted to the investigated steel grade resulting in a remarkable saving of time and costs.

Despite the mentioned advances, automated SEM/EDS analyses are afflicted with limitations. The macro-cleanness has reached a very high level in the last 20 years. Thus, due to the fact that macro-inclusions are distributed rather arbitrarily in steel, their detection is also almost left to chance. Furthermore, it must be considered that most inclusion characterisation methods only offer a two-dimensional view on the inclusion landscape. As shown in the experimental part of this thesis, the maximum detected inclusion diameter varies considerably in automated SEM/EDS measurements of comparable samples, while the mean diameter is in good concordance.

It can be concluded that automated SEM/EDS analyses do not provide significant information concerning the maximum inclusion diameter. In order to get representative information on this aspect, clearly a larger analysed sample volume is required. The most effective way to get a mostly entire impression of the inclusion landscape, is the combination of different analysing methods. Within this work, next to automated SEM/EDS analyses also electrolytic extraction was used offering two essential advantages: Firstly, through the dissolution of steel matrix a three-dimensional view of the inclusions is gained and secondly, the possibility of detecting a macro-inclusion is remarkably higher.

Finally, it can be stated that no inclusion characterisation method can be seen to be the ultimate one. Every method offers several advantages and disadvantages and it is therefore of great importance to deal with the particular limitations of the used method before interpreting the obtained results. Nevertheless, through the detailed examination of automated SEM/EDS analysis and the development of a geometric-statistical model combined with experimental analyses also a first important step towards the extension of the application of this method, which has up to now mainly been employed for research-dominated topics, was made.

6.2 Inclusion Modification through Remelting

Through Electroslag Remelting an essential modification of non-metallic inclusions is observed. Within the present work this modification was examined out of a experimental as well as thermodynamic viewpoint. For all calculations and experiments the steel grade X38CrMoV5-1 was used. Samples of electrode material as well as remelted ingots were analysed. Moreover, the liquid film at the electrode tip as well as the droplets were investigated in detail. Two different initial electrode conditions were compared. Since Al_2O_3 and $MgOAl_2O_3$ were the predominant oxide inclusion types in the electrodes, this work mainly concentrated on these inclusions.

The results of the performed investigations of samples from the ESR process can be summarised as follows:

- Despite different initial electrode conditions, the chemical compositions of non-metallic inclusions within the system CaO-Al_2O_3-MgO in the remelted ingots were similar if the same slag composition was used. However, considerable differences concerning the morphology of inclusions between the electrode and the remelted ingot have been determined.

- Under the defined conditions, the performed kinetic calculations predict a significantly faster dissolution of Al_2O_3 in the liquid metal film at the electrode tip than of $MgOAl_2O_3$. As a consequence of a higher dissolution time of $MgOAl_2O_3$ at the electrode tip, also the possibility of surviving from the electrode to the ingot for this inclusion type—assuming that the inclusion does not get in contact with the slag—is increased.

- The presence of Ca-containing oxisulfides in the electrode has a great influence on the inclusion behaviour at the electrode/slag as well as at the droplet/slag interface. Due to the favourable conditions for desulfurisation, the content of oxisulfides is significantly decreased at these reaction sites. The dissolved Ca is supplied to the slag and the Ca-activity in the liquid metal increases; CaO respectively $xCaO\ yAl_2O_3$ are formed.

- Comparing the inclusion size distributions between electrode, droplet and ingot, the electrode/slag interface is seen to be the decisive reaction site for inclusion removal, since the inclusion size distribution in the droplet is already very similar to the final inclusion distribution in the remelted ingot. Furthermore, considering the relation between droplet and inclusion size, a separation of an inclusion from the droplet centre is rather unlikely in the view of very short available reaction times.

- The dwell time of an inclusion in the liquid pool strongly influences its final morphology. Basically, if an inclusion re-precipitates at the pool/slag interface or in the liquid pool it is remarkably smaller than residual inclusions from the electrode which have much more time to grow or modify.

In the present case, a modification was primarily observed for $MgOAl_2O_3$, acting as heterogeneous nuclei for carbides and nitrides, resulting in an considerably increased mean inclusion diameter. Consequently, on the one hand a relatively short dwell time of inclusions in the pool seems to be advantageous for the stated reasons, but on the other hand a longer dwell time would increase the possibility of flotation and subsequent inclusion separation.

- Due to the changes in slag composition during remelting caused by continuous deoxidation, a shift of inclusion composition towards the Al_2O_3-rich corner within the system CaO-Al_2O_3-MgO was determined with increasing ingot height.

The results of laboratory experiments with the Tammann Furnace with slags out of the systems CaO-Al_2O_3-MgO and CaO-Al_2O_3-CaF_2 are in good agreement with the findings stated above as far as the change in chemical composition, size and morphology of inclusions is concerned. Out of the variation of slag composition and duration time the following conclusions are drawn:

- The variation of slag composition causes a significant change of the chemical composition of inclusions within the system CaO-Al_2O_3-MgO. Higher Al_2O_3-contents in the slag cause a considerable shift towards the Al_2O_3-rich corner. Additionally, an increased mean inclusion diameter of oxides was found with increasing Al_2O_3-content of the slag.
- Comparing the results between the two different slag systems examined in laboratory experiments, the influence of CaF_2 on the inclusion composition is seen to be marginal. Since CaF_2 mainly influences the physical properties of the slag, differences were only observed for the percentage of inclusion separation. A Laser Scanning Confocal Microscope was used for additional in-situ studies of the dissolution behaviour of oxides in CaF_2-slags. The obtained results affirm significant differences in dissolution time of Al_2O_3 in fluoride-slags compared to CaF_2-free slags.
- With longer duration time at reaction temperature—imitating longer dwell time in the liquid pool—a significant increase of the mean inclusion diameter was observed due to the nucleation of $(Ti, V)(C, N)$ and Mo-rich phases primarily attached to $MgOAl_2O_3$.

Generally, thermodynamic calculations with *FactSage* provide a good indication for the prediction of the influence of different slag compositions on inclusion modification. Despite the limited available data for CaF_2-slags, a satisfying consistency with the experimental results was observed. Nevertheless, an experimental verification of calculated results is recommended. The laboratory set-up offers a valuable tool for the experimental simulation of the modification of inclusions through metal/slag interactions. Although the Electroslag Remelting process itself could not be simulated in detail with the available experimental layout, fundamental knowledge concerning the modification behaviour of oxides during remelting and the decisive influencing factors was gained which might be useful for further industrial process optimisation, especially concerning the formation of rather large multi-phase inclusions.

Based on the considerations and conclusions within the present thesis, the main new findings concerning the modification of oxides through remelting are:

1. The morphology of inclusions in remelted samples is seen to be a decisive indicator for the understanding of inclusion behaviour during remelting. In contrast to the explanations published

in literature so far which do not propose a suitable way for the distinction between inclusions coming from the electrode and those who re-precipitated in the pool, within the present thesis a first approach based on the changes in inclusion morphology is developed in order to identify inclusions which are most possibly relics from the electrode.

2. The initial inclusion composition in the electrode significantly influences the final inclusion size and composition in the remelted ingot. Since $MgOAl_2O_3$ inclusions tend to act as heterogeneous nuclei for carbides and nitrides, the avoidance of this inclusion type in the electrode is highly recommended.

3. The initial number and size of inclusions in the electrode have not shown to be the most decisive factor for the final overall inclusion content in the remelted ingot. On the contrary, the overall removal rate of inclusions through Electroslag Remelting strongly depends on the initial inclusion composition in the electrode.

4. The effect of inclusion modification with longer dwell time in the pool, especially as far as $MgOAl_2O_3$ are concerned, is found to affect the final inclusion size much more negatively than the improvement achieved through longer time for possible flotation. This is concluded primarily from the fact that the cleanness of the electrode already is comparatively high and therefore the percentage of initial macro-inclusions is rather small.

With regards to a further process optimisation, these finding not only enable an estimation of the percentage of inclusions which are separated due to steel/slag interactions under different conditions and thus yields important results about the decisive influencing factors. Moreover, important knowledge is gained with regard to the question of which inclusion types should be avoided in the initial electrode as their dissolution or removal is rather unlikely.

6.3 Outlook

Although many questions were answered within the present work through the combination of analytic, thermodynamic and experimental considerations, there are still numerous aspects which future works should focus on. Firstly, since CaF_2 in the slag has a major influence on the separation of inclusions during remelting, the dissolution behaviour of oxides in fluoride-slags should be studied more precisely, particularly as currently only very limited data is published in the literature for the mentioned slag systems. One of the most adequate tools for this purpose is certainly the Laser Scanning Confocal Microscope.

Additionally, the further development of thermodynamic databases concerning fluoride-slags is of major importance. Although reliable results with *FactSage* are gained for slags up to a CaF_2-content of approximately 35 %, the effect of higher CaF_2-contents on inclusion behaviour cannot be investigated satisfactorily with today's available databases.

Secondly, the presence of $MgOAl_2O_3$ inclusions in steels manufactured via different steelmaking processes has substantially increased in recent years due to application of different refractory material as well as slags containing MgO. 25 years ago this inclusion type was not in the focus of interest of research work and therefore not all questions about its behaviour in different steels and process routes have been answered yet. In the present thesis, the behaviour of $MgOAl_2O_3$ in a hot-work tool steel was studied during the Electroslag Remelting. Further examinations considering other stainless steel types would be very interesting.

As far as inclusion characterisation is concerned, there certainly a potential for the further improvement of the today commonly applied methods exists. A main challenge will be the simultaneous detection of a large inclusion size spectrum with one method, resulting in a more comprehensive view of the overall inclusion landscape.

Finally, as shown within the present thesis, the micro-cleanness can significantly influence the appearance of meso- and even macro-inclusions, which might be detrimental to steel properties in unfavourable conditions. Thus, the aim for future work necessarily seems to be an enhanced understanding of the relation between macro- and micro-cleanness in different steelmaking processes as well as steel types, in order to meet the continuously increasing requirements on special steels.

Bibliography

[1] R. Kiessling. Clean steel – a debatable concept. *Metal Science*, 14(5):161–172, 1980.

[2] B. Klarenfjord, A. Schindler, and I. Schruff. A new rating chart for the microstructure of hot-work tool steel. In H. Berns, editor, *Progress in Tool Steels—Proceedings of the 4th International Conference on Tooling*, pages 147–155, Bochum, Germany, 1996. Ruhr-Universität Bochum.

[3] J. Angeli. *Prüftechnik und Analytik zur Einschlussbestimmung*. ASMET Seminar, Leoben, 2006.

[4] H. V. Atkinson and G. Shi. Characterization of inclusions in clean steels: a review including the statistics of extremes methods. *Progress in Materials Science*, 48(5):457–520, 2003.

[5] R. Kiessling and N. Lange. *Non-metallic inclusions in steel*. The Institute of Materials, London, 1989.

[6] T. Gladman. Developments in inclusion control and their effect on steel properties. *Ironmaking and Steelmaking*, 19(6):457–463, 1992.

[7] S. H. Lee, C. Tse, K. W. Yi, P. Misra, V. Chevrier, C. Orrling, S. Sridhar, and A. W. Cramb. Separation and dissolution of Al_2O_3 inclusions at slag/metal interfaces. *Journal of Non-Crystalline Solids*, 282(1):41–48, 2001.

[8] K. Yamada, T. Watanabe, K. Fukuda, T. Kawaragi, and T. Tashiro. Removal of nonmetallic inclusion by ceramic filter. *Transactions of the Iron and Steel Instiute of Japan*, 27(11):873–877, 1987.

[9] Verein Deutscher Eisenhüttenleute, editor. *Schlackenatlas*. Verlag Stahleisen, Düsseldorf, 1981.

[10] S. Yang, L. Zhang, J.Li, L. Sun, K. Peaslee, and Y. Chen. Formation and modification of $MgOAl_2O_3$-based inclusions in alloy steels. In *AISTech 2011*, pages 591–606, Indianapolis, USA, 2011. AIST—Association for Iron & Steel Technology.

[11] H. Tang and J. Li. Thermodynamic analysis on the formation mechanism of $MgO \cdot Al_2O_3$ spinel type inclusions in casing steel. *International Journal of Minerals, Metallurgy, and Materials*, 17(1):32–38, 2010.

[12] J. T. Haddock, I. Hussain, A. G. Fox, J. K. Batham, and E. T. R. Jones. New MgO-CaO based reagent for ladle treatment of steel. *Ironmaking and Steelmaking*, 21(6):479–486, 1994.

[13] S. K. Saxena. Production of ultra-clean steels with better mechanical properties with magnesium treatment. In *Steelmaking Conference*, volume 79, pages 89–96, Pittsburgh, USA, 1996. Iron and Steel Society of AIME.

[14] C. Bertrand, J. Molinero, S. Landa, R. Elvira, M. Wild, G. Barthold, P. Valentin, and H. Schifferl. Metallurgy of plastic inclusions to improve fatigue life of engineering steels. *Ironmaking and Steelmaking*, 30(2):165–169, 2003.

[15] K. Mizuno, H. Todoroki, M. Noda, and T. Tohge. Effects of *Al* and *Ca* in ferrosilicon alloys for deoxidation on inclusion composition in type 304 stainless steel. *Iron and Steelmaker*, 28(8):93–101, 2001.

[16] H. Todoroki, K. Mizuno, M. Noda, and T. Tohge. Formation mechanism of spinel type inclusion in 304 stainless steel deoxidized with ferrosilicon alloys. In *Steelmaking Conference*, volume 84, pages 331–341, Baltimore, USA, 2001. Iron and Steel Society of AIME.

[17] J.H. Park and Y.Y. Lee. Formation of spinel phase in the liquid inclusions during stainless steelmaking processes. In *Sohn International Symposium—Advanced Processing of Metals and Materials*, pages 405–419, San Diego, CA, USA, 2006. The Minerals, Metals & Materials Society.

[18] J.H. Park. Formation mechanism of spinel-type inclusions in high-alloyed stainless steel melts. *Metallurgical and Materials Transactions B*, 38(4):657–663, 2007.

[19] H. Itoh, M. Hino, and S. Ban-Ya. Deoxidation equilibrium of magnesium in liquid iron. *Tetsu-to-Hagane (Journal of the Iron and Steel Institute of Japan)*, 83(10):623–628, 1997.

[20] H. Itoh, M. Hino, and S. Ban-Ya. Assessment of Al deoxidation equilibrium in liquid iron. *Tetsu-to-Hagane (Journal of the Iron and Steel Institute of Japan)*, 83(12):773–778, 1997.

[21] H. Itoh, M. Hino, and S. Ban-Ya. Thermodynamics on the formation of spinel nonmetallic inclusion in liquid steel. *Metallurgical and Materials Transactions B*, 28B:953–956, 1997.

[22] H. Itoh, K. Fuji, T. Nagasaka, and M. Hino. Gibbs free energy and conditions of spinel ($MgO \cdot Al_2O_3$) formation in liquid steel. *Steel Research International*, 74(2):86–90, 2003.

[23] H. Itoh, M. Hino, and S. Ban-Ya. Thermodynamics on the formation of non-metallic inclusion of spinel ($MgOAl_2O_3$) in liquid steel. *Tetsu-to-Hagane (Journal of the Iron and Steel Institute of Japan)*, 84 (2):85–90, 1998.

[24] W.G. Seo, W.H. Han, J.S. Kim, and J.J. Pak. Deoxidation equilibria among Mg, Al and O in liquid iron in the presence of $MgO \cdot Al_2O_3$ spinel. *ISIJ International*, 43(2):201–208, 2003.

[25] S.K. Jo, B. Song, and S.H. Kim. Thermodynamics on the formation of spinel ($MgO \cdot Al_2O_3$) inclusion in liquid iron containing chromium. *Metallurgical and Materials Transactions B*, 33B:703–709, 2002.

[26] K. Fuji, T. Nagasaka, and M. Hino. Activities of the constituents in spinel solid solution and free energies of formation of MgO, $MgO \cdot Al_2O_3$. *ISIJ International*, 40(11):1059–1066, 2000.

[27] M. Jiang, X. Wang, B. Chen, and W. Wang. Formation of $MgO \cdot Al_2O_3$ inclusions in high strength alloyed structural steel refined by CaO-SiO_2-MgO-Al_2O_3 slag. *ISIJ International*, 48(7):885–890, 2008.

[28] H. Todoroki and K. Mizuno. Effect of silica in slag on inclusion compositions in 304 stainless steel deoxidized with aluminium. *ISIJ International*, 44(8):1350–1357, 2004.

[29] H. Ohta and H. Suito. Deoxidation equilibria of calcium and magnesium in liquid iron. *Metallurgical and Materials Transactions B*, 28B(6):1131–1139, 1997.

[30] J.H. Park, S.B. Lee, and H.R. Gaye. Thermodynamics of the formation of MgO-Al_2O_3-TiO_x inclusions in Ti-stabilized 11Cr-ferritic stainless steel. *Metallurgical and Materials Transactions* B, 39(6): 853–861, 2008.

[31] T. Nishi and K. Shinme. Variation of inclusion morphology in molten *Fe-Ni* alloys. *Tetsu-to-Hagane (Journal of the Iron and Steel Institute of Japan)*, 84(2):97–102, 1998.

[32] T. Nishi and K. Shinme. Formation of spinel inclusions in molten stainless steel under *Al* deoxidation with slags. *Tetsu-to-Hagane (Journal of the Iron and Steel Institute of Japan)*, 84(12):837–843, 1998.

[33] W.Y. Cha, D.S. Kim, Y.D. Lee, and J.J. Pak. A thermodynamic study on the inclusion formation in ferritic stainless steel melt. *ISIJ International*, 44(7):1134–1139, 2004.

[34] J.W. Kim, S.K. Kim, D.K. Kim, Y.D. Lee, and P.K. Yang. Formation mechanism of *Ca-Si-Al-Mg-Ti-O* inclusions in type 304 stainless steel. *ISIJ International*, 36(Supplement):140–143, 1996.

[35] Y. Ehara, S. Yokoyama, and M. Kawakami. Control of formation of spinel inclusion in type 304 stainless steel by slag composition. *Tetsu-to-Hagane (Journal of the Iron and Steel Institute of Japan)*, 93 (7):475–482, 2007.

[36] J.H. Park and D.S. Kim. Effect of CaO–Al_2O_3–MgO slags on the formation of MgO–Al_2O_3 inclusions in ferritic stainless steel. *Metallurgical and Materials Transactions* B, 36B(4):495–502, 2005.

[37] J.H. Park, D.S. Kim, and S.B. Lee. Inclusion control of ferritic stainless steel by aluminum deoxidation and calcium treatment. *Metallurgical and Materials Transactions* B, 36B(1):67–73, 2005.

[38] G. Okuyama, K. Yamaguchi, S. Takeuchi, and K. Sorimachi. Effect of slag composition on the kinetics of formation of $MgO \cdot Al_2O_3$ inclusions in aluminum killed ferritic stainless steel. *ISIJ International*, 40(2):121–128, 2000.

[39] S.A. Nightingale and B.J. Monaghan. Kinetics of spinel formation and growth during dissolution of MgO in CaO-Al_2O_3-SiO_2 slag. *Metallurgical and Materials Transactions* B, 39(5):643–648, 2008.

[40] M. Jiang, X. H. Wang, and W. J. Wang. Control of non-metallic inclusions by slag-metal reactions for high strength alloying steels. *Steel Research International*, 81(9):759–765, 2010.

[41] M. Jiang, X. Wang, B. Chen, and W. Wang. Laboratory study on evolution mechanisms of non-metallic inclusions in high strength alloyed steel refined by high basicity slag. *ISIJ International*, 50(1):95–104, 2010.

[42] Y.J. Kang, F. Li, K. Morita, and D. Sichen. Mechanism study on the formation of liquid calcium aluminate inclusion from $MgO \cdot Al_2O_3$ spinel. *Steel Research International*, 77(11):785–792, 2006.

[43] J.H. Park. Thermodynamic investigation on the formation of inclusions containing $MgO \cdot Al_2O_3$ spinel during 16Cr – 14Ni austenitic stainless steel manufacturing processes. *Materials Science and Engineering* A, 472(1-2):43–51, 2008.

[44] J. H. Park. Solidification structure of CaO-SiO_2-MgO-Al_2O_3($-CaF_2$) systems and computational phase equilibria: Crystallization of $MgAl_2O_4$ spinel. *Calphad*, 31(4):428–437, 2007.

[45] G.W. Shannon. *Oxide Inclusion Behaviour at the Steel/Slag Interface.* PhD thesis, Carnegie Mellon University, 2007.

[46] A. K. Sinha and Y. Saha. Mathematical modeling of inclusion transport and removal in continuous casting tundishes. *ISIJ International*, 33(5):556–566, 1993.

[47] Y. Miki and B. G. Thomas. Modeling of inclusion removal in a tundish. *Metallurgical and Materials Transactions B*, 30B(4):639–654, 1999.

[48] K. Okazawa, T. Toh, J. Fukuda, T. Kawase, and M. Toki. Fluid flow in a continuous casting mold driven by linear induction motors. *ISIJ International*, 41(8):851–858, 2001.

[49] Q. Yuan, B. G. Thomas, and S. P. Vanka. Study of transient flow and particle transport in continuous steel caster molds: Part I. Fluid flow. *Metallurgical and Materials Transactions B*, 35B(4):685–702, 2004.

[50] Q. Yuan, B. G. Thomas, and S. P. Vanka. Study of transient flow and particle transport in continuous steel caster molds: Part II. Particle transport. *Metallurgical and Materials Transactions B*, 35B(4): 703–714, 2004.

[51] L. Zhang, S. Taniguchi, and K. Matsumoto. Water model study on inclusion removal from liquid steel by bubble flotation under turbulent conditions. *Ironmaking and Steelmaking*, 29(5):326–336, 2002.

[52] K. Nakajima and K. Okamura. Inclusion transfer behavior across molten steel-slag interface. In 4th *International Conference on Molten Slag and Fluxes*, page 505, Sendai, Japan, 1992.

[53] D. Bouris and G. Bergeles. Investigation of inclusion re-entrainment from the steel-slag interface. *Metallurgical and Materials Transactions B*, 29B(3):641–649, 1998.

[54] J. Strandh, K. Nakajima, R. Eriksson, and P. Jonsson. A mathematical model to study liquid inclusion behavior at the steel-slag interface. *ISIJ International*, 45(12):1838–1847, 2005.

[55] G. Shannon, L. White, and S. Sridhar. Modeling inclusion approach to the steel/slag interface. *Materials Science and Engineering A*, 495(1-2):310–315, 2008.

[56] P. Kozakevitch and L.D. Lucas. The part played by surface phenomena in the elimination of solid inclusions in a metal bath. *Revue de Métallurgie*, 65(9):589–598, 1968.

[57] P. Kozakevitsch and M. Olette. Role of surface phenomena in the mechanism for eliminating solid inclusions. *Revue de Métallurgie*, 68(10):635–646, 1971.

[58] P. V. Riboud and M. Olette. Mechanisms of some of the reactions involved in secondary refining. In 7th *International Conference on Vacuum Metallurgy*, pages 879–898, Tokyo, Japan, 1982.

[59] G. N. Shannon and S. Sridhar. Separation of alumina inclusions across interfaces between molten steel and ladle-, tundish-, and mold slags. In *EPD Congress held at the TMS Annual Meeting*, San Francisco, USA, 2005.

[60] J. Strandh. *A Study on the Solid and Liquid Inclusion Separation at the Steel/Slag Interface.* PhD thesis, KTH Royal Institute of Technology, 2005.

[61] J. Strandh, K. Nakajima, R. Eriksson, and P. Jonsson. Solid inclusion transfer at a steel-slag interface with focus on tundish conditions. *ISIJ International*, 45(11):1597–1606, 2005.

[62] J. Wikstroem. *A Mathematical and Experimental Study of Inclusion Behavior at a Steel-Slag Interface.* PhD thesis, KTH Royal Institute of Technology, 2007.

[63] J. Wikstroem, K. Nakajima, H. Shibata, A. Tilliander, and P. Joensson. In situ studies of agglomeration between Al_2O_3-CaO inclusions at metal/gas, metal/slag interfaces and in slag. *Ironmaking and Steelmaking*, 35(8):589–599, 2008.

[64] K. Beskow, P. Dayal, J. Bjorkvall, M. Nzotta, and Du Sichen. A new approach for the study of slag-metal interface in steelmaking. *Ironmaking and Steelmaking*, 33(1):74–80, 2006.

[65] P. Dayal, K. Beskow, J. Bjorkvall, and Du Sichen. Study of slag/metal interface in ladle treatment. *Ironmaking and Steelmaking*, 33(6):454–464, 2006.

[66] S. Taira, K. Nakashima, and K. Mori. Kinetic behavior of dissolution of sintered alumina into CaO-SiO_2-Al_2O_3 slags. *Steel Research International*, 33(1):116–123, 1993.

[67] X. Yu, R. J. Pomfret, and K. S. Coley. Dissolution of alumina in mold fluxes. *Metallurgical and Materials Transactions B*, 28B(2):275–279, 1997.

[68] S. Sridhar and A.W. Cramb. Kinetics of Al_2O_3 dissolution in CaO-MgO-SiO_2-Al_2O_3 slags: in situ observations and analysis. *Metallurgical and Materials Transactions B*, 31B(2):406–410, 2000.

[69] M. Valdez, K. Prapakorn, A.W. Cramb, and S. Seetharaman. A study of the dissolution of Al_2O_3, MgO and $MgAl_2O_4$ particles in a CaO-Al_2O_3-SiO_2 slag. *Steel Research International*, 72(8):291–297, 2001.

[70] M. Valdez, K. Prapakorn, A.W. Cramb, and S. Sridhar. Dissolution of alumina particles in CaO-Al_2O_3-MgO slags. *Ironmaking and Steelmaking*, 29(1):47–52, 2002.

[71] K. W. Yi, C. Tse, J.H. Park, M. Valdez, A. W. Cramb, and S. Sridhar. Determination of dissolution time of Al_2O_3 and MgO inclusions in synthetic Al_2O_3-CaO-MgO slags. *Scandinavian Journal of Metallurgy*, 32(4):177–184, 2003.

[72] B.J. Monaghan, L. Chen, and J. Sorbe. Comparative study of oxide inclusion dissolution in CaO-SiO_2-Al_2O_3 slag. *Ironmaking and Steelmaking*, 32(3):258–264, 2005.

[73] B. J. Monaghan and L. Chen. The dissolution of alumina in CaO-SiO_2-Al_2O_3 slags. *Steel Research International*, 76(5):348–354, 2005.

[74] C. Tse, S. H. Lee, S. Sridhar, and A. W. Cramb. In situ observations relevant to clean steel: dissolution of alumina particles in slags. In *Steelmaking Conference*, volume 83, pages 331–341, Pittsburgh, USA, 2000. Iron and Steel Society of AIME.

[75] A. B. Fox, M. E. Valdez, J. Gisby, R. C. Atwood, P. D. Lee, and S. Sridhar. Dissolution of ZrO_2, Al_2O_3, MgO and $MgAl_2O_4$ particles in a B_2O_3 containing commercial fluoride-free mould slag. *ISIJ International.Vol.44*, 44(5):836–845, pp. 836-845. 2004.

[76] O. Levenspiel. *Chemical Reaction Engineering.* John Wiley and Sons, New York, 1999.

[77] M. Valdez, G.S. Shannon, and S. Sridhar. The ability of slags to absorb solid oxide inclusions. *ISIJ International*, 46(3):450–457, 2006.

[78] M. Valdez, K. Prapakorn, S. Sridhar, and A. W. Cramb. Dissolution of inclusions in steelmaking slags. In *Iron & Steel Society International Technology Conference and Exposition*, pages 789–798, Indianapolis, USA, 2003.

[79] B.J. Monaghan and L. Chen. Effect of changing slag composition on spinel inclusion dissolution. *Ironmaking and Steelmaking*, 33(4):323–330, 2006.

[80] Jin-Hong Park, In-Ho Jung, and Hae-Geon Lee. Dissolution behavior of Al_2O_3 and MgO inclusions in the CaO-Al_2O_3 SiO_2 slags: Formation of ring-like structure of $MgAl_2O_4$ and Ca_2SiO_4 around MgO inclusions. *ISIJ International*, 46(11):1626–1634, 2006.

[81] R.K. Hopkins. Manufacture of metal articles, 1940. United States Patent 2,191,475.

[82] R.K. Hopkins. Manufacture of alloy ingots, 1940. United States Patent 2,191,479.

[83] H. Jäger. Electroslag remelting processes. In H. Trenkler and W. Krieger, editors, *Gmelin-Durrer – Metallurgy of Iron*. Springer Verlag, Berlin, 1988.

[84] A. Mitchell. Solidification in remelting processes. *Materials Science and Engineering A*, 413-414: 10–18, 2005.

[85] P. Machner. Die Hauptparameter des ESU-Prozesses und deren Einfluss auf den Blockaufbau und die Wirtschaftlichkeit des Verfahrens. *Berg- und Hüttenmännische Monatshefte*, 118(11):365–373, 1973.

[86] D. A. Povolotskii, V. E. Roshchin, and V. A. Golubtsov. Removal of the products of deoxidation in the successive states of electroslag and vacuum arc remelting. *Steel in the USSR*, 6(6):326–328, 1976.

[87] G.A. Khasin, V. I. Lazarev, and G. A. Antropova. Reducing the non-metallic inclusion content of steel during electroslag remelting. *Stal'*, pages 520–521, 1976.

[88] A. Mitchell. Electroslag and vacuum arc remelting processes. In Charles R. Taylor, editor, *Electric Furnace Steelmaking*. Book Crafters, Chelsea, 1985.

[89] B.K. Damkroger, J.B. Kelley, M.E. Schlienger, J.A. van den Avyle, R.L. Williamson, and F.J. Zanner. The influence of VAR processes and parameters on white spot formation in alloy 718. In E.A. Loria, editor, *Superalloys 718, 625, 706, and Various Derivatives*, pages 125–135, The Minerals, Metals & Materials Society, 1994.

[90] F.J. Zanner, L.A. Bertram, R. Harrison, and H.D. Flanders. Relationships between furnance voltage signature and the operation parameter arc power, arc current, CO pressure and electrode gap during vakuum arc melting INCONEL 718. *Metallurgical Transactions B*, 17B:357–365, 1986.

[91] F.J. Zanner, C. Adsczik, T. O'Brian, and L.A. Bertram. Observations of melt rate as a function of arc power, CO pressure, and electrode gap during vacuum consumable arc remelting of Inconel 718. *Metallurgical Transactions B*, 15B:117–125, 1984.

[92] W. Zhang, P.D. Lee, and M.McLean. Inclusion behaviour during vacuum arc remelting of nickel based superalloys. In *European Congress on Advanced Materials and Processes*, pages 123–128, Munich, Germany, 1999. Leybold-Heraeus GmbH & Co KG.

[93] X. Wang, M.D. Barratt, R.M. Ward, and M.H. Jacobs. The effect of VAR process parameters on white spot formation in INCONEL 718. *Journal of Materials Science*, 39:7169–7174, 2004.

[94] K. Koch. *Schlacken in der Metallurgie*. Verlag Stahleisen, Düsseldorf, 1984.

[95] A. Mitchell. Slag functions in the ESR process. In *International Symposium on Liquid Metal Processing and Casting*, pages 195–200, Santa Fé, USA, 2005. ASM International.

[96] W.E. Durckworth and G. Hoyle. *Electro-slag Refining*. Chapman and Hall Ltd., London, 1969.

[97] G. Hoyle. *Electroslag Processes*. Applied Science Publishers, New York, 1982.

[98] W. Holzgruber. *Das Elektorschlacke-Umschmelzverfahren*. PhD thesis, Montanuniversität Leoben, 1967.

[99] J.C. Korp. Optimierung der Aufstickung mit Si_3N_4 in einer Druck-Elektro-Schlacke-Umschmelzanlage. Master's thesis, Montanuniversität Leoben, 2001.

[100] R. Hasenhündl, S. Eglsäer, H. Orthaber, R. Tanzer, and W. Schützenhöfer und R. Schneider. Herstellung, Eigenschaften und Anwendung ausgewählter korrosionsbeständiger, stickstofflegierter Stähle. *Berg- und Hüttenmännische Monatshefte*, 154(5):194–199, 2009.

[101] R. Schneider, F. Koch, P. Wurzinger, G. Reiter, and J. Korp. DESU-Prozessoptimierung zur Herstellung stickstofflegierter Stähle mit höchsten Reinheitsgraden. *Berg- und Hüttenmännische Monatshefte*, 147(1):1–6, 2002.

[102] R. Hasenhündl. *Neue Schlackentechnologie zur Herstellung hoch stickstofflegierter Stähle im Druck-Elektroschlackeumschmelzverfahren*. PhD thesis, Montanuniversität Leoben, 2009.

[103] H. Holzgruber. *ESRR – Electro Slag Rapid Remelting*. PhD thesis, Montanuniversität Leoben, 2005.

[104] K.C. Mills and B.J. Keene. Physicochemical properties of molten CaF_2-based slags. *International Metals Reviews*, 26(1):28–69, 1981.

[105] R.H. Nafziger. The system $CaF_2 + Al_2O_3 + CaO$ under one-third atmosphere of helium. *High Temperature Science*, 5:414–422, 1973.

[106] A.K. Chatterjee and G.I. Zhmoidin. The phase equilibrium diagram of the system $CaF_2 + Al_2O_3 + CaO$. *Journal of Material Science*, 7:93–97, 1972.

[107] R. Ries and K. Schwerdtfeger. Contribution to the phase diagram CaO-Al_2O_3-CaF_2. *Archiv für das Eisenhüttenwesen*, 51(4):123–129, 1980.

[108] A. Mitchell. The chemistry of ESR slags. *Canadian Metallurgical Quarterly*, 20(1):101–112, 1981.

[109] P.P. Eseev. The physical properties of industrial CaO-Al_2O_3-CaF_2 system slags. *Automatic Welding*, 11(1):42–47, 1967.

[110] M.W. Davies and Wright F.A. Methods, apparatus: new product research, process development and design—The viscosity of calcium fluoride-based slags. *Chemistry and Industry*, pages 359–363, 1970.

[111] M. Hajduk and T.E. Gammal. Schriftumszusammenstellung von Leitfähigkeitsmessungen an CaF_2-haltigen Schlackenschmelzen. *Stahl und Eisen*, 99(3):113–116, 1979.

[112] W. Chiho and X. Shunhua. Electrical conductivity of molten ESR slags of $CaF_2 + Al_2O_3$ and $CaF_2 + Al_2O_3 + CaO$ systems for ESR. *ISIJ International*, 33(2):239–244, 1993.

[113] A. Mitchell and J. Cameron. Electrical conductivity of some liquids in the system CaF_2+CaO+Al_2O_3. *Metallurgical Transactions*, 2(12):3361–3366, 1971.

[114] J.C. Korp. *Einfluss ausgewählter Schlackenkomponenten auf den Energieverbrauch beim Elektroschlacke Umschmelzen (ESU)*. PhD thesis, Montanuniversität Leoben, 2007.

[115] J. Korp, R. Schneider, P. Presoly, and W. Krieger. Experimentelle Bestimmung der spezifischen elektrischen Leitfähigkeit hoch CaF_2-haltiger Schlacken. Teil II Ergebnisse aus Labor und industrieller Praxis. *Berg- und Hüttenmännische Monatshefte*, 153(5):175–181, 2008.

[116] J. Korp, R. Rabitsch, R.Schneider, and W. Krieger. Experimentelle Bestimmung der spezifischen elektrischen Leitfähigkeit hoch CaF_2-haltiger Schlacken. Teil I Experimenteller Aufbau und Auswertungsmethode. *Berg- und Hüttenmännische Monatshefte*, 151(5):184–189, 2006.

[117] K. Ogino and S. Hara. Density, surface tension and electrical conductivity of calcium fluoride based fluxes for electroslag remelting. *Tetsu-to-Hagane (Journal of the Iron and Steel Institute of Japan)*, 63(13):2141–2151, 1977.

[118] K. Ogino, H. Shitaike, and S. Hara. Density and surface tension of CaF_2-based binary melts. *Tetsu-to-Hagane (Journal of the Iron and Steel Institute of Japan)*, 66(2):169–178, 1980.

[119] S. Hara and K. Ogino. The densities and surface tensions of fluoride melts. *ISIJ International*, 29 (6):477–485, 1989.

[120] B.V. Muu, S. Krauss, and H. Burghardt. Untersuchung der Grenzflächenspannung zwischen Schlacken des Systems CaO-Al_2O_3-CaF_2 und Stahlschmelzen aus 100Cr6 und X85WMoCo655. *Neue Hütte*, 21(6):335–340, 1976.

[121] S. Hara and K. Ogino. Density of CaO-Al_2O_3-CaF_2-melts for electroslag remelting. *Canadian Metallurgical Quarterly*, 20(1):113–116, 1981.

[122] T. E. Gammal and M. Hajduk. The use of CaF_2 free slags in the ESR-process. In 5^{th} *International Conference on Vacuum Metallurgy and Electroslag Remelting Processes*, pages 141–147, Munich, Germany, 1976.

[123] G. Pateisky. The application of fluoride-free slag in aproduction ESR-plant. In 5^{th} *International Conference on Vacuum Metallurgy and Electroslag Remelting Processes*, pages 145–148, Munich, Germany, 1976. Leybold-Heraeus GmbH & Co KG.

[124] J.Medved, V. Kontarev, and L. Kosec. Fluorspar free slags for the electro-slag-remelting process. In 5^{th}*International Conference on Clean Steel*, pages 147–152, Balatonfured, Hungary, 1977.

[125] G. Brückmann and K. Schwerdtfeger. Änderungen in der Betriebsweise des ESU-verfahrens: Verwendbarkeit calciumfluoridfreier Schlacken und Schmelzen unter nichtoxidierender Atmosphäre. *Stahl und Eisen*, 103(8):387–399, 1983.

[126] C. K. Cooper, D. Ghosh, D. A. R. Kay, and R. J. Pomfret. ESR reaction sites. In *Electric Furnace Conference*, pages 8–12., Pennsylvania, USA, 1970.

[127] J. Kreyenberg and K. Schwerdtfeger. Stirring velocities and temperature field in the slag during electroslag remelting. *Archiv für das Eisenhüttenwesen*, 50(1):1–6, 1979.

[128] A. Mitchell and S. Joshi. The thermal characteristics of the electroslag process. *Metallurgical Transactions*, 4(3):631–642, 1973.

[129] M. Choudhary and J. Szekely. Modelling of fluid flow and heat transfer in industrial-scale ESR system. *Ironmaking and Steelmaking*, 8(5):225–231, 1981.

[130] B. Korousic. Tropfenbildung beim Elektro-Schlacke-Umschmelzverfahren. *Archiv für das Eisenhüttenwesen*, 47(5), 1976.

[131] W. Holzgruber and E. Plöckinger. Metallurgische und verfahrenstechnische Grundlagen des Elektroschlacke-Umschmelzens von Stahl. *Stahl und Eisen*, 88(12):638–648, 1968.

[132] L. Zhengbang. Mechanism of oxide inclusions removal in the ESR process. In G.K. Bhat, editor, *Special Melting and Processing Technologies*. Park Ridge, New York, 1989.

[133] M. E. Fraser and A. Mitchell. Mass transfer in the electroslag process. Part I: mass-transfer model. *Ironmaking and Steelmaking*, 5(5):279–287, 1976.

[134] M. E. Fraser and A. Mitchell. Mass transfer in the electroslag process. Part II: Mass-transfer coefficients. *Ironmaking and Steelmaking*, 3(5):288–301, 1976.

[135] M. Kljuev and V. Spicberg. Abscheidung und Bildung nichtmetallischer Einschlüsse im Metall beim Elektroschlacke-Umschmelzverfahren. *Stal'*, pages 590–594, 1969.

[136] H. Miska and M. Wahlster. Verhalten des Sauerstoffs beim Elektro-Schlacke-Umschmelzen. *Archiv für das Eisenhüttenwesen*, 44(1):19–24, 1974.

[137] W. Thomas. The influence of the electrode and in particular its tip on the operating behaviour of electroslag remelting furnaces. In 5th *International Conference on Vacuum Metallurgy and Electroslag Remelting Processes*, pages 161–164, Munich, Germany, 1976. Leybold-Heraeus GmbH & Co KG.

[138] B. Korousic and W. Holzgruber. Über die Oxidationsgleichgewichte beim Elektro-Schlacke-Umschmelzen. *Berg- und Hüttenmännische Monatshefte*, 122(7):287–291, 1977.

[139] M. Klujev and J. Mironov. Über die Größe der Reaktionsoberfläche beim Elektroschlackenumschmelzverfahren. *Stal'*, pages 964–968, 1967.

[140] A. Mitchell, S. Joshi, and J. Cameron. Electrode temperature gradients in the electroslag process. *Metallurgical Transactions*, 2(2):561–567, 1971.

[141] A.H. Dilawari and J. Szekely. A mathematical model of slag and metal flow in the ESR process. *Metallurgical Transactions C*, 8B:227–236, 1977.

[142] M. Choudhary and J. Szekely. The modeling of pool profiles, temperature profiles and velocity fields in ESR systems. *Metallurgical Transactions B*, 11:439–453, 1980.

[143] B. Hernandez-Morales and A. Mitchell. Review of mathematical models of fluid flow, heat transfer, andmass transfer in electroslag remelting process. *Ironmaking and Steelmaking*, 26(6):423–438, 1999.

[144] A. Kharicha, A. Ludwig, and M. Wu. Simulation of droplet formation during DC electro-slag-remelting. In *First International Conference on Modelling and Simulation of Metallurgical Processes – Steelsim*, pages 343–360, Brno, Czech Republic, 2005.

[145] A. Kharicha, A. Ludwig, M. Wu, H. Scholz, W. Schützenhöfer, G. Reiter, R. Tanzer, A. Mackenbrock, O. Köser, A. Carosi, R. Sorci, and F. Arcobello-Varlese. Integrated simulation of advances protective gas electro-slag remelting for the production of high-quality steels. In *Research Fund for Coal and Steel*, volume 23917. European Commission, 2009.

[146] A. Kharicha, W. Schützenhöfer, A. Ludwig, and G. Reiter. Simulation of the slag/pool interface in the ESR process by using a VOF technique. In C.A. Gandin and M. Bellet, editors, *Modeling of Casting, Welding and Advanced Solidification Processes – XI*, pages 985–992, Opio, France, 2006. The Minerals, Metals & Materials Society.

[147] A. Kharicha A., A. Ludwig, and M. Wu. Shape and stability of the slag/melt interface in a small DC ESR process. *Materials Science and Engineering A*, 413-414:29–134, 2005.

[148] A. Kharicha, A. Mackenbrock, A. Ludwig, W. Schützenhöfer, V. Maronnier, M. Wu, O. Köser, and R. Tanzer. Selected numerical investigations on ESR process. In *International Symposium on Liquid Metal Processing and Casting*, pages 113–119, Nancy, France, 2007.

[149] H.-J Klingelhöfer, P. Mathis, and A. Choudhury. Ein Beitrag zur Metallurgie des Elektro-Schlacke-Umschmelzverfahrens. *Archiv für das Eisenhüttenwesen*, 42(5):299–306, 1971.

[150] H. Miska. *Verhalten von Sauerstoff und Schwefel während des Elektroschlacke-Umschmelzens.* PhD thesis, Technische Universität Clausthal, 1971.

[151] S. Ban-Ya, M. Hobo, T. Itoh, T. Kaji, and M. Hino. Sulphide capacity and sulphur solubility in $CaO\text{-}Al_2O_3$ and $CaO\text{-}Al_2O_3\text{-}CaF_2$ slags. *ISIJ International*, 44(11):1810–1816, 2004.

[152] W. Holzgruber and H. Holzgruber. Recent innovations in electroslag remelting. *Iron and Steelmaker*, 25(10):107–112, 1998.

[153] A. Mitchell. Oxide inclusion behaviour during consumable electrode remelting. *Ironmaking and Steelmaking*, 1(3):172–179, 1974.

[154] J. F. Liddle. Removal of inclusions during electroslag refining. *Internatational Symposium on Chemical Metallurgy of Iron and Steel*, pages 66–74, 1973.

[155] G. W. Lloyd, T. A. Owen, and L. A. Baker. Mechanism of electroslag refining. *Journal of the Australian Institute of Metals*, 16(1):17–25, 1971.

[156] T. E. Gammal and F. A. Denkhaus. Verbesserung des mikroskopischen Reinheitsgrades beim Elektroschlacke-Umschmelzen. *Stahl und Eisen*, 109(23):39–43, 1989.

[157] D. A. R. Kay and R. J. Pomfret. Removal of oxide inclusions during AC electroslag remelting. *Journal of the Iron and Steel Institute*, 209(12):962–965, 1971.

[158] B. E. Paton, B. I. Medovar, Y. U. G. Emelianenko, G. A. Boiko, and V. A. Tihonov. Investigation methods, transformation and removal of non-metallic inclusions during ESR. In *Fifth Internatational Symposium on Electroslag and Other Special Melting Technologies*, pages 433–448, Pittsburgh, USA, 1975.

[159] D. A. Povolotskii, V. Voronov, and B. Nikitin. Removal of non-metallic inclusions during electroslag remelting. *Steel in the USSR*, 1:952–954, 1971.

[160] A. Mitchell and B. Burel. The solution rate of alumina in CaF_2-Al_2O_3 slags. *Metallurgical Transactions*, 1:2253–2256, 1970.

[161] V. Roshchin, N. Mal'kov, D. A. Povolotskii, S. Gimadeev, and P. Biryukov. Transformation of nonmetallic inclusions in metal of consumable electrodes during remelting. *Steel in the USSR*, 8(12): 37–41, 1978.

[162] B. Rehak, I. Kasik, and M. Karnovsky. A contribution to the study of the behaviour of nonmetallic inclusions in electroslag remelting process. In 5th *International Conference on Vacuum Metallurgy and Electroslag Remelting Processes*, pages 147–152, Munich, Germany, 1976. Leybold-Heraeus GmbH & Co KG.

[163] T. McAloon. Clean steel is harder to measure than produce. *Iron and Steelmaker*, 16(6):5–6, 1989.

[164] M.Pohl, M.Merz, and W.G. Burchard. Über den Zusammenhang zwischen Tiefätzung und Rückstandsisolierung bei der metallkundlichen Analyse nichtmetallischer Einschlüsse. *Praktische Metallographie*, 14:126–139, 193.

[165] DIN 50602. *Mikroskopische Prüfung von Edelstählen auf nichtmetallische Einschlüsse mit Bildreihen.* Deutsches Institut f"ur Normung, Berlin, 1985.

[166] ASTM E45. *Annual Book of ASTM Standards*. American Society for Testing and Materials, Philadelphia, 2002.

[167] D. Moll. Grundlagen der Reinheitsgradbestimmung nach der neuen Norm DIN EN 10247:2007 "Metallographische Prüfung des Gehaltes nichtmetallischer Einschlüsse in Stählen mit Bildreihen". *Sonderband Praktische Metallographie*, 40:255–260, 2008.

[168] L. Zhang and B. Thomas. State of the art in evaluation and control of steel cleanliness. *ISIJ International*, 43(3):271–291, 2003.

[169] R. Meilland and L. Dosdat. Rapid characterisation of inclusionnary cleanliness in steels by PDA-OES mapping. *La Revue de Métallurgie*, 99(4):373–382, 2002.

[170] R. Meilland, H. Hocquaux, C. Louis, L. Pollino, and F. Hoffert. Rapid characterization of heterogeneities (inclusions and segregations) by spectral techniques. *La Revue de Métallurgie*, 96(1): 89–97, 1999.

[171] M. Goransson and P.G. Jonsson. Ideas for process control of inclusion characteristics during steelmaking. *ISIJ International*, 41(Supplement):S42–S46, 2001.

[172] F. Reinholdsson, A. Lind, R. Nilsson, P. Sjödin, and P. Jönsson. A metallurgical tool for rapid determination of micro inclusion characteristics in bearing steel production. *ISIJ International*, 37 (6):637–639, 1997.

[173] H. Th Ploegaert and J. von der Stel. Small inhomogeneities in flat steel products to be seen or not to be seen. *La Revue de Métallurgie*, 93(1):111–118, 1996.

[174] M. Nuspl, W. Wegscheider, J. Angeli, W. Posch, and M. Mayr. Qualitative and quantitative determination of micro-inclusions by automated SEM/EDX analysis. *Analytical and Bioanalytical Chemistry*, 379(4):640–645, 2004.

[175] M.D. Jaraković, L.B. Nedelijković, and M.B. Durdević. Influence of sample preparation and examination procedures on the results of the quantitative metallographic assessment of the nonmetallic oxide inclusions in steel. *Praktische Metallographie*, 33(6):280–293, 1996.

[176] L. Zhang and B. G. Thomas. State of the art in the control of inclusions during steel ingot casting. *Metallurgical and Materials Transactions B*, 37B(5):733–761, 2006.

[177] H. Eichelkraut and M. Weinberg. Silenos – steel inclusion level evaluation by numerical optical systems. In *XXIX. Verformungskundliches Kolloquium*, Planneralm, Austria, 2010.

[178] S.R. Story, G.E. Goldsmith, and G.L. Klepzig. Study of cleanliness and castability in Ti-stabilized ultra low carbon steels using automated SEM inclusion analysis. *La Revue de Métallurgie*, 105(5): 272–279, 2008.

[179] G. Gigacher, W. Krieger, P. Scheller, and C. Thomser. Non-metallic inclusion in high-managanese-alloy steels. *Steel Research International*, 76(9):644–649, 2005.

[180] W. Winkler, J. Angeli, and M. Mayr. Automated SEM-EDX cleanness analysis and its application in metallurgy. *Berg- und Hüttenmännische Monatshefte*, 152(1):4–9, 2007.

[181] S.L Flegler, J.W. Heckmann, and K.L. Komparens. *Elektronenmikroskopie*. Spektrum Akademischer Verlag, Heidelberg, 1995.

[182] P.F. Schmidt. *Praxis der Rasterelektronenmikroskopie und Mikrobereichsanalyse*. Expert Verlag, Renningen-Malmsheim, 1994.

[183] J. Cybo. Sterelogical alterations of non-metallic inclusions, fracture morphology and alloy impact strength after blowing active powders into liquid steel. *Steel Research*, 66(4):167–171, 1995.

[184] H. V. Atkinson, G. Shi, C. M. Sellars, and C. W. Anderson. Application of the generalized pareto distribution to the estimation of the size of the maximum inclusion in clean steels. *Acta Materialia*, 47(5):1455–1468, 1999.

[185] C. W. Anderson, G. Shi, H. V. Atkinson, C. M. Sellars, and J. R. Yates. Interrelationship between statistical methods for estimating the size of the maximum inclusion in clean steels. *Acta Materialia*, 51(8):2331–2343, 2003.

[186] Y. Murakami, Y. Uemura, and K. Kawakami. Some problems in the application of statistics of extreme values to estimation of the maximum inclusion size of non-metallic inclusions in metals. *Journal of the Japan Society of Mechanical Engineers*, 88:58–62, 1989.

[187] Y. Uemura and Y. Murakami. A numerical simulation of evaluating the maximum size of inclusions to examine the validity of the metallographic determination of the maximum size of inclusions. *Journal of the Japan Society of Mechanical Engineers*, 89:162–167, 1990.

[188] H. V. Atkinson, G. Shi, C. M. Sellars, and C. W. Anderson. Statistical prediction of inclusion sizes in clean steels. In A. Strang and J. Cawley, editors, *Quantitative Microscopy of High Temperature Materials*, volume 16, pages 1175–1180, Sheffield, UK, 2000. Institute of Materials.

[189] H. V. Atkinson, C. W. Anderson, G. Shi, and C. M. Sellars. The precision of methods using the statistics of extremes for the estimation of the maximum size of inclusions in clean steels. *Acta Materialia*, 48(17):4235–4246, 2000.

[190] Y. Murakami, T. Toriyama, and E. M. Coudert. Instructions for a new method of inclusion rating and correlations with the fatigue limit. *ASTM Journal of Testing and Evaluation*, 22(4):318–326, 1994.

[191] Y. Murakami. Inclusion rating by statistics of extreme values and its application to fatigue strength prediction and quality control of materials. *Journal of Research at the National Institute of Standards and Technology*, 99(4):345–351, 1994.

[192] T. Toriyama, Y. Murakami, T. Yamashita, K. Tsubota, and K. Furumura. Inclusion rating by statistics of extreme for electron beam remelted super clean bearing steel and its application to fatigue strength prediction. *Tetsu-to-Hagane (Journal of the Iron and Steel Institute of Japan)*, 81(10):1019–1024, 1995.

[193] Y. Murakami, M. Takada, and T. Toriyama. Super-long life tension-compression fatigue properties of quenched and tempered 0.46 % carbon steel. *International Journal of Fatigue*, 20(9):661–667, 1998.

[194] S. Zhou, Y. Murakami, Y. Fukushima, and S. Beretta. Statistics of extremes analysis of nonmetallic inclusions based on 3D inspection. *Tetsu-to-Hagane (Journal of the Iron and Steel Institute of Japan)*, 87 (12):748–755, 2001.

[195] G. Shi, H. V. Atkinson, C. M. Sellars, and C. W. Anderson. Comparison of extreme value statistics methods for predicting maximum inclusion size in clean steels. *Ironmaking and Steelmaking*, 26(4): 239–246, 1999.

[196] G. Shi, H. V. Atkinson, C. M. Sellars, C. W. Anderson, and J. R. Yates. Computer simulation of the estimation of the maximum inclusion size in clean steels by the generalized pareto distribution method. *Acta Materialia*, 49(10):1813–1820, 2001.

[197] G. Shi, H. V. Atkinson, C. M. Sellars, and C. W. Anderson. Maximum inclusion size in two clean steels. i. comparison of maximum size estimates by statistics of extremes and generalised pareto distribution methods. *Ironmaking and Steelmaking*, 27(5):355–360, 2000.

[198] G. Shi, H. V. Atkinson, C. M. Sellars, and C. W. Anderson. Maximum inclusion size in two clean steels. ii. use of data from cold crucible remelted samples and polished optical cross-sections. *Ironmaking and Steelmaking*, 27(5):361–366, 2000.

[199] S. Beretta, C. Anderson, and Y. Murakami. Extreme value models for the assessment of steels containing multiple types of inclusion. *Acta Materialia*, 54(8):2277–2289, 2006.

[200] S. Beretta and Y. Murakami. Largest-extreme-value distribution analysis of multiple inclusion types in determining steel cleanliness. *Metallurgical and Materials Transactions B*, 32(3):517–523, 2001.

[201] J. Takahashi and H. Suito. Effect of omitting small sectioned particles with limited cross-sectional area on characterisation of secondary phase particles. *Material Science and Technology*, 18(1):103–110, 2002.

[202] P. Klinger and W. Koch. Beitrag zur elektrolytischen Bestimmung von nicht-metallischen Einschlüssen im Stahl. *Archiv für das Eisenhüttenwesen*, 11:569–582, 1938.

[203] W. Koch and I. Ramsauer. Die elektrochemischen Vorgänge bei der elektrolytischen Isolierung von Gefügebestandteilen der Stähle mit Wechselstrom. *Archiv für das Eisenhüttenwesen*, 25:93–106, 1954.

[204] W. Koch and H. Sundermann. Grundlagen der Isolierung von Gefügebestandteilen in Stählen. *Radex Rundschau*, 5/6:679–693, 1957.

[205] W. Koch and H. Sundermann. Beiträge zur Isolierung der Sulfide. *Radex Rundschau*, 5/6:725–726, 1957.

[206] O. Ericson. *An Experimental Study of Liquid Steel Sampling*. PhD thesis, Department of Material Science and Engineering Stockholm, 2009.

[207] proionic GmbH. proionic. `http://www.proionic.at`, 2011.

[208] S.K. Michelic, G. Wieser, and C. Bernhard. On the representativeness of automated SEM/EDS analyses for inclusion characterisation with special regard to the measured sample area. *ISIJ International*, 51(5):769–775, 2011.

[209] S.K. Michelic, M. Hartl, G. Wieser, and C. Bernhard. Kombinierter Einsatz von analytischen und statistischen Methoden zur qualitativen und quantitativen Bestimmung des Reinheitsgrads von Stählen. In *Sonderband Praktische Metallographie*, volume 42, pages 359–364, 2010.

[210] Verein deutscher Eisenhüttenleute, editor. *Werkstoffkunde Stahl*. Springer Verlag, Berlin, 1985.

[211] Böhler Edelstahl GmbH & Co KG. Special steel manual, 2006.

[212] D.C. Hilty and T. H. Kaveney. Stainless steel melting. In C. R. Taylor, editor, *Electric Furnace Steelmaking*. Book Crafters, Chelsea, 1985.

[213] G.K. Sigworth and J.F. Elliot. The thermodynamics of liquid dilute iron alloys. *Metal Science Journal*, 8:298–310, 1974.

[214] M. Nadif and C. Gatellier. Influence d'une addition de calcium ou de magnésium sur la solubilité de oxygène et du soufre dans l'acier liquide. *La Revue de Métallurgie*, 83(8):377–394, 1986.

[215] T. Hong and T. Debroy. Time-temperature-transformation diagrams for the growth and dissolution of inclusions in liquid steels. *Scripta Materialia*, 44:847–852, 2003.

[216] M.J. Whelan. On the kinetics of precipitate dissolution. *Metal Science Journal*, 3(5):95–97, 1969.

[217] S.S. Babu, S.A. David, J.M. Vitec, K. Mundra, and T. DebRoy. Development of macro- and microstructures of carbon-maganese low alloy steel welds: inclusion formation. *Materials Science and Technology*, 11(2):186–199, 1995.

[218] E.T. Turkdogan. *Physical Chemistry of High Temperature Technology*. Academic Press, New York, 1980.

[219] S.K. Michelic, M. Hartl, and C. Bernhard. Interactions of non-metallic inclusions with steel and slag: Thermodynamic modeling, experiments and metallographic analyses. In *EPD Congress*, pages 723–730, San Diego, USA, 2011. The Minerals, Metals & Materials Society.

[220] S.K. Michelic, M. Hartl, and C. Bernhard. Thermodynamic and experimental study on the modification of non-metallic inclusions through contact with CaO-Al_2O_3-MgO slags. In *AISTech 2011*, pages 617 – 626, Indianapolis, USA, 2011. AIST—Association for Iron & Steel Technology.

[221] C. Bernhard, S. Schider, A. Sormann, G. Xia, and S. Illie. Erste Ergebnisse des neuen Hochtemperatur-Konfokalmikroskops and Lehrstuhl für Metallurgie. *Berg- und Hüttenmännische Monatshefte*, 156(5):161–167, 2011.

[222] E. Andersson and D. Sichen. The effect of Caf_2 in the slag in ladle refining. *Steel Research International*, 80(8):544–551, 2009.

[223] S. Michelic, R. Tanzer, W. Schützenhöfer, and C. Bernhard. Modification of non-metallic inclusions in the ESR process by steel-slag interaction: Thermodynamic and experimental considerations. In *International Symposium on Liquid Metal Processing and Casting*, page forthcoming, 2011.

Nomenclature

Roman Alphabet

a	Activity
A	Area
b	Constant
d	Diameter
c	Concentration
D	Diffusion coefficient
$\Delta G^\circ(T)$	Gibbs Free Energy
f	Activity coefficient
F_b	Buoyancy force
F_d	Drag force
F_m	Added mass force
$F_{\sigma,Z}$	Capillary force
g	Gravitational acceleration constant
i	Index
k	Mass transfer coefficient
K	Equilibrium constant
m	Melt rate
M	Mass
N	Number of inclusions
p	Partial pressure
r	Radius
R_e	Reynolds number
t	Time
T	Temperature
U	Velocity
v_E	Solidification rate
v_B	Ingot growth rate
V	Volume
W_A	Work of adhesion
X	Molar fraction
Y	Mass action concentration
z	Index

Greek Alphabet

α	Scale parameter of the Gumbel distribution
β_M	Static velocity of the melt
δ	Boundary layer
Δ	Flotation coefficient
η	Viscosity
η_{dA}	Harmonic mean
κ	Electrical conductivity
λ	Location parameter of the Gumbel distribution
μ	Mean
ϱ	Density
σ	Interfacial tension or Standard deviation
σ'	Scale parameter of the GPD distribution
τ	Total dissolution time
θ	Contact angle
φ	Deformation degree
ξ	Shape parameter of the GPD distribution
ζ	Reaction rate constant

Superscripts, Subscripts and Indices

$\Box^*$	Calculated
$\Box_0$	Starting or initial condition
$\Box_A$	Area
$\Box_D$	Droplet
$\Box_E$	Electrode
$\Box_G$	Gas
$\Box_i$	Index
$\Box_I$	Inclusion
$\Box_m$	Index
$\Box_M$	Metal
$\Box_P$	Pool
$\Box_S$	Slag
$\Box_T$	Total
$\Box_V$	Volume

Acronyms

AOD	Argon Oxygen Decarburisation
BSE	Back-scattered Electron
CFD	Computational Fluid Dynamics
ECD	Equivalent Circle Diameter
EDS	Energy Dispersive X-ray Spectroscopy
EPMA	Electron Probe Micro Analyser
ESR	Electroslag Remelting
ESRR	Electroslag Rapid Remelting
GPD	General Pareto Distribution
ICP-MS	Inductive Coupled Plasma Mass Spectrometry
LF	Ladle Furnace
LSCM	Laser Scanning Confocal Microscope
NMI	Non-metallic Inclusion
OES/PDA	Optical Emission Spectrometry with Pulse Discrimination Analysis
PESR	Pressure Electroslag Remelting
SEM	Scanning Electron Microscope
SEN	Submerged Entry Nozzle
SEV	Statistics of Extreme Values
SILENOS	Steel Inclusion Level Evaluation by Numerical and Optical Systems
US	Ultrasonic Sound
VAR	Vacuum Arc Remelting
VOD	Vacuum Oxygen Decarburisation
VOF	Volume of Fluid
XRD	X-ray Diffraction

List of Figures

List of Tables